Density functional theory study of phase stability and defect thermodynamics in Fe-oxyhydroxide mineral materials

By:

Nathan Douglas Pinney

A dissertation submitted in partial fulfillment of
the requirements for the degree of

Doctor of Philosophy
(Materials Science)

at the
UNIVERSITY OF WISCONSIN–MADISON
2013

Date of final oral examination: August 27, 2013

THESIS COMMITTEE:
Dane Morgan, Associate Professor, Materials Science and Engineering
Izabela Szlufarska, Associate Professor, Materials Science and Engineering
Huifang Xu, Associate Professor, Geoscience
Donald Stone, Professor, Materials Science and Engineering
Xudong Wang, Assistant Professor, Materials Science and Engineering

Acknowledgements and Preface

In my career at the University of Wisconsin-Madison I have benefitted greatly by having access not only to world-class scientific and learning resources, but also to a network of advisors, instructors, colleagues and friends that challenged me and broadened my knowledge in myriad ways. Particular acknowledgements are deserved by those individuals without whom my success as a graduate student and researcher would not have been possible.

First and foremost I recognize the professional and personal guidance provided by my graduate advisor, Prof. Dane Morgan. Prof. Morgan's brand of scientific inquiry has set a high standard for research quality that I hope to replicate in future endeavors. I thank him for his patience, flexibility and personal support throughout my graduate career.

I also extend special thanks to Prof. Izabela Szlufarska, whose feedback throughout the progression of my research work has resulted in improvements to the quality of the work, as well as my own understanding of the material.

My research work at the University of Wisconsin-Madison was funded by a National Science Foundation (NSF) Collaborative Research in Chemistry grant, which involved cross-disciplinary research collaborations with faculty, students, and scientists from several other institutions. Prof. Clare Grey provided considerable research expertise and valuable constructive feedback as our research efforts began to take shape. Geochemical and crystallographic expertise and insight from collaborators Dr. F. Marc Michel, Prof. Brian Phillips, Prof. John Parise, Prof. Daniel Strongin were invaluable to our collaborative progress. Prof. James Kubicki and Dr. Derek Middlemiss aided me by sharing their considerable computational and scientific expertise toward the completion of my research goals.

I thank my colleagues, both past and present, in the Computational Materials Group for

their work to maintain a symbiotic and collaborative work environment from which we all benefit. Due to the computational nature of our research work, I recognize in particular the efforts of CMG system administrators, and computer software and hardware teams for their dedicated efforts to keep our shared CPUs running smoothly day and night.

On a more personal level, I am thankful for the support of my family and friends throughout the tedious process of graduate research. My parents have been a source of encouragement and unflinching support, as well as, on occasion, gas money. My friends, especially those with whom I began graduate school in 2007, have provided a sympathetic outlet for commiseration as well as co-development as we made our way through professional and personal challenges.

As my thesis completion process draws to a close, I must thank my thesis committee members, Profs. Huifang Xu, Don Stone, and Xudong Wang, for their patience and willingness to contribute their time and thoughts toward the successful completion of my degree.

This document was prepared independently by the author and as such the author takes full responsibility for any errors found herein.

Nathan D. Pinney

Thesis Abstract

Continuing economic development and population growth has placed increasing demands on global freshwater aquifers and surface waters for drinking water, and industrial and agricultural purposes. The search for abundant, safe, and sustainable water supplies in the face of growing stresses on water resources has led to ongoing study of the natural and anthropogenic factors that govern water quality, chemistry, and contamination. Natural and man-made contaminants found in groundwater, surface water, and soil environments can threaten aqueous ecosystems, and can in turn harm humans dependent on these natural resources. Research efforts to understand, predict and ultimately control the fate of contaminant species are often anchored by the understanding of (geo)chemical phenomena at mineral surfaces with which aqueous contaminants interact.

Fe-(oxyhydr)oxide materials are among the most important minerals for determining the geochemical fate of many common contaminant species. These materials are ubiquitous, commonly found in soils, sediments, and groundwater environs across the globe, and they react strongly with many of the heavy metal and oxyanion pollutants that cause serious damage to water safety and quality around the world. Often embodied as nanoparticulate or nanocrystalline materials, the Fe-(oxyhydr)oxides typically present large amounts of reactive surface area. At these surfaces, contaminant ions can adsorb and bind, or be enveloped and mineralized within the bulk of the material. However, the nature of these favorable reactions is not necessarily permanent, as changing solution conditions (e.g., temperature, pH) can destabilize, dissolve or restructure Fe-(oxyhydr)oxide particles and surfaces, causing the release of previously contained contaminants back into the environment.

The ready synthesis of Fe-(oxyhydr)oxide materials from common and inexpensive reactants makes these materials attractive as possible candidates for engineered filtration media that are designed for a particular contaminant sorption loading in mind. However, much work remains with regard to the fundamental properties of these materials and the

control thereof for targeted applications.

Using computational materials science techniques, this thesis examines several phenomena that are observed to influence the thermodynamic and structural properties of natural and synthetic Fe-(oxyhydr)oxides, namely bulk crystal structure and energetics, surface energy and surface reactivity, and two point defect types found on Fe-(oxyhydr)oxide cation lattices; aluminum substituents and cation vacancies replaced with structurally-bound water molecules.

In this work, particular attention is paid to the structure, stability and reactivity of ferrihydrite, arguably the most important of the Fe-(oxyhydr)oxide phases in the context of aqueous contaminant sorption phenomena. While the fundamental crystal structure of ferrihydrite is still a matter of debate in the geological/geochemical community, this work adopts the single-phase structural model of Michel et al. for computational study for a variety of reasons. In each sub-study, the conclusions drawn about Michel-model ferrihydrite (i.e., its stability, magnetism, tendency to form defects) is compared to experimental data on ferrihydrite where available. This thesis does not seek to champion the Michel structural model of ferrihydrite, but rather to evaluate the properties of this model derived from computational study in the context of known properties of this material in the real world.

Table of Contents

1 Thesis Overview

1.1 Fe-(oxyhydr)oxide material occurrence, characteristics and applications

Fe-oxyhydroxides and oxides are common, naturally occurring mineral materials in soils, ground and surface water environments. They are formed by the weathering of other Fe-bearing materials, or as the products of the precipitation of aqueous Fe^{3+}, often in association with acidic conditions caused when groundwater dissolves sulfides, especially pyrite, exposed by metal and coal mining activities (acid mine drainage) [1]. While the formation of Fe-oxyhydroxide and oxide materials in streams and aquifers can lead to direct negative outcomes (e.g., disruption or clogging of water flows by large volumes of mineral flocculants, light and nutrient deprivation of plants coated by mineral sediments, etc.), these materials can also serve useful roles in the remediation of other negative impacts associated with mining activities and soil disturbances. Due to their high surface area and reactivity toward aqueous ions, Fe-(oxyhydr)oxides can act as sorbents of contaminants that have even greater potential for environmental damages and thus play an important role in determining the geochemical fate of heavy metals and oxyanion species of environmental importance (e.g. Pb^{2+}, AsO_4^{3-}, SO_4^{2-}, among others) [2]. However, these desirable surface properties are not shared identically across the family of Fe-(oxyhydr)oxide phases and lead to differing sorption profiles of contaminant ions dependent on Fe-(oxyhydr)oxide phase composition, temperature, and pH. Because redissolution or other release of contaminant species adsorbed on or coprecipitated within Fe-(oxyhydr)oxide materials would be undesirable, the long-term surface reactivity and phase stability of the materials over a range of composition and environmental conditions are issues of primary interest.

Fe-(oxyhydr)oxides exist in an array of phases and polymorphs, as well as in a range of particle sizes and morphologies. Crystallinity also varies, with some phases exhibiting well-ordered crystalline forms, while others are typically nanocrystalline or amorphous. The Fe-(oxyhydr)oxides of greatest environmental significance are typically less-ordered nanocrystalline and/or nanoparticulate materials with correspondingly high surface area.

Figure 1-1: The author, Nathan Pinney, near a stream in which orange-colored Fe-(oxyhydr)oxide precipitates, likely ferrihydrite, have coated the stream bed. The location where these photos was taken, near Oglesby, IL, is a few kilometers downhill from several open-pit cement mines.

The metastable oxyhydroxide ferrihydrite ($Fe_5O_8H•xH_2O$) is among the most common initial precipitate phases in natural environments and is exclusively nanoparticulate. Lepidocrocite (γ-FeOOH) is also observed naturally, but it is metastable with respect to its polymorph goethite (α-FeOOH), the most stable of the oxyhydroxides under typical surface conditions. Hematite (α-Fe_2O_3), which often forms as the result of hydrothermal phase transformation of ferrihydrite or goethite, is competitively stable with goethite in surface water and soil environments and is the long-term stable phase in the absence of water. Hematite can exist in annealed micro- or macro-crystalline forms, but is also commonly formed in the nanoparticle size ranges typical of the related oxyhydroxide materials. Other oxide materials of common interest include magnetite (Fe_3O_4) and maghemite (γ-Fe_2O_3), which share a common oxygen and cation lattice and are notable for their ferromagnetic properties, which lend them to common use in magnetic data storage tapes and discs. These two oxide materials are of minor prevalence in ground and surface water environments, and are thus not extensively studied in this work.

Historically, Fe-oxides and oxyhydroxides have been (and still are) used as components of dyes and pigments due to their deep red, yellow, and brown colorations, which are dependent on phase composition, particle size, and dopant/contaminant content. In modern times, these materials are used as inexpensive sorption substrates for waterborne contaminants, especially heavy metals, in industrial-scale water filtration and purification systems, but the potential for broader application in water filtration and contaminant

plume control is high. Oxide phases are also used as catalysts for industrial processes, including the water gas shift reaction used to form high purity hydrogen gas preceding the synthesis of ammonia [1]. Oxyhydroxide phases including ferrihydrite and goethite have been shown to strongly adsorb aqueous carbonate ions and have accordingly been proposed as components of carbon capture and sequestration technologies for the mitigation of anthropogenic climate change caused by carbon dioxide emissions [3-5].

1.2 Computational study of mineral structure and reactivity

To better understand the structural and thermodynamic properties of Fe-(oxyhydr)oxide materials and the interplay among various parameters that govern the reactivity and stability of real materials, this work presents an in-depth computational study of various material phenomena. Strategically designed *ab initio* calculations allow targeted investigation of thermodynamic phenomena, without the confounding influence of interrelated or concomitant phenomena that are often unavoidable when studying real material samples (e.g., particle size and surface phenomena, additional contaminants or defects, etc).

The bulk of this work relies on *ab initio* methods, specifically density functional theory (DFT) methods, as implemented in the popular and powerful Vienna Ab-initio Software Package (VASP) [6-8], which is based on periodic plane-wave basis sets. Starting with a set of initial coordinates for atomic nuclei and an initial approximate basis set configuration, DFT methods optimize basis set parameters to determine the minimum-energy electronic structure of the simulated material, from which many thermodynamic quantities can be extracted. Optimization of atomic coordinates at zero- and finite-temperature is also possible, and a powerful means of discovering the locally-stable structures of defects, alloys, and surface configurations. Magnetic properties are explored through the use of spin-polarized implementations of the code. Refinement of the technical details of DFT methods is not among the primary goals of this work. Most components of this research employ well-studied and widely available implementations of DFT methods. Where there is uncertainty about the applicability or accuracy of certain techniques, benchmark cases are used to test and verify the usefulness of the

method in question, and are described in the chapters that follow.

1.3 Overview of Chapters

The progression of this research thesis proceeds in a linear fashion that begins by modeling the bulk crystal structure and thermodynamic properties of well-studied Fe-(oxyhydr)oxide materials, then applies the same model parameters to a material with uncertain structure and properties (ferrihydrite). Further work studies the properties of the same family of materials in the presence of dopants, defects, and surfaces/interfaces and draws conclusions about the impact of these variables on overall surface and phase stability for real-world materials, which almost always exhibit multiple forms of material imperfections simultaneously.

Chapter 2 establishes and benchmarks the methodological foundation for this thesis, in which the DFT methods chosen are benchmarked against experimental data on the atomic structure, magnetism, and thermodynamic stability of the better-studied Fe-(oxyhydr)oxide phases hematite, goethite, and lepidocrocite. These methods are then applied toward the optimization of the uncertain atomic structure of ferrihydrite, as well as the optimization of the magnetic groundstate of this material. To round out this study, a simple surface energy model is used to describe the energetics of particles at the nanoparticle scale, largely in keeping with experimental observations about the stability of nano-scale Fe-(oxyhydr)oxide materials.

Chapter 3 investigates one of the most common material imperfections found in natural Fe-(oxyhydr)oxide materials – aluminum cation doping. Each of the Fe-(oxyhydr)oxide phases studied (all based on Fe^{3+} cations) has an isostructural Al^{3+} analogue, making the case for charge-neutral, isomorphous cation substitution relatively straightforward. However, the thermodynamic impacts of Al doping vary in degree across the family of Fe-(oxyhydr)oxides, which results in shifts in relative thermodynamic stability among Al-doped materials that influence phase transformation behavior and can result in the stabilization of Al-doped structures that are only metastable in the pure-Fe composition.

Additionally, Al dopants may not distribute evenly throughout the Fe-(oxyhydr)oxide cation lattice, and may instead cluster or phase segregate, leading to alternative thermodynamic conclusions. This chapter also represents the first computational exploration of surface phenomena, wherein the thermodynamics of Al substitution at the goethite (110) surface are examined in comparison to substitution within the bulk.

Chapter 4 deals with another common defect type found in natural samples, often referred to as structurally-bound water or excess hydroxyl content. This defect, in its simplest form, can be described as a single cation vacancy charge-compensated with hydroxyl ions on neighboring oxygen sites. Especially for nanocrystalline or nanoparticulate forms of Fe-(oxyhydr)oxides, partial cation occupancy and excess water content are the rule rather than the exception in natural mineral samples. This study determines the structure of this defect type in each Fe-(oxyhydr)oxide crystal lattice, then isolates its impact on relative thermodynamic stability and crystal structure of the phases studied. Also considered is the case of simultaneous cation vacancy and Al-dopant defects, which are often observed in tandem for both synthetic and natural Fe-(oxyhydr)oxides. Vibrational frequencies of the defect OH groups are calculated and shown to be distinctly higher than those of stoichiometric OH groups, indicating that these defect OH may be discernible in FTIR spectroscopic analysis.

Chapter 5 explores the sorption and surface binding configuration of Li^+ at the goethite (110) surface. Goethite is among the most common naturally-occurring Fe-(oxyhydr)oxide materials and is often the lasting product of the phase transformation of ferrihydrite, the most prevalent metastable phase. The goethite (110) face comprises roughly 90% of the surface area of common goethite particles, and is appreciably reactive toward both (de)protonation and sorption of cations and oxyanions. Li^+ is chosen as a model sorbate due to its small atomic radius, which can possibly conform to various binding topologies at the mineral surface, unlike larger metal ions or and less point-like sorbates such as phosphate or carbonate. The study of Li^+ adsorption also benefits from the existence of experimental NMR data examining the sorption of this ion on goethite and lepidocrocite over a range of pH conditions that serves as a benchmark and guide for

novel computational study.

The computational study of hydrated surfaces and especially *charged* hydrated surfaces presents considerable theoretical and computational challenges that must be dealt with by careful control of model parameters to avoid the undue influence of spurious physical phenomena that may obscure the desired results. In this case, the broad range of possible configurations of liquid water molecules at the hydrated mineral surface requires a much broader configurational study to explore possible orderings and hydrogen bonding configurations for the water molecules at the mineral surface. To accomplish this, ab initio molecular dynamics simulations are performed to test a range of configurations, from which low-energy configurations were identified and selected for further study. Surface charge is a fundamental factor that drives sorption of charged cations and must be considered for a sorption model to be complete. However, the introduction of a net charge to a periodic surface slab model like those used here introduces electrostatic interactions between the surface and its periodic images that are not representative of any real physical phenomenon. Without careful control of model parameters, it is difficult to ascertain the influence that these spurious interaction may have on the sorption/binding phenomena of interest. In this study, the Li^+ sorption thermodynamic model is constructed such that undesired electrostatic terms largely cancel, leaving only the targeted Li^+ sorption energies. An alternative charge-compensation method is tested in parallel to examine the degree to which spurious electrostatic interactions cancel, although results are incomplete at the time of the completion of this thesis.

2 Structure, magnetism and thermodynamic stability of crystalline Fe-(oxyhydr)oxides

Note: The contents of this chapter are principally derived from a peer-reviewed article published in Chemistry of Materials *[9]. The article was adapted for use in this thesis document.*

2.1 Chapter Abstract

The atomic and magnetic structure, and thermodynamic stability, of ferrihydrite (Fe_5O_8H) are calculated based on the structure recently proposed by Michel et al [10]. Ferrihydrite stability is compared with that of the Fe-(oxyhydr)oxide polymorphs goethite (α-FeOOH) and lepidocrocite (γ-FeOOH), and the oxide hematite (α-Fe_2O_3). The GGA+U method is employed to correct known errors in treating correlated *d*-electrons in Fe atoms. GGA+U yields smaller errors in calculated thermodynamic quantities relative to experiment as compared with a standard GGA functional for all of the Fe-(oxyhydr)oxides studied. Good agreement is obtained between the DFT-predicted and experimental ferrihydrite structure when the effects of varying crystallinity and particle size are taken into account. The ferrihydrite magnetic behavior is modeled using a Heisenberg model parameterized with DFT-based magnetic coupling constants. The groundstate magnetic ordering of bulk ferrihydrite is predicted to be ferrimagnetic, with the Fe-site spins order with alternating alignment in layers stacked along the c-direction in the crystallographic unit cell. The groundstate is predicted to disorder to a paramagnetic structure at T_N = 250 K, undergoing a Néel transition. The formation enthalpy and Gibbs free energy of bulk crystalline ferrihydrite at 298.15K are predicted to be $\Delta H^{298.15K}_{rxn}$ (Fe_5O_8H) = 6.4 kJ/(mol-Fe) and $\Delta G^{298.15K}_{rxn}$ (Fe_5O_8H) = 6.9 kJ/(mol-Fe), respectively, relative to bulk hematite and liquid water. The values demonstrate that fully crystalline ferrihydrite is metastable with respect to the formation of both hematite and goethite at 298.15 K, but may be stabilized at small particle sizes due to favorably low surface formation energy. A simple surface energy model is used to predict the formation energy of ferrihydrite nanoparticles of arbitrary size, yielding results consistent with the observed formation

energies for nanoparticle samples.

2.2 Introduction

Fe-oxyhydroxides and Fe-oxides are common minerals found in a wide range of environmental settings. They play an important role in the adsorption of contaminants (As, Sr, U, Cs, Pb, Cd among others) in groundwater systems, and in the remediation and contaminant-plume control of acid mine tailings via adsorption or coprecipitation of heavy metals resulting from the processing of pyrite-containing metal ores and coals [1]. Their adsorptive properties are also important in industrial applications, e.g., water treatment plants, wherein the contaminant heavy metals are either co-precipitated with, or otherwise adsorbed by, Fe-(oxyhydr)oxide nanoparticles, and disposed of as solid waste [1]. The stability and structure of Fe-(oxyhydr)oxides are therefore of considerable interest. However, the wide variety of often poorly crystalline polymorphs makes a simple description of the Fe-(oxyhydr)oxide family an ongoing research challenge.

Often, the relative thermodynamic stabilities of the phases and polymorphic forms of Fe-(oxyhydr)oxides differ by only a few kJ/mol [11-13, 2], and two or more phases are often observed in close association in natural environments having only slight gradients in temperature, moisture, oxygen, or contaminant availability [1]. Varying levels of surface and structural hydration, defect and dopant content, and widely varying particle sizes, ranging from less than 2 nm to micron-sized crystalline samples, complicate the thermodynamic landscape of this family of minerals.

An Fe-(oxyhydr)oxide of particular interest is ferrihydrite, a common material in groundwater, surface and near-surface waters, sediment and soil environments [1], whose small size (typically 2-7 nm) and poor crystallinity renders crystal structural determination challenging [14-18]. Samples of natural or synthetic ferrihydrite are usually characterized by the number of discernible broad x-ray diffraction peaks. The most common synthetic types are 2-line and 6-line ferrihydrite, manifesting 2 and 6 broad and poorly resolved diffraction peaks, respectively. Better-resolved diffraction peaks are generally associated with higher crystallinity (lower structural disorder) and larger

particle sizes; properties that tend to occur together [19, 14, 20, 15]. Previous structural models for ferrihydrite have suggested a multi-phase system based on the hexagonal packing of oxygen atoms, which incorporates both defected and defect-free phases (the d- and f-phases, respectively), and includes variable amounts of nanocrystalline hematite, maghemite/magnetite, and/or highly defective material [19, 14, 20, 15, 16, 18]. These models do not propose specific atomic positions, especially for structural H_2O groups or H atoms, and also propose random alternation of oxygen stacking arrangements[6] and random Fe occupancies in both d- and f-phases [15]. Poorly determined atomic positions and multi-phase nanoscale systems with significant interfaces present considerable obstacles for current DFT methods, which, in terms of computational tractability, are limited to systems of the order of hundreds of atoms, and cannot easily locate optimal complex structures without a good estimate for initial atomic coordinates. Michel et al. [10] in 2007 proposed a single-phase crystal structure for ferrihydrite with uniquely defined positions for all the atoms (although with partial occupancies and no information on H positions, the treatment of which is discussed further below), making the new structure well suited for DFT studies.

The goal of this study is to use solid-state DFT calculations to explore the structure and energetics of, and magnetic coupling within, the newly proposed ferrihydrite structure, and to assess the application of GGA+U methods to the Fe-(oxyhydr)oxide series. In order to estimate the accuracy of the calculations, we performed a thorough comparison of GGA+U energetics with experimental data for the major Fe-(oxyhydr)oxide polymorphs. In the case of ferrihydrite, however, a number of different aspects must be considered.

First, the atomic positions and lattice parameters for ferrihydrite are predicted and compared to the experimental data for defected nanoparticles. This requires that the H positions, not determined in the experimental structure, be identified as described in Section 2.5.1.

Second, the correct magnetic ground state must be used for accurate DFT energy

calculations, but the ferrihydrite bulk magnetic structure is currently unknown. Thus, in Section 2.5.2, a DFT-based magnetic model is constructed for bulk crystalline ferrihydrite, which is then used in the following calculations. Finally, having developed and, where possible, validated the DFT atomic and magnetic structural models for ferrihydrite, the computed energetics are compared with experimental values in Section 2.5.3. Considering the small experimentally-measured relative stabilities separating the Fe-(oxyhydr)oxide structures [11-13, 2], every effort must be made to obtain accurate DFT values. In particular, the GGA+U method is used to treat Fe *d*–electron correlation effects, and it is shown that the introduction of the strong on–site Coulomb and exchange interactions, represented by the Hubbard U parameter, reduces errors in Fe-(oxyhydr)oxide energies and relative stabilities significantly (Section 2.5.3). For example, GGA calculations used to obtain the stability of goethite and lepidocrocite relative to hematite+water give errors of 9.5 and 24.8 kJ/(mol-Fe) respectively, compared to experiment, whereas optimal GGA+U calculations give errors of only -1.7 and 2.1 kJ/(mol-Fe) respectively. We then develop a thermodynamic model for Fe-oxide and -(oxyhydr)oxide relative stability that includes treatment of the water reference state, zero point H vibrational energies, and corrections for thermal excitations and nanoparticle effects. Analogous calculations on isostructural Al-(oxyhydr)oxides, which are somewhat simpler due to the absence of magnetic and correlated *d*-electron effects, are also used to validate the thermodynamic model. Taken together, these results help assess the Michel model, improve our understanding of the complex ferrihydrite structure, and provide a validated computational approach for studying Fe-(oxyhydr)oxides with GGA+U methods.

2.3 Properties of Fe-(oxyhydr)oxide materials

Multiple common Fe-(oxyhydr)oxide compounds [1] contain Fe^{3+} cations on a variety of oxygen/hydroxyl anion arrangements (Table 2-1). Goethite (α-FeOOH) and hematite (α-Fe_2O_3) are generally considered the most stable forms as bulk crystalline solids under atmospheric conditions. Lepidocrocite (γ-FeOOH) and ferrihydrite (nominally Fe_5O_8H) [10] are typically thought to be less stable as fully crystalline structures, but may be stabilized as small particles, due to their relatively low surface enthalpy [2]. Ferrihydrite

often forms as a metastable precursor phase, formed as the kinetic product of rapid precipitation of Fe^{3+} hexa-aquo ion $Fe^{3+}(OH_2)_6^{3+}$ in solution, which then transforms over time into one of the more stable phases (typically goethite or hematite) [1].

Table 2-1 Isostructural Fe- and Al-(oxyhydr)oxides

Fe-based structure	Al-based analogous structure
hematite, α-Fe_2O_3	corundum, α-Al_2O_3
goethite, α-FeOOH	diaspore, α-AlOOH
lepidocrocite, γ-FeOOH	boehmite, γ-AlOOH
ferrihydrite, Fe_5O_8H	akdalaite, Al_5O_8H
$Fe(OH)_3$ structural analog unknown	gibbsite, $Al(OH)_3$

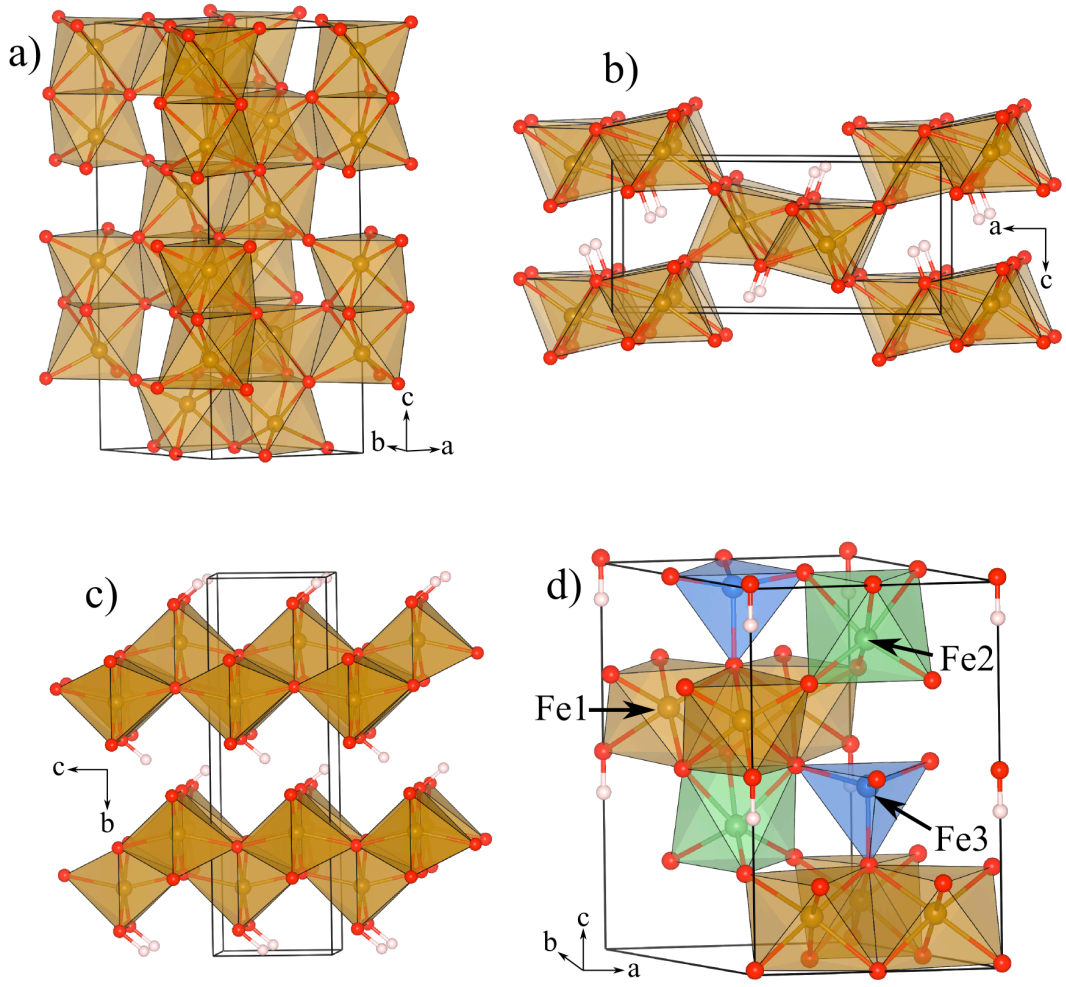

Figure 2-1: The four Fe-(oxyhydr)oxide structures of principal interest in this work, a) hematite, b) goethite, c) lepidocrocite, and d) ferrihydrite, with symmetry-distinct Fe-site labels shown. Fe atoms shown in brown (also, blue and green for ferrihydrite). Oxygen atoms shown in red, hydrogen atoms (protons) shown in white.

Other relatively common FeOOH and Fe-oxide polymorphs are not included in this study due to uncertainties in their crystal structure or chemical composition. Specifically, akaganéite (β-FeOOH) is excluded due to the presence of the Cl^- anion in the crystal structure, which complicates the thermodynamic analysis by requiring an additional reference state for Cl. Maghemite (γ-Fe_2O_3) and magnetite (Fe_3O_4) are also important structures in the Fe-(oxyhydr)oxide family, but are again excluded due to random Fe–vacancy ordering in the former, and the presence of mixed Fe^{2+} and Fe^{3+} sites in the latter; both of these conditions add considerable complexity to a rigorous DFT investigation. Therefore, this work will focus on hematite, goethite, lepidocrocite, and ferrihydrite, with a particular focus on the recently proposed structure of ferrihydrite.

The three Fe-(oxyhydr)oxide materials studied (goethite, lepidocrocite, ferrihydrite) can be formed, at least with respect to stoichiometry, from a combination of hematite and water:

$$Fe_2O_3 + H_2O \rightarrow (Fe_2O_3)\cdot H_2O \rightarrow 2(FeOOH) \quad (2.1)$$

$$5(Fe_2O_3) + H_2O \rightarrow 5(Fe_2O_3)\cdot H_2O \rightarrow 2(Fe_5O_8H) \quad (2.2)$$

Equation 2.1 is for goethite and lepidocrocite while Equation 2.2 is for ferrihydrite. Here the ferrihydrite stoichiometry is assumed to be that given in the Michel model [10]. The single-phase crystalline Michel model is based on the hexagonal $P6_3mc$ space group and incorporates Fe atoms in both octahedral (80% of Fe sites) and tetrahedral (20% of Fe sites) O coordinations. Fe atoms are arranged in layers perpendicular to the crystallographic *c*-axis (Figure 2-2), occupying three symmetry-distinct sites, referred to as Fe1, Fe2, and Fe3, matching the convention of the original Michel reference [10]. The Fe1 sites comprise edge-sharing Fe-octahedra forming layers consisting exclusively of Fe1. These layers are separated by a mixed layer of octahedrally-coordinated Fe2 sites (which occupy a different Wyckoff symmetry position, and show slightly different Fe-O bonding geometries from the Fe1 octahedra) and tetrahedrally-coordinated Fe3 sites. The Michel model incorporates many structural features akin to magnetite, including the

mixed tetrahedral and octahedral coordination of Fe. However, in contrast with magnetite, no ferrous iron is expected in ferrihydrite.

Important for comparison in the study of the Fe-(oxyhydr)oxide materials are the isostructural Al-(oxyhydr)oxide materials (Table 2-1) that form under relatively similar conditions and display roughly similar stability relationships [21]. Calculations based on the isostructural Al-based materials are arguably simpler, as they lack the additional complications arising from magnetic and *d*-electron correlation effects. Thus, the pure DFT–based thermodynamics computed for Al materials might effectively serve as a benchmark for the more technically complex Fe-containing materials. Note the Michel ferrihydrite structure is isostructural (at least up to the H positions, which were not given) to the Al-based akdalaite structure.

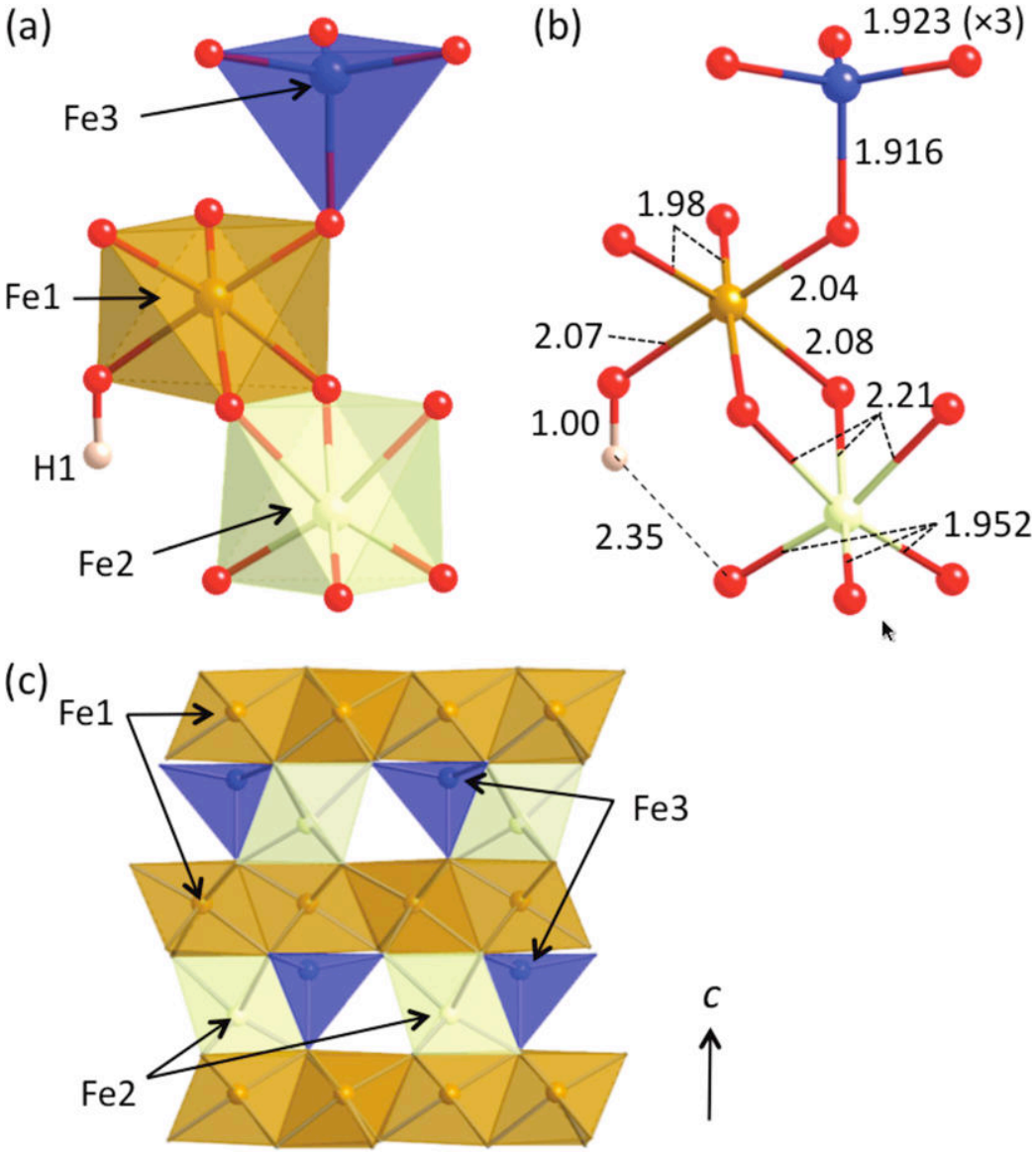

Figure 2-2: The DFT–optimized Michel et al. ferrihydrite structure including H atoms (initial positions taken from akdalaite structure [22]). The structure has three symmetry-distinct Fe atoms (a) in the primitive cell, Fe1 (brown) (greyscale: medium grey) and Fe2 (white) (greyscale: light grey) are octahedrally coordinated by 6 oxygen atoms each (red) (greyscale: dark grey, polyhedral corners), Fe3 (blue) (greyscale: black) is tetrahedrally coordinated. Calculated bond lengths (Å) are shown in part (b). Part (c) shows the layering arrangement of Fe1 and mixed Fe2/Fe3 layers.

2.4 Methodology

This section describes the basic computational methods used to perform the DFT calculations (Section 2.4.1) and the theoretical background for the finite temperature thermodynamics used to compare the *ab initio* and experimental Fe-(oxyhydr)oxide energetics (Section 2.4.2). The thermodynamic theory is applied in Section 2.5.3.

2.4.1 Computational methods

Calculations were performed using density functional theory (DFT) and the projector-augmented wave (PAW) method [23, 24], with the Vienna Ab-initio Simulation Package (VASP)[7, 8]. Exchange-correlation was treated in the Generalized Gradient Approximation (GGA), as parameterized by Perdew, Burke, and Ernzerhof (PBE)[25]. The following valence electron configurations were employed in the PAW potentials: $2s^2 2p^4$ for O, $3p^6 3d^7 4s^1$ for Fe, and $3s^2 3p^1$ for Al. The GGA+U method is used to correct the poor description in pure DFT/GGA of the on-site Coulomb repulsion of 3*d* electrons in Fe atoms. The GGA+U method modifies GGA energies with an explicit correction for the Coulomb interaction of the 3*d* electrons [26], and has been shown to improve experimental agreement for calculated geometries, band structures, magnetic properties[27], and redox energies [28, 29] in Fe-containing compounds. The rotationally-invariant approach to the GGA+U method was used, as described by Dudarev [30]. This model approach is parameterized by a single parameter, U_{eff}=U-J, where U is a spherically averaged Hubbard parameter that describes the effective Coulomb interaction, and J represents the screened exchange energy between electrons in the same orbital manifold. The parameters were set at U=4 eV and J=1 eV (or, U_{eff} = 3 eV) for all Fe atoms unless otherwise noted. However, to assess the optimization of the U parameter for Fe-(oxyhydr)oxides, thermodynamic quantities were calculated over a range of U values from U=1 eV (the GGA limit) to U=7 eV (U_{eff} = 0 to 6 eV) and compared with experimentally known benchmarks. The best agreement for all materials studied is achieved for approximately U=4 eV, in agreement with Rollman, et al. [31]. U parameters were applied only to Fe atoms.

Both hard and soft oxygen PAW potentials (calculated with energy cutoffs of 1050 and 650 eV, respectively) were tested for accuracy in multiple Fe-(oxyhydr)oxide materials, but the results showed little dependence on the potential used when the chosen energy cutoff is sufficiently high that all output geometries and energies are converged. The electronic SCF convergence tolerance was set to 10^{-4} eV/cell, and the ionic relaxation convergence tolerance was set at 10^{-3} eV/cell for all results reported here, with the exception of calculations of vibrational frequencies. For vibrational frequency calculations, a high-precision geometry relaxation was first performed, with smaller SCF and ionic relaxation convergence tolerances of at 10^{-5} eV/cell and 10^{-4} eV/cell, respectively. The high precision relaxation is done to obtain atomic positions located precisely at energetic minima for the subsequent calculation of vibrational frequencies. All results presented in this paper were therefore obtained with the soft oxygen potential, which is less computationally intensive, and using an energy cutoff of 650 eV and a k-point mesh with a density per a reciprocal atom of approximately 5000 or more. A shifted Monkhorst-Pack [32] mesh is used for all structures except ferrihydrite and akdalaite, where a k-point mesh centered at the origin (Γ-point) was employed, as the structure is hexagonal. Results were converged within 1-2 meV per atom with respect to energy cutoff and k-point density. All calculated data shown in this paper for hematite, goethite and lepidocrocite result from spin-polarized calculations performed using the experimental antiferromagnetic ground states [1]. The magnetic structure for ferrihydrite is not experimentally known and has been predicted in this work. Aluminum-based structures were calculated as nonmagnetic. The predicted Fe and Al structural information is compared to experimental data in Table 2-2. The errors in lattice parameters are generally around 1%, which is typical for DFT GGA studies. A notable exception, where a significantly larger error is observed, is the c lattice parameter for ferrihydrite, which is discussed in detail in Section 2.5.1.

Table 2-2: Fe/Al-(oxyhydr)oxide structural information and experimental (calculated) unit cell dimensions.

Structure	Formula	Space Group	*a* (Å)	% error	*b* (Å)	% error	*c* (Å)	% error	Ref.
hematite	α-Fe_2O_3	R-3c	5.03 (5.08)	0.8	5.03 (5.08)	0.8	13.75 (13.95)	1.4	[1]
goethite	α-FeOOH	Pnma	9.96 (10.05)	0.9	3.02 (3.06)	1.3	4.61 (4.63)	0.4	[1]
lepidocrocite	γ-FeOOH	Bbmm	3.07 (3.09)	0.7	12.52 (12.48)	-0.3	3.87 (3.95)	2.1	[1]
ferrihydrite	Fe_5O_8H	$P6_3mc$	5.93 (5.99)	1.0	5.93 (5.99)	1.0	9.13 (9.35)	2.4	[10]
corundum	α-Al_2O_3	R-3c	5.12 (5.18)	1.1	5.12 (5.18)	1.1	5.12 (5.18)	1.1	[33]
diaspore	α-AlOOH	Pbnm	4.40 (4.41)	0.2	9.43 (9.48)	0.5	2.85 (2.88)	1.0	[34]
boehmite	γ-AlOOH	Cmcm	2.87 (2.90)	1.0	12.23 (12.04)	-1.6	3.70 (3.73)	0.8	[35]
gibbsite	$Al(OH)_3$	P21/n β= 94.54° (92.36°)	8.68 (8.78)	1.2	5.08 (5.10)	0.4	9.74 (9.63)	-1.1	[33]
akdalaite	Al_5O_8H	$P6_3mc$	5.58 (5.63)	0.9	5.58 (5.63)	0.9	8.77 (8.85)	0.9	[22, 36]

2.4.2 Thermodynamic model

A primary goal of this work is to compare enthalpies and free energies predicted by DFT for Fe- (or Al-) (oxyhydr)oxides with experimental values. These comparisons will both assess the GGA+U methods being applied here and determine the energetics implied by the Michel ferrihydrite structure. To make such comparisons possible, it is necessary to compare energetics at the same temperature, which is typically room temperature for the experimental data. As the DFT energetics are effectively at zero temperature, they are adjusted for the effects of finite temperature using experimental specific heat values; the details of this approach are given in this section. In addition, the relevant transformation reactions typically involve water, whose energy must also be calculated. Direct DFT calculation of room temperature liquid water energetics is very challenging and not the focus of the present study. Therefore, below we describe a semi-empirical approach to obtain accurate water energetics with the same reference state as the DFT solid phase calculations. This section will focus on the determination of enthalpy. Although some free energy results will be given in the paper, no effort is made to calculate entropic

contributions from DFT; the non-enthalpic free energy contributions are treated entirely empirically. The free energy approach is described with the free energy results in Section 2.5.3.

Relative stabilities will be calculated as enthalpies of reaction (or transformation) from solid hematite α-Fe_2O_3 (or for Al, corundum, α-Al_2O_3) and liquid water, and normalized to one mole of Fe atoms (or Al atoms). As an example, Equation 2.3 shows the reaction enthalpy of goethite (FeOOH) relative to hematite. $\Delta H_{rxn}^{hem \rightarrow goe}$ refers to the enthalpy of reaction (‘*rxn*’) for the (hypothetical) transformation of hematite into goethite.

$$\Delta H_{rxn}^{hem \rightarrow goe} = \Delta H_f^{FeOOH} - \frac{1}{2}\left[\Delta H_f^{Fe_2O_3} + \Delta H_{H_2O}^{liquid}\right] \qquad (2.3)$$

The complete room-temperature enthalpy for a solid phase at temperature *T* is given by

$$\Delta H_f(T) = \Delta H_f^{ab\ initio} + \mathrm{ZPE} + \int_0^T C_p(T)dT = \Delta H_f(0\mathrm{K}) + \int_0^T C_p(T)dT \qquad (2.4)$$

where $\Delta H_f^{ab\ initio}$ is the DFT energy, ZPE is the calculated zero-point energy contribution, and $C_p(T)$ is the specific heat per Fe of the solid phase. $\Delta H_f(0\mathrm{K})$ is the calculated enthalpy at 0 K, which includes both the DFT energy and the ZPE. Note that no distinction is made between enthalpies and energies, as the results are for standard pressure conditions (1 atm) and the pressure contributions to the enthalpy are a fraction of a meV/atom and can be approximated as zero. While elemental reference states will affect the specific values for the enthalpies in Equations 2.3 and 2.4, the reference states cancel from the overall enthalpy of reaction in Equation 2.3. As the reaction enthalpy is the focus of this work and only reaction enthalpies will be given the elemental reference states will not be specified or discussed. Equation 2.4 can also be used to obtain $\Delta H_f(0\mathrm{K})$ from finite temperature experimental enthalpy data, as done for the Al and Fe compounds of interest in Table 2-3. Table 2-3 can be used for direct comparison to DFT energies ($\Delta H_f^{0\ K}$), as reported later, or alternatively to shift DFT values (by $H^{298.15\ K} - H^{0\ K}$) for comparison to room temperature values ($\Delta H_f^{298.15\ K}$).

Table 2-3: Experimental formation enthalpies of Fe and Al (oxyhydr)oxides at standard conditions (298.15 K, 1 atm), extrapolated to 0 K using low temperature specific heat measurements. Citations give the source for the formation enthalpy value or the specific heat.

Structure	$\Delta H_f^{298.15\ K}$ (kJ/mol)	$H^{298.15\ K} - H^{0\ K}$ (kJ/mol)	$\Delta H_f^{0\ K}$ (kJ/mol)
hematite	-826.2 ± 1.3 [2]	15.560 [37]	-831.8
goethite	-561.5 ± 1.5 [2]	10.74 [12]	-572.2
lepidocrocite	-552.0 ± 1.6 [2]	11.05 [12]	-563.1
corundum	-1675.7 ± 1.2 [38]	13.58 [38]	-1689.3
diaspore	-1002.7 ± 1.0 [38]	6.85 [39]	-1009.6
boehmite	-996.10 ± 1.30 [38]	7.075 [40]	-1002.95
gibbsite	-1293.1 ± 1.2 [38]	12.456 [41]	-1305.6

ZPEs for solid Fe-(oxyhydr)oxides are estimated for each structure assuming the only significant contribution comes from H vibrations. This approximation is justified both by the fact that the heavier Fe and O atoms will have smaller zero-point contributions than H and that the Fe and O contributions will largely cancel in the calculation of relative reaction enthalpies due to the generally similar coordination environments of these atoms in both product and reactant (oxyhydr)oxide structures. The H ZPE is evaluated in the local harmonic approximation (all other atoms fixed), which is expected to be accurate due to the lighter mass of H compared to the other atoms [42, 43]. Small displacements about the equilibrium position of the H atom, with other atoms held fixed, allow the determination of the corresponding force constant matrices, which is diagonalized to yield the vibrational frequencies and normal modes [44]. The ZPE is obtained as the sum of the contributions from each H mode, as shown in Equation 2.5.

$$\mathrm{ZPE} \approx \frac{1}{2}\sum_i \hbar \nu_i^{\mathrm{H}} \qquad (2.5)$$

Here h is Planck's constant and ν_i^{H} is a vibrational frequency for an H atom. The summation runs over all $3N$ vibrational modes derived from the N H atoms in the cell. The ZPE contribution is simply added to the calculated internal energy of the system to construct the enthalpy of the structure at 0 K, as shown in Equation 2.4. The calculated vibrational frequencies and predicted ZPE value for each compound considered in this

study are given in Table 2.4. The calculated frequencies are largely in agreement with previous DFT studies on Al- and Fe-(oxyhydr)oxide vibrational frequencies [45-47] and with experimental IR-spectra [48, 1]. For example, O-H stretch in goethite has been measured by Cambier at 3150 cm^{-1}, with uncoupled O-H bending modes at 850 and 938 cm^{-1} [48]. The calculated wavenumbers are all within 8% of these experimental values. Interestingly, it is found that the ZPE for the compounds of a given cation (Fe or Al) all fall within a narrow range of less than 2 kJ/(mol H) of each other, suggesting that this contribution plays a small role in relative stability overall.

Table 2-4: Calculated 0 K vibrational wavenumbers and associated zero-point energies for H atoms in Fe- and Al-(oxyhydr)oxides. The gibbsite primitive cell has 6 symmetry distinct H-atoms so vibrational wavenumbers are calculated for each site and the average zero-point energy is given.

Structure	H vibrational wavenumbers (cm^{-1})	Zero-point energy kJ/(mol H)
goethite	2985, 1016, 954	29.6
lepidocrocite	2789, 1069, 1012	29.1
ferrihydrite	3574, 699, 502	28.5
diaspore	2761, 1173, 1099	30.1
boehmite	2921, 1108, 1097	30.6
gibbsite		
H1	3720, 798, 715	
H2	3600, 880, 643	31.9
H3	3470, 1068, 905	*(avg. of 6 H positions*
H4	3531, 980, 878	
H5	3413, 1094, 902	
H6	3392, 1060, 986	

In order to apply Equation 2.3 it is necessary to determine the enthalpy of liquid water with the same reference as the DFT based solid-phase energies. Due to the unavailability of low-temperature thermodynamic data for liquid water (from near 0 K to room temperature) and the considerable difficulty of modeling bulk liquid water with DFT, the correction proposed by Wolverton et al. [49] is here extended to simplify the calculation of the enthalpy of liquid water at arbitrary temperature. In this approach DFT is used to calculate the energy of an isolated water molecule at 0 K, which is then extended to finite

temperature by analytic thermodynamic expressions, and then finally adjusted to give the enthalpy of liquid water by subtracting the heat of vaporization. The expression for the water enthalpy at finite temperature in our approach is given by

$$\begin{aligned}\Delta H_{H_2O}^{liquid}(T) &= E_{H_2O}^{molecule} + \Delta H_{H_2O}^{excitations}(T) - \Delta H_{H_2O}^{vaporization}(T) \\ &= E_{H_2O}^{molecule} + 16.69\,kJ/mol \text{ at } T = 298.15\text{K}\end{aligned} \tag{2.6}$$

The description of the terms in this expression and the derivation of the final value on the second line are given here. $E_{H_2O}^{molecule}$ is the internal energy of the water molecule in isolation at zero temperature and is modeled by DFT calculation of a single water molecule in a periodic supercell measuring 10×10×10 Å. The size of the box is such that the calculated energy of the system is converged within about 1meV/molecule relative to an infinite box, indicating no intermolecular interactions due to periodic boundary conditions. The DFT internal energy of the isolated molecule is then augmented by $\Delta H_{H_2O}^{excitations}(T)$, which contains the vibrational, rotational, and translational contributions to the enthalpy at finite temperature (note – this term also includes zero-point vibrational energy, which is not a thermal excitation, but a distinct addition to the internal energy). The $\Delta H_{H_2O}^{excitations}(T)$ contributions are obtained from experimental parameters and analytic expressions as a function of temperature [50] and together with $E_{H_2O}^{molecule}$ approximate the enthalpy of steam at arbitrary temperature. The equation for the finite temperature excitation contribution to the enthalpy is [50]:

$$\Delta H_{H_2O}^{excitations}(T) = k_B \sum_{j=1}^{3}\left(\frac{\theta_{D,j}}{2} + \frac{\theta_{D,j}\cdot e^{-\theta_{D,j}/T}}{1-e^{-\theta_{D,j}/T}}\right) + \left(\frac{3}{2}k_BT\right)_{rot.} + \left(\frac{3}{2}k_BT\right)_{trans.} \tag{2.7}$$

The first summation is over the two O-H stretching and single O–H–O bending frequencies in the water molecule, as obtained from [50] (Debye temperatures for these modes are θ_D= 5360, 5160, and 2290 K, respectively, where $\theta_D = \frac{\hbar\nu}{k_B}$). The contributions from the rotational degrees of freedom are modeled classically. While fully quantum mechanical models for the rotational degrees of freedom have been developed,

the low Einstein temperatures for H atom degrees of freedom make the classical approximation used in Equation 1.7 very accurate above about 50 K. The excitations contribute a value $\Delta H_{H_2O}^{excitations}(298.15K) = 60.70$ kJ/mole at room temperature (the bulk of this contribution comes from the ZPE of the water). Finally, the enthalpy of vaporization of liquid water to steam, $\Delta H_{H_2O}^{vaporization}$, is subtracted from the total energy of the H_2O model to obtain the enthalpy of liquid water. The enthalpy of vaporization of water at room temperature is $\Delta H_{H_2O}^{vaporization}(298.15K) = 44.01$ kJ/mole [51]. Combining the values for $\Delta H_{H_2O}^{excitations}(298.15K)$ and $\Delta H_{H_2O}^{vaporization}(298.15K)$ yields the second line in Equation 2.6.

By combining Equation 2.4 and Equation 2.5 for the solid phases, and Equation 2.6 and Equation 2.7 for liquid water, we can now apply Equation 2.3 to predict DFT-based finite temperatures reaction energetics for the Fe- and Al-(oxyhydr)oxides. In order to assess the accuracy of the overall approach, and, in particular, our expression for $\Delta H_{H_2O}^{liquid}(T)$ in Equation 2.6, we have applied Equation 2.3 to predict the enthalpies of transformation of Al-(oxyhydr)oxide phases and compared them to experimental data. The Al-(oxyhydr)oxides are a logical set of test compounds to assess our approach, given that they are isostructural to the Fe-(oxyhydr)oxides.

Table 2-5 shows the calculated stabilities (enthalpies of reaction) for diaspore, boehmite, and gibbsite relative to corundum and water. The uncorrected energies use only the DFT energy for the isolated water molecule, i.e., $\Delta H_{H_2O}^{liquid}(T) = E_{H_2O}^{molecule}$. The corrected energies, meanwhile, use the full expression for $\Delta H_{H_2O}^{liquid}(T)$ presented in Equation 2.6. Note that the large errors relative to experiment for the uncorrected energies are greatly reduced by including the water corrections, demonstrating their importance and their (at least qualitative) accuracy.

Table 2-5: Experimental, uncorrected calculated, and corrected calculated relative stabilities at 298.15 K, 1atm for the Al-(oxyhydr)oxides relative to corundum, α-Al_2O_3 + water

Structure	ΔH_{rxn}^{expt} (experiment) kJ/(mol-Al)	$\Delta H_{rxn}^{ab\ initio}$ (uncorrected) kJ/(mol-Al)	$\Delta H_{rxn}^{ab\ initio}$ (corrected via Eqn. 6) kJ/(mol-Al)
diaspore, α-AlOOH	-20.55 ± 2.6[33]	-9.6	-17.9
boehmite, γ-AlOOH	-15.65 ± 2.6[33]	-13.3	-21.6
gibbsite, $Al(OH)_3$	-26.55 ± 1.8[33]	0.4	-24.6

The final, predicted reaction enthalpies for Al-(oxyhydr)oxides remain in somewhat poor agreement with experiment, with errors of up to 6 kJ/(mol-Al) in size. However, this is almost certainly not attributable to an error in $\Delta H_{H_2O}^{liquid}(T)$, as there is no consistent trend toward under- or overestimation of the errors. To show that the Al-(oxyhydr)oxide calculated energies are, on average, consistent with our water model, we can fit the non-DFT terms in Equation 1.6 and compare the result to our model. First we write

$$\Delta H_{H_2O}^{liquid}(T) = E_{H_2O}^{molecule} + \Delta H_{H_2O}^{excitations}(T) - \Delta H_{H_2O}^{vaporization}(T) = E_{H_2O}^{molecule} + \delta h_{corr} \qquad (2.8)$$

where δh_{corr} contains all the corrections necessary to correct the molecular DFT water energy so as to match experiments. Now, if rather than using experimental values for the terms in δh_{corr}, it is instead fit to minimize the least square error in the predicted vs. experimental reaction enthalpies in Table 2-5 then one obtains $\delta h_{corr} = 14.9$ kJ/mol. This is quite close to the value of 16.7 kJ/mol obtained analytically for the second two terms in Equation 2.6, in support of the assertion that these terms yield an accurate representation of the energetics, and that the DFT based water energy is close to experiment. The discrepancies between predicted and measured enthalpies in the Al-(oxyhydr)oxides are therefore likely due to errors in the experimental determinations, or in the DFT solid phase energetics. Section 2.5.3 discusses the application of this thermodynamic model to the Fe-(oxyhydr)oxides.

2.5 Results

Section 2.5 describes the results of detailed DFT-based modeling of ferrihydrite in the Michel structure. Section 2.5.1 focuses on the optimized geometry, where the primary goal is to determine whether the DFT-derived atomic positions are consistent with those given in the Michel model. Such agreement is neither trivial to demonstrate nor a foregone conclusion, as the DFT based model proceeds from conjectured initial H positions, predicts a new magnetic structure, removes all partial occupancies, and, moreover, corresponds to a idealized bulk phase, in contrast to the nanoparticulate form characterized experimentally. Section 2.5.2 presents and discusses the results obtained from the magnetic modeling, and compares such with the limited experimental results on magnetic structure. The magnetic study is of interest in its own right, but also essential for providing the correct magnetic arrangement for the structural studies in 2.5.1 and the energetic studies in 2.5.3. Finally, Section 2.5.3 provides a validation of the GGA+U approach used in all of the foregoing sections, and predicts the energy and relative stability of ferrihydrite in the Michel structure.

2.5.1 Ferrihydrite bulk structure

GGA+U calculations, adopting the predicted groundstate ferrimagnetic ordering model (see Section 2.5.2 on magnetic model for ferrihydrite), yield the structural data for bulk crystalline ferrihydrite shown in Table 2-6. Calculated geometries largely agree with those given by Michel et al. The H positions were not determined in the original experimental study [10] and so approximate initial H positions have been taken from DFT structural optimizations of the isostructural Al-based akdalaite structure [36]. The H positions were then fully relaxed in the ferrihydrite structure.

Figure 2-2 shows the calculated bonding geometries of the three symmetry-distinct Fe polyhedra, and the equilibrium H positions. Table 2-7 presents the calculated relaxed fractional coordinates of all symmetry-distinct atoms in the ferrihydrite unit cell.

Table 2-6: Comparison of calculated and experimental lattice parameters, and selected calculated bond lengths and angles for ferrihydrite. The notation ×N denotes N bonds of the same length. Note the increase in the *c*-lattice parameter and cell volume with increasing crystallinity.

	GGA+U (U = 4 eV) (bulk crystalline)	Expt. *Michel et al.*[1] (in order of most to least crystalline)		
		6-line	3-line	2-line
Space Group	$P6_3mc$	$P6_3mc$	$P6_3mc$	$P6_3mc$
a (Å)	5.97	5.9289	5.9537	5.9587
c (Å)	9.37	9.1267	9.0967	8.9657
Volume (Å^3)	289.6	277.8	279.2	275.7
O-H (Å)	1.00	-	-	-
H Bond (Å)	2.35	-	-	-
Fe1-O_{oct} (Å)	1.981(×2), 2.040, 2.068, 2.075(×2)	1.933, 2.012(×2), 2.140(×2), 2.042	1.923, 2.005, 2.017, 2.140(×2), 2.064	1.918, 1.979(×2), 2.036(×2), 2.052
Fe2-O_{oct} (Å)	1.952(×3), 2.206(×3)	1.874(×3), 1.964(×3)	1.879(×3), 1.985(×3)	1.883(×3), 2.082(×3)
Fe3-O_{tet} (Å)	1.916 (×1) 1.923 (×3)	1.790 (×1) 1.953 (×3)	1.773 (×1) 1.961 (×3)	1.959 (×1) 2.019 (×3)
Fe-O-H (°)	123	-	-	-
O-H---O (°)	133	-	-	-

Table 2-7: DFT irreducible atom coordinates for ferrihydrite (fractional coordinates, relaxed from Michel geometry [10]). Spin states (up/down) used for Fe sites in the calculation are given and described in detail in Section 2.5.2.

Atom (spin)	*a*	*b*	*c*
Fe1 (up)	0.1668	0.8332	0.6336
Fe2 (down)	0.3333	0.6667	0.3353
Fe3 (down)	0.3333	0.6667	0.9545
O1	0.0000	0.0000	0.0124
O2	0.3333	0.6667	0.7501
O3	0.1672	0.8328	0.2368
O4	0.5145	0.4855	0.0000
H1	0.0000	0.0000	0.4062

The most notable discrepancy between the experimental and the DFT calculated geometries (Table 2-6) is the considerable overestimation of the *c*-lattice parameter compared to the Michel et al. data, the GGA+U value exceeding that reported for 6-line ferrihydrite by 2.4%. However, it is clear from Table 2-6 that the *c*-lattice parameter is sample dependent, and evidently increases from 2-line to 6-line ferrihydrite. The appearance of more lines in the diffraction pattern typically corresponds to larger particles with higher crystallinity. In addition, the refinements reported by Michel et al. suggest that the larger particles have significantly fewer cation vacancies, tending toward full occupation of all Fe sites for more highly crystalline samples. Taken together, these observations suggest a trend toward increasing c-lattice parameter with increasing particle size (and associated increased crystallinity and reduced vacancy content). Recent results on even larger particles of highly crystalline ferrihydrites from Michel suggest that the *c* lattice parameter continues to expand [52-54], and that crystalline ferrihydrite would have a *c* lattice constant of 9.36(3) Å, quite similar to our predicted value. Therefore, we believe that our structural predictions, which describe ideal crystalline bulk ferrihydrite with no vacancies, constitute an accurate representation of the bulk, undefected Michel model structure.

The ferrihydrite bulk crystal structure obtained here may also help to resolve a concern about the tetrahedral Fe3 positions arising in the Michel model. The asymmetry and bond

lengths of this site were identified as problematic in a recent criticism of the Michel model by Manceau [18, 55]: the experimental tetrahedral Fe-O bond distance along the c-axis of the structure is only 1.790 Å, while the 3 other Fe-O bonds in the tetrahedron are 1.952 Å in length. The bond-length of 1.790 Å is considerably shorter than would be expected for tetrahedral Fe^{3+}. However, the bulk crystalline DFT-relaxed structure of ferrihydrite obtained here shows an approximately symmetrical tetrahedral Fe3-O bonding arrangement, with 4 Fe-O bonds of nearly equivalent length (1.916 Å×1, 1.923 Å×3) consistent with tetrahedral Fe^{3+}. Careful examination of the experimental and calculated structures shows that the *c* lattice parameter discrepancy described above is due to the variations in Fe3-O bond distances between the experimental and calculated geometries. Therefore, the calculations suggest that the unusual Fe3-O bond length is not inherently part of the un-defected Michel structure, but instead may be a byproduct of surface effects, poor crystallinity, defects, and/or refinement errors on small nanoparticles. More specifically, the Michel model cannot be interpreted as implying that Fe3 sites in a putative bulk crystalline phase would manifest one short Fe3-O bond of length 1.79 Å.

2.5.2 Modeling magnetism in ferrihydrite

In order to accurately model thermodynamic properties of Fe-oxide and (oxyhydr)oxide materials, close attention must be paid to the specific arrangement of the moments borne by Fe atoms in the crystal lattice. The energies associated with changes in the magnetic ordering in Fe-(oxyhydr)oxides are often of larger magnitude than the differences in the relative stabilities of the structures. Hematite, goethite and lepidocrocite are all antiferromagnetic at low temperatures, with specific spin arrangements and magnetic ordering temperatures as presented in Table 2-8 [1]. For these materials, failure to model the correct magnetic orderings causes significant errors in calculated energies. Table 2-9 presents the DFT-derived energy differences separating the hypothetical ferromagnetic ordering from the magnetic ground state. The experimentally determined antiferromagnetic ground states are applied in all cases, save for ferrihydrite, where the ground state ordering is ferromagnetic, as obtained in the present work. Note that we are interested here in obtaining only the zero-temperature magnetic energetics for the solid

phases, for the effects of the finite-temperature magnetism upon the thermodynamic quantities (e.g. the Néel transition in lepidocrocite and the Morin transition in hematite) are all included through the integration of specific heats (see Equation 2.4).

Table 2-8: Experimental low-temperature magnetic structures and magnetic transition temperatures of the Fe-oxides and (oxyhydr)oxides.

Structure	Experimental magnetic ordering at 0 K	Magnetic transition temperature (K)
hematite	antiferromagnetic	260 (Morin transition) [1]
		948 (Néel transition) [1]
goethite	antiferromagnetic	400 (Néel transition) [1]
lepidocrocite	antiferromagnetic	77 (Néel transition) [1]
magnetite	ferrimagnetic	120 (Verwey transition) [1]
		850 (Curie transition) [1]
maghemite	ferrimagnetic	820-986 (Curie transition) [1]
ferrihydrite	AFM /29erromagnetic	120-550 (Néel transition) [51-56] 250 (Néel transition – this work)

Table 2-9: Calculated energy differences separating ferromagnetic (FM) and groundstate (GS) orderings in Fe-(oxyhydr)oxides.

Structure	FM-GS energy kJ/(mol-Fe)
hematite	+25.7
goethite	+15.4
lepidocrocite	+3.3
ferrihydrite	+20.0

The low temperature magnetic properties of bulk ferrihydrite are not well known, as experimental studies of the magnetic properties of ferrihydrite are complicated by uncertainties in particle size, structure, and surface effects. In addition, ferrihydrite particles are often agglomerated into clusters where interparticle magnetic interactions are expected. Superparamagnetism, in which the net ferromagnetic moments of nanoparticles are subject to flipping due to thermal fluctuations, is observed in nanoparticle samples at temperatures greater than 120 K [56]. Superparamagnetic and particle-size dependent magnetic effects have been confirmed and further resolved in investigations on ferrihydrite particles coated with sugar or alginate to reduce or eliminate interparticle interactions [57, 58]. Previous studies [59, 60, 56, 61-63] suggest

a ferrimagnetic or antiferromagnetic ordering for ferrihydrite at low temperature, where, in the case of antiferromagnetism, the presence of remnant ferromagnetic moments associated with uncompensated spins randomly distributed in either the bulk or at the surface of the nanoparticles is often suggested. Experimental estimates of the Néel ordering transition temperature in ferrihydrite range from 120 K to over 500 K (see Table 2-10). Comparison of the neutron scattering- and x-ray diffraction data suggests that the magnetic and crystallographic unit cells are equivalent [60]. However, absent a fully descriptive crystallographic structural model, previous studies have not determined a specific magnetic ordering structure for ferrihydrite.

This study investigates the magnetic ordering structure of bulk crystalline ferrihydrite using a pairwise magnetic interaction model (Heisenberg model) developed for the ferrihydrite structure. The approach follows that used by Morgan et al. [64], wherein the Heisenberg model parameters were fitted to reproduce the DFT energies of different magnetic orderings. The set of magnetic structures for fitting was initially taken to include all the symmetry-distinct collinear antiferromagnetic arrangements representable in the primitive Michel model unit cell, based on the assumption that an antiferromagnetic ground state would prevail. Using the Alloy Theoretic Automated Toolkit (ATAT) code [65], a set of 36 symmetry-distinct antiferromagnetic arrangements were identified, each containing 10 Fe atoms (arranged 5 spin–up and 5 spin–down). An attempt was made to obtain energies for all of these magnetic states, but convergence problems were experienced for approximately half of them, likely due to initialization in a highly unstable magnetic configuration. In the end, 19 antiferromagnetic energies and the single ferromagnetic energy were computed (including full relaxation of each structure), which together were sufficient to parameterize the Heisenberg model. Calculated magnetic moments were all high-spin and gave a value of about 4 m_B per Fe. All pairwise (two-spin) interactions between Fe sites less than 5Å apart were fit with the ATAT code using the 20 DFT energies. Multi-spin interactions (e.g. interactions between three Fe sites) were also considered, butwhen fit, were found to be energetically insignificant compared to the dominant pairwise interactions. Eight pairwise interactions were used in the final fit, yielding an optimized cross-validation score of 1.2 meV/spin

(amounting to 0.6% of the total 208 meV/spin range of the magnetic energies, or 2.7% of the standard deviation of the distribution of magnetic ordering energies, σ=43.7 meV/spin). The small cross-validation score suggests that the fitted interactions represent the DFT energetics accurately.

Table 2-10: Selected experimental studies of magnetism in ferrihydrite.

Study	T_N (K), Néel temperature	Low-temperature ordering	Method(s)
Pankhurst et al. (1992) [59]	n/a	2-line: ferrimagnetic 6-line: antiferromagnetic	low-temperature Mössbauer spectroscopy
Zergenyi et al. (2000) [56]	120	antiferromagnetic with parasitic ferromagnetic moment	Mössbauer spectroscopy, magnetometry
Seehra et al. (2000) [60]	350	antiferromagnetic with uncompensated surface spins	neutron scattering
Guyodo et al. (2006) [62]	500-550	antiferromagnetic with ferromagnetic-like moment due to uncompensated spins	Mössbauer spectroscopy, magnetometry
Berquó et al. (2007) [66], Berquó et al (2009) [58]	422	antiferromagnetic, superparamagnetic interactions likely increase for small, agglomerated particles	Mössbauer spectroscopy, magnetometry, HRTEM, XRD

Table 2-11 describes the eight parameterized interactions, including the interaction distance, the Fe-sites involved, the anion sharing geometry (edge, corner, etc), the Fe–O–Fe angle subtended by the interaction, and the cluster multiplicity per unit cell. The pairs are also shown in Figure 2-3. The majority of the parameterized interactions proceed through single intervening O anions, so that they are of the superexchange type. Clusters 5 and 8, however, stand as exceptions, where the coupling presumably proceeds by direct Fe–Fe overlap (more likely for cluster 5) and/or by higher order through-bond interactions such as super-superexchange (more likely for cluster 8). The largest pairwise interaction energies are obtained for interlayer antiferromagnetic superexchange interactions (Fe1/Fe3 and Fe1/Fe2 pairs: clusters 3, 4, and 6).

Table 2-11: Pairwise effective cluster interactions (ECIs) in ferrihydrite primitive unit cell. The fifth column indicates the Fe sites involved in the pair, and also the oxygen anion sharing arrangement. ECI(K/pair) defined as [ECI(*energy*)]/[$k_B S(S+1)$] with S=5/2 for Fe^{3+}.

Cluster number	ECI (meV/pair)	ECI (K/pair)	Distance (Å)	Fe sites involved, anion sharing geometry	Cluster multiplicity (per unit cell)	Fe-O-Fe angle (°)
1	5.8	7.7	2.99	Fe1-Fe1, edge	12	92, 94
2	4.9	6.5	3.28	Fe1-Fe2, edge	6	100,100
3	25.0	33.2	3.43	Fe1-Fe3, corner	12	118
4	31.9	42.3	3.47	Fe1-Fe3, corner	6	122
5	20.5	27.2	3.63	Fe2-Fe3, no sharing	2	-
6	43.2	57.3	3.54	Fe2-Fe1, corner	12	128
7	20.5	27.2	3.63	Fe2-Fe3, corner	6	123
8	5.8	7.7	4.99	Fe1-Fe1, no sharing	12	-

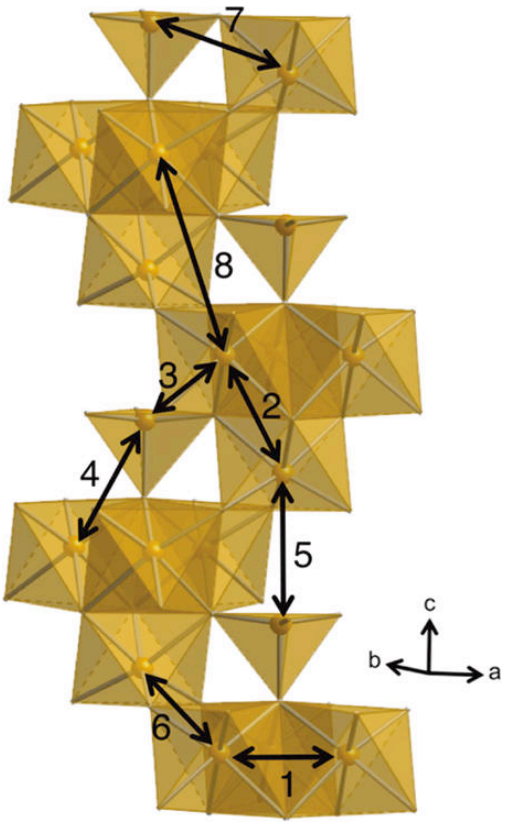

Figure 2-3: Pairwise spin interactions included in the Heisenberg mode for ferrihydrite. Only Fe atoms and associated polyhedra are shown for clarity.

Using the fitted interactions, a Monte Carlo simulation of the classical Heisenberg model was performed so as to determine the ground state magnetic ordering at low temperature. Beginning with a large supercell based on the ferrihydrite unit cell (600 ferrihydrite unit cells, length approximately 50 Å per side) with a random spin ordering at high temperature (800 K), a cooling simulation was performed in which the spins were annealed into their low-temperature ordering. A large supercell is chosen to ensure that ordered configurations were not forced by any limited dimension of the unit cell. Various supercell sizes were also tested, and it was ensured that supercell dimension had no effect upon either the ground state magnetic ordering obtained, or the transition temperature. The Monte Carlo simulation shows a transition from randomly ordered paramagnetism to ordered ferrimagnetism at 250±5 K. Here, the error represents only that due to the numerical accuracy of the determination of the Néel temperature, and does not reflect the considerably larger uncertainties inherent to the model. Essentially no hysteresis in the magnetic transition temperature was observed when the simulation is performed in reverse (heating a fully ordered cell from 0K to high temperature), suggesting a second-order or weakly first-order transition.

The Monte Carlo simulation predicts a ferrimagnetic groundstate, as shown in Figure 2-4, wherein uncompensated Fe moments are distributed regularly in layers throughout the bulk (20% of moments, or 2 moments per unit cell, are uncompensated) (Figure 2-4). Surprisingly, the low-temperature spin-alignment from the Monte Carlo simulations is slightly non-collinear. However, it is identical to a perfectly collinear ferrimagnetic state except for small, seemingly random deviations from collinearity of typically just a few degrees (never more than 10°).

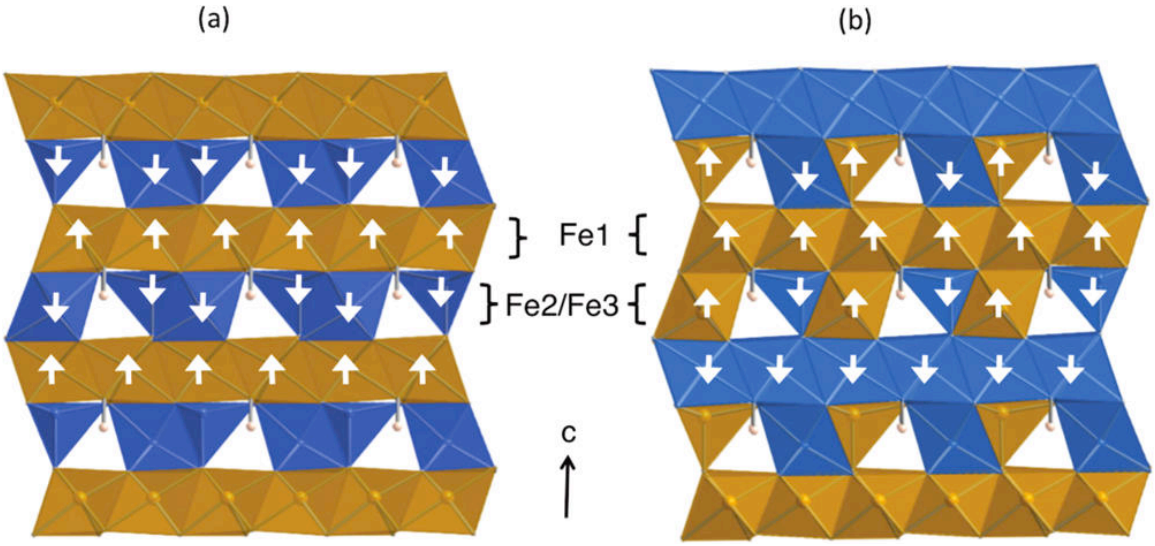

Figure 2-4: (a) Predicted stable ferrimagnetic ordering for ferrihydrite. O atoms are omitted for clarity. Up spins (color: brown)(greyscale: light grey) outnumber down spins (color: blue)(greyscale: dark grey) 3:2. (b) The most stable predicted antiferromagnetic ordering has energy 1 kJ/(mole-Fe) relative to ferrimagnetic groundstate ordering.

The small deviation from collinearity observed in the Monte Carlo simulation is potentially a real property of the ground state, but may easily be an artifact of the Heisenberg model due to, for example, the lack of longer-range pairwise interaction energies. Removing these small non-collinear deviations, a collinear structure corresponding to the Monte Carlo groundstate was obtained, the energy of which was further assessed within a full collinear DFT calculation. The noncollinear structure should not be misconstrued as a failure to achieve convergence of the Monte Carlo simulation, as it is actually lower in energy than the corresponding collinear structure. However, regardless of its source, the non-collinearity is of almost no energetic consequence, leading to reductions in energy of only 0.1 kJ/(mol-Fe) as compared with the corresponding collinear ferrimagnetic state when evaluated within the Heisenberg model. Thus, it is concluded that the collinear structure is a good representation of the ferrihydrite magnetic ground state. The collinear ferrimagnetic structure is used in all the ferrihydrite calculations presented in other sections of this paper and the magnetic structure is discussed in more detail below.

The predicted ferrimagnetic ground state corresponds to a layered structure in which planes of Fe moments alternate in alignment along the c-axis (Figure 2-4a). Planes of octahedrally coordinated Fe atoms (site Fe1 in the Michel model, see Figure 2-2) that share two O atoms along an octahedral edge show ferromagnetic ordering, indicating frustration on the spin lattice, as all the interactions favor antiferromagnetic coupling. Stronger antiferromagnetic interactions between pairs of Fe1/Fe2 and Fe1/Fe3 atoms (clusters #3, 4, and 6 in Table 2-11) override the weaker antiferromagnetic interaction between Fe1 atoms (cluster #1) and put the Fe1-site spins into a ferromagnetic (like-spin) arrangement with respect to each other. The next plane of atoms along the c-direction includes the symmetry-inequivalent octahedral site (Fe2, Figure 2-2), and also a tetrahedral Fe site (Fe3, Figure 2-2), in equal proportion. The second octahedral site (Fe2) shares three corner oxygen atoms with the layer of Fe1 sites below, and three edges with the Fe1 octahedra above. The tetrahedral Fe3 site shares corner oxygen atoms with both Fe1 and Fe2 polyhedra. Antiferromagnetic ordering is found between the Fe1 and Fe2/Fe3 layers in the ferrimagnetic model. As Fe1 sites outnumber the Fe2 and Fe3 sites (six Fe1, and two each of Fe2 and Fe3 per primitive unit cell), the overall ratio of up- to down moments is 3 to 2, leaving 20% of the moments uncompensated. Thus, the general trend of layering of antiparallel moments (in this case, along the c-axis) noted in other Fe-(oxyhydr)oxides (e.g. lepidocrocite, wüstite) is reproduced here [1]. Notably, the predicted ferrimagnetic ordering of ferrihydrite is similar to that of the ferrimagnets magnetite and maghemite, both of which also share structural elements with ferrihydrite, including mixed tetrahedral and octahedral Fe sites arranged in layers. In magnetite and maghemite, parallel spins occupy all symmetry-equivalent sites, as in the predicted ferrimagnetic ordering for ferrihydrite; antiferromagnetic ordering is observed only between symmetry-distinct sites (e.g. octahedral A sites are antiparallel to tetrahedral B sites, using the conventional site labeling scheme for magnetite and maghemite)[1].

Another Monte Carlo simulation was performed with the constraint of zero net spin, forcing an antiferromagnetic ordering to result at low temperature. The predicted low-temperature antiferromagnetic ordering is shown in Figure 2-4b, and also shows layering of spins stacked along the c-axis. The energy of this ordering was also assessed with a

full collinear DFT calculation, and was found to be unstable relative to the collinear ferrimagnetic structure by slightly more than 1kJ/(mol-Fe). Therefore, the most stable magnetic structure is the ferrimagnetic ordering, although this is nearly degenerate with a similar antiferromagnetic ordering. The antiferromagnetic stacking sequence includes ferromagnetic ordering along the planes of Fe1 sites, as in the ferrimagnetic model, albeit with alternating spin directions from layer to layer. Unlike the ferrimagnetic model, Fe2 and Fe3 sites have antiparallel spins within the same layer, and ferromagnetic ordering is observed for the Fe1-Fe2 pair identified by cluster #2 in Figure 2-3.

Proceeding on the basis that 20% of the Fe moments are uncompensated in the ferrimagnetic model, and based on the cation density of ferrihydrite (~35 Fe^{3+}/nm^3), it can be shown that a 4 nm diameter spherical nanoparticle of ferrihydrite would contain roughly 230 uncompensated Fe moments, distributed regularly throughout the bulk. In the case of Fe^{3+}, for which S=5/2, the spin-only magnetic moment per Fe is $\mu_{Fe} = g(S(S+1))^{1/2}\ \mu_B = 5.9\ \mu_B$. Hence, the net magnetic moment due to uncompensated Fe moments in a 4 nm perfectly-ordered ferrimagnetic particle amounts to approximately 1360 μ_B. This value is considerably larger than estimates based on indirect evidence in experimental studies that assume a random distribution of uncompensated spins either in the bulk, or on or near the nanoparticle surface, in which a net magnetic moment of 242-290 μ_B/particle is obtained (Seehra et al. [60]) Much of this difference could be explained by the high fraction of spin-bearing sites in a 4 nm particle that are impacted by defects and surfaces and therefore could deviate from the ideal ferrimagnetic ordering. Roughly 40% of all Fe atoms in a 4 nm particle can be considered “surface spins”, as they are in the outer monolayer of Fe-polyhedra and have at least one missing magnetic interaction (i.e. a missing ‘magnetic bond’). In addition, if even a modest fraction of Fe lattice sites within the “bulk” are vacant, local magnetic disorder due to the concomitant missing exchange interactions could noticeably affect the bulk magnetic ordering, likely reducing the net moment of a nanoparticle in the case of randomly disordered spins, and potentially affect spin ordering to the extent that a different low energy magnetic structure is stabilized. While a quantitative comparison cannot be made between the model and experimental moments at this point, the fact that a larger magnetic moment is

predicted for the ideal ferrimagnetic structure than that measured for ferrihydrite nanoparticles is to be expected.

2.5.3 Fe-(oxyhydr)oxide stability and GGA+U method

In order to accurately model the thermodynamic properties of Fe-containing materials it is necessary to have accurate DFT energetics. In the Fe-based (oxyhydr)oxides, the correlations between the 3*d* electrons localized on the same Fe atoms are not treated accurately within the GGA. The GGA+U method is employed here to correct these known errors (for specific details, see Section 2.4.1). In previous studies, the best agreement with experimental thermodynamic, structural, electronic, and magnetic behavior [67] in Fe-oxides was achieved at U = 4-5.5 eV [27, 68, 29, 67, 69] (or U_{eff} = U-J = 3-4.5 eV, with J set at a constant 1 eV, following the example of Rollman et al. [31]).

To assess the effectiveness of GGA+U for the specific set of Fe-(oxyhydr)oxides under consideration, the energetics and relative stability of each structure have been calculated as a function of U and compared with experiment. Relative stabilities for the Fe-(oxyhydr)oxide structures with reference to hematite and water were calculated following the methods described in Section 2.4.2. The stabilities are calculated for a range of U values from 1-7 eV, or equivalently U_{eff} = 0-6 eV, where, again, J is fixed at 1 eV. Note that U=1 is therefore equivalent to standard GGA. A significant dependence on U is observed for the relative stabilities of goethite and lepidocrocite (Figure 2-5). The best agreement with experimental relative thermodynamic stabilities (reaction enthalpies) is achieved for U ≈ 4 eV, consistent with the range of optimal U values discussed above.

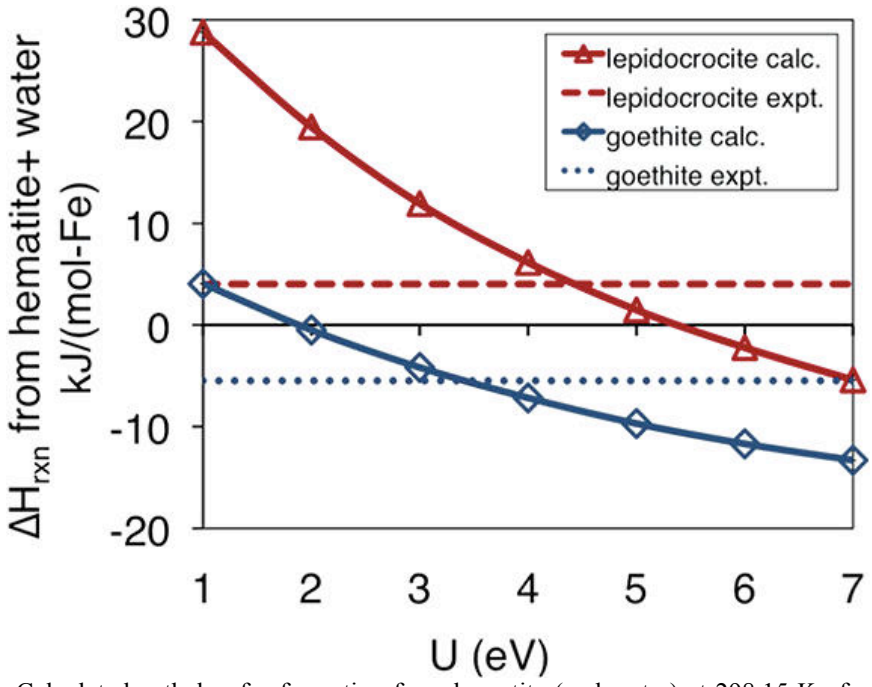

Figure 2-5: Calculated enthalpy for formation from hematite (and water) at 298.15 K of goethite and lepidocrocite versus the U parameter, and as compared with experiment [11]. The region of best agreement with experimental thermodynamic data is achieved for U≈4 eV. For U=4 eV, DFT values differ from experimental data by less than ±2.2 kJ/(mol-Fe) for both goethite and lepidocrocite.

In a manner similar to lepidocrocite and goethite, the relative stability of bulk ferrihydrite was also obtained as a function of U, applying the ground state ferrimagnetic ordering described in Section 2.5.2. Low-temperature specific heat data for ferrihydrite was not available, but is needed to apply the thermodynamic model described by Equation 2.4. As an estimate of the low-temperature specific heat profile for ferrihydrite between 0 and 298.15 K, the $\int_{0K}^{298.15K} C_p dT$ value (equivalent to $H^{298.15\ K}$-$H^{0\ K}$) for ferrihydrite was estimated using a linear combination of the values for hematite and goethite ($\int_{0K}^{298.15K} C_p dT$= 15.56 and 10.74 kJ/(mol-Fe), respectively), based on the fact that the ferrihydrite stoichiometry can be formed from two parts hematite and one part goethite formula units (Equation 2.9), and the observation that, as a first approximation, formation enthalpy is mainly dependent on stoichiometry (or in the case of Fe-oxides and (oxyhydr)oxides, degree of hydration). The proxy materials used to predict the ferrihydrite specific heat (hematite and goethite) do not have a magnetic disordering transition between 0-298.15 K. In order to account for the presence of this transition in

ferrihydrite an additional term is added to the ferrihydrite enthalpy. This term is determined from the Monte Carlo simulation of the ferrihydrite magnetic Heisenberg-model described in Section 2.5.2. The enthalpy as a function of temperature shows a smooth increase until near $T_N \approx$ 250K, at which point it jumps significantly. The difference between the extrapolated enthalpy based on the low temperature behavior and the actual enthalpy at 298.15K is 0.7 kJ/(mol-Fe), which is taken to be the enthalpy associated with the magnetic disordering transition. This term has therefore been added to the enthalpy determined from the proxy materials to account for the magnetic disordering and is included in Equation 2.10.

$$2 \cdot Fe_2O_3 + FeOOH \rightarrow Fe_5O_8H \qquad (2.9)$$

Normalizing per mole of Fe atoms, the $\int_{0K}^{298.15K} C_p dT$ value for ferrihydrite is estimated as:

$$\int_{0K}^{298.15K} C_p dT_{ferrihydrite} = \frac{4}{5}\left(7.78 \tfrac{\text{kJ}}{\text{mol-Fe}}\right) + \frac{1}{5}\left(10.74 \tfrac{\text{kJ}}{\text{mol-Fe}}\right) + 0.7 = 9.07 \text{ kJ/(mol-Fe)} \qquad (2.10)$$

All of the Fe-(oxyhydr)oxides studied in this paper display similar low-temperature specific heat profiles, with $\int_{0K}^{298.15K} C_p dT$ values ranging from 7.78-10.83 kJ/(mol-Fe), so basing our estimated thermodynamic correction for ferrihydrite upon the data for other structures besides hematite and goethite would likely yield a shift of only 1-2 kJ/(mol-Fe), at most, in the calculated relative stability of ferrihydrite. At U=4 eV, bulk crystalline ferrihydrite is predicted to be metastable in terms of formation enthalpy relative to hematite + water, as can be seen in Figure 2-6. At 298.15 K, the standard formation enthalpy of ferrihydrite is calculated as $\Delta H°_f$ (Fe_5O_8H) = -435.3 kJ/(mol-Fe) relative to the elements in their standard states, or 6.4 kJ/(mol-Fe) relative to hematite + liquid water. The significant deviation (5-9 kJ/(mol-Fe)) from the experimental enthalpies is interpreted as being due to particle size effects and will be discussed in Section 2.5.4.

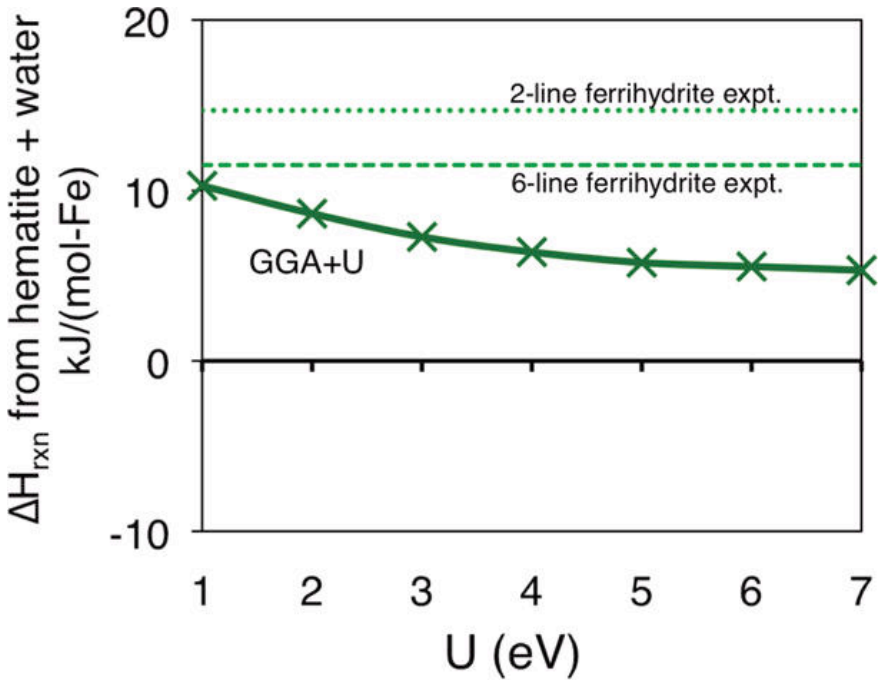

Figure 2-6: Calculated enthalpy of formation of bulk ferrihydrite, relative to hematite and water at 298.15 K, as a function of the U parameter. The experimental formation enthalpies of 6-line and 2-line ferrihydrite are obtained from Majzlan et al. [13] and represent samples of synthetic nanoparticles.

Next, the enthalpy calculation is extended to give an estimate for the Gibbs energy of bulk ferrihydrite, which is a better gauge of overall stability. In order to evaluate this quantity is it necessary to determine the standard entropy $S°$ ($G° = H° - TS°$). We estimated the standard entropy of the bulk ferrihydrite phase following the method of Majzlan et al. [13] in which an empirical relationship is fitted to interpolate between the entropies of isostructural Fe^{3+} and Al^{3+}-based (oxyhydr)oxides whose standard entropy values are known (Figure 1.6). The Majzlan study estimated the standard entropy of ferrihydrite under the assumption that ferrihydrite has the stoichiometry $Fe(OH)_3$, similar to the gibbsite structure, $Al(OH)_3$. However, assuming the Michel model for ferrihydrite, the appropriate corresponding isostructural Al-(oxyhydr)oxide is akdalaite, Al_5O_8H. The akdalaite standard entropy is estimated by Hemingway et al. [40] as $S°_{akdalaite}$=29.3 J/(mol-Al K). Based on a linear fit of the correlation between entropy values for four isostructural Fe and Al phases (Figure 1.6), the standard entropy of ferrihydrite is estimated as $S°_{fhyd}$=49.1 J/(mol-Fe K), or 245.5 J/(mol K) per formula unit Fe_5O_8H.

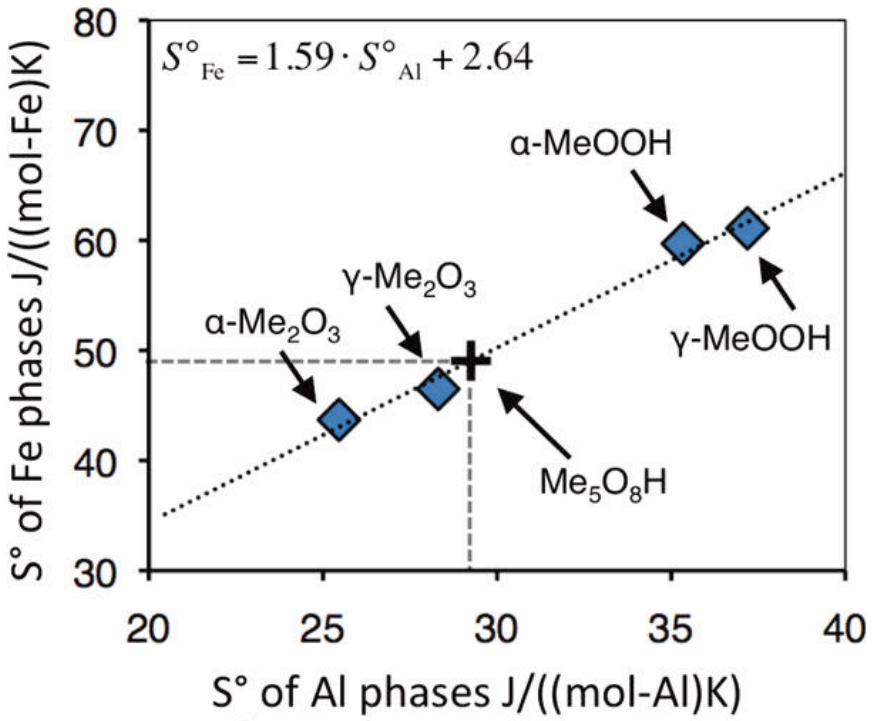

Figure 2-7: Linear correlation of the standard entropies of isostructural Fe- and Al-(oxyhydr)oxides (following the approach of Majzlan et al. [13]). The standard entropy of ferrihydrite is estimated to be 49.1 J/(mol-Fe K) based on the correlation of known entropy values and assuming ferrihydrite Fe_5O_8H corresponds to the aluminum isostructure akdalaite, Al_5O_8H (marked with a '+'). Error bars for experimental standard entropies are smaller than the symbol size (less than 0.5 J/(mol-Me K)).

The Gibbs free energy at 298.15 K of bulk ferrihydrite relative to hematite + water is calculated by the above method to be $\Delta G_{rxn}\left(Fe_5O_8H\right) = 6.9$ kJ/(mol-Fe) for U=4 eV (Table 2-12). The entropic terms for hematite and water were calculated using experimental standard entropy values [70, 2]. The Gibbs free energy can also be expressed relative to hematite and water vapor at 298.15 K by noting that H_2O liquid and vapor are in equilibrium at 100% relative humidity (*RH*), and thus their free energies are equal (e.g. $\mu\left(\mathrm{H_2O}\right)_{\mathrm{liquid}} = \mu\left(\mathrm{H_2O}\right)_{\mathrm{vapor}}$). The Gibbs free energy of ferrihydrite relative to hematite and water vapor at arbitrary *RH* and T_0 = 298.15 K can therefore be obtained from $\Delta G_{rxn}\left(Fe_5O_8H\right) = 6.9 - 0.1RT_0 \ln\left(RH/100\right) = 6.9 - 0.248\ln\left(RH/100\right)$ kJ/(mol-Fe).

Figure 2-8 shows the calculated stability of ferrihydrite and goethite relative to hematite and water vapor over the full range of relative humidity values, the latter shown in logarithmic scale. It emerges that ferrihydrite becomes stable relative to goethite only at extremely low relative humidity (roughly 0.1% *RH*). Note that this crossover *RH* value will change for nanoparticles due to surface energy effects, as discussed in Section 2.5.4.

Table 2-12: Gibbs free energies of formation relative to hematite + water for the Fe-(oxyhydr)oxides at T=298.15 K and 100% relative humidity. Calculated results shown for U=4 eV. Experimental values obtained from Ref. [2].

Structure	$\Delta G_{rxn}^{\text{experiment}}$ kJ/(mol-Fe)	ΔG_{rxn}^{GGA+U} kJ/(mol-Fe)
hematite	0.00	0.00
goethite	0.15	-1.5
lepidocrocite	8.05	10.2
ferrihydrite (bulk)	n/a	6.9

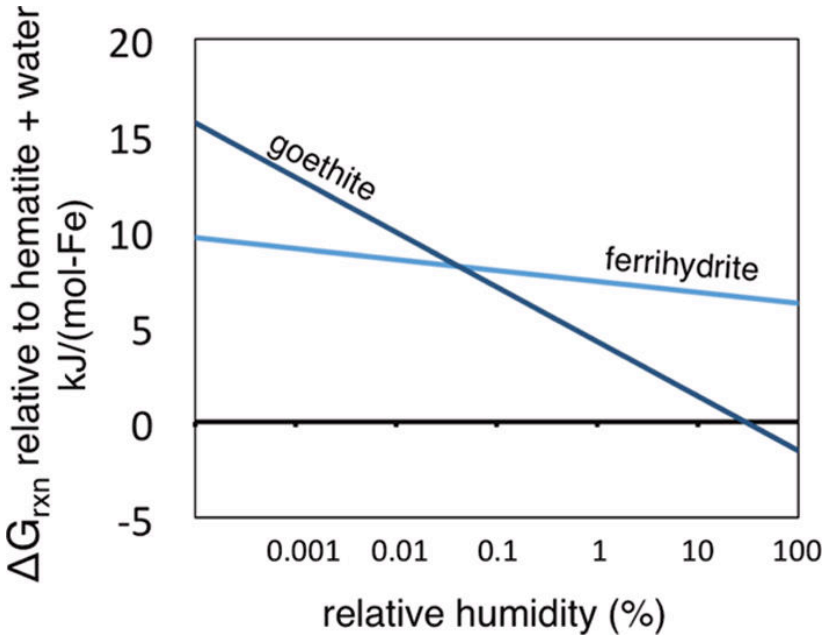

Figure 2-8: Stability of ferrihydrite and goethite relative to hematite and water vapor versus the logarithm of relative humidity. A crossover stabilizing ferrihydrite relative to goethite is apparent at very low relative humidity (less than 0.1%)

2.5.4 Effect of surface energy on the stability of nanoparticle ferrihydrite

Figure 2-6 shows that the bulk ferrihydrite relative formation enthalpy is predicted to be well below the experimentally measured value. However, experimental studies of ferrihydrite deal exclusively with nanoparticle samples, thus the surface energy contribution must be included before a direct comparison between the experimental and DFT based enthalpies is made. The formation energy of a mineral nanoparticle can be approximately constructed by adding bulk and surface energies. Assuming spherical particles, the particle surface energy is obtained as (Equation 2.11):

$$E_f^{surface}(d) = \Delta H_s^h \cdot 4\pi\left(\frac{d}{2}\right)^2 \qquad (2.11)$$

where d is the nanoparticle diameter and ΔH_s^h is the effective hydrous surface formation enthalpy (the expression could also be written in terms of the anhydrous surface formation enthalpy, ΔH_s). In this work we will assume a single, constant, effective surface energy. The use of a constant effective surface energy does not take into account a number of factors that can cause changes in the surface energy with diameter, such as changes in bonding strengths, surface reconstructions, defect concentrations, variations in the fraction with which different terminations contribute to the surface morphology, the latter including important effects such as low-coordination corner- and edge sites [71, 72]. These effects are likely to become more important for the smallest particles, in the 1-2nm size range, and a more accurate treatment of the surface energetics may be required in the future for quantitative modeling of the smallest ferrihydrite particles. Both anhydrous and hydrated surface enthalpies for hematite, goethite, lepidocrocite, and other Fe-(oxyhydr)oxides are tabulated in Ref. [2]. Notably absent from the literature is the surface formation energy of ferrihydrite, which is estimated in this section. This paper will focus on the hydrated surface case, as the hydrated surface best represents natural conditions in which mineral precipitations and transformations take place. In all Fe-(oxyhydr)oxide phases, it is found that the hydrated surfaces are stable relative to their anhydrous counterparts in aqueous environments or under typical relative humidity values in air. Hydrated surfaces typically consist of a layer of chemisorbed water

molecules overlaid by physisorbed water molecules that behave like bulk water. The chemisorbed water molecules are strongly bound and likely affect surface geometries of the (oxyhydr)oxide and oxide surfaces [2]. The nanoparticle thermodynamic analysis derived here does not explicitly distinguish chemisorbed water from physisorbed water molecules. The thermodynamic analysis of the nanoparticles of the material treat the material in the particle as bulk and water molecules as bulk water, and then the effective surface formation enthalpy term in Equation 2.11 accounts for the changes in energy from these bulk states due to the presence of a surface, chemisorption of surface waters, and surface reconstruction.

The formation energy of a complete nanoparticle can be written as formation energy of the volume of the particle cut from bulk crystalline material, plus the particle surface energy, as shown in Equation 2.12. Surface entropy contributions to the free energy of nanoparticle Fe-(oxyhydr)oxides are not considered in this study, i.e., only the enthalpy of surface formation is included.

$$\Delta G_f^{particle}(d) = \Delta G_f^{bulk} \cdot \frac{4\pi}{3}\left(\frac{d}{2}\right)^3 + E_f^{surface}(d) \qquad (2.12)$$

The surface energy of ferrihydrite is estimated by considering the fairly narrow size range in which ferrihydrite particles are observed (roughly 2-7 nm), and the bulk stability calculated in Section 2.5.3. To estimate the surface energy of ferrihydrite, we examine Figure 2-9, which shows the calculated stability, or free energy of formation relative to bulk hematite + water, as a function of surface area (or inversely, particle size), for a number of Fe-(oxyhydr)oxides. The y-intercepts of this plot are the calculated bulk stabilities (Section 2.5.3). The positive slope of each line represents the energy cost of forming 1 m^2 of a hydrated mineral surface per Fe, cut from bulk material. The slope of each solid line comes from experimental data [2]. The surface energy of ferrihydrite is estimated to be within the range of 0.2-0.4 J/m^2. The lower bound is drawn such that ferrihydrite becomes thermodynamically stable relative to goethite at particle sizes smaller than d=7 nm, at a specific surface area (SSA) of roughly 20,000 m^2/(mol-Fe). This bound is based on the fact that ferrihydrite particles larger than ~7 nm are difficult to

obtain or synthesize under normal conditions (e.g. without the incorporation of stabilizing agents such as Si or citrate, which have been shown to aid in the synthesis of ferrihydrite particles larger than 7 nm) [57, 53, 54]. Ferrihydrite is typically considered to have a low surface formation energy relative to the common Fe-(oxyhydr)oxides[73], thus the upper bound of the estimated surface energy range is set to that of lepidocrocite, which has the lowest experimentally measured surface energy (0.4 J/m^2) [2]. Proceeding on this basis and drawing conclusions from the lower-bound surface energy, ferrihydrite becomes stable relative to nanoparticle hematite for ferrihydrite particle sizes around d=10-12 nm, or at a SSA of approximately 12,000 m^2/(mol-Fe).

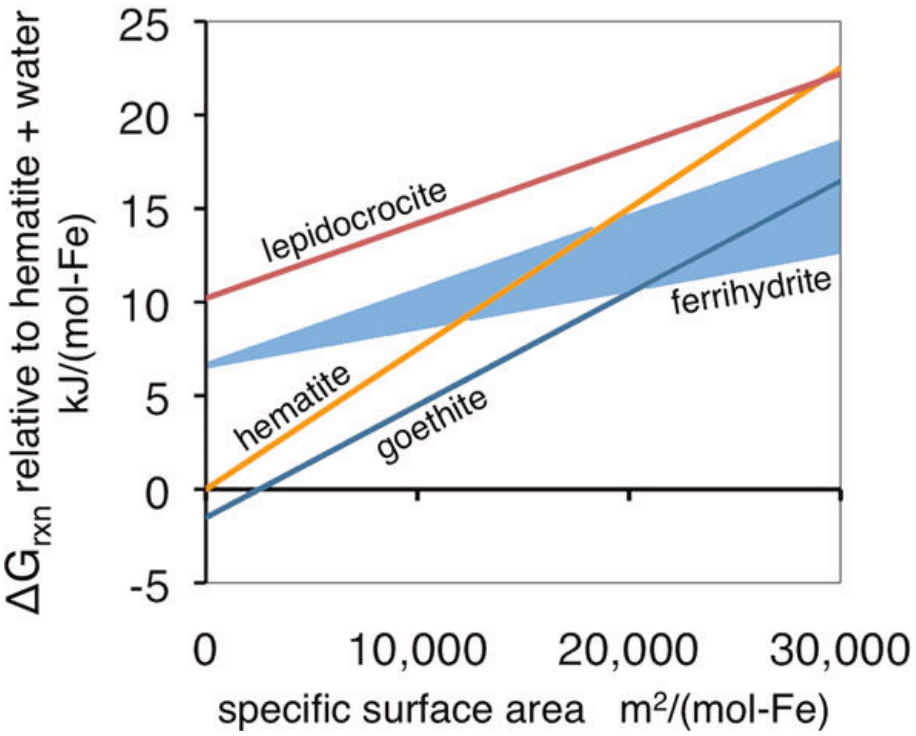

Figure 2-9: Gibbs free energy of formation relative to bulk hematite and water of nanoparticle Fe-(oxyhydr)oxides as a function of specific surface area. The slope of each line is the hydrated surface formation enthalpy for each (oxyhydr)oxide, as tabulated in Ref. [2]. The y-intercepts are the calculated bulk stabilities (Section 2.5.3). The shaded wedge shows the estimated Gibbs free energy of formation of ferrihydrite, with the hydrated surface energy range estimated based on empirical observations of particle stability and transformation characteristics.

Figure 2-10 shows the predicted formation enthalpy of nanoparticle ferrihydrite obtained from Equation 2.12 as a function of particle diameter. The experimental formation enthalpies of 2-line and 6-line ferrihydrite nanoparticles [13] are shown as dotted lines at approximately 10-15 kJ/(mol-Fe) higher enthalpy than bulk hematite + water. The lower, dashed line is the DFT formation enthalpy of bulk, crystalline ferrihydrite as calculated in Section 2.5.3. The shaded region corresponds to the calculated formation enthalpy of spherical ferrihydrite nanoparticles as a function of particle diameter, assuming the estimated surface formation energy range described above. As particle diameter decreases, surface formation energy plays a progressively larger role in destabilizing the nanoparticle system relative to the bulk mineral structure. The predicted formation of a ferrihydrite nanoparticle of diameter 4 nm, for instance, ranges from 10-15 kJ/(mol-Fe) less stable than bulk hematite and water, consistent with the experimental energetics of nanoparticle ferrihydrite. The range of particle formation enthalpies is a consequence of the estimated range of possible surface formation energy values. In the nanoparticle regime, ferrihydrite is the most stable of the modeled Fe-(oxyhydr)oxides for particle sizes below 7 nm, consistent with its observed formation during early stages of Fe-(oxyhydr)oxide nucleation and growth. However, the stability of ferrihydrite at the smallest particle sizes is largely determined by the approximate methods used to fit the ferrihydrite surface energy and cannot be regarded as predictive.

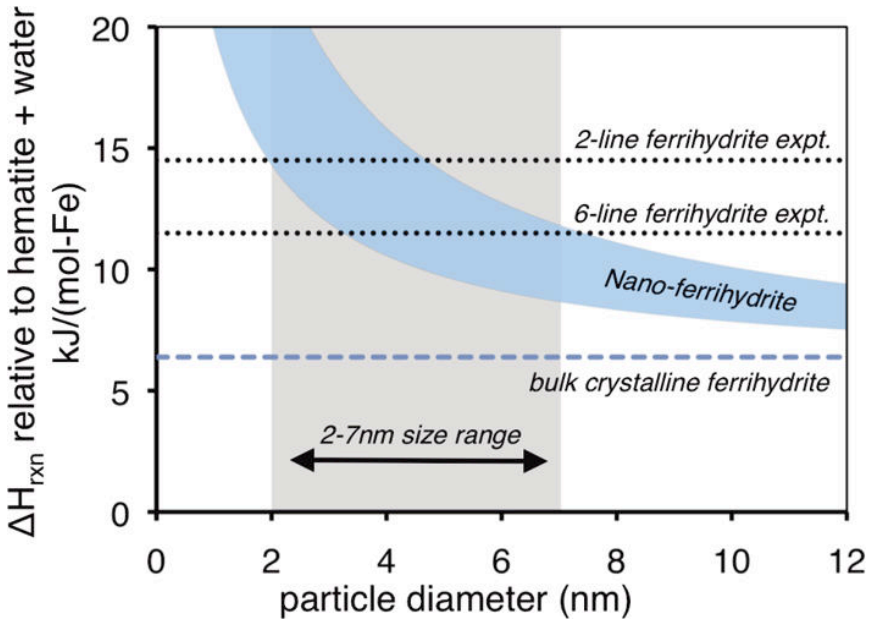

Figure 2-10: Formation energy model relative to hematite and water for spherical nanoparticles of ferrihydrite (Fhyd) with average surface energy ΔH_s^h = 0.2-0.4 J/m^2 (hydrated surface assumed). Experimental reaction enthalpies are shown for 2-line and 6-line nanoparticle samples [13]. Based on the DFT energy of un-defected bulk crystalline ferrihydrite, destabilization due to positive surface formation energy is of appropriate magnitude to account for the experimentally observed energetics of nanoparticle samples given a realistic distribution of particle sizes from 2-7 nm.

2.6 Conclusions

We have performed a DFT investigation of the structure, magnetism and relative thermodynamic stability of ferrihydrite and related Fe- and Al-(oxyhydr)oxides. All of the calculations are based on the Michel model of the ferrihydrite structure [10]. This model is particularly attractive from a computational standpoint, as it contains a fully periodic, single-phase structure upon which models for more complicated phenomena such as surfaces, defects and nanoparticles can be built.

The calculations provide structural parameters consistent with those proposed within the Michel model, and suggest that the unusual tetrahedral Fe3–O bond lengths found by Michel et al. [10] are not an intrinsic property of the bulk crystalline structure, but are instead likely to be due to the compounded influence of surfaces, poor crystallinity, defects, and the structural refinement errors reasonably anticipated for small nanoparticles.

The ground state magnetic ordering for ferrihydrite is predicted by means of a Heisenberg model incorporating exchange couplings fitted to DFT magnetic energetics. A ferrimagnetic ordering is predicted in ferrihydrite, with Fe moments counter–aligning in layers stacked along the c-axis. The ferrimagnetic structure leaves 20% of the Fe moments uncompensated. Monte Carlo simulation of the Heisenberg Hamiltonian places the Néel temperature of bulk ferrihydrite at 250 K, the transition manifesting either second-order or weak first-order character. The magnetic data obtained are in good agreement with the range of experimental Néel temperatures determined experimentally for the Fe-(oxyhydr)oxides, and with the experimental consensus that ferrihydrite should manifest antiferromagnetic coupling, with the presence of some fraction of uncompensated moments. It is likely that nanoparticle ferrihydrite will exhibit considerably more magnetic disorder than the bulk calculations, lowering the net excess moment per atom and possibly lowering the Néel temperature.

It is demonstrated that the DFT thermodynamic model can be made more accurate by the

inclusion of an improved description of the correlation effects present in the Fe 3*d*-electrons, here achieved via the GGA+U method. The best agreement with experimental Fe-(oxyhydr)oxide enthalpy data is achieved for U=4 eV. Using this U value and assuming the Fe_5O_8H stoichiometry of the Michel model, the formation enthalpy at 298.15 K of bulk crystalline ferrihydrite is calculated to be -435.3 kJ /(mol-Fe) relative to the elements (in their standard state), or 6.4 kJ/(mol-Fe) relative to bulk hematite (α-Fe_2O_3) and liquid water. The Gibbs free energy of formation at 298.15 K is calculated to be ΔG_{rxn} (Fe_5O_8H) = 6.9 kJ/(mol-Fe) relative to hematite (α-Fe_2O_3) and liquid water. Bulk crystalline ferrihydrite is thus metastable relative to goethite and hematite, but somewhat more stable than lepidocrocite. Using a hydrous surface formation enthalpy estimate of 0.2-0.4 J/m^2, which is in the lower end of the typical range for Fe-oxides and oxyhydroxides, and the calculated bulk formation enthalpy, hydrated spherical ferrihdyrite particles of diameter 4-5 nm should have a formation enthalpy of roughly 10-15 kJ/(mol-Fe) relative to bulk hematite and water, which is in agreement with published experimental values for 2- and 6-line nanoparticles. The calculated stability of ferrihydrite lends credence to the Michel model, given that an incorrect or inaccurate structure might have led to a significantly higher energy and poorer agreement with the experimental enthalpies. We note that a similar thermodynamic assessment as performed in this work for the Michel model is not applied to other proposed models [19, 14-16] for the ferrihydrite structure due to the highly defected, multi-phase nature of these models making them particularly challenging for ab initio investigation.

The results support the Michel model as a plausible candidate for the bulk ferrihydrite structure, since our DFT study of the structural, magnetic and thermodynamic properties of the hypothetical bulk model are in general agreement with experimentally observed properties when the effects due to nanoparticle formation are considered. Assuming that the Michel model is correct, these calculations provide new insights into the atomic, magnetic, and thermodynamic properties of ferrihydrite.

2.7 Chapter Acknowledgements

I gratefully acknowledge input from co-authors Prof. Clare Grey and Dr. Derek Middlemiss of SUNY Stony Brook, and Prof. Jim Kubicki of Penn State University, during the writing of this chapter.

I must also recognize the clarifying guidance provided by helpful discussions with Dr. F. Marc Michel and Prof. John Parise of SUNY Stony Brook.

I benefited greatly from the use of Monte Carlo codes developed by Anton Van der Ven, which were modified for the Heisenberg model Monte Carlo simulations.

I gratefully acknowledge funding support for the research reported in this chapter from the National Science Foundation, through a Collaborative Research in Chemistry grant, award number CHE 0714183.

3 Thermodynamics of Al-substitution in Fe-(oxyhydr)oxides

Note: The contents of this chapter are principally derived from a peer-reviewed article published in Geochimica et Cosmochimica Acta *[74]. The article was adapted for use in this thesis document.*

3.1 Chapter Abstract

Ab initio simulation results are presented for dilute Al-substitution in the common Fe-(oxyhydr)oxide materials hematite, goethite, lepidocrocite and ferrihydrite. Experimental evidence from the literature suggests that Al-substitution in these materials may influence particle stability and phase transformation behavior, typically stabilizing the (oxyhydr)oxide phases relative to the oxide, hematite. We find that all the alloyed phases studied are unstable with respect to phase separation into their unalloyed Fe/Al-(oxyhydr)oxide end members. Among the phases studied, ferrihydrite is predicted to allow Al-substitution with the lowest energy cost, while hematite appears to have the strongest tendency for phase separation. Considering the effect on thermodynamic stability relative to the stable Fe-oxide hematite, the three Fe-(oxyhydr)oxide materials (goethite, lepidocrocite, ferrihydrite) are shown to be stabilized relative to doped Al-hematite as Al content is increased. Interactions between Al dopant atoms on neighboring Fe sites are simulated and are shown to have minimal influence on Fe-Al alloying thermodynamics in each of the materials simulated within the range of Al-dopant concentrations calculated. Simulations of Al-substitutions at the goethite (101) surface indicate that surface segregation of Al dopants is energetically favored for low Al concentrations, however this tendency diminishes when Al dopants form a full monolayer at the mineral surface.

3.2 Introduction

In the context of natural occurrence of Fe-(oxyhydr)oxide materials, rapid precipitation of aqueous Fe^{3+} typically results in the formation of amorphous or poorly crystalline nanoparticulate Fe-(oxyhydr)oxide precipitates that incorporate significant fractions of non-stoichiometric dopants and other crystallographic defects, including excess structural water and disordered or partial occupancy of cation sites [75]. Given sufficient thermal energy or annealing time, these materials can phase transform into more stable, more crystalline Fe-(oxyhydr)oxides or oxides, possibly incorporating some fraction of the original defect/dopant content into the product phase. A variety of cations are observed to substitute on the Fe lattice of the Fe-(oxyhydr)oxides and oxides, including Al, Mn, Cr, Zn, Cd and Si, among others [76-78, 1, 79, 80], with Al being the most commonly observed in natural samples.

The common Fe-(oxyhydr)oxides have known stable (or metastable) isostructural Al-(oxyhydr)oxide analogues (*e.g.,* goethite and diaspore, lepidocrocite and boehmite, hematite and corundum) suggesting that Al^{3+} and Fe^{3+} have similar enough chemistry to readily enable substitution. However, these materials do not form Al/Fe solid solutions across all compositions. Al dopant concentrations lower than 10-15% of Fe sites are typical, and ~30% Al represents an upper limit for Al substitution achieved for synthetic goethites [81-83, 1]. This limited alloying behavior is perhaps explained by the smaller ionic radius of Al^{3+} as compared with Fe^{3+}, leading to destabilizing lattice strain in mixed Al/Fe structures [77].

The incorporation of Al as a metastable defect in Fe-(oxyhydr)oxides has been examined by various experimental studies [81, 82, 84, 83, 85, 1, 86-90], in which the inclusion of Al has been shown to cause measurable changes in particle morphology, precipitation and phase transformation characteristics, magnetic properties, and reactivity toward sorption of aqueous ions and other surface processes. Al substitution is observed to occur in association with excess OH and cation vacancy defects in hematite and goethite, and in association with excess hydration content in ferrihydrite [91, 85, 92-95, 75]. Al

substitution within the structure of ferrihydrite is observed for synthetic ferrihydrites formed under rapid precipitation conditions, whereas slower precipitation processes are found to produce some amount of structurally-distinct Al-(oxyhydr)oxide co-precipitate phases [89].

Al incorporation in Fe-(oxyhydr)oxides induces a contraction of unit cell lattice parameters associated with the smaller ionic radius of Al^{3+} as compared with Fe^{3+}. Even though the Fe-(oxyhydr)oxides and oxide hematite have corresponding Al-based isostructures, the substitution of Al often does not induce linear or Vegard-like shifts in lattice parameters in response to increasing Al content [96, 1, 89]. Dependent on the structural details of the material, Al substitution affects lattice parameters non-uniformly, causing larger contractions in dimensions more tolerant of strain. Additionally, the influence of Al on lattice parameters in real samples can be masked by the simultaneous presence of other point defects (*e.g.,* excess OH) and surface/nanoparticle properties that may induce conflating strain and bond-length effects.

The presence of Al can affect phase transformations between Fe-based mineral structures (*e.g.,* goethite to hematite). Phase transformations in these materials occur via several pathways, most commonly via thermal dehydration or dehydroxylation reactions leading to structural transformation (e.g. ferrihydrite to hematite), or via dissolution-reprecipitation reactions in solution (e.g. ferrihydrite to goethite) [97, 1]. Aluminum doping is shown to favor the formation of hematite over goethite in the hydrothermal transformation of Al-ferrihydrite, as compared to undoped ferrihydrite, as well as influencing the morphology of the hematite particles produced [82, 98, 88], The suppression of the formation of goethite from Al-ferrihydrite is arguably due to the retarding influence of Al on mineral dissolution kinetics at the ferrihydrite surface, thus disfavoring the dissolution steps involved in the formation of goethite from ferrihydrite [99, 87]. Al doping is also shown to increase the thermal stability of goethite, inducing a systematic upward shift in the dehydroxylation temperature at which goethite transforms to hematite as a function of Al content, although this phenomenon is interrelated with excess OH defect content [100].

The impact of Al on phase transformation behavior can be imagined to work through several mechanisms. One possibility is that Al substitution influences relative thermodynamic stability between phases to a degree that the driving force for topotactic phase transformation is appreciably altered. Another possibility is that Al impedes surface reactions that lead to phase transformation (*e.g.,* the dissolution of Fe^{3+} as a step in a dissolution-reprecipitation process).

It is not clear to what degree Al dopants tend to cluster or disperse when co-precipitated within the Fe-(oxyhydr)oxides, however some data is available. In goethite, XRD results in combination with reflectance spectra suggest that Al dopants are distributed on the Fe lattice and not found in diaspore-like clusters [77]. This result stands in contrast to that observed for Mn substitution in goethite, in which dopants cluster in Mn-rich, groutite-like local environments [78]. Contrasting the results of Scheinost, a recent computational study [101] showed that Al dopants in goethite are more stable when found in close proximity to other Al atoms, however the accompanying experimental results did not detect any diaspore-like regions in the Al-goethites examined.

In addition to the possibility of forming dopant-rich clusters within the bulk, dopant clustering at the surface of particles is also hypothesized as a possible result of Al incorporation or co-precipitation. Surface segregation of Al would lead to pronounced impacts on surface reactivity, as Al^{3+} atoms crowd out redox-active Fe^{3+} sites. Additionally, the effects of Al-dopants may be different in truly nanoparticulate Fe-(oxyhydr)oxides where surface physics are expected to dominate particle thermodynamics. For example, a recent computational study [102] examined the impacts of Al substitution in goethite and ferrihydrite nanoclusters and showed that an isolated Al substitution in a 24-Fe nano-goethite was energetically favorable compared to Al substitution in a 13-Fe nano-ferrihydrite, in contrast with empirical observations that show that the ferrihydrite to goethite transformation is impeded by the presence of Al dopants [99]. This result suggests that Al behavior in nanoparticle Fe-(oxyhydr)oxides may differ from that in bulk-like systems.

To better understand the structural and thermodynamic impacts of Al substitution in Fe-oxides and oxyhydroxides we here conduct an *ab initio* study of dilute aluminum doping in the common minerals hematite, goethite, lepidocrocite, and ferrihydrite, whose structures are illustrated in Figure 2-1. Strategically designed *ab initio* calculations allow targeted investigation of thermodynamic phenomena, in this case Al substitution, without the confounding influence of interrelated or concomitant phenomena that are often unavoidable when studying real material samples (e.g., particle size and surface phenomena, additional contaminants or defects, etc). In Section 3.4.1 of this study, Al-substitution enthalpies are compared among the four phases, and the impact of Al on the relative stability of the different phases is explored. In Section 3.4.2, Al-Al near-neighbor pair interaction energies are calculated, which aids in the determination of whether Al dopants are likely to be distributed evenly on Fe sites throughout the bulk lattice, or rather clustered in Al-rich regions.

Section 3.4.3 describes an investigation into the tendency of Al dopants to segregate to the surface or near-surface region of a model Fe-(oxyhydr)oxide material. The goethite (101) surface is chosen as the model system due to the predominance of this reactive crystal face in natural and synthetic goethites. In this model, Al dopants are placed at or near the surface of a periodic slab of goethite, and the energies of these configurations are compared to those of Al dopants within the bulk. Surface Al doping is considered in the context of both hydrated and anhydrous goethite surfaces. Al-Al interactions are also evaluated at the slab surface and compared to those from bulk calculations.

3.3 Computational Methods

3.3.1 Ab Initio Methods and Bulk Calculations

Density functional theory (DFT) calculations were performed using the Vienna Ab-initio Simulation Package (VASP) [7, 8], employing the projector-augmented wave (PAW) method [23, 24]. The generalized-gradient approximation (GGA) was used, as parameterized by Perdew, Burke and Ernzerhof (PBE) [25]. A plane-wave cutoff energy of 650 eV was chosen for all bulk calculations, in keeping with the total energy convergence trends observed in [9]. A soft PAW pseudopotential ($2s^2 2p^4$ valence configuration) was chosen for oxygen atoms, while a standard pseudopotential was chosen for hydrogen ($1s^1$). The *Fe_pv* pseudopotential was used for iron, which treats 3p electrons as part of the calculated valence shell ($3p^6 3d^7 4s^1$ valence configuration). Aluminum was treated with a standard PAW pseudopotential ($3s^2 3p^1$ valence configuration).

Kpoint meshes were chosen using the Monkhorst-Pack scheme [32] for the orthorhombic cells, and the Γ-centered scheme for hexagonal cells (calculation details are reported in Table 2.2). For bulk simulations, reciprocal space kpoint densities were chosen such that kpoint sampling was roughly equivalent in all reciprocal-space dimensions, and such that total energy was converged within 1-2 meV/atom with respect to an increase in kpoint density. This corresponds to a kpoint density of approximately 4000 kpoints per reciprocal atom, or roughly 30 kpoints per $Å^{-1}$ along any one dimension, for the bulk Fe- and Al-oxide and oxyhydroxide structures. Identical kpoint meshes were employed for Al-substitution simulations and pure-Al and pure-Fe isostructural end members with equivalent supercell sizes.

The GGA+U method was employed for Fe atoms [26, 27]. This method more accurately treats onsite Coulomb interactions for the localized *3d* electrons present for Fe. The rotationally invariant approach to the GGA+U method introduced by Dudarev was used for all GGA+U applications. In this approach, the onsite Coulomb interaction is

described by a single effective parameter, $U_{eff} = U - J$, which represents the difference between U, the spherically-averaged Hubbard parameter measuring the Coulomb interaction and J, the screened exchange energy between the localized electrons [30]. U_{eff} was set at 3 eV (U = 4 eV, J = 1 eV) for the *3d* electrons in Fe atoms for all calculations, and set to $U_{eff} = 0$ eV (the GGA limit) for all other electrons/atoms. This U_{eff} value is chosen such that calculated thermodynamic stabilities of the Fe-oxide/oxyhydroxide materials most closely match measured experimental stabilities [9]. U_{eff} values between 3-4 eV have also been shown to be optimal for calculating Fe-oxide/oxyhydroxide lattice parameters, magnetic properties, and redox energies [27, 28, 31, 29].

Spin-polarized GGA+U calculations were performed for hematite, goethite, and lepidocrocite and spins were initialized using experimentally determined antiferromagnetic groundstate spin orderings for these materials [1], with initial magnetic moments of ± 5 μ_B per Fe. In the case of ferrihydrite, the groundstate magnetic ordering employed is 58erromagnetic, also with magnetic moments of ± 5 μ_B per Fe [9, 54]. Al-doped Fe oxide/oxyhydroxide structures were initialized with Fe-spins identical to the magnetic groundstate orderings except for the Al dopant atoms, which were assigned zero spin. While spins were permitted to relax during the simulations, no re-orderings or reconfigurations of magnetic moments of Fe atoms (*e.g.,* spin flips or high-to-low spin transitions for Fe atoms) in Al-doped structures were observed during any of the calculations. Spin-polarized calculations of structures containing only Al^{3+} cations were performed with zero spin values assigned to all atoms. During optimization, Al atoms were observed to remain zero spin, consistent with expectations that these atoms are nonmagnetic.

The structure and composition of the Fe-(oxyhydr)oxide ferrihydrite is a subject on ongoing debate. The ferrihydrite structural model evaluated in this work was described in 2007 by Michel et al. as a single-phase material isostructural with the Al-(oxyhydr)oxide akdalaite (Al_5O_8H) [10]. This model is characterized by having three symmetry-distinct cation sites, labeled Fe1, Fe2, and Fe3 throughout this work (and equivalently Al1, Al2 and Al3 for akdalaite) (Figure 2-1d). In undefected Michel-model

ferrihydrite (nominally Fe_5O_8H), 60% of Fe atoms lie on Fe1 symmetry sites. These sites have octahedral oxygen coordination and form a planar hexagonal arrangement similar to that of hematite, maghemite, and magnetite that repeats in an ABAB pattern along the *c*-axis. The remaining 40% of Fe atoms are found between the layers of Fe1 sites and are split evenly between two other symmetry-distinct sites; 20% sit on the Fe2 site (also octahedral oxygen coordination, but at a different Wyckoff position) and 20% on the Fe3 site (tetrahedral oxygen coordination). In this study, the bulk-crystalline geometry, magnetic properties, and thermodynamic stability of the Michel-model ferrihydrite bulk-crystalline structure and the (nonmagnetic) Al^{3+} analog akdalaite were evaluated using the *ab initio* approaches described in [9]

3.3.2 Surface Slab Calculations

For the study of surface doping properties, periodic slabs of the goethite (101) surface [*Pnma* spacegroup setting [1]] were constructed using the GDIS freeware utility [103] from the DFT-relaxed goethite primitive unit cell (4×FeOOH). The primitive unit area of the goethite (101) surface is 3.05 × 11.07 Å. In the interest of limiting spurious Al-Al interactions across periodic boundary conditions, the primitive unit slab was doubled in the [010] dimension (along the goethite double chains) to an area of 6.11 × 11.07 Å. In this larger supercell, a single Al dopant placed in the slab cell has only Fe atoms in nearest-neighbor cation sites, whereas in the non-doubled cell, a single Al-dopant would have its own periodic image as a nearest-neighbor cation along the [010] direction. Both top and bottom slab surfaces are characterized by Fe with full octahedral oxygen coordination (no dangling Fe-O bonds). The surface slab geometry used for all reported simulations has a thickness (z-dimension) of eight layers of Fe atoms, each consisting of two goethite 'double chain' units (32 Fe atoms total). For anhydrous slabs, the vacuum region in the slab cell was set to a thickness of approximately 12Å, and the total slab + vacuum thickness was 30 Å. For hydrated slabs (details regarding hydration structures to follow), total slab + vacuum thickness was increased to 35 Å to accommodate the addition of water molecules on both top and bottom slab surfaces, while preserving vacuum separation of at least 10 Å. To ensure that this slab depth was sufficient to avoid image interactions across the vacuum layer, a test calculation was performed for a

hydrated Al surface substitution slab supercell having a Z dimension of 50 Å, with a vacuum layer of over 25 Å. The absolute total energy of the 50 Å slab differed by less than 5 meV from that of the 35 Å slab, indicating that image interactions along Z are negligible. Magnetic moments for Fe atoms in the slab cell were initialized according to the antiferromagnetic groundstate ordering of bulk goethite, while Al atoms were assigned zero spin. For all slab simulations, the internal coordinates of all the atoms in the slab were optimized (relaxed), while the slab cell parameters, angles, and volume were held fixed.

A reduced plane-wave cutoff energy of 350eV was used for surface slab calculations in the interest of increased computational speed. The choice of a reduced cutoff energy saves computation time and has little impact on the relative defect energetics of the Al-doped systems. Table 3-1 compares doping energetics in bulk goethite at 350 and 650 eV and shows a change in the key thermodynamic quantity, the dilute of heat of formation, of just 3 meV/Al, or about 1% of the calculated value, when the lower cutoff value is used in place of the higher one.

Table 3-1: Comparing Al substitution energetics in bulk goethite for plane wave cutoff energies of 650 eV and 350 eV. The 650 eV cutoff was used for simulation of bulk materials, whereas the lower 350 eV cutoff was used for slab geometry simulations, in the interest of increased computational speed. While the larger cutoff energy is required for convergence of total energy, the calculation of a relative quantity like dilute impurity energy reaches satisfactory convergence at a much lower cutoff energy.

Structure	Stoichiometry	650 eV cutoff		350 eV cutoff	
		Total Energy (eV)	*dilute impurity energy* (eV)	Total Energy (eV)	*dilute impurity energy* (eV)
goethite	$Fe_{32}O_{64}H_{32}$	-804.6647	-	-803.7497	-
diaspore	$Al_{32}O_{64}H_{32}$	-841.0946	-	-839.8832	-
Al-goethite	$Fe_{31}Al_1O_{64}H_{32}$	-805.5766	0.227	-804.6493	0.230

A 5×3×1 Monkhorst-Pack-style kpoint mesh was chosen for the doubled goethite (101) surface slab geometry, which results in roughly equivalent kpoint sampling for the in-plane (xy) dimensions as was used in bulk calculations. One kpoint was used in the z-dimension (30 or 35 Å in length in real space), which yields k-point density in the z-

dimension equivalent to the density that was sufficient to converge the bulk calculations (~30 k-points per $Å^{-1}$).

Surface protonation was arranged according to the MUSIC model for the goethite (101) surface [104-106], corresponding to a neutrally charged slab and neutral surface (*i.e*. the point of zero charge). The end result is a primitive slab geometry that is stoichiometrically-equivalent to 32×FeOOH + $4H_2O$, where two dissociated water molecules have been used to provide additional H and OH groups (in equal number) to the mathematically-cleaved FeOOH (101) surface to fulfill protonation and Fe octahedral coordination demands. An additional set of hydrated slab geometries were created, in which an additional 20 water molecules (10 per side) were added. On each side of the slab, six water molecules were initially placed manually in positions above FeOOH six surface OH groups forming hydrogen bonds approximately 1.6 Å in length. An additional four water molecules per side were added in bridging positions that connected the already-added waters with additional hydrogen bonds. This initial hydration structure was optimized in a static relaxation within VASP and the resulting relaxed geometry was used to initialize the simulations of Al substitution at the surface. In any case, the addition of physisorbed surface waters had minor influence on the energetics of Al-doping at the mineral surface, which appear to be largely independent of surface hydration (Section 3.4.3).

3.3.3 Thermodynamic Analysis Methods

We calculate the thermodynamics of dilute aluminum dopants on the Fe-(oxyhydr)oxide cation lattice following the ab initio thermodynamic approach of [49]. We consider the following substitutional defect formation reaction, in which X fraction of Fe atoms on an undefected Fe-oxide/oxyhydroxide host structure, $Fe(OH)_{host}$, are removed and substituted with Al atoms (Equation 3.1):

$$\mathrm{Fe(OH)_{host}} - \mathrm{X}\mu_{\mathrm{Fe}} + \mathrm{X}\mu_{\mathrm{Al}} \rightarrow \mathrm{Fe_{1-X}Al_X(OH)_{host}} \qquad (3.1)$$

The generalized $(OH)_{host}$ notation refers to the arrangements of oxygen atoms and hydroxyl groups in the Al-substituted Fe compound, which vary in composition and structure between materials.

We define the *formation enthalpy of Al substitution* $\Delta H_{formation}^{Al\ subst.}$ (per cation site) on the Fe-(oxyhydr)oxide host lattice in Equation 3.2:

$$\Delta H_{formation}^{Al\ subst.} = E_{DFT}\left[Fe_{1-X}Al_X(OH)_{host}\right] - E_{DFT}\left[Fe(OH)_{host}\right] + X\mu_{Fe} - X\mu_{Al} \qquad (3.2)$$

$E_{DFT}\left[Fe_{1-X}Al_X(OH)_{host}\right]$ is the calculated total energy of the Fe-oxide or oxyhydroxide host structure containing a single Al atom, after relaxation. Equation 3.2 will be evaluated using two different sets of thermodynamic reference states for μ_{Fe} and μ_{Al}, with each analysis giving different insight on Al-substitution thermodynamics in Fe-(oxyhydr)oxides (Analyses I and II below).

3.3.3.1 Analysis I

The first method of analysis uses isostructural Fe- and Al-oxide or oxyhydroxide compounds as cation thermodynamic reference states, μ_{Fe} and μ_{Al}. The isostructures goethite, α -FeOOH, and diaspore, α -AlOOH, are an example choice of isostructural reference states for μ_{Fe} and μ_{Al}, respectively (Equations 3.3 and 3.4). In this example the chemical potentials would be:

$$\mu_{Fe} = E_{DFT}\left[\alpha - FeOOH\right] \qquad (3.3)$$

$$\mu_{Fe} = E_{DFT}\left[\alpha - AlOOH\right] \qquad (3.4)$$

Note that in this analysis both reference states will have the same $(OH)_{host}$ structure as the Al-substituted material being evaluated. With this set of reference states, Equation 3.1 represents the energetic cost of mixing Fe and Al on a coherent atomic lattice, relative to isostructural, pure Fe- and Al-(oxyhydr)oxide end members. The isostructural Fe/Al pairs considered in this study are hematite/corundum (α-Me_2O_3), goethite/diaspore (α-MeOOH), lepidocrocite/boehmite (γ-MeOOH), and ferrihydrite/akdalaite (Me_5O_8H), with "Me" representing either an Fe^{3+}or Al^{3+} metal cation respectively. The Al-doped

formulations of these host materials will be referred to as "Al-*host*" throughout this work (*e.g.,* Al-goethite).

Equation 3.5 defines the *dilute impurity energy* of Al substitution in the isostructural reference case, $H_{\text{Al imp.}}^{\text{iso. ref.}}$, which is the energetic cost of substituting a single Al atom on the Fe cation lattice, measured per Al atom.

$$H_{\text{Al imp.}}^{\text{iso. ref.}}(\text{per Al atom}) = \lim_{X \to 0}\left[\frac{1}{X}\left(\Delta H_{\text{formation}}^{\text{Al subst.}}\right)^{\text{iso. ref.}}\right] \qquad (3.5)$$

$H_{\text{Al imp.}}^{\text{iso. ref.}}$ can be illustrated graphically as the slope of the Fe/Al mixing enthalpy (expressed per cation site) at the limit of dilute Al (X=0). This quantity measures the mixing tendency for isostructural Fe- and Al-(oxyhydr)oxides in a manner independent of supercell defect concentration so that values from calculations with different Al concentrations can be compared directly. These comparisons are possible provided all simulated Al-doping configurations used to calculate $H_{\text{Al imp.}}^{\text{iso. ref.}}$ are sufficiently dilute to remove any significant Al dopant interactions. Positive values for $H_{\text{Al imp.}}^{\text{iso. ref.}}$ indicate a phase-separation tendency (at least for dilute concentrations). This tendency is the expected behavior for the Fe-(oxyhydr)oxide materials, which are not generally observed to form high concentration solid solutions when synthesized with Al. Thus, at equilibrium these minerals are thermodynamically stable as separate regions of pure-Fe and pure-Al oxyhydroxides.

3.3.3.2 Analysis II

In order to evaluate the impact of Al on the relative phase stability of different Al-doped Fe-(oxyhydr)oxide compounds we again apply Equation 3.2, but this time using constant, common reference states for μ_{Fe} and μ_{Al} for the Fe atoms removed from, and the Al atoms added to, the defect dopant site, respectively, across all of the host structures. In this manner, when evaluating the *relative* formation enthalpy of Al substitution between host structures, the common reference states for the defect-site Fe and Al atoms cancel, making the result independent of the reference state chosen. Only the defect cation site is

treated with the common reference state – the host structure surrounding the defect, $Fe(OH)_{host}$, is accounted for using the DFT energy of the undefected host structure. Equation 3.6 shows the formulation of the formation enthalpy of Al substitution in an arbitrary host material relative to Al substitution in hematite.

$$\begin{aligned}\left(\Delta\Delta H^{\text{common ref.}}_{\text{Al subst.}}\right)_{\text{rel. hematite}} &= \left(E_{DFT}\left[Fe_{(1-x)}Al_x(OH)_{host}\right] - E_{DFT}\left[Fe(OH)_{host}\right] + x\mu_{Fe} - x\mu_{Al}\right) \\ &\quad - \left(E_{DFT}\left[Fe_{(1-x)}Al_x(OH)_{hematite}\right] - E_{DFT}\left[Fe(OH)_{hematite}\right] + x\mu_{Fe} - x\mu_{Al}\right) \\ &= \left(E_{DFT}\left[Fe_{(1-x)}Al_x(OH)_{host}\right] - E_{DFT}\left[Fe(OH)_{host}\right]\right) - \left(E_{DFT}\left[Fe_{(1-x)}Al_x(OH)_{hematite}\right] - E_{DFT}\left[Fe(OH)_{hematite}\right]\right)\end{aligned} \quad (3.6)$$

Again, we normalize defect energies per Al solute atom, in the limit of dilute Al ($X_{Al} \to 0$), to define the *relative dilute enthalpy of mixing*, $H^{\text{common ref.}}_{\text{rel. mix}}$, for Al-doped Fe-(oxyhydr)oxides, here expressed relative to equivalently-doped Al-hematite (Equation 3.7):

$$H^{\text{common ref.}}_{\text{rel. mix}} = \lim_{x \to 0}\left[\frac{1}{X}\left(\Delta\Delta H^{\text{common ref.}}_{\text{Al subst.}}\right)_{\text{rel. hematite}}\right] \quad (3.7)$$

$H^{\text{common ref.}}_{\text{rel. mix}}$ represents the relative (de)stabilization effect of Al doping for the Fe-(oxyhydr)oxide family. We choose to use hematite as a baseline, in effect setting $\left(H^{\text{common ref.}}_{\text{rel. mix}}\right)_{\text{hematite}} = 0.0 \text{ eV/Al}$. Values for $H^{\text{common ref.}}_{\text{rel. mix}}$ for the Fe-(oxyhydr)oxide host structures relative to the hematite reference are given in Table 3-2, final column.

The evaluation of $H^{\text{common ref.}}_{\text{rel. mix}}$ (Equation 2.7) can also be considered to be an approximate evaluation of the *relative Gibbs free energy of mixing*, $G^{\text{common ref.}}_{\text{rel. mix}}$, once one considers the large amount of expected cancellation between the relevant terms necessary to construct the free energies of the defected and undefected materials. The true $G^{\text{common ref.}}_{\text{rel. mix}}$ is the difference in Gibbs free energy change per Al dopant atom between hematite and another Fe-(oxyhydr)oxide host lattice. The vibrational and electronic excitations of Al substitutional defects on the various lattices are relatively small contributions at near room temperature and furthermore should behave similarly between any two phases being compared. These contributions can therefore be assumed to largely cancel from

$G_{rel.\,mix}^{common\ ref.}$. Additionally, because $G_{rel.\,mix}^{common\ ref.}$ is an evaluation of the relative Al substitution energy between phases having equivalent Al concentrations, we can also generally assume that the configurational entropy contributions to the free energy cancel in the calculation of $G_{rel.\,mix}^{common\ ref.}$. The exception to this rule is when considering ferrihydrite and Al-ferrihydrite, which contain 3 distinct cation sites in varying concentrations. For this material the configurational entropy terms in the calculation of $G_{rel.\,mix}^{common\ ref.}$ will not cancel in the same way as for the materials having only one Fe symmetry site, because the Al dopant is relegated to the limited configurational space of only a subset of total cation sites. Assuming all Al dopants in ferrihydrite lie on the energetically-favored Fe1 doping sites (comprising 60% of Fe sites in ferrihydrite), the Gibbs free energy of reaction from Al-hematite + water (Figure 3-2) for Al-ferrihydrite as a function of Al content (X) would be written as:

$$\Delta G_{rxn}^{fhyd}(X) = X\cdot\left(H_{rel.\,mix}^{common\ ref.}\right)_{fhyd} - RT\begin{bmatrix} 0.6\left(\frac{X}{0.6}\cdot\ln\frac{X}{0.6} + \left(1-\frac{X}{0.6}\right)\cdot\ln\left(1-\frac{X}{0.6}\right)\right)_{fhyd} \\ -\left(X\cdot\ln x + (1-X)\cdot\ln(1-X)\right)_{hem} \end{bmatrix} \qquad (3.8)$$

The temperature*entropy contribution to the relative free energy in Equation 3.8 has a value of +0.29 kJ/mol (~0.003 eV) at 20% Al doping content (X=0.2) at 298.15K. Thus, the inclusion of this relative configurational entropy associated with the ferrihydrite host structure has a relatively small impact on the conclusions drawn about the relative stability of Al-ferrihydrite. Furthermore, it is arguable that cation motion is insignificant under most relevant environmental conditions, which would mean that configurational entropy terms associated with Fe and Al disorder would not enter into $G_{rel.\,mix}^{common\ ref.}$ at all. Nonetheless, we will include the configurational entropy term from Equation 3.8 in the calculation of $G_{rel.\,mix}^{common\ ref.}$ for Al-ferrihydrite.

Under the preceding assumptions, we take $G_{rel.\,mix}^{common\ ref.}$ as equal to $H_{rel.\,mix}^{common\ ref.}$ for all phases except (Al-)ferrihydrite, where $G_{rel.\,mix}^{common\ ref.}$ is modified by Equation 3.8. We use these values of $G_{rel.\,mix}^{common\ ref.}$ to predict the changes in Gibbs free energies of the Fe-

(oxyhydr)oxide phases relative to hematite as a function of Al content, as shown in Figure 3-2 where $G_{\text{rel. mix}}^{\text{common ref.}}$ determines the initial slope of the relative stability line for each material.

3.4 Results

3.4.1 Thermodynamics of Dilute Aluminum Substitution

Fully periodic simulation cells were constructed with single Al^{3+} dopants on cation sites previously occupied by Fe^{3+}. As the limiting case of a truly 'dilute' Al solution (X<<1 in Equation 3.1) are a practical impossibility for DFT calculations limited to cell sizes on the order of hundreds of atoms, reasonably large simulation supercells were constructed with single-atom Al substitutions, and the 'dilute' solution thermodynamics were calculated from these approximately-dilute simulations. Supercells were typically 4-8 primitive unit cells, yielding Al concentrations well below 10%, with insignificant Al-Al interactions. The simulation cell stoichiometries and %Al concentrations for each calculation are given in Table 3-2.

Referring to the energies reported in Table 3-2, the hematite (α-Fe_2O_3) host structure shows the highest *dilute impurity energy* for an Al dopant. Goethite, lepidocrocite, and the ferrihydrite Fe1 site have successively smaller dilute impurity energies (Figure 3-1). The dilute impurity energy for goethite (0.227 eV/Al) agrees reasonably well with a recent published DFT result [101] for a pair of separated Al^{3+} placed in a goethite supercell consisting of 24 FeOOH formula units. Using the total energies reported by Bazilevskaya, one computes the dilute impurity energy to be 0.269 eV/Al, neglecting the influence of Al-Al interactions. In ferrihydrite, Al-substitution energies are shown to be highly dependent on the particular Fe site chosen for substitution. The symmetry site dependence of the formation energy of the Al substitution defect in ferrihydrite has also observed for another defect type, the excess hydroxyl defect, found at vacant cation sites [75]. While the octahedral Fe1 site in ferrihydrite has the lowest Al-substitution energy of

all calculated structures, the tetrahedral Fe2 and octahedral Fe3 sites have Al-substitution energies higher than that of hematite. The favorability of Al substitution on the octahedral Fe1 site is in agreement with experimental XANES data suggesting that Al dopants in ferrihydrite are predominantly octahedrally coordinated [89].

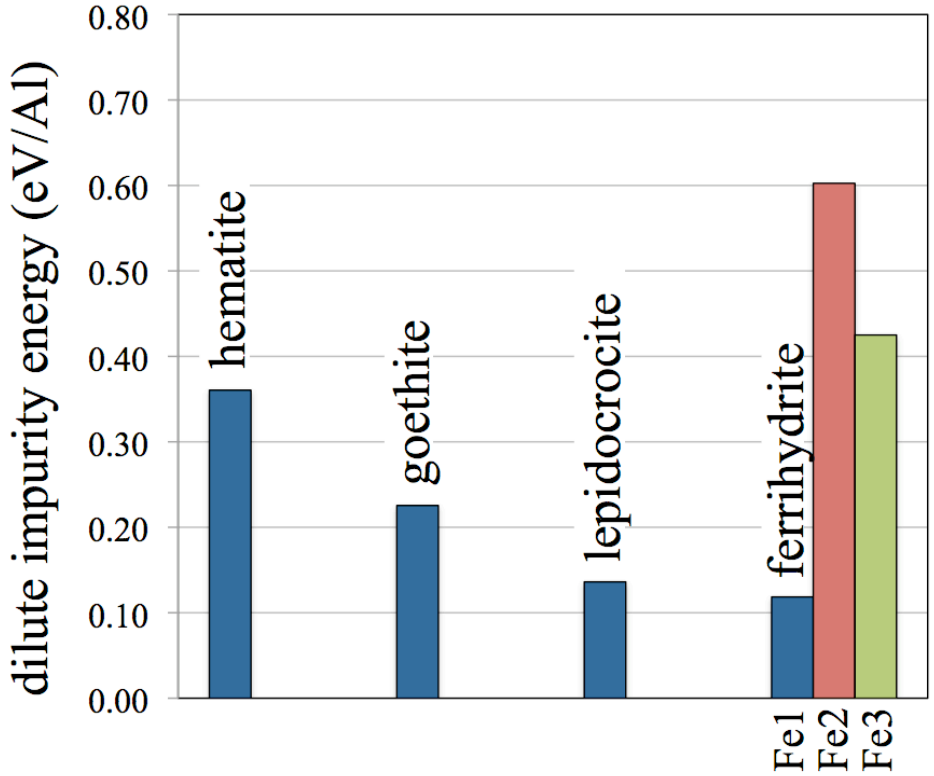

Figure 3-1: *Dilute impurity energies* (Equation 3.5) of single-atom Al-substitutions on Fe-oxide and oxyhydroxide host structures. Ferrihydrite has three symmetry-distinct Fe cation sites, and thus three distinct impurity energies.

Table 3-2: *Ab initio* simulation data for pure-Fe, pure-Al and Al-doped (labeled as Al-hematite, Al-goethite, etc.) oxide/oxyhydroxide isostructures, including total energy and cell dimensions after full atomic relaxation. Hematite/corundum are calculated using the hexagonal setting of space group $R\bar{3}c$, having a hexagonal unit cell containing 12 cations. Goethite/diaspore cell parameters reflect the Pnma space group setting. The kpoint meshes are labeled as M for Monkhorst-Pack configurations, or G for Γ-centered. All simulation data reported in this table used a 650 eV plane wave cutoff energy.

Isostructure	Simulation Stoichiometry	Supercell Size	Kpoint Mesh	Relaxed Cell Parameters (Å)			cell volume (Å^3)	Total Energy (eV)	*dilute impurity energy (eV/Al)*	*relative enthalpy of mixing (eV/Al)*
				a	*b*	*c*				
hematite	$Fe_{12}O_{18}$	1×1×1	662G	5.09	5.09	13.94	312.46	-213.139	-	-
	$Fe_{48}O_{72}$	2×2×1	332G	10.17	10.17	13.94	1249.23	-852.568	-	-
corundum	$Al_{12}O_{18}$	1×1×1	662G	4.81	4.81	13.12	262.73	-225.270	-	-
	$Al_{48}O_{72}$	2×2×1	332G	9.62	9.62	13.12	1051.35	-901.088	-	-
Al-hematite (8.33% Al)	$Fe_{11}Al_1O_{18}$	1×1×1	662G	5.07	5.07	13.88	308.53	-213.816	0.334	-0.027
Al-hematite (2.1% Al)	$Fe_{47}Al_1O_{72}$	2×2×1	332G	10.16	10.16	13.92	1243.91	-853.218	0.360	0.000
goethite	$Fe_4O_8H_4$	1×1×1	386M	10.05	3.05	4.63	142.06	-100.579	-	-
	$Fe_8O_{16}H_8$	1×2×1	346M	10.05	6.11	4.63	284.37	-201.158	-	-
	$Fe_{32}O_{64}H_{32}$	1×4×2	323M	10.05	12.22	9.26	1138.22	-804.665	-	-
diaspore	$Al_4O_8H_4$	1×1×1	386M	9.49	2.87	4.42	120.48	-105.137	-	-
	$Al_8O_{16}H_8$	1×2×1	346M	9.49	5.75	4.42	241.00	-210.273	-	-
	$Al_{32}O_{64}H_{32}$	1×4×2	323M	9.49	11.50	8.83	963.58	-841.095	-	-
Al-goethite (25% Al)	$Fe_3Al_1O_8H_4$	1×1×1	386M	9.92	3.01	4.58	136.90	-101.474	0.245	-0.244
Al-goethite (12.5% Al)	$Fe_7Al_1O_{16}H_8$	1×2×1	346M	9.98	6.06	4.61	279.03	-202.081	0.217	-0.272
Al-goethite (3.1% Al)	$Fe_{31}Al_1O_{64}H_{32}$	1×4×2	323M	10.03	12.19	9.26	1132.84	-805.577	0.227	-0.261
lepidocrocite	$Fe_8O_{16}H_8$	2×1×1	638M	6.19	12.51	3.94	304.82	-200.007	-	-
	$Fe_{24}O_{48}H_{24}$	3×1×2	434M	9.28	12.51	7.87	913.19	-600.024	-	-
boehmite	$Al_8O_{16}H_8$	2×1×1	638M	5.80	12.05	3.74	260.93	-210.336	-	-
	$Al_{24}O_{48}H_{24}$	3×1×2	434M	8.69	12.01	7.47	780.28	-631.002	-	-
Al-lep. (12.5% Al)	$Fe_7Al_1O_{16}H_8$	2×1×1	638M	6.14	12.48	3.91	299.74	-201.104	0.194	-0.447
Al-lep. (4.2% Al)	$Fe_{23}Al_1O_{48}H_{24}$	3×1×2	434M	9.26	12.52	7.84	909.43	-601.179	0.136	-0.504
ferrihydrite	$Fe_{10}O_{16}H_2$	1×1×1	664G	5.97	5.97	9.37	288.94	-191.585	-	-
	$Fe_{40}O_{64}H_8$	2×2×1	334G	11.94	11.94	9.38	1157.74	-766.363	-	-
akdalaite	$Al_{10}O_{16}H_2$	1×1×1	664G	5.64	5.64	8.85	243.40	-202.586	-	-
	$Al_{40}O_{64}H_8$	2×2×1	334G	11.27	11.27	8.85	973.72	-810.346	-	-
Al-fhyd, Fe1 (10% Al)	$Fe_9Al_1O_{16}H_2$	1×1×1	664G	5.94	5.94	9.33	285.12	-192.559	0.127	-0.323
Al-fhyd, Fe1 (2.5% Al)	$Fe_{39}Al_1O_{64}H_8$	2×2×1	334G	11.92	11.92	9.35	1153.54	-767.344	0.119	-0.331
Al-fhyd, Fe2 (2.5% Al)	$Fe_{39}Al_1O_{64}H_8$	2×2×1	334G	11.93	11.93	9.34	1153.56	-766.860	0.602	0.153
Al-fhyd, Fe3 (2.5% Al)	$Fe_{39}Al_1O_{64}H_8$	2×2×1	334G	11.93	11.93	9.37	1154.83	-767.037	0.425	-0.024
surface slab (anhydrous)	$Fe_{32}O_{60}H_{40}$	2×1×1	531M	6.11	11.07	30.00	-	-	-	-
surface slab (hydrated)	$Fe_{32}O_{60}H_{40} + 20(H_2O)$	2×1×1	531M	6.11	11.07	35.00	-	-	-	-

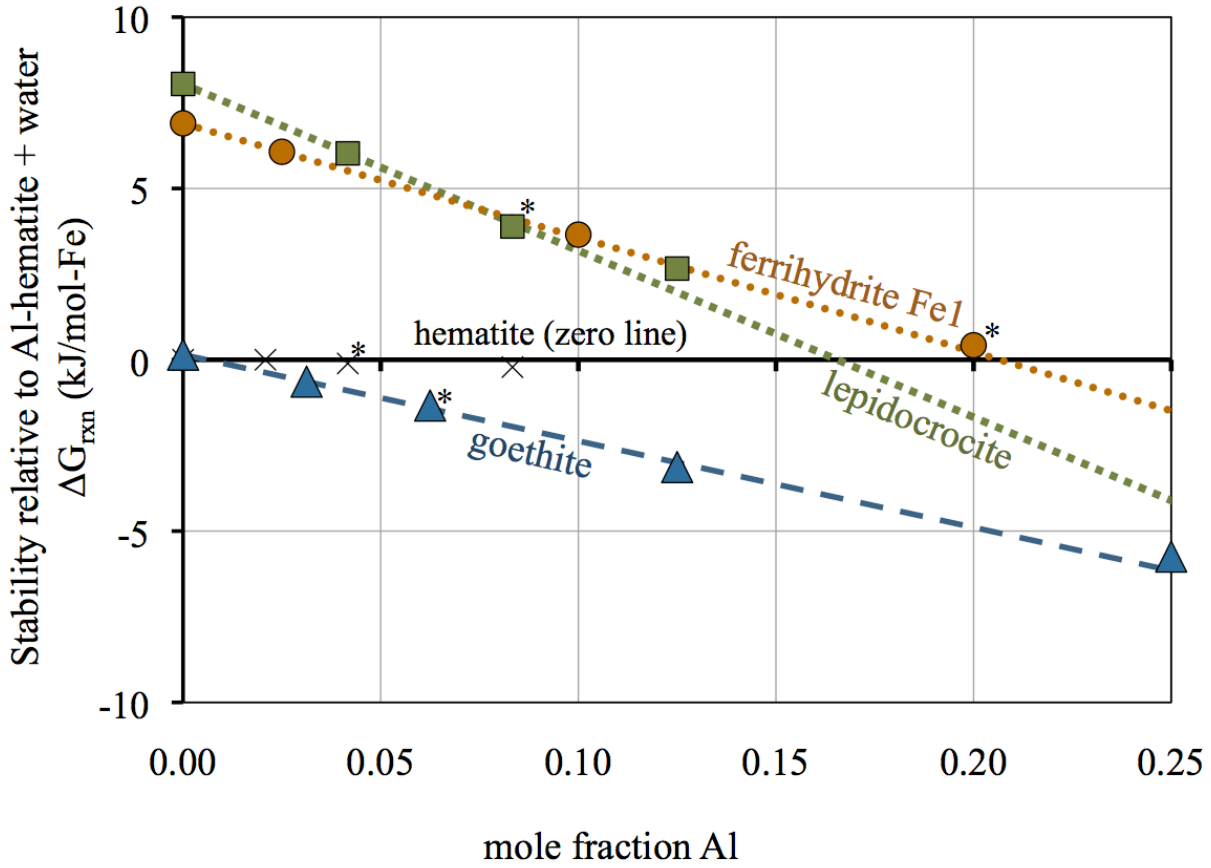

Figure 3-2: Relative stabilization effect of Al-doped Fe-(oxyhydr)oxides. Equivalently-doped Al-hematite + water form the baseline (x-axis) for the plot. All three Fe-(oxyhydr)oxides are shown to be stabilized relative to Al-hematite for increasing Al concentrations. Data points for supercell calculations of varying size and Al content are shown explicitly, while the dashed lines extrapolate the dilute mixing energy obtained from the lowest-Al concentration supercells. Data points marked with an asterisk indicate that these data are associated with supercells in which two Al dopants were placed on nearest-neighbor cation sites (see Section 3.4.2).

Figure 3-2 plots the calculated relative stabilities of Al-goethite, Al-lepidocrocite, and Al-ferrihydrite (Fe1 site only), expressed as the Gibbs free energy of reaction (ΔG_{rxn}) from equivalently-doped Al-hematite + water. Pure-Fe (oxyhydr)oxide relative stabilities set the y-intercepts (ΔG_{rxn} at 0% Al content) shown as the leftmost data points for each material. For goethite and lepidocrocite, the values of ΔG_{rxn} for the undefected material are obtained from experimental thermodynamic references [11, 12, 2]. The 0% Al relative stability of bulk ferrihydrite is taken from *ab initio* results described in [9]. The slope of the dashed line linking the data points for each host material is set by the $G_{\text{rel. mix}}^{\text{common ref.}}$ value calculated using the most dilute Al substitution calculation for that material, and thus passes directly through the first data point at nonzero %Al concentration for each material. This slope is extrapolated to higher Al concentration without regard for Al-Al interactions. Each additional data point represents a supercell calculation with a higher Al concentration. These data necessarily include the influence of any Al-Al interactions that occur within supercells or across periodic boundary conditions. Data points marked with an asterisk indicate a calculation where two Al dopants were placed on neighboring cation sites within the supercell (Section 3.4.2), whereas all other calculations at nonzero %Al concentration involve a single Al placed in the supercell, which is thus separated from other (image) Al at distances equivalent to the periodic dimensions of the supercell. The good agreement between the low-concentration extrapolation and the higher concentration data shows the Al-Al interactions play only a minor role on the overall stability of the phases for the concentrations considered. These interactions will be discussed further in Section 3.4.

Considering Figure 3-2, all three Al-doped (oxyhydr)oxide host materials (goethite, lepidocrocite, ferrihydrite) show a stabilization trend relative to equivalently-doped Al-hematite, with the largest relative stabilization effect observed for lepidocrocite. The magnitude of the effect that Al-doping has on Fe-(oxyhydr)oxide relative stability is considerable even for small concentrations of Al. Al-goethite is stabilized relative to Al-hematite at almost any appreciable Al content. The metastable structures lepidocrocite and ferrihydrite are stabilized relative to Al-hematite at approximately 17% and 20% Al content, respectively. The stabilization of Al-ferrihydrite relative to Al-goethite is not

predicted for any amount of dilute Al doping.

Al-Al pairwise interactions in bulk Fe-(oxyhydr)oxides

Using the dilute Al-substitution energies from the previous section as a point of reference, calculations were performed to explicitly test the interaction tendencies of pairs of Al dopants placed in close proximity on the cation lattice of the same Fe-oxide/oxyhydroxide materials. In each host structure, two Al atoms were substituted into a variety of neighboring cation sites and the structures fully relaxed. The defect formation energy of this relaxed configuration is compared to that of two Al dopants found in isolation by referring back to the dilute doping energies reported in Section 3.4.1. The change in energy is referred to here as the interaction energy and is positive for cases where the Al repel each other. In the case of ferrihydrite, which has site-specific Al-substitution energies for each of its three Fe symmetry sites, the interaction energies are calculated relative to the dilute-Al substitution energies of the specific sites substituted in the pair-defect calculation. As with the single-Al substitution calculations, magnetic configurations of the Fe atoms surrounding the Al substitution atoms were initialized in their bulk antiferromagnetic spin orderings, or 72erromagnetic ordering in ferrihydrite. In this work we will assign the interaction energy to the nearest-neighbor Al-Al pair and consider it a pair interaction associated with that Al-Al pair. However, due to the periodic nature of the *ab initio* methods chosen, for the calculations of cells with two neighboring Al that are used to determine the Al-Al interactions, many Al-Al pair interactions at longer Al-Al distances are introduced in addition to those found in the dilute single-Al dopant cells. These additional pairs (and potentially three-site and higher order cluster effects) will also contribute to the calculated interaction of the Al. We make the assumption that these additional contributions are small and that the Al-Al interactions are dominated by the nearest-neighbors. This approximation becomes increasingly accurate for larger supercell sizes, as the excluded contributions come from far-separated Al atoms and are therefore likely weak. The first- and second-nearest Al pair distances for each interaction supercell calculation are reported in Table 3-3 alongside the calculated interaction energies, which we approximate by attributing them to only to the shortest pairs within a given surface configuration. The multiplicities of the Al pair distances are shown in brackets where these interactions take place more than

once per supercell due to image interactions across periodic boundary conditions. 1NN configurations marked with an asterisk in Table 3-3 indicate that the energies from these calculations are included as data points on Figure 3-2.

Table 3-3: Pairwise Al-Al interaction data in the bulk Fe-oxide/oxyhydroxides. Interaction energies are shown in the final column. Shown are the Al-Al interatomic distances between the nearest Al-Al pairings within the cell, after full relaxation of the Al-substituted cell, in comparison with the corresponding Fe-Fe distances in an undefected cell. Nearest-pair Al-Al distances are uniformly shorter than the corresponding Fe-Fe distances, but Al-Al interactions are not uniformly attractive (negative interaction energy). Also reported are the second-nearest Al-Al pairings, which are considerably longer than those associated with the first-nearest pairs, All first-nearest Al-Al pairs only occur once (multiplicity = 1) within the tested supercells, while some longer-range Al-Al pairings have multiplicities >1. Interaction types shown with an asterisk (*) indicate that these data points are shown in Figure 3-2.

.

Isostructure	Al-Al Interaction Type	Total Energy (eV)	First Al-Al distance, relaxed (Å) [multiplicity]	Equiv. Fe-Fe distance (Å)	Second Al-Al distance, relaxed (Å) [multiplicity]	Al-Al Interaction Energy (eV)
Al-Al-hematite (4.2% Al)	1NN*	-853.8862	2.78 [1]	2.92	10.15 [6]	-0.018
	2NN	-853.8955	2.91 [1]	3.00	7.80 [2]	-0.027
	3NN	-853.8988	3.38 [1]	3.41	8.00 [2]	-0.030
Al-Al-goethite (6.25% Al)	1NN*	-806.4586	2.98 [1]	3.05	9.19 [1]	0.030
	2NN	-806.4751	3.17 [1]	3.33	7.44 [1]	0.013
	3NN	-806.5141	3.47 [1]	3.49	7.48 [1]	-0.026
Al-Al-lepidocrocite (8.33% Al)	1NN*	-602.3603	2.99 [1]	3.09	6.31 [1]	-0.027
	2NN	-602.2880	3.03 [1]	3.13	6.20 [1]	0.045
	3NN	-602.2323	3.92 [2]	3.93	7.84 [2]	0.050
Al-Al-ferrihydrite (20% Al)	1NN (Me1-Me1)	-193.5327	2.94 [2]	2.98	5.13 [2]	0.010
	2NN (Me1-Me3)	-193.2936	3.36 [1]	3.43	5.42 [2]	-0.047
	3NN (Me1-Me2)	-193.1436	3.50 [2]	3.53	5.46 [2]	-0.037

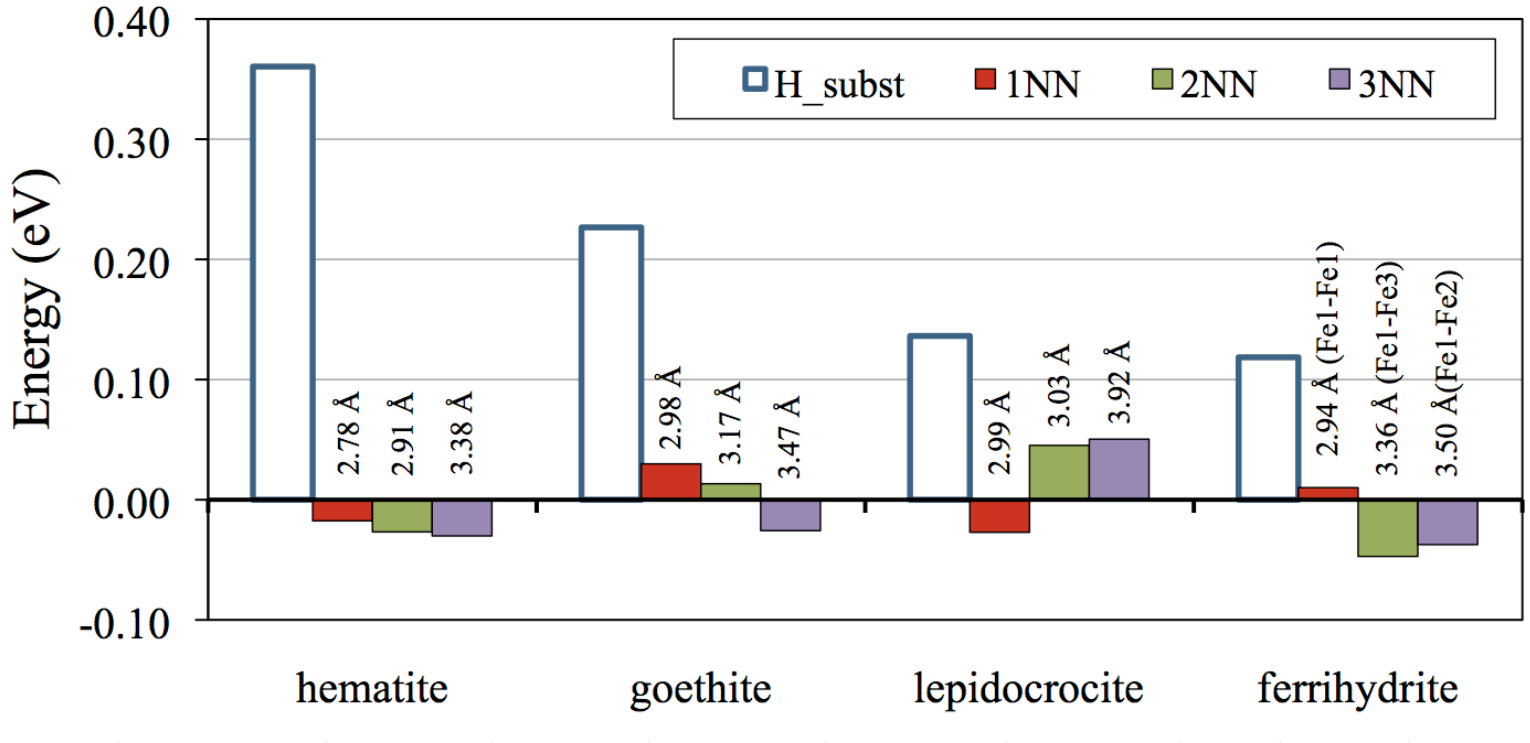

Figure 3-3: Al-Al pairwise interaction energies (solid columns) as compared to the dilute impurity energy of an isolated Al substitution in Fe-oxide/oxyhydroxde materials (open columns). The numbers labeling each Al-Al interaction column indicate the Al-Al separation distance (Å) in the relaxed simulation cell. The dilute impurity energy for ferrihydrite is for Al substitution on the favored Fe1 site, whereas the Al-Al interaction energies are computed for interactions involving Al substitution pairs with one dopant on the Fe1 site, and the second on the Fe1, Fe2, or Fe3 site, as labeled in the figure.

Figure 3-3 shows the calculated Al-Al pair interaction energies (filled columns), as compared to the dilute impurity energies for Al substitution in hematite, goethite, lepidocrocite, and ferrihydrite (open columns). These data are also reported in Table 3-3. The calculated interaction energies are small in comparison to the Al substitution energies, especially for hematite and goethite. The minor importance of Al interactions is also visible in Figure 3-2, where the free energies of supercell configurations specifically aimed to explore Al-Al interactions (marked with asterisks) deviate only slightly from the free energy trend set from the low-concentration calculations with minimal Al-Al interaction. Examining the interaction data apart from the larger free energy picture, we note that Al-Al interaction energies in hematite are negative, indicating a slight tendency toward Al-dopant clustering. Al-Al interactions in goethite, lepidocrocite and ferrihydrite yield mixed results, with some positive and some negative interaction energies, and thus no clear trend toward Al-clustering nor mixing behavior. In ferrihydrite, the dilute impurity energy shown in Figure 3-3 (open column) corresponds to an Al substitution at the Fe1 cation site only, and all reported interactions involve at least one Al placed on this site. The interaction energies for Al-Al pairings with dopants placed on other sites (Fe2, Fe3) are given relative to the site-specific dilute impurity energies of those sites.

3.4.2 Stability of surface-segregated Al-dopants in goethite (101)

Simulations of Al-dopants placed on or near the Fe-(oxyhydr)oxide surface demonstrate that Al substitutions immediately at the particle surface have a lower energetic cost than Al-doping within the bulk. Al-substitutions placed in the near surface region, even as shallow as the second layer of Fe sites, have energies very similar to bulk substitutions (i.e. far from the mineral surface).

Here we focus on the well-studied goethite (101) surface, as the structure and properties of this crystal face are better established than those of the other materials, especially ferrihydrite. While the following analysis therefore applies strictly to only the goethite (101) surface, the trends observed are expected to be general characteristics of the Fe-(oxyhydr)oxide materials having topologically similar Fe-O bonding arrangements, Fe-O-Fe corner and edge-sharing arrangements, and similar surface charge/protonation

properties to goethite (101). In particular, the calculations may provide guidance for the ferrihydrite mineral surface as there is similarity between goethite (101) and ferrihydrite nanoparticle samples in terms of sorption site type/density and charge behavior [107]. Direct computational study of ferrihydrite mineral surfaces is impractical due to the lack of crystallographic data characterizing the dominant surfaces as well as uncertainty regarding the fundamental crystal structure upon which a surface model would be based.

Al-substitution energies for Al placed at the (101) surface are compared to the substitution energy at an Fe site internal to the slab (labeled 'int') using the common reference state approach (Section 3.4.2, Analysis II). Cancellation of the common reference states in the pursuit of the relative energetics between a bulk-like, embedded dopant versus a surface dopant yields Equation 3.9, which describes the surface segregation tendency as the Al-substitution energy at the goethite (101) slab surface relative to Al-substitution embedded within the bulk.

$$\begin{aligned} E_{\text{rel. int.}}^{\text{surf. sub.}} &= \left(E_{\text{DFT}}^{\text{slab}}\left[Fe_{31}Al_1^{\text{surface}}(OOH)_{32}\cdot xH_2O\right] - E_{\text{DFT}}^{\text{slab}}\left[Fe_{32}(OOH)_{32}\cdot xH_2O\right]\right) \\ &-\left(E_{\text{DFT}}^{\text{slab}}\left[Fe_{31}Al_1^{\text{int}}(OOH)_{32}\cdot xH_2O\right] - E_{\text{DFT}}^{\text{slab}}\left[Fe_{32}(OOH)_{32}\cdot xH_2O\right]\right) \\ &= \left(E_{\text{DFT}}^{\text{slab}}\left[Fe_{31}Al_1^{\text{surface}}(OOH)_{32}\cdot xH_2O\right] - E_{\text{DFT}}^{\text{slab}}\left[Fe_{31}Al_1^{\text{int}}(OOH)_{32}\cdot xH_2O\right]\right) \end{aligned} \quad (3.9)$$

Table 3-4 lists the total energies for Al dopants at the surface and at the embedded 'int' site, for both hydrated and anhydrous slab geometries. Relative substitutions energies, as calculated by Equation 3.9, are shown in the fourth and fifth columns.

Table 3-4: Total and relative slab supercell energies for Al dopants placed at the goethite (101) surface. The relative energies in Columns 4 and 5 are expressed relative to the embedded 'int' Al dopant using Equation 3.9. The energies in the final two columns are expressed relative to a dilute Al dopant within a bulk goethite supercell (3.1% Al, Table 3-2) using the Analysis II technique, Equation 3.6.

Al site	Total Energy (eV)		Relative to embedded dopant ('int') Eq. 3.9 (eV/Al)		Relative enthalpy of mixing, vs. Al-goethite (3.1%) (Analysis II, Eq. 3.6) (eV/Al)	
	anhydrous	hydrated	anhydrous	hydrated	anhydrous	hydrated
int	-860.0698	-1151.8168	0.000	0.000	0.002	0.024
1	-860.2420	-1151.9679	-0.172	-0.151	-0.170	-0.127
2	-860.0223	-1151.7876	0.048	0.029	0.050	0.054
3	-860.2585	-1151.9499	-0.189	-0.133	-0.187	-0.109
4	-860.0520	-1151.8100	0.018	0.007	0.020	0.031
All sites, Al monolayer (8 Al)	-866.3458	-1158.0656	-	-	0.003	0.009
pure Fe slab, no dopant	-859.1723	-1150.9416	-	-	-	-

The surface segregation tendency expressed by Equation 3.9 could alternatively be written relative to Al substitution within a more bulk-like environment, e.g., the bulk supercell Al substitution simulations (Section 3.4.1). The comparison between slab energies alone was chosen to minimize uncertainty associated with comparisons between cells of different size, shape, and Al concentration. By comparing cells and configurations of Al that are identical except for having moved the Al from inside the slab to the surface, we expect cancellation of many possible sources of error, including defect image interactions, 2-D versus 3-D relaxation effects due to the constrained nature of the slab cell parameters, any remnant slab-vacuum effects, and any kpoint sampling mismatch between cells of different sizes. Furthermore, if Equation 3.9 is rewritten to compare the energies of surface dopants to dopants within a bulk goethite supercell, the overall conclusions about surface segregation are not appreciably altered, since the embedded Al dopant ('int') has a substitution energy very close to that of bulk substitution (Table 3-4, final two columns) for both anhydrous and hydrated slabs.

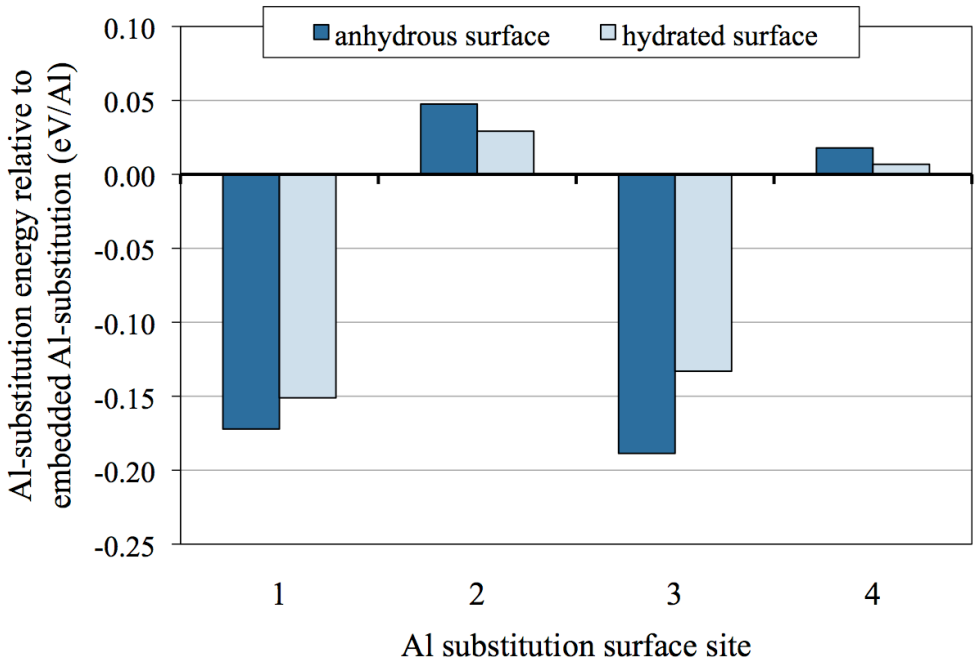

Figure 3-4: Substitution energies of Al atoms placed at/near the goethite (101) surface relative to a dilute Al-substitution in bulk goethite. Figure 2.6 illustrates the surface doping sites. Sites 1 and 3 comprise the topmost, terminal layer of cation sites in the goethite (101) surface, while sites 2 and 4 are the second layer.

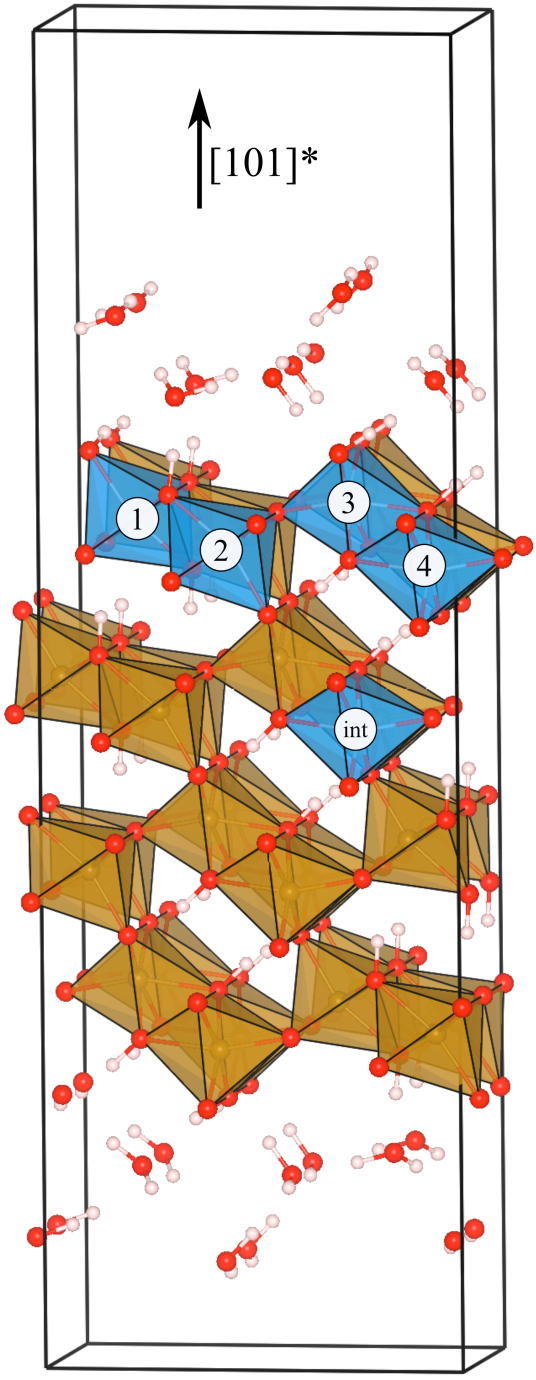

Figure 3-5: Illustration of Al dopant sites at, and embedded into, the goethite (101) surface. Fe octahedra are shown in brown (unlabeled), O atoms shown in red, H atoms in white. Al-dopant sites are shown in blue and labeled by site number corresponding to the energies shown in Figure 3-4. Slab surface protonation and hydration are described in Section 3.3.2. The internal "int" site is approximately 6 Å from the terminal oxygen layer at the (101) surface.

Figure 3-4 shows the magnitude of the stabilization effect of placing an Al-dopant at each of the four distinct cation sites present at the (101) surface of goethite (the sites are illustrated in Figure 3-5). Calculation data are shown for both anhydrous (dark columns) and hydrated surfaces (light columns). Cation sites 1 and 3 share coordinating oxygen atoms with only the Fe sites located below them. The oxygen atoms that complete the tops of the octahedral environments of sites 1 and 3 form dangling surface OH groups, instead of bridging to another neighboring cation, as in the bulk. Due to this topological change to their immediate bonding environment, octahedral sites 1 and 3 can be considered to be "true surface sites". This designation cannot be extended to sites 2 and 4, which have neighboring octahedral edge- and corner-sharing arrangements unchanged from that of the bulk structure. Al doping on the "true surface sites" (1 and 3) is favored by nearly 0.2 eV/Al for an anhydrous surface, and by 0.10-0.15 eV/Al for a hydrated surface. Sub-surface sites (2 and 4) show small positive relative doping energies, indicating that these sites are slightly less favorable than bulk substitution, but the effect is much less pronounced than that favoring surface segregation in sites 1 and 3. Thus, an Al surface segregation tendency exists, but is found only at the very topmost cation layer of the surface in sites with clearly changed local topology from the bulk. The thermodynamic driving force for surface segregation essentially disappears for other sites, even just 1-2 cation layers into the bulk of the material.

Additional slab calculations, here using only an anhydrous surface for computational efficiency, were performed with clusters of paired Al dopants added at the mineral surface. The interaction energy between neighboring Al dopants at the mineral surface is calculated by comparing the two-dopant system with the individual Al dopant site energies via Equation 3.10, describing the interaction energy between two surface Al dopants on arbitrary sites A and B. The resulting energies are shown in Table 3-5. Equation 3.10 references the energy of an undoped, pure-Fe slab of identical size/shape as the Al-substituted slabs. This additional reference state is necessary because the paired-Al interaction slabs have differing concentration of Al as compared to the single-substitution slabs, and thus a direct configurational energy comparison between slabs of identical atomic composition (like that performed in Equation 3.9) is not possible.

$$E_{A\text{-}B}^{\text{Al interaction}} = \left(E_{DFT}^{slab}\left[Fe_{30}Al_1^A Al_1^B (OOH)_{32} \cdot xH_2O\right] - E_{DFT}^{slab}\left[(FeOOH)_{32} \cdot xH_2O\right]\right)$$
$$- \left(E_{DFT}^{slab}\left[Fe_{31}Al_1^A (OOH)_{32} \cdot xH_2O\right] - E_{DFT}^{slab}\left[(FeOOH)_{32} \cdot xH_2O\right]\right) \quad (3.10)$$
$$- \left(E_{DFT}^{slab}\left[Fe_{31}Al_1^B (OOH)_{32} \cdot xH_2O\right] - E_{DFT}^{slab}\left[(FeOOH)_{32} \cdot xH_2O\right]\right)$$

Due to the limited size of the surface slab area (~6×11 Å), for some pair configurations, Al-Al interactions occur twice within the simulation cell - once within the slab geometry, and once again through the cell boundaries due to periodic boundary conditions. Where these doubled interactions occur, the Al-Al interaction energy calculated from Equation 3.10 is halved (since the calculated energy includes two identical interactions). This doubled interaction occurs for 'like-site' Al-Al pairings (e.g. '1,1', '2,2) because within the periodic boundary condition framework these pairs constitute line-defects of Al along the [010] direction (the 6.11 Å dimension in the simulation slab). The number of equivalent Al-Al pairs in each interaction calculation are given in Table 3-5.

Table 3-5 Calculated Al-Al pair interactions at the goethite (101) surface, as compared to symmetry-equivalent interactions within bulk goethite. Equivalent interaction types are grouped and labeled in Column 2 ('1NN' = 'first nearest neighbor" cation site). The nearest Al-Al distances associated with the interaction are reported, as are the multiplicities of the interaction type, which may be >1 due to image interactions across periodic boundary conditions. Because of the relatively small slab supercell area, other Al-Al interactions also occur at slightly longer distances, including additional pairs due to image interactions. The second-nearest Al-Al pair distances and multiplicities for each interaction cell simulated are also shown to clarify this issue. Pair interaction energies are assigned to the nearest-distance Al pairs and normalized by the multiplicity of that pair type only.

Pair	Interaction Type	Total Energy (eV)	Pair Interaction Energy (eV)	1st Al-Al relaxed distance (Å) [multiplicity]	2nd Al-Al relaxed distance (Å) [multiplicity]
bulk 1NN	1NN	-	0.030	2.98 [1]	9.19 [1]
1,1 1NN	1NN	-861.1844	0.064	3.06 [2]	6.11 [2]
2,2 1NN	1NN	-860.7316	0.070	3.06 [2]	6.11 [2]
3,3 1NN	1NN	-861.2229	0.061	3.06 [2]	6.11 [2]
4,4 1NN	1NN	-860.7943	0.069	3.06 [2]	6.11 [2]
int,int 1NN	1NN	-860.8260	0.071	3.06 [2]	6.11 [2]
bulk 2NN	2NN	-	0.013	3.17 [1]	7.44 [1]
1,2 2NN	2NN	-861.0672	0.025	3.19 [1]	5.39 [1]
3,4 2NN	2NN	-861.1130	0.025	3.14 [1]	5.36 [1]
bulk 3NN	3NN	-	-0.026	3.47 [1]	7.48 [1]
1,4 3NN	3NN	-861.1308	-0.009	3.47 [1]	5.57 [1]
2,3 3NN	3NN	-861.1213	-0.013	3.40 [1]	5.56 [1]
1,3 (separated)	n/a	-861.3045	0.024	6.11 [2]	6.15 [2]
2,4 (separated)	n/a	-860.8612	0.041	5.31 [1]	5.79 [1]

As in the bulk case, the effects of bringing Al close together are assigned to a pair interaction associated with only the closest symmetry-equivalent Al pairs in the specific cell. This approximation was expected to be reasonable for the bulk calculations due to the fairly large supercells used. However, the slab geometry used for the surfaces is more computationally demanding in terms of total number of atoms, and as a consequence somewhat smaller periodic lattice vectors in the plane of the surface are used for the slabs than were used in the bulk. For the surface slabs, the second closest Al pairs after the

nearest-neighbor interactions reported often have Al-Al distances around 5-6 Å (Table 3-5), and interactions at these ranges may make significant contributions. Therefore, the surface nearest-neighbor interaction parameters should be taken as very qualitative, and a more complete cluster expansion type approach [108] would be needed for more quantitative pair interaction determination. This issue is particularly important for the Al pairs on cation sites 1,3 and 2,4, which do not share coordinating oxygen atoms and are separated at larger distances. These interactions are between sites that are not in neighboring Fe octahedral that share oxygen atoms and we will therefore call these pairs "non-neighboring" sites or pairs. For these non-neighbor sites, second-nearest Al distances are comparable to the nearest-pair separations, and there is no obvious justification to assign a single interaction energy to any one of the pair types present for these supercells. For consistency with the other calculations we still choose to assign the reported interaction energies to the nearest-distance pairings, but these interaction energies should be considered only as a qualitative guide to the scale of the interactions strengths, not as a true pair interactions for these particular pairs.

Figure 3-6 shows graphically the interaction energies of paired Al-dopants (listed by the nearest Al-Al distances) at the goethite (101) surface (filled columns), grouped alongside the symmetry-equivalent interactions calculated within bulk goethite (open columns). All the data needed to construct Figure 3-6 can be found in Table 3-5. In particular, Table 3-5 has the total energies of the slabs used to calculate Al interactions, the pair interaction energies and Al-Al distances associated with each interaction type, and the second-nearest Al-Al distances to illustrate the possible influence of more-distant Al-Al pairs.

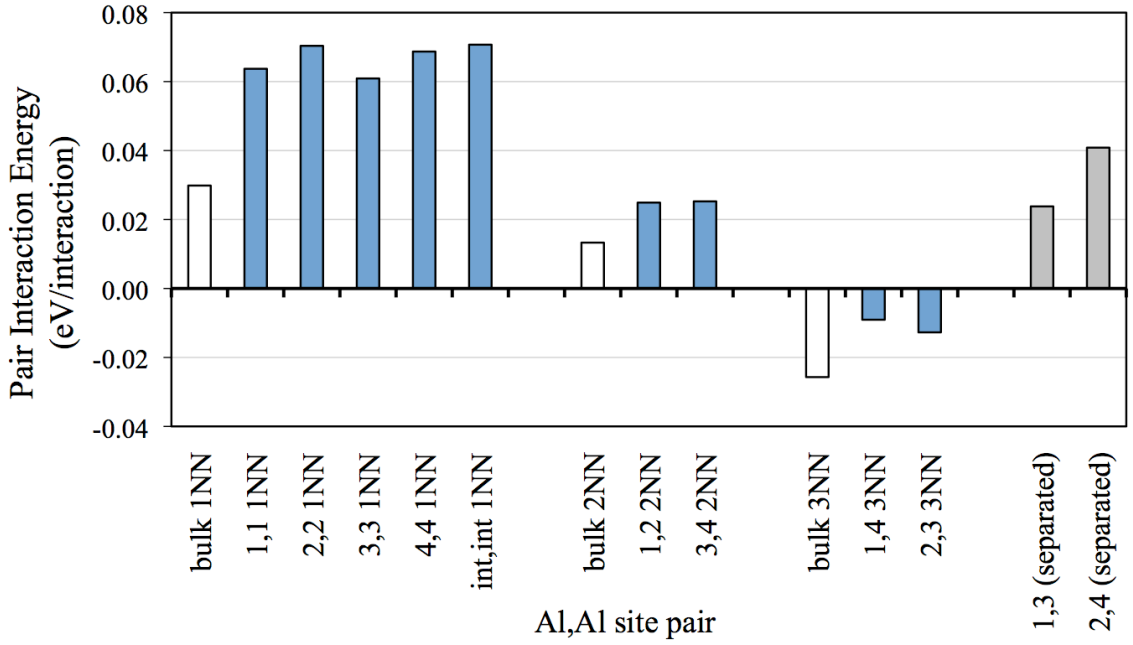

Figure 3-6: Pairwise interaction energies for neighboring Al-Al dopant pairs placed at the goethite (101) surface (dark columns) and within the goethite bulk (white columns), grouped by symmetry-equivalent interaction types. The two-number labels refer to the site numbers shown in Figure 3-4 (*e.g.,* "2,3" is the interaction energy between Al dopants placed on sites 2 and 3 simultaneously). The ordinal type of interaction is shown at each column (e.g. '1NN' = 'first-nearest-neighbor' interaction). Al-Al interactions at the mineral surface behave qualitatively like the corresponding equivalent interactions within the bulk, but have slightly more positive interaction energies. The final two grey columns report the interaction energies for non-neighboring pairs 1,3 and 2,4, for which equivalent interactions were not calculated within the bulk.

All 'like-site' 1NN Al-Al pairs show positive interaction energies between +60 and +70 meV, indicating weak repulsion between the Al dopants placed in first-nearest-neighbor (1NN) cation positions. The 1NN interaction for Al dopants in bulk goethite (Section 3.4.2) shows a weaker but qualitatively similar interaction energy of +30 meV at an Al-Al distance of 2.99 Å. The 1NN interactions calculated at the surface sites all occur at a distance of 3.06 Å, which is an effect of the fixed lattice parameters of the slab supercell. These 1NN interactions span across the periodic boundaries of the supercell in both directions and thus cannot relax to form closer Al-Al pairing distances, as was observed for the bulk Al-Al pairs. This symmetry constraint on the plane of surface interactions may help explain the slightly more-positive energies of the Al-Al interactions calculated

at the surface as compared with bulk interactions. Larger (and more computationally-intensive) supercell calculations could resolve whether this supercell symmetry artifact could account for the small energy differences between surface and bulk Al interactions, but the differences are expected to be minor enough to not substantially affect overall conclusions about surface doping.

Other interaction pairs occur at larger Al-Al distances and topologically correspond to the 2NN and 3NN interaction types reported for the bulk. The 2NN and 3NN Al-Al pairings also have interaction energies similar to, but more positive (repulsive) than their counterpart bulk interactions (Figure 3-6), with the 2NN dopant configurations having weakly repulsive interactions (~+25 meV) and the 3NN interactions having weakly attractive couplings (-10-15 meV). The non-neighbor site interaction pairs '1,3' and '2,4' do not topologically correspond to any calculated bulk interactions. The interaction energies between these non-neighboring sites are comparable to those associated with nearest-neighbor cation sites, suggesting that Al-Al interactions may remain significant over longer distances (>5Å), perhaps mediated by local strain interaction effects. However, as noted above, these non-neighboring site interactions can only be taken as very qualitative due to the presence of multiple types of neighbors at similar distances in the cells studied.

To provide some measure of surface Al-substitution behavior beyond the limit of dilute Al, a final simulation was performed in which all surface Fe-sites were substituted with Al (sites 1-4). This arrangement constitutes a complete monolayer of Al coverage on the goethite surface, in which all Al-Al surface interactions take place simultaneously (eight Al substitutions per slab supercell). This simulation was performed on both anhydrous and hydrated surfaces and gives some insight into the high Al-coverage case. The per-Al relative doping energy of the full-coverage case shows little energetic difference from bulk Al substitution for either anhydrous or hydrated surfaces (Table 3-4), suggesting that any surface segregation tendency at low Al concentrations should diminish as the surface is 'plated' with Al. This arrangement also evinces non-negligible Al-Al interaction at the surface, supporting the non-uniform interaction data shown in Figure 3-4, because a

simple superposition of the relative dilute doping energies for sites 1-4, without considering Al-Al interaction energies, would yield an aggregate energetic result that favors surface segregation. Summing the doping energies of sites 1-4 in isolation (relative to the bulk dopant) and normalizing per Al yields roughly -72 meV/Al and -38 meV/Al, where the case of full Al coverage has a relative doping energy of +1 meV/Al and -15 meV/Al for the anhydrous and hydrated surface cases, respectively, indicating overall repulsive Al-Al interactions for the full coverage case.

3.5 Discussion

Here we consider what the calculated Al doping and interaction energies might imply for the overall thermodynamic and kinetic stability of Fe-(oxyhydr)oxide and oxide materials. Arguably the most significant conclusions that can be drawn from the simulation data relate to the shift in relative stabilities between the metastable phase ferrihydrite and the stable bulk phases, goethite and hematite. In the formation process of these minerals, ferrihydrite often precipitates first as a precursor phase that later transforms to goethite or hematite. If we assume that the fraction of incorporated Al content stays nearly fixed during any phase transformation (i.e., Al^{3+} cations are not expelled during structural transformation), then the presence of Al dopants will reduce the driving force for transformation of ferrihydrite to the more-stable alloyed hematite phase. Under the condition that Al dopant atoms are not expelled, Al-ferrihydrite is predicted to be thermodynamically stable relative to Al-hematite for Al concentrations above about 20% Al.

Although it is interesting to consider the affect of Al-doping under the constraint of fixed alloy composition, it is likely that during phase transformations some or all of the Al will be expelled from an Fe-rich region to form a separate, stable Al-(oxyhydr)oxide, as this is the most stable final product state. This phenomenon is especially probable in the case of dissolution/reprecipitation assisted phase transformations, where cations are freed from their local environments within the solid by dissolution. In contrast, thermally-driven solid-state/topotactic transformations involving only internal displacements of atoms (perhaps also including expulsion of H, OH or H_2O as well) should be expected to better retain dilute Al dopants during and after the transformation process. If cation segregation results from the phase transformation process, then Al content will destabilize Al-ferrihydrite relative to the final products, which will be phase-separated regions of more stable Fe and Al oxides or oxyhydroxides.

Experimentally it has been observed that lightly-doped Al-ferrihydrites synthesized by the co-precipitation of mixed Fe^{3+}/Al^{3+} solutions (pH=9) up to 12% Al undergo solid-

state transformation to hematite at higher temperatures (increasing with increasing Al content) than for undoped ferrihydrite synthesized in the same manner [109, 88]. In some cases, Al-ferrihydrite is also shown to delay or indefinitely resist the transformation to hematite, and after heating only a fraction of the original material transforms to hematite, leaving behind amorphous material bearing the XRD signature of poorly-crystalline Al-ferrihydrite (Liu et al., 2010b). In general, co-precipitated Al-ferrihydrites transform to crystalline hematite (or Al-hematite) more slowly, at higher temperature, or less-completely with increasing Al content. We interpret such observations to be due to the reduced thermodynamic driving force (ΔG_{rxn}) for transformation associated with Al doping.

An additional point of interest is the experimental observation that Al-doping in ferrihydrites favors the formation of hematite over goethite via phase transformation, whereas undoped ferrihydrites can transform to either hematite or goethite [110, 81, 99]. In apparent contrast with this observation, our simulation results suggest that Al-goethite would be the thermodynamically favored product of Al-ferrihydrite phase transformation. However, the distinct phase transformation mechanisms for the ferrihydrite-goethite and ferrihydrite-hematite transformations must be taken into account when interpreting the implications of our calculations. The ferrihydrite-goethite transformation occurrs primarily as a dissolution-reprecipitation process [111] whereas the ferrihydrite-hematite transformation is better described as a topotactic/solid-state process involving internal rearrangements of cations and expulsion of water/OH content. Since goethite formation involves dissolution of the ferrihydrite precursor, the assumption that Al dopant content would remain contained within the bulk of the structure is no longer tenable. Therefore, the stabilizing effect of Al for goethite predicted in Figure 2.3 would not be realized in this transformation and there is no contradiction with the modeling results. It is not clear from our calculations why an increased tendency to form hematite is observed. The influence of Al impurities on the relative kinetics of the dissolution vs. solid-state rearrangement processes remains a likely candidate for explaining the favorability of the ferrihydrite-hematite transformation in the presence of Al substitution.

More generally, the favorability of Al doping in the oxyhydroxides goethite, lepidocrocite and ferrihydrite, as compared to the oxide hematite, can be reasonably interpreted as a consequence of the stability of the Al-OH bond, as compared to Fe-OH. Comparing the relative stabilities of the isostructural pure-Fe and pure-Al oxyhydroxides/oxides, we find that the Al-(oxyhydr)oxides are considerably more stable than the Fe-(oxyhydr)oxides when stability is expressed relative to the $(Al/Fe)_2O_3$ oxide. In the Fe-based materials, only goethite is competitively stable with hematite, having roughly equivalent free energies of formation at equilibrium with liquid water, whereas in the Al-based materials the AlOOH polymorphs diaspore and boehmite are considerably more stable than the oxide, corundum. Additionally, the common and thermodynamically stable Al-(oxyhydr)oxide gibbsite, $Al(OH)_3$, is a fully hydroxylated structure for which there is no commonly-occurring Fe-based structural analogue, suggesting that such a structure is unstable with a cation lattice comprised purely of Fe^{3+}. These observations about bulk stability align with calculation results that favor Al dopants on host lattices containing hydroxyls. Additionally, the presence of an OH group in the octahedral shell of the ferrihydrite Fe1 site, and lack thereof in the case of the Fe2 and Fe3 sites, may help explain the dramatic difference in Al doping energy calculated for these sites, which favors Al doping at the Fe1 site particularly.

The non-uniform nature of calculated Al-Al pairwise interactions in the bulk of the (oxyhydr)oxides does not provide conclusive evidence of a trend toward Al-Al clustering or mixing behavior in the limit of dilute Al. Overall, Al-Al interaction energies in the limit of dilute Al are relatively small compared to the dilute impurity energies of each Al substitution performed, indicating that the overall thermodynamic impact of Al substitution on bulk stability is primarily influenced by the amount of Al substitution, rather than the particular atomic arrangement of the Al on the bulk Fe lattice. Further study into the nature of Al-Al interactions and/or ordering phenomena at Al concentrations above ~20% would require a significantly more complicated simulation model and is thus beyond the scope of this work.

Calculated Al doping energetics and Al-Al interactions at the goethite (101) surface are

non-uniform, demonstrating that Al-Fe alloying physics at the mineral surface are dependent on both surface termination (the types and topologies of sites available) and the concentration of dopants at the surface, especially at higher dopant concentrations where significant dopant clustering or interaction must be expected. The dilute Al-doping energies at the goethite (101) surface show that Al dopants found on the topmost surface Fe sites are significantly more stable than an Al dopant within the bulk, thus a surface segregation effect in which Al dopants are disproportionately located at the mineral surface might be expected. However these favorable doping energetics do not extend beyond the first surface layer, as Fe sites below the topmost layer appear effectively indistinct from bulk Al dopants having no exposure to the mineral surface. Akin to their bulk counterparts, Al-Al pairwise interactions at the mineral surface do not uniformly show a trend toward Al-clustering/phase segregation or Al/Fe mixing at the mineral surface. The overall balance of calculated interactions suggests repulsion/mixing, but the effect is energetically weak.

3.6 Conclusions

We have performed an *ab initio* study of aluminum substitution in the common Fe-oxide and oxyhydroxide structures, including investigation of the thermodynamics of dilute Al-substitution within the bulk of the mineral material and dilute and high-coverage Al-substitution thermodynamics at the (101) surface of goethite. In all Fe-oxide and oxyhydroxide structures dilute Al-substitution is destabilizing, although the effect varies significantly across the family of materials. Lower Al-substitution energies for the oxyhydroxides goethite, lepidocrocite and ferrihydrite indicate that Al-substitution in these materials might be more readily accomplished in a mixed-Al/Fe precipitation environment than for the oxide, hematite. We demonstrate that dilute Al-doping improves the relative stability of Al-lepidocrocite and Al-ferrihydrite relative to Al-hematite, and wholly stabilizes Al-goethite relative to Al-hematite at even low Al concentrations (<5% Al). The shift in relative stability between the oxyhydroxide and oxide phases may impact phase transformation processes, especially in the case of thermally-driven topotactic/solid-state phase transformations not involving the release of kinetically-trapped Al^{3+} dopants. The anticipated effect of increased relative stability of the oxyhydroxide phases when doped with Al is a reduced thermodynamic driving force for transformation (smaller ΔG_{rxn} between Al-ferrihydrite and Al-hematite, as compared to undoped ferrihydrite and hematite). In the case of dissolution/reprecipitation-based phase transformations, notably the formation of goethite from ferrihydrite, Al dopants in the parent phase cannot be assumed to be transferred to the product phase as in the case of topotactic transformations. In this case, dissolved Fe^{3+} and Al^{3+} should be expected to more easily segregate into separate mineral materials upon reprecipitation.

Explicit calculation of Al-Al interaction energies in the bulk Fe-oxide and oxyhydroxides yields a mixed set of interactions types that do not suggest a simple phase segregation/clustering or mixing trend. Al-Al interactions are small in magnitude as compared to the Al substitution energies. Thus, for low levels of Al substitution, the overall impact of Al substitution on thermodynamic stability of the bulk Fe-oxide/oxyhydroxide materials is primarily dependent on the amount of Al substituted,

with the particular Al configurations within the bulk having secondary influence.

Surface slab calculations support the hypothesis that Al surface segregation is energetically favored at the goethite (101) mineral/particle surface, which may be considered an analog for some other Fe-(oxyhydr)oxide surfaces, particularly those of ferrihydrite. However, the surface segregation tendency applies only to the topmost surface layer of Fe sites, while Al doping on underlying layers of Fe sites appears little different from bulk substitution. Al-Al interactions at the goethite (101) surface show no uniform trend toward clustering nor mixing in the dilute limit, similar to the Al interactions in the bulk material. The goethite (101) surface is not significantly stabilized by a full terminal monolayer of Al, indicating that the surface segregation tendency observed for dilute Al substitution cannot be extended to the high-coverage limit.

These results add atomic-level insight into the behavior of Al dopants in the common Fe-oxide/oxyhydroxide materials hematite, goethite, lepidocrocite and ferrihydrite. Considering that Al-doping in natural Fe-oxides and oxyhydroxides is common in natural environments, the thermodynamic impacts of Al-substitution are a relevant component of a more complete understanding of mineral phase stability, formation and transformation, composition, crystal and surface structure, and reactivity toward aqueous contaminants.

3.7 Chapter Acknowledgements

We gratefully acknowledge funding support from the National Science Foundation's Collaborative Research in Chemistry Program under award number CHE 0714183.

Calculation results benefitted from the use of parallel supercomputing resources provided by the Extreme Science and Engineering Discovery Environment (XSEDE), supported by National Science Foundation grant number OCI-1053575.

4 Vacancy Defects in Fe-(oxyhydr)oxide Materials

Note: The contents of this chapter are principally derived from a peer-reviewed article published in Geochimica Et Cosmochimica Acta [75]. *The article was adapted for use in this thesis document.*

4.1 Chapter Abstract

The structure and energetics of proton-compensated cation vacancies in crystalline Fe- and Al-oxide and oxyhydroxide materials are investigated using *ab initio* methods. In this defect model, a vacant Me^{3+} cation site is charge compensated by the presence of three protons, forming hydroxyls with the O atoms surrounding the vacant cation site. Proton-compensated cation vacancies are chemically equivalent to excess hydroxyl content, and are also known as hydrogarnet defects, or Ruetschi defects. These defects can be considered a particular form of structurally bound water, as the formation of the defect can be written as the product of the ideal crystalline material and water. Proton-compensated cation vacancy defects are shown to cause lattice expansion in all calculated Fe and Al materials, and are shown to destabilize all materials relative to the ideal crystalline phases. The magnitude of the destabilization due to the vacancy defects is structure dependent, thus defect content can induce shifts in the relative stability between crystalline phases.

In all of the Fe-(oxyhydr)oxide materials, proton-compensated cation vacancy defects are shown to be slightly co-stabilized in the presence of nearby Al dopant atoms, likely due to the stronger nature of Al-OH bonding (relative to Fe-OH), or from the cancellation of the opposing lattice strains introduced by the two defect types when considered in isolation. FTIR data in the literature confirms that these two defect types (proton-compensated cation vacancies and Al substitutions) have been observed to occur in tandem.

Infrared vibrational frequencies are calculated for the non-stoichiometric hydroxyl groups

found at the vacancy defect sites and compared with those of stoichiometric OH groups found in ideal crystalline (oxy)hydroxides. The calculated O-H stretching modes of the defect hydroxyls have higher frequencies than the modes of stoichiometric hydroxyl groups found in Fe-(oxyhydr)oxide materials, consistent with experimental FTIR observations.

4.2 Introduction

Fe- and Al-oxides and -oxyhydroxides are common minerals found in soil, surface and groundwater environments. Fe-oxides and oxyhydroxides are widely studied as sorption substrates for a variety of waterborne contaminants, including heavy metals (*e.g.,* Cd^{2+}, Pb^{2+}, Zn^{2+}) and contaminant oxyanions (*e.g.*, PO_4^{3-}, AsO_4^{3-}, CrO_4^{2-}). They show promise as engineered materials used in water supply infrastructures for the capture and disposal of aqueous contaminants. In addition to being commonly found as natural mineral precipitates in surface and groundwater environments, laboratory synthesis techniques can produce a wide variety of oxide and oxyhydroxide nanoparticle products of varying sizes, morphologies, elemental compositions and consequently, varying chemical properties.

Fe- and Al-(oxyhydr)oxides are often initially formed via the precipitation of aqueous Fe^{2+}/Fe^{3+} or Al^{3+} ions. Varying precipitation conditions (*e.g.,* temperature, pH, cation oxidation state and concentration) yield the formation of many different mineral phases and polymorphs, with widely varying crystallinity, particle morphology and size, structural hydration, and defect content. The initial products of rapid precipitation are often metastable materials manifested as amorphous or nanocrystalline particles with high surface area. Over time, and/or with sufficient thermal energy, these poorly crystalline particles can aggregate, anneal, and transform to more stable, crystalline phases. However, metastable bulk phases may also be preserved over long periods of time in cases where low surface energy, high surface area, defect content, or other factors act to impede transformation kinetics or reduce the thermodynamic driving force for structural phase transformation.

Proton-compensated cation vacancy defects (equivalently, excess hydroxyl units, hydrogarnet defects, or Ruetschi defects [112, 113]) are an elementary defect type in many crystalline oxide and (oxy)hydroxide materials, and are observed in goethite [114, 85, 115, 116] and hematite [117], and are an essential element of the recently-proposed single-phase crystal structure model of ferrihydrite [10, 54]. In Fe and Al-(oxy)hydroxide

minerals, these defects are characterized by a vacancy on a Me^{3+} cation site, charge-compensated with protons that form hydroxyl groups with the O atoms surrounding the vacant cation site. The defect can also be conceptualized as structurally bound water, since in all cases the defect formation reaction can be written as the hydration of the host Fe- or Al-(oxyhydr)oxide material (Table 3.1). However, XRD and TEM analyses [118] of hematite have suggested that non-stoichiometric bound waters may also exist in mineral pore or interlayer spaces without forming cation vacancies.

Cation defects play a particularly prominent role in the recently proposed structure of ferrihydrite from Michel, et al. [10]. The three-site, single-phase structural model for ferrihydrite was originally proposed in [10] and has been supported by later works that refine the structure, stoichiometry and magnetism of the material [54, 119]. This model is characterized by Fe^{3+} cation vacancies compensated by protons forming OH groups. The model proposes cation vacancies on up to 18% of Fe^{3+} sites, primarily located on the Fe2 and Fe3 symmetry sites (sites discussed later in this work). Defects in ferrihydrite may play both a role in the bulk of the materials and its surface properties. For example, based on the Michel model, the Surface Depletion (SD) model for ferrihydrite was recently proposed [120]. This model places the Fe2- and Fe3-site cation vacancies near the surface of ferrihydrite nanoparticles, resulting in a high density of reactive surface sites anchored on the remaining Fe1 octahedra.

The proton-compensated cation vacancy defect can be formed during rapid precipitation of metastable nanocrystalline particles or amorphous aggregates (e.g., hydrous ferric oxide, or 'HFO', ferrihydrite, gibbsite etc.). In this process, chemisorbed/dissociated water molecules at the mineral surface are trapped within the crystallizing mineral material as it precipitates, leaving excess hydroxyl groups crowded around the lattice site where an Me^{3+} cation would otherwise be found. If temperatures are sufficiently low to impede diffusion of H and OH out of the material, these excess hydroxyls fail to anneal away as the particle grows and stabilizes, to the point of being preserved through structural phase transformation [114, 100, 121]. Thus, these excess hydroxyls can be transferred to the bulk of more crystalline structures (e.g., hematite, goethite) that are the

products of phase transformation from less-crystalline precursors. Hematite containing excess hydroxyls or structural water content is referred to as hydrohematite when vacancy content ranges between 0-8%, or in the case of very high water content (8-16% vacant cation sites), protohematite [117, 115]. Trapped hydroxyls found in materials that have undergone structural phase transformations may be the result of either the incomplete dehydroxylation of the (oxy)hydroxide precursor during the phase transformation process to the more stable forms (which typically involves removing structural water), or by trapping/pinning of defect excess hydroxyls at vacant cation sites already present in the precursor structure.

Of particular interest is the impact cation vacancies can have on the thermodynamics and kinetics of Fe- and Al-(oxyhydr)oxide phase transformations, and the goethite to hematite transformation (a dehydroxylation reaction) has received particular attention. Experimental evidence suggests that excess OH groups on vacant cation sites in goethite and hematite can be identified by characteristic FTIR modes (see Section 4.3), and are at least partially preserved through the goethite-hematite topotactic/hydrothermal phase transformation. Due to their presence in both phases, these defects can potentially impact the phase stability and transformation rates. In a study on goethite containing excess OH content [100], vibrational modes assigned to excess OH were observed in the goethite parent phase at 110 °C and remained visible as temperature was increased, inducing transformation to hydrohematite that was complete by 230 °C. Additionally, the FTIR band centers and bandwidths of the excess OH modes in goethite did not significantly vary through the transformation process, indicating that the excess OH defects are transferred to the hematite structure without being greatly distorted or rearranged [100, 94]. TGA analysis revealed that these excess OH comprised 5.9 wt% of the original goethite material (in addition to the 10.1 wt% attributable to stoichiometric OH), and 5.0 wt% and 3.4 wt% of the hydrohematite product at 230 and 270 °C, respectively. Assuming that these excess OH are found at the sort of cation vacancy defects described in this work, these defects would occupy ~14% of Fe sites in the goethite and hematite phases near the phase transition temperature. Not until the sample was heated to 600 °C were the excess OH groups completely expelled from the hydrohematite product. This

observation aligns with an earlier study in which trapped hydroxyl units in hydrohematite were still observed in FTIR spectra after heating at 500°C, and only fully expelled after heating at 900°C [96].

Additional studies examining the dehydroxylation behavior of goethite prepared with increasing amounts of Al substitution [83, 122, 94] have found that excess OH content is observed to increase as a function of increasing Al concentration, although specific excess OH concentrations are not reported. In DSC/TGA analysis of the transformation process, the endothermic peak associated with goethite bulk dehydroxylation systematically shifts to higher temperatures as a function of Al content, varying from 230 °C at 0% Al content to over 270 °C for 30% substituted Al-goethites. This result suggests that the increasing OH content may increase the transition temperature, although it is difficult to deconvolve the contributions of the OH and Al.

Finally, we note that studies observing the dehydroxylation temperature of precursor goethites of varying crystallinity show that phase transformation temperature *increases* with increasing crystallinity, varying from 260 °C for small, less crystalline particles to 320 °C for larger, more crystalline goethites. This result might suggest that increasing OH content reduces the transition temperature, as more OH filled cation defects would be associated with lower crystallinity. However it is unclear whether these variations in crystallinity, which were based on peak broadening effects observed in particle XRD patterns, are primarily due to bulk defects like the cation vacancies discussed in this work, or surface and nanoparticle morphology effects that might play a larger role in phase transformation physics. Overall, these studies suggest that OH content may have a significant influence on the Fe- and Al-(oxyhydr)oxide phase transformations, but do not provide a robust picture of even the qualitative direction of these effects.

Excess OH defects are not widely discussed in the experimental literature relating to pure Al-(oxyhydr)oxides. However, FTIR studies of synthetic and natural corundum have identified defect OH groups [123], albeit at very low concentrations (<0.01 mol%), although it is unclear to whether these defects are found at cation sites or elsewhere in the

structure.

Our previous work [9] used DFT methods to assess the thermodynamic stability of ideal crystalline Fe-(oxyhydr)oxide materials. That work details the optimization of the single-phase crystal structure and magnetic groundstate of ferrihydrite initially proposed in [10] and further supported in [54]. The present work extends the DFT model to investigate the structural and thermodynamic impacts of introducing defects to the ideal crystalline Fe- and Al-(oxyhydr)oxide mineral materials. In this study, two major defect structures are considered: proton-compensated cation vacancies (excess hydroxyls) and their interaction with nearby Al dopants on the Fe cation lattice.

An earlier study by Blanchard et al. [95] investigates the proton-compensated cation vacancy defect in hematite and Al-hematite, focusing on the impact of the Al substitution and OH content on cell lattice parameters, and the effect of Al and OH incorporation on the isotopic fractionation properties of hematite, based on the determination of the reduced partition functions of ^{57}Fe and ^{18}O. Al content is shown to influence isotopic fractionation in hematite, an important consideration when using Al-contaminated hematite as a marker for historical environmental conditions. In contrast, the incorporation of water (excess OH) at proton-compensated cation vacancies is not shown to significantly affect the isotopic properties of hematite. The work presented herein replicates the calculation of the proton-compensated cation vacancy defect in hematite, and extends to evaluate the same defect type in goethite, lepidocrocite and ferrihydrite. This work describes a systematic approach to finding stable proton positions within the vacant cation interstitial area, and adds an assessment of the impact of this defect type on thermodynamic relative stability in all four materials, including hematite.

4.3 Computational methods

Density Functional Theory calculations were performed using the Vienna Ab-initio Software Package (VASP) [6-8] and the projector-augmented wave (PAW) method [23]. The generalized gradient approximation (GGA) parameterization of Perdew, Burke and Ernerhoff (PBE) [25] was implemented to treat the exchange correlation. The DFT+U (here, GGA+U) method was employed to treat the localized 3*d*-electrons in Fe atoms, where on-site Coulomb interactions are not captured by standard DFT [26]. The GGA+U chosen is implemented using the method of Dudarev [30], where a single parameter, $U_{effective}$ = U-J describes the magnitude of the correction. U is a spherically averaged Hubbard parameter that describes the coulomb interaction between the localized electrons treated by the method. J is the screened exchange energy between electrons in the d orbitals. The GGA+U method is widely used for transition metal materials and is shown to optimize experimental agreement for calculated thermodynamic quantities (*e.g.,* formation enthalpy), geometry, and magnetic, electronic and redox properties in Fe-containing materials for a U_{eff} = U-J value between 3-5 eV [27-29, 9]. In this work, U_{eff} was set at 3 eV (U=4 eV, J=1 eV) for 3*d* electrons in all Fe atoms, and set to 0 eV (i.e. no correction) for all other atoms/electron orbitals.

All reported calculated data used soft PAW/PBE pseudopotentials for O atoms and standard PAW pseudopotentials for Fe, Al and H atoms. The Fe pseudopotential chosen includes 3p electrons as part of the calculated valence shell. The valence electron configurations calculated were $2s^2 2p^4$ for O, $3p^6 3d^7 4s^1$ for Fe, and $3s^2 3p^1$ for Al. A maximum plane wave energy cutoff of 350 eV was used for all data reported herein. A cutoff of 650 eV was tested for several sets of calculations and did not significantly affect the relative energies or geometries of the defected systems compared to ideal crystalline materials. Modern functionals that incorporate corrections to the standard GGA [124-126] to account for dispersion interactions were not used in this study. While such corrections arguably could aid in the description of loosely-bound H atoms at vacancy defect sites, when applied to ionic oxide materials where dispersion interactions are expected to be small, and where periodic boundary conditions apply, the corrections lead

to overbinding errors in bulk cohesive energies and are not shown to significantly improve accuracy in calculated lattice parameters as compared to conventional functionals that do not include dispersion physics [127]. An exception to this trend might be expected for the layered structure lepidocrocite, where interlayer dispersion forces could play a significant role in energetics and interlayer spacing. A detailed study of the impacts of dispersion corrections for the Fe- and Al-oxide and oxyhydroxide materials would be warranted before these corrections could be used with confidence for the defect energy calculations performed here. However, such a study is beyond the scope of the present work.

Reciprocal space k-point mesh densities were chosen such that the total energies of primitive cells of the ideal crystalline reference materials were converged within 1-2 meV/atom with respect to an increase in k-point density, and corresponding to a k-point density of minimally 2160 k-points per reciprocal-atom. For defect calculations, large supercells (see Sec. 4.1 for specific cells) were constructed to minimize the defect self-interaction introduced by periodic boundary conditions. Where possible, defect supercells used the same k-point meshes scaled inversely with the supercell multiplication of the primitive cells, resulting in equivalent k-point sampling across all supercell sizes of a given host material.

In each host oxide/oxyhydroxide structure, the hydroxyl arrangement at the proton-compensated cation vacancy defect site was determined by calculating all possible topological arrangements of hydroxyls within the vacant Me^{3+} site. In the case of hematite, goethite, and lepidocrocite, all Fe^{3+} are sixfold-coordinated by oxygen. The three-site single-phase structural model for ferrihydrite used for this study contains both octahedral ("Fe1", "Fe2") and tetrahedrally-coordinated ("Fe3") Fe atoms [10]. In the case of a proton-compensated vacancy on an octahedral Me^{3+} site, three of the six oxygen atoms become hydroxyls. Using a reduced level of k-point sampling (1 k-point) for computational expediency, all of the 6 choose 3 = $\frac{6!}{3!\cdot 3!}$ = 20 unique O/OH topological configurations within the octahedral site were relaxed for each host structure. For the Fe3 tetrahedral site in ferrihydrite, 4 choose 3 = 4 configurations of three protons are

possible on the four O atoms surrounding the site. Although analysis of symmetry-equivalence of various hydroxyl arrangements could be used to reduce the number of configurations calculated (*e.g.,* perhaps Configuration 2 is a mirror image of Configuration 1), a brute-force approach was employed calculating all possible configurations within a given cation interstice without eliminating redundant calculations. This approach resulted in a set of configuration defect energetics that showed some redundancy or degeneracy, as some configurations were topologically and energetically equivalent to others. Nonetheless, the resulting energies form a complete exploration of the configuration space of the hydroxyl arrangements on the vacant cation sites.

In these preliminary simulations, the H atoms were initially placed approximately 1 Å from coordinating O atoms, with OH bonds oriented toward the inside of the vacant Fe site. During relaxation, significant movement of H atoms was observed – typified by movement of H atoms toward neighboring oxygen atoms forming bent OH--O hydrogen bonds. In some cases, H atoms moved from the initially-bonded O atom to the O atom across the hydrogen bond, forming a more stable arrangement degenerate with another starting topology. After relaxation, those hydroxyl arrangements with energies within +0.2 eV/defect of the most stable arrangement for each host structure were re-relaxed using full k-point sampling, and the most stable result from these sets of higher precision calculations are reported here. For all the materials studied, the range of formation energies across the spectrum of the 20 possible OH positions for each structure was approximately 0.8 eV/defect – meaning the least stable OH arrangement in each host structure was approximately 0.8 eV higher in energy, per vacancy defect, than the most stable arrangement. The second most-stable (and symmetry-distinct) hydroxyl arrangement in each case was roughly 0.1/defect eV higher in energy than the most-stable arrangement. The high energetic cost of proton reconfiguration (~4-30 kT at 300K) implies that the proton configuration within the vacancy defect does not explore many possible hydroxyl arrangements, but rather adopts one of a set of symmetric/degenerate hydroxyl arrangements within the vacant cation site and largely remains there.

The vibrational modes of protons trapped at the defect sites were calculated using VASP

after performing a high precision relaxation of the atomic coordinates of the defect cells. The vibrational frequencies of the stoichiometric/non-defect protons in goethite, lepidocrocite and ferrihydrite were also calculated by similar methods for comparison. The high precision calculation procedure uses tight electronic SCF and ionic energy convergence criteria ($1e^{-6}$ and $1e^{-5}$ eV, respectively) to place atomic positions precisely at local minima. Starting with these geometries, the vibrational frequencies of OH bonds were calculated by inducing small displacements (~0.01Å) of the H atoms about their local minima to determine the curvature of the energy landscape about the local minimum. Vibrational frequencies are obtained as the eigenvalues of the Hessian dynamical matrix computed from the energies associated with the spatial displacements. For the defect proton calculations, vibrational modes are reported as the coupled modes of the three protons trapped on the vacant cation site. For stoichiometric (non-defect) protons in goethite, lepidocrocite and ferrihydrite, vibrational modes are calculated using a single proton, i.e., no multi-proton vibrational coupling is probed by the simulation.

The coordinates of the heavier O, Fe and Al atoms were held fixed in the calculation of OH modes, which greatly reduces the computational cost of these calculations and simplifies the assignment of calculated frequencies to individual OH bonds. A qualitative estimate of the impact of this constraint of degrees of freedom on calculated vibrational frequencies can be estimated by substituting the reduced mass of the OH system (0.948 u) instead of the mass of H (1.008 u) in the harmonic oscillator analysis, where vibrational frequency ω is inversely proportional to the square root of the effective mass of the oscillating body. Based on this correction alone, fixing the heavier atoms results in calculated OH frequencies approximately 3% lower than what would be expected of a more complete vibrational analysis. However, the errors associated with these reduced frequencies largely cancel in the calculation of vacancy defect energetics due to the relatively similar atom arrangements in both the defect and undefected bulk simulations across the set of materials studied, where the most significant differences in atomic bonding are observed for protons at the vacancy defect site. To further support the choice of this simplifying approximation, for a sample subset of defect energy calculations in ferrihydrite (Fe1 site vacancy), a full vibrational analysis was performed in which all

atoms were perturbed and the calculated defect energy differs +0.036 eV from that calculated using only the ZPE associated with H atoms with all other atoms being frozen, a difference which is roughly one order of magnitude smaller than the defect energy differences between phases.

4.4 Defect Thermodynamic Analysis

Proton-compensated cation vacancy defect formation energies in Fe- and Al-(oxyhydr)oxides are reported as enthalpies of reaction from the undefected bulk material and water. In all cases, the formation of the cation vacancy defect can be written as a hydration reaction in which one or more water molecules, dissociated into H and OH groups, are placed into an uncharged structural void in the crystalline host material. Table 4-1 shows the defect formation reactions schemes proposed for the proton compensated cation vacancies.

In this reaction scheme, the only reference states needed to assess the defect formation enthalpy are the total energies of the undefected bulk structure and liquid water. For the liquid water reference state, the method described in [9] was used to adapt the gas-phase total energy of an isolated water molecule to the condensed liquid state at low temperature. In this approach the DFT energy of the isolated, gaseous water molecule was shifted by the enthalpy of condensation (-44.01 kJ/mol H_2O), creating a reference state for bulk liquid water at low temperature. Thermal vibrational effects beyond groundstate vibrational energy at 0K were not factored into the defect, bulk, or molecular water calculations – the energies reported herein reflect the T=0K condition inherent in static DFT calculations and should be considered as defect formation enthalpies, not free energies.

The zero-point energies (ZPE) of the ideal and defected structures are calculated from the vibrational frequencies of the stoichiometric and defect protons, assuming that H vibrational modes are the main contributors to structural ZPE due to the relatively low

mass of H, as compared to the other atomic species in the study (O, Fe, Al) (See Sec. 4.3 for details). We calculate ZPE as the sum of the vibrational modes of each H atom: $\mathrm{ZPE} = \frac{1}{2}\sum_{i=1}^{3} h\nu_i$ where ν_i are the vibrational frequencies of the H atom, and h is Planck's constant. The energetic contributions of electronic total energy and zero point energy are reported separately in the results to clarify the relative contribution of each of these factors, each calculated using a different calculation technique, in the final defect formation energy.

Table 4-1: Formation reactions of the proton-compensated cation vacancy defect in the common Fe- and Al-oxides and oxyhydroxides. Ferrihydrite stoichiometry assumes the undefected crystal structure and stoichiometry of the Michel model. The reactions shown are for arbitrary sample/simulation size (i.e. x unit cells). Specific calculation details and calculated reaction energies (defect formation energies) for these reactions are given in Table 4-2. ('Me' = metal cation, either Fe or Al)

Isostructure	Defect Formation Reaction	Eq. #
hematite, α-Fe_2O_3, corundum, α-Al_2O_3	$Me_{2x}O_{3x} - \frac{1}{2}(Me_2O_3) + \frac{3}{2}(H_2O) \rightarrow Me_{2x-1}V_{Me}O_{3x}H_3$	(4.1)
goethite, α-FeOOH lepidocrocite, γ -FeOOH diaspore, α-AlOOH boehmite, γ-AlOOH	$Me_xO_x(OH)_x - MeOOH + 2(H_2O) \rightarrow Me_{x-1}V_{Me}O_x(OH)_xH_3$	(4.2)
ferrihydrite, Fe_5O_8H akdalaite, Al_5O_8H	$Me_{5x}O_{8x}H_x - \frac{1}{5}(Me_5O_8H_1) + \frac{8}{5}(H_2O) \rightarrow Me_{5x-1}V_{Me}O_{8x}H_{x+3}$	(4.3)

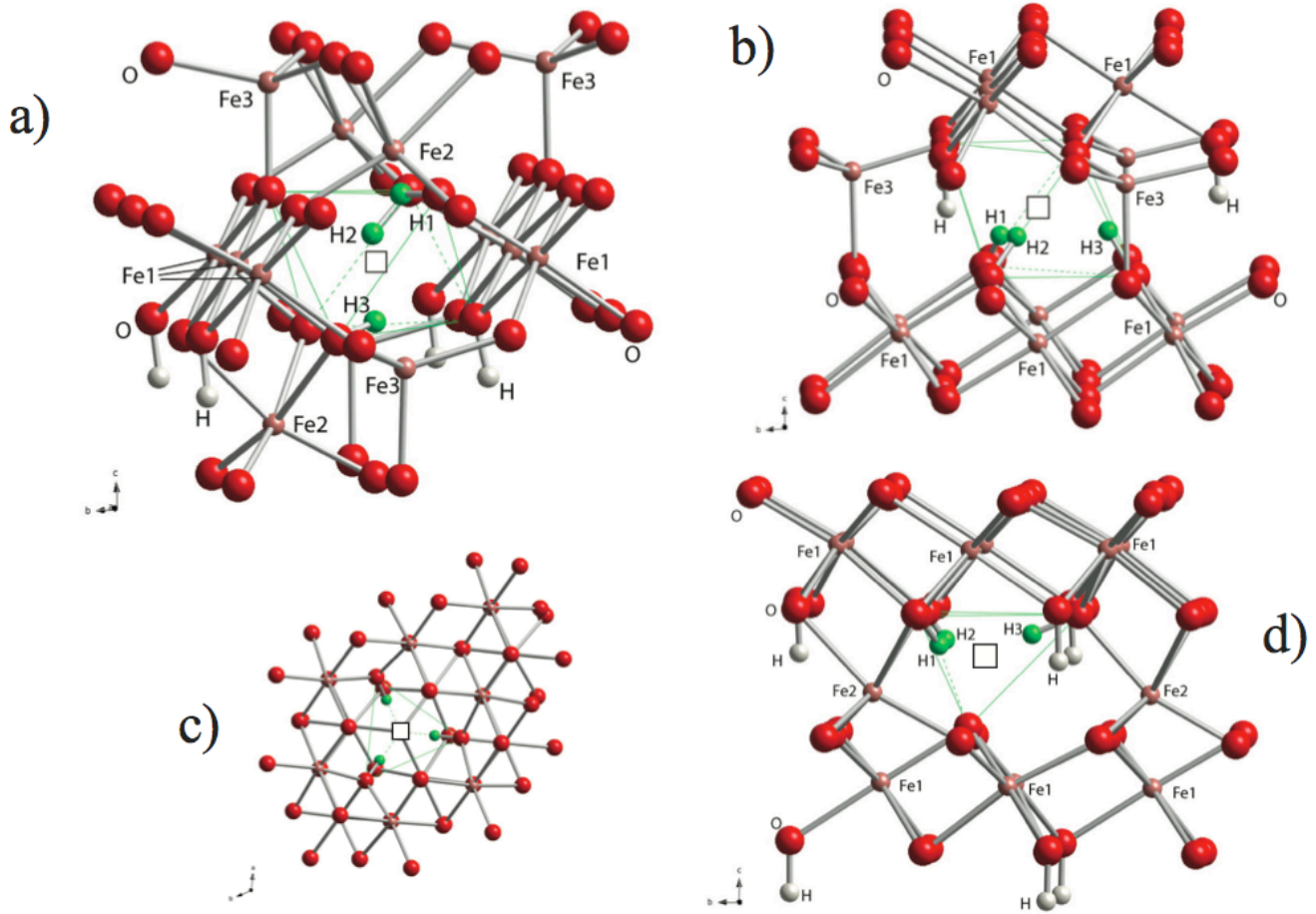

Figure 4-1: Stable hydroxyl arrangements of the excess hydroxyl vacancy defect in the three symmetry-distinct Fe sites in ferrihydrite. The vacant Fe cation site is indicated by an empty square and is highlighted with a polyhedral outline (green). Defect hydroxyl protons are shown in green and are labeled H1, H2, and H3 in each image, while stoichiometric protons are shown in white and labeled as H. Image index: a) ferrihydrite Fe1 site vacancy, viewed essentially along the a-axis, b) ferrihydrite Fe2 site vacancy, viewed along the a-axis, c) ferrihydrite Fe3 site vacancy, viewed down the c-axis, d) ferrihydrite Fe3 site vacancy, viewed along the a-axis.

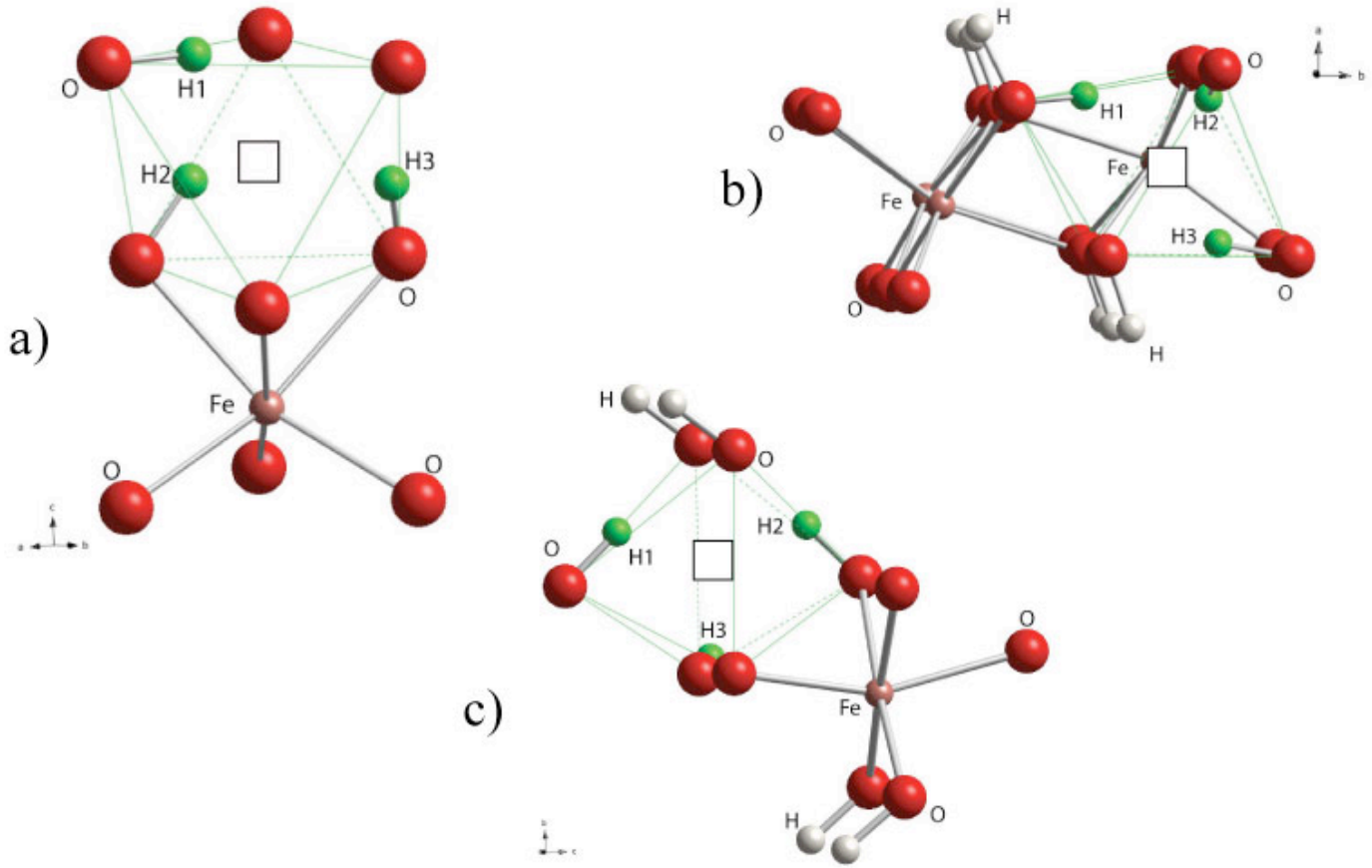

Figure 4-2: Calculated stable proton/hydroxyl arrangements of the excess hydroxyl vacancy defect in a) hematite, b) goethite, and c) lepidocrocite. The vacant Fe cation site is indicated by an empty square and is highlighted with a polyhedral outline (green). Defect protons are shown in green and are labeled as H1, H2 and H3. Stoichiometric protons found in the oxyhydroxides goethite and lepidocrocite are shown in white and simply labeled as H.

4.5 Results

4.5.1 Defect Geometry and Strain Effects

Figure 4-1 shows the relaxed geometries of the most-stable OH configurations found for the proton-compensated cation vacancy defects in each of the three Fe sites in ferrihydrite. A green polyhedral frame outlines the vacant Fe^{3+} site, marked by an empty square. The three defect protons are numbered as H1, H2, and H3, where the stoichiometric protons are simply labeled as H. Only one distinct stoichiometric proton site is found in the Michel model for ferrihydrite [10, 9]. Figure 4-2 shows the relaxed geometries of the proton-compensated cation vacancy defect in hematite, goethite, and lepidocrocite. In both Figure 4-1 and Figure 4-2, the simulation geometries are significantly cropped to allow visualization of the excess hydroxyl bonding arrangement at the defect cation site. The actual calculated simulation cells are larger than is shown, in order to minimize the interaction of defects with their images across periodic boundaries.

Table 4-2 reports the simulation data for a series of calculations using large supercell geometries, with a single proton-compensated cation vacancy defect placed in cells with 24-48 Fe cation sites (one of which is vacant, containing the defect hydroxyls). Calculations using smaller supercells, with 10-16 Fe^{3+} cation sites, were also performed using identical initial defect geometries. These smaller supercells showed similar defect energetics (Figure 4-2) and geometries (*e.g.,* OH bond lengths, defect formation volumes), indicating that convergence with respect to system size is achieved for the larger supercell sizes, and that defect-defect interactions are minor at distances corresponding to the cell parameters of the smaller-sized cells.

Table 4-2: Simulation details for small and large supercell proton-compensated cation vacancy calculations in the Fe-(oxyhydr)oxides and the oxide, hematite. Defect Formation Energies (DFE) (final column) for the proton-compensated vacancy defects are calculated using the hydration reaction energy approach illustrated in Equations 4.1-4.3 The 'V' notation indicates a simulation containing an Fe^{3+} cation vacancy compensated by 3 H^{+}. The final two rows give the total energy of the isolated water molecule as calculated from VASP, and the energy of condensed water at 0K. The condensed water reference state is used in the calculation of the DFE's as reaction enthalpies for hydration reactions involving the undefected Fe-oxide/oxyhydroxide host structures. Kpoint mesh styles employed are labeled as G (gamma-centered) and M (Monkhorst-Pack).

Isostructure	Simulation Stoichiometry	Cation Vacancy Conc. (%)	Total Energy (eV)	Supercell Size	kpoint Mesh	Relaxed Cell Parameters (Å)			Cell Volume (Å^3)	*Defect Formation Energy (eV/defect)*	
						a	*b*	*c*		*w/o ZPE*	*w/ZPE*
hematite, small	$Fe_{12}O_{18}$	-	-213.0056	1×1×1	662G	5.08	5.08	13.93	311.70	-	-
hematite, large	$Fe_{48}O_{72}$	-	-852.0394	2x2x1	332G	10.17	10.17	13.93	1247.05	-	-
V-hematite, small	$Fe_{11}O_{18}H_3$	8.33%	-216.2084	1×1×1	662G	5.12	5.08	14.01	315.83	0.80	0.98
V-hematite, large	$Fe_{47}O_{72}H_3$	2.08%	-855.2058	2×2×1	332G	10.17	10.18	13.95	1250.79	0.84	1.01
goethite, small	$Fe_{16}O_{32}H_{16}$	-	-401.8746	1×2×2	343M	10.04	6.10	9.25	566.49	-	-
goethite, large	$Fe_{32}O_{64}H_{32}$	-	-803.7497	1×4×2	323M	10.04	12.19	9.25	1132.11	-	-
V-goethite, small	$Fe_{15}O_{32}H_{19}$	6.25%	-404.9180	1×2×2	343M	10.01	6.12	9.30	569.19	0.85	1.07
V-goethite, large	$Fe_{31}O_{64}H_{35}$	3.13%	-806.8507	1×4×2	323M	10.03	12.19	9.29	1135.50	0.79	1.01
lepidocrocite, small	$Fe_{16}O_{32}H_{16}$	-	-399.5851	2×1×2	424M	6.17	12.48	7.86	605.51	-	-
lepidocrocite, large	$Fe_{24}O_{48}H_{24}$	-	-599.3866	3×1×2	324M	9.26	12.49	7.86	909.18	-	-
V-lepidocrocite, small	$Fe_{15}O_{48}H_{19}$	6.25%	-402.9846	2×1×2	424M	6.18	12.46	7.87	606.08	0.63	0.82
V-lepidocrocite, large	$Fe_{23}O_{48}H_{27}$	4.17%	-602.8173	3×1×2	324M	9.25	12.49	7.86	909.03	0.60	0.79
fhyd, small	$Fe_{10}O_{16}H_2$	-	-191.4445	1×1×1	664G	5.97	5.97	9.36	288.89	-	-
fhyd, large	$Fe_{40}O_{64}H_8$	-	-765.7990	2×2×1	334G	11.94	11.94	9.37	1156.64	-	-
V-fhyd, Fe1, small	$Fe_9O_{16}H_5$	10.00%	-195.2972	1×1×1	664G	5.99	5.90	9.54	292.21	0.21	0.38
V-fhyd, Fe1, large	$Fe_{39}O_{64}H_{11}$	10.00%	-769.6038	2×2×1	334G	11.96	11.91	9.42	1161.73	0.26	0.42
V-fhyd, Fe2, small	$Fe_9O_{16}H_5$	10.00%	-194.7877	1×1×1	664G	6.02	6.02	9.36	293.09	0.72	0.82
V-fhyd, Fe2, large	$Fe_{39}O_{64}H_{11}$	2.50%	-769.0679	2×2×1	334G	11.98	11.97	9.35	1161.53	0.79	0.89
V-fhyd, Fe3, small	$Fe_9O_{16}H_5$	2.50%	-195.1428	1×1×1	664G	6.03	6.03	9.22	290.58	0.36	0.49
V-fhyd, Fe3, large	$Fe_{39}O_{64}H_{11}$	2.50%	-769.5396	2×2×1	334G	11.97	11.97	9.34	1159.29	0.32	0.44
water, gas phase 0K	H_2O	-	-14.0477	n/a	888M	10.00	10.00	10.00	-	-	-
water, condensed phase, 0K	H_2O	-	-14.5041	-	-	-	-	-	-	-	-

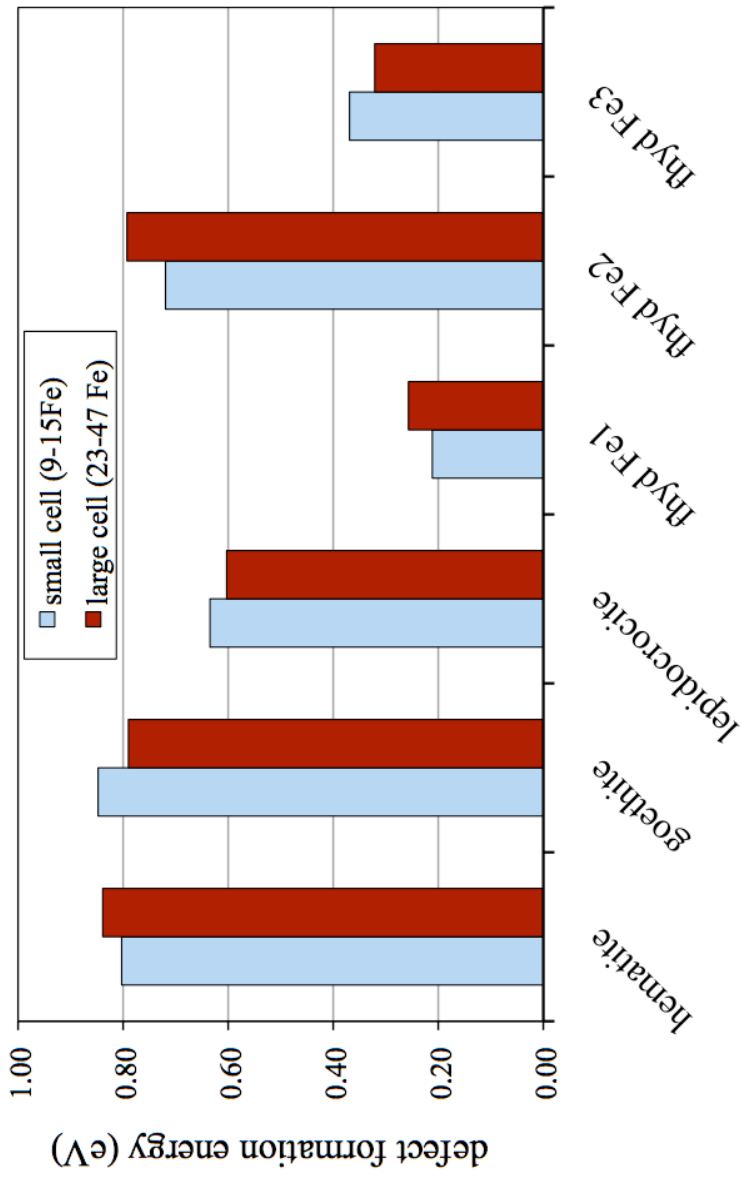

Figure 4-3: Proton-compensated cation vacancy defect formation total energies (enthalpies) for Fe-oxides/oxyhydroxides are calculated as hydration reaction energies, Equations 4.1-4.3, Table 4-1, above. These defect formation energy values do not take into account ZPE, which was not calculated separately for large and small supercells. Light blue columns correspond to smaller supercell calculations with 10-16 metal cation sites, one being occupied by the proton-compensated vacancy defect. Dark red columns correspond to the larger supercell calculations reported in Table 4-2 (24-48 metal cation sites). The small differences in defect energies between small and large supercells indicate that defect-defect interactions are small relative to the point defect energies for low vacancy content.

The proton-compensated cation vacancy defects show positive formation volume (dilatation) for each of the Fe- and Al-oxide and oxyhydroxide materials investigated, with the exception of lepidocrocite, where the defect has a small negative formation volume. The general trend of dilatation is caused by the repulsive coulomb interactions between the three defect protons packed tightly in the vacant Me^{3+} site, which induces an outward strain on the material. The small negative vacancy defect formation volume calculated for lepidocrocite can be attributed to the layered nature of lepidocrocite, where layers are joined only by hydrogen bonds that are more flexible and accommodating of small local distortions around the vacancy defect site. The Al-based isostructure of lepidocrocite, boehmite, shows a small but positive formation volume for the proton-compensated cation vacancy defect. The difference between the Al and Fe cases is perhaps due to the smaller cation atomic volume and shorter lattice spacing in the Al-(oxyhydr)oxides as compared to the Fe-based materials, however differences in valence electron characteristics of Al^{3+} and Fe^{3+} may also play some role.

4.5.2 Defect Stability

Table 4-2 shows calculated defect formation energies both omitting and including H ZPE of products and reactants in the defect formation energy calculation. The inclusion of ZPE induces an increase in the proton-compensated cation vacancy defect formation energy for all the materials studied, with increases of 170, 100, and 120 meV for the 3 vacancy defect sites in ferrihydrite, respectively, and 170, 220, and 190 meV for hematite, goethite and lepidocrocite, respectively (Figure 4-4). Overall, the variation in defect formation energies between materials are primarily due to differences in the total energy of the defects, whereas differences in ZPE have a relatively smaller impact, as illustrated in Figure 4-4.

Results for proton-compensated cation vacancy defects in the Al-oxide/oxyhydroxide isostructures are reported for large simulation cells in Table 4-3. For the Al-based materials, defect formation energies and formation volumes show strong similarity to their Fe-based isostructures. Figure 4-4 shows the defect formation energies of the

proton-compensated cation vacancy in Al-materials as compared to their Fe-based isostructures.

While the proton-compensated cation vacancies are calculated to be destabilizing in each of the Fe- and Al-oxide and oxyhydroxide materials studied, the magnitude of the destabilization varies significantly between phases/polymorphs. In both the Fe and Al-based materials, defect formation energies are highest (less stable) for the bulk oxide phase (hematite/corundum), with lower formation energies (more stable) for the common oxyhydroxides (goethite/diaspore, lepidocrocite/boehmite) and the lowest defect energies (most stable) for the metastable and often amorphous phases (ferrihydrite/akdalaite). In ferrihydrite, the defect formation energy calculated is highly site-dependent. The octahedral Fe1 and tetrahedral Fe3 sites show similar defect formation energies, and are the lowest defect energies calculated among the materials studied. The cation vacancy defect at the Fe2 octahedral site has a relatively high formation energy, roughly 0.5 eV higher than that of the most-stable Fe1 site, suggesting that defects of this type are unlikely to be stable at the Fe2 site given nearby alternatives of significantly lower energy. This result contrasts the site occupancy model described in [54], which proposes near-complete occupancy of the Fe1 site and vacancies on the Fe2 and Fe3 sites.

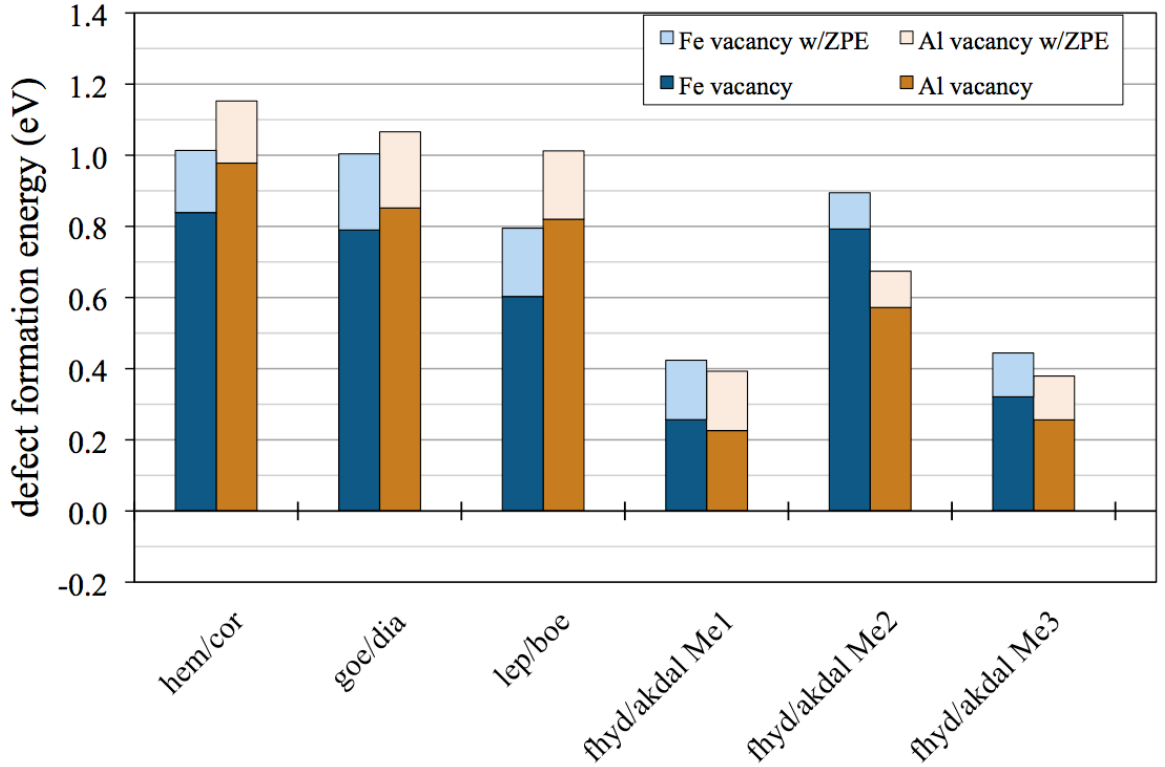

Figure 4-4: Comparison of defect formation energies for proton-compensated cation vacancy defects for isostructural materials containing Fe vs. Al cations (large-supercell calculations). Isostructural Fe/Al material pairs are hematite/corundum, goethite/diaspore, lepidocrocite/boehmite and ferrihydrite/akdalaite. The defect formation energies for the Fe-based materials are shown in blue (left columns), and for the Al-based materials in orange (right columns). Me1, Me2 and Me3 refer to the three metal (Me) cation sites in the ferrihydrite structure. The energetic contributions of calculated total energy (enthalpy) and zero-point energy (ZPE) are differentiated to illustrate the relative magnitude of each component on the total defect formation energy. See section 4.5.3 for discussion of OH bond lengths and vibrational frequencies used to determine ZPE.

Table 4-3: Simulation details for large supercell proton-compensated cation vacancy calculations in the Al-(oxyhydr)oxides and the oxide, corundum. These materials are all isostructural with the Fe-(oxyhydr)oxides and oxide materials reported in Table 4-2. These relaxed geometries were obtained by full relaxation of the defected Fe-(oxyhydr)oxide supercells, after replacing all Fe with Al and performing a slight volume contraction of the unit cell to reflect the smaller ionic radius of Al and resultant contraction of lattice parameters. After this initial geometry relaxation, all Al-oxide/oxyhydroxide simulations were re-initialized and re-relaxed to avoid basis set errors associated with large volume changes during cell relaxation.

Isostructure	Simulation Stoichiometry	Cation Vacancy Concentration	Total Energy (eV)	Supercell Size	kpoint Mesh	Relaxed Cell Parameters (Å)			cell volume (Å^3)	defect formation energy (eV/V)	
						a	*b*	*c*		*w/o ZPE*	*w/ZPE*
corundum	$Al_{48}O_{72}$	-	-900.1957	2×2×1	332G	9.62	9.62	13.12	1050.79	-	-
V-corundum	$Al_{47}O_{72}H_3$	2.1%	-902.2198	2×2×1	332G	9.63	9.63	13.13	1053.73	0.98	1.16
diaspore	$Al_{32}O_{64}H_{32}$	-	-839.8832	1×4×2	323M	9.49	11.48	8.81	958.98	-	-
V-diaspore	$Al_{31}O_{64}H_{35}$	3.1%	-841.7818	1×4×2	323M	9.50	11.48	8.84	963.68	0.86	1.12
boehmite	$Al_{24}O_{48}H_{24}$	-	-630.0961	3×1×2	324M	8.68	12.00	7.46	777.14	-	-
V-boehmite	$Al_{23}O_{48}H_{27}$	4.2%	-632.0299	3×1×2	324M	8.68	12.01	7.48	779.50	0.82	1.10
akdalaite	$Al_{40}O_{64}H_8$	-	-809.3837	2×2×1	334G	11.27	11.27	8.84	972.22	-	-
V-akdal, Al1 site	$Al_{39}O_{64}H_{11}$	2.5%	-812.1297	2×2×1	334G	11.29	11.24	8.88	975.56	0.23	0.44
V-akdal, Al2 site	$Al_{39}O_{64}H_{11}$	2.5%	-811.7836	2×2×1	334G	11.30	11.30	8.84	977.13	0.57	0.76
V-akdal, Al3 site	$Al_{39}O_{64}H_{11}$	2.5%	-812.0996	2×2×1	334G	11.30	11.30	8.82	975.68	0.26	0.44

The discussion that follows focuses on the impact of the proton-compensated cation vacancy defect in the Fe-oxide/oxyhydroxide system, but this discussion can be extended to include the Al-oxide/oxyhydroxides as well, as the defect geometries and energies are similar for both metal cations.

All else held constant, the introduction of proton-compensated cation vacancies will induce a shift in the free energy of the defected material away from that of the undefected bulk phase. When considering the impact of vacancy defects on a set of related materials (*e.g.,* Fe- and Al-oxides and oxyhydroxides), the defects may induce changes in *relative* phase stability that will affect the phase composition of materials under a given set of conditions. Sufficient defect content might cause an inversion in phase stability relative to the undefected materials. Falling short of a stability inversion, defect content will alter the conditions under which phase transformations occur, due to the change induced in the thermodynamic driving force for phase transformation (ΔG_{rxn}), in effect reducing or increasing the barrier to transformation. The free energies of the *undefected bulk* Fe-oxide and oxyhydroxide materials studied vary in relative stability by less than 10 kJ/mol-Fe, enabling *non-bulk* material phenomena of modest energy scale (*e.g.,* defect content, surface area) to induce inversions of phase stability [1, 2, 9].

Figure 4-5a shows the relative stability of the common Fe-oxide/oxyhydroxide phases as a function of vacancy defect content. Figure 4-5b shows the analogous data for the Al-oxide/oxyhydroxide phases. In these plots the *y*-intercepts, the leftmost data points of each series, correspond to the relative stability (free energy of reaction, ΔG_{rxn}) of the undefected bulk material with respect to bulk hematite/corundum + water at 298.15 K. Experimental ΔG_{rxn} values [2] are used for each of the materials with the exception of ferrihydrite and akdalaite, where experimental thermodynamic data are unavailable or incomplete. For these two materials, the relative stabilities are constructed from *ab initio* calculations of the formation energy at T=0 K (including ZPE) coupled with experimental thermodynamic data that measure changes in the formation free energy at T>0 [2, 9]. The x-axis of Figure 4-5 can be equivalently defined as either cation vacancy concentration or excess structural water content normalized per cation site. The data series for each

material shows two additional data points at nonzero defect concentration, corresponding to the large and small defect supercell calculations. The dashed lines extrapolate the thermodynamic impact of the large supercell defect calculation (middle of the three data points) to higher defect concentrations without consideration of defect interactions. Given the computational difficulty of calculating the energies of even lower concentrations of defects, the large supercell defect simulations are the best-available representatives of isolated, non-interacting vacancy defects. The smaller supercell calculations (rightmost points) do not deviate significantly from this zero-interaction extrapolation, indicating that defect-defect interactions are of minor significance for vacancy defect concentrations below ~10%. Figure 4-5 extrapolates the thermodynamic impact of vacancy defect content no further than 20% of cation sites. Beyond ~20% defect concentration, nearest-neighbor defect arrangements are unavoidable from a configurational standpoint. Defect ordering and significant structural distortion may occur at higher defect concentrations, both of which are phenomena beyond the scope of this work.

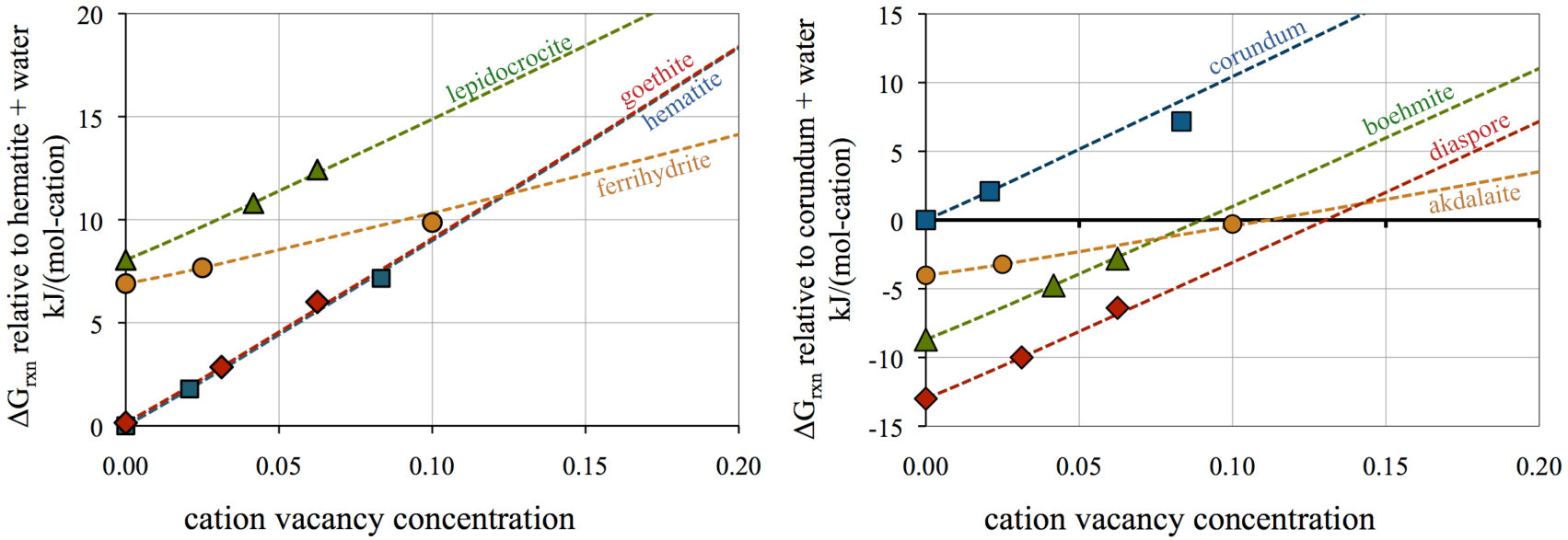

Figure 4-5: The introduction of structurally-bound water in the form of proton-compensated cation vacancies has a significant impact on relative stability, expressed as free energy of reaction relative to bulk hematite/corundum + water. In this figure, the reaction energies of ferrihydrite and akdalaite are calculated using the energetics of proton-compensated cation vacancies on the Fe1/Al1 symmetry site, which is the most stable cation vacancy site. These data are based on the proton-compensated cation vacancy defect formation energies that include consideration of ZPE. Each series consists of three data points: the calculated thermodynamic stability of the bulk, undefected phase (y-intercept), and two points corresponding to the defect energies of the large (low concentration) and small (higher concentration) supercell calculations, each containing an isolated vacancy defect. The dashed lines extrapolate the thermodynamic impact of the isolated vacancy defect calculated in the large supercell to higher defect concentrations, without taking into account defect interactions. The smaller supercell calculations (rightmost points) do not deviate significantly from this extrapolation, indicating that defect-defect interactions are of minor significance for vacancy defect concentrations below ~10%.

In Figure 4-5, the increase in free energy associated with adding excess hydroxyl defects is accounted for via the formation energy (including ZPE) of those defects (Figure 4-4) plus configurational entropy of the occupied and unoccupied cation sites ($\Delta S_{config} = -R \cdot \sum x_i \ln x_i$). The energies reported are not true defect free energies, which would explicitly include additional vibrational terms associated with the materials at nonzero temperature. This approximation is justified by the similarity in the vibrational frequencies of the proton-compensated vacancy defect across the family of Fe-based materials, which will result in a cancellation of the vibrational entropy contributions to the defected-phase free energy when calculated relative to another phase with identical defect content.

Because of their similar proton-compensated vacancy defect formation energies, the relative stabilities of the hematite and goethite are practically indistinguishable across a wide range of vacancy defect concentration. This suggests that this defect type would not dramatically affect the thermodynamic driving force for phase transformation between these two materials, but may still influence the transformation process due to kinetic factors beyond the scope of this work.

Among the Fe-based materials, the relative stability of ferrihydrite responds the least strongly to the incorporation of vacancy defects due to the relatively low formation energy of the defect on sites Fe1 and Fe3 (while Figure 4-5 shows only the relative stability of ferrihydrite with defects on the energetically preferred Fe1 sites, the defect on Fe3 sites would have a similar thermodynamic effect). In the case of Al^{3+} cations, similar stability behavior is observed for the ferrihydrite isostructure, akdalaite, also due to the very low defect formation energy on the Al1 and Al3 symmetry sites.

While some phase transformation mechanisms (*e.g.*, dissolution/reprecipitation) would not be expected to preserve the defect content of the parent phase through the phase transformation, in the case of topotactic/solid state phase transformation it can reasonably be expected that some amount of defect/dopant content will be preserved through a local rearrangement of Fe and O atoms. In this scenario, the solid-state transformation of the

more defect-tolerant ferrihydrite phase may be shifted to higher transformation temperatures even at relatively low defect concentrations (<10%), due to the reduced free energy difference driving the transformation forward. Again assuming that the defect hydroxyls are trapped in the atomic lattice instead of being driven out during the transformation, the ferrihydrite/hematite or ferrihydrite/goethite phase transformations could be impeded altogether for proton-compensated cation vacancy defect concentrations of more than ~13% of available cation sites. Similar conclusions can be drawn about the Al^{3+} materials, where akdalaite containing vacancy defects on more than 15% of cation sites will be stable relative to equivalently defected diaspore.

4.5.3 OH bonds and vibrational frequencies

In this section we calculate the vibrational frequencies of the excess hydroxyl groups compared to stoichiometric hydroxyls to aid in the identification of such groups in the Fe- and Al-(oxyhydr)oxides. Experimental FTIR studies by Ruan et al. [100, 94, 121] demonstrate that excess hydroxyl groups in goethite and hematite have higher-frequency OH stretching modes, (~3400 cm^{-1}), as compared to the O-H stretching frequencies associated with the stoichiometric hydroxyls found in goethite (~3150 cm^{-1}). These higher-frequency modes have also been observed in Al-substituted goethites and hematites, increasing in intensity with increasing Al content [94, 121]. At lower temperatures and under humid or aqueous conditions, the FTIR study of the defect hydroxyl O-H stretching modes at ~3400 cm^{-1} can be complicated by the presence of similar modes associated with similar OH and H-O-H configurations associated with water molecules at the particle surface. At temperatures sufficient to evaporate surface-bound water molecules (>180-190 °C)[94], any remaining OH vibrations distinct from the stoichiometric bulk OH modes can be assigned to internally trapped excess hydroxyls, or proton-compensated cation vacancies.

The water molecules dissociated at the cation vacancy sites form hydroxyl groups in cooperation with the 6 O atoms surrounding the cation site (or 4 O atoms in the case of the tetrahedral Fe3 cation site). The arrangement of these excess/non-stoichometric

hydroxyl groups is distinct from the stoichiometric hydroxyls found in the oxyhydroxide phases. As compared to stoichiometric OH groups in goethite or lepidocrocite, the OH bonds at the defect sites are generally shorter by 0.01Å -0.03Å, while the opposing hydrogen bonds are typically longer (>1.7Å) or absent entirely, owing to the non-ideal bonding environment in which the defect hydroxyls are constrained. The shorter OH bonds lead to higher O-H stretching frequencies, as observed in the FTIR studies.

Table 4-4 shows the calculated O-H stretching modes for the stoichiometric hydroxyls in goethite, lepidocrocite and ferrihydrite, and the corresponding OH bond lengths from the relaxed structures, and hydrogen bond lengths where applicable. The corresponding data for the Al^{3+} cation materials corundum, diaspore, boehmite and akdalaite are shown in Table 3.7. The *ab initio* O-H stretch modes of the stoichiometric hydroxyls in goethite and lepidocrocite (2954 and 2634 cm^{-1}, respectively) are considerably lower than the accepted values from experimental literature [~3100-3200cm^{-1} for goethite [128, 100, 1, 129], ~2850-3160 for lepidocrocite [1]]. This discrepancy is likely in part a consequence of the tendency of GGA to slightly overestimate bond lengths and lattice parameters (*e.g.*, calculated goethite lattice parameters are approx. 1% larger than experimental values [9], thereby reducing bond stretching frequencies. Another contribution to the discrepancy is the choice to calculate OH modes by only perturbing H atoms with other atoms frozen, which was done for computational expediency. As a test, a full vibrational analysis was performed for the ferrihydrite bulk and Fe1 defect structures in which all atoms were perturbed, and the resultant O-H stretch frequencies for both structures were uniformly 3% higher than those calculated using the approximate method in which heavy atoms were held fixed.

Table 4-4: Calculated OH stretch frequencies of stoichiometric OH units (excluding hematite) and excess hydroxyls found at Fe^{3+} cation vacancy sites in hematite, goethite, lepidocrocite and ferrihydrite ('V' notation refers to the host structure in which the vacancy is found). The modes of the 3 hydroxyl units trapped at the defect cation vacancy sites are calculated as coupled modes (see Section 4.3 above). Vibrational stretching modes are compared with the OH and O—H hydrogen bond lengths in the relaxed defect structures. For goethite and lepidocrocite, the range of experimental OH stretch frequencies are shown in parentheses after the calculated values. Corresponding data for the isostructural Al^{3+} materials corundum, diaspore, boehmite and akdalaite are shown in Table 4-7.

OH group(s)	ν, OH stretch (cm^{-1})	OH bond (Å)	O---H bond (Å)	ν, OH deform (cm^{-1})		ZPE (eV/H^+)	ZPE (eV/defect)
hematite, stoichiometric	*n/a*	*n/a*	*n/a*	*n/a*	*n/a*	*n/a*	*n/a*
V-hematite ($Fe_{11}O_{18}H_3$)	3487	0.999	-	1092	902	0.633	1.900
	3170	1.013	1.867	1076	838		
	3077	1.018	1.820	996	686		
goethite, stoichiometric ($Fe_{16}O_{32}H_{16}$)	*2954 (expt. 3100-3200)*	*1.021*	*1.665*	*1024*	*993*	0.616	*n/a*
V-goethite ($Fe_{31}O_{64}H_{35}$)	3555	0.995	-	1083	799	0.634	1.903
	3466	0.999	-	959	726		
	3217	1.009	1.904	926	617		
lepidocrocite, stoichiometric ($Fe_4O_8H_4$)	*2634 (expt. 2850-3160)*	*1.038*	*1.555*	*1119*	*1114*	0.603	*n/a*
V-lepidocrocite ($Fe_{15}O_{32}H_{19}$)	*3376*	1.003	1.960	*1161*	*787*	0.628	1.884
	3288	1.007	1.932	*1001*	*736*		
	3280	1.007	1.956	*926*	*639*		
ferrihydrite, stoichiometric ($Fe_{10}O_{16}H_2$)	*3510*	*0.995*	-	*628*	*606*	0.588	*n/a*
V-fhyd1, Fe1 vacant ($Fe_9O_{16}H_5$)	3557	0.995	-	1024	859	0.630	1.889
	3373	1.003	1.977	959	747		
	3168	1.014	1.872	952	600		
V-fhyd2, Fe2 vacant ($Fe_9O_{16}H_5$)	3565	0.995	-	935	826	0.608	1.824
	3117	1.013	1.776	914	736		
	3097	1.013	1.776	849	676		
V-fhyd3, Fe3 vacant ($Fe_9O_{16}H_5$)	3634	0.990	-	950	645	0.615	1.846
	3603	0.991	-	912	592		
	3161	1.010	1.789	841	550		
water molecule (H_2O)	3806	0.985	*n/a*	1477	31	ZPE (eV/H_2O)	
	3754	0.986	*n/a*	137	72	1.150	

Absolute errors aside, the calculated O-H stretch modes of the defect hydroxyl units in lepidocrocite and goethite are all distinctly higher *relative* to those of the stoichiometric units. This result follows the trend illustrated in Figure 4-6, which demonstrates the correlation between high O-H stretch frequencies and short OH bond lengths, often found in the absence of an opposing hydrogen bond that lengthens the OH bond. The dashed line shown in each of the parts of Figure 4-6 is a linear fit of all the calculated data demonstrating the linear relationship between OH bond length d (in Å) and O-H stretch frequency ν_{OH} (cm^{-1}) across the family of materials. The equation of this fitted line is ν_{OH}= -21790d+25220, with R^2=0.987. A strong linear relationship between OH bond length and calculated O-H stretch frequency has been observed in other computational studies investigating OH modes in water clusters [130] and the modes of surface and bulk-like OH groups in a cluster model simulating the goethite (110) surface [131]. The observed slope of the wavenumber vs. OH bond-length relationship in this work (~ -218 cm^{-1}/pm) is similar to, although somewhat larger than, the values computed by Ohno *et al.* (~ -150 cm^{-1}/pm) and Rustad and Boily (~ -175 cm^{-1}/pm). The origin of these different slopes is not clear, but the range of values observed suggests that the precise linear relationship is sensitive to specific aspects of the calculations, e.g., the material, exchange-correlation function, or cluster vs. bulk computational models.

In general for lepidocrocite and goethite, other than being of higher-frequency than the stoichiometric O-H stretch modes, the O-H stretch modes calculated for the defect hydroxyls are non-uniform and depend on the specific proton configuration within the defect cation site. While the calculated vibrational frequencies are not in excellent quantitative agreement with experiment, the excess OH found at defect cation sites are shown to be qualitatively distinct from stoichiometric OH groups in terms of bond lengths and vibrational frequencies.

Unlike in goethite and lepidocrocite, the stoichiometric OH unit in ferrihydrite is unable to form an opposing hydrogen bond, and thus has a short OH bond and high O-H stretch frequency, much like the defect hydroxyls found at vacant cation sites in hematite, goethite and lepidocrocite. While the ferrihydrite stoichiometric OH unit cannot find a

suitable hydrogen bond arrangement, several defect hydroxyl units in the vacant cation sites in ferrihydrite are able to form long hydrogen bonds across the cation interstitial volume, perhaps contributing to the relative ease of forming the proton-compensated vacancy defect in this material. The trend correlating OH bond length inversely with O-H stretch frequency is maintained in the ferrihydrite calculations (Figure 4-6). The high OH stretch frequency of the stoichiometric hydroxyl in ferrihydrite overlaps with those of excess OH in the ferrihydrite structure, likely making it difficult to distinguish stoichiometric from defect hydroxyls using FTIR analysis on this material.

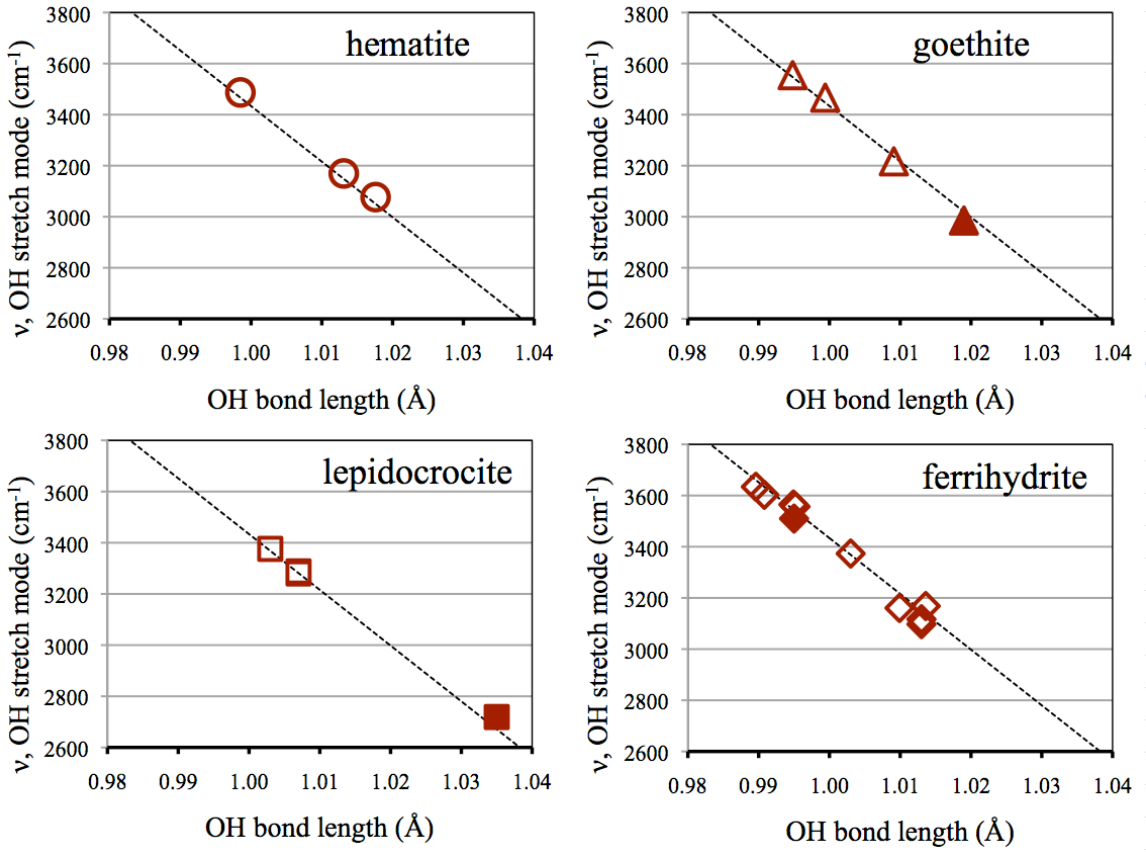

Figure 4-6: Calculated O-H stretch frequencies and OH bond lengths for stoichiometric hydroxyls (filled symbols) and excess hydroxyls trapped at vacant Fe^{3+} cation sites (open symbols). In ferrihydrite, the single stoichiometric hydroxyl site in the structure is not hydrogen bonded across O layers, and thus this hydroxyl (filled diamond) has an OH bond and stretching mode akin to the defect hydroxyls found associated with vacant cation sites. The dashed line shown is a linear fit of all the calculated data demonstrating the relationship between OH bond length d (in Å) and O-H stretch frequency, ν (cm^{-1}) across the family of materials. The equation of this fitted line is ν_{OH}=-21785.2d+25218.9, with R^2=0.987.

4.6 Al-doping and excess hydroxyl content

Experimental evidence shows that excess hydroxyl content is correlated with Al-for-Fe substitution, another common defect in natural Fe-oxides and oxyhydroxides [91, 85, 115, 116, 93, 94]. Al doping in the Fe-containing materials induces a contraction of the unit cell, arguably due to the smaller ionic radius of Al. The contraction typically follows Vegard's law, in which lattice parameters linearly shift toward the values of the Al-based isostructures as Al alloying increases. In the event of combined Al and vacancy defects, the dilatory nature of the excess hydroxyls within the cation vacancy defect counteracts the contraction induced by the Al. This phenomenon has been observed in XRD as a deviation of lattice parameters from the ideal Fe-Al Vegard relationship in experimental samples containing both Al and excess OH [116].

To investigate the interaction of Al dopants and proton-compensated cation vacancy defects, the vacancy defect geometries were calculated again with the substitution of Al atoms on Fe sites near the cation vacancy. Where multiple symmetry-distinct Fe sites were found near the vacancy defect, each symmetry-distinct Al substitution site was calculated separately, and the most stable values are reported here. The interaction effects are assessed by comparing energies and geometries of these tandem-defect calculations to the isolated vacancy defect calculations described in Section 4 and the energies of isolated, dilute Al substitutions in the Fe-based materials (Table 4-6), which are described in detail in a forthcoming study. [74].

Figure 4-7 shows the defect formation energies of the coupled Al-vacancy defect calculations. The first/left set of columns are the summation of the isolated defect formation energies – the lower section being the dilute impurity energy of an isolated Al dopant, and the upper section being the formation energy of the proton-compensated vacancy, or excess hydroxyl defect (not including ZPE, as vibrational frequencies of the coupled Al-vacancy defect were not calculated separately). It should be noted that all Al substitutions in the ferrihydrite structure calculations for coupled Al-vacancy defects are

at the Fe1 symmetry site, whereas the notation on the x-axis refers to the location of the vacancy defect. Other Al-vacancy couplings in ferrihydrite (*e.g.*, vacancy on site Fe1, Al on site Fe2) were calculated as well, but were higher in overall defect formation energy (see Table 4-5), mainly due to the high substitution energy of Al dopants on the ferrihydrite Fe2 and Fe3 sites.

The Al-dopants and proton-compensated vacancies display weak but attractive couplings (negative interaction energies) for each of the Fe-materials studied, with the exception of lepidocrocite, where the coupling is very weakly repulsive. One possible explanation for the favorable coupling of Al-dopants with nearby excess hydroxyl content is that Al binds OH more strongly, having a smaller ionic radius for the same 3+ charge [85]. The stronger nature of the Al-OH bond is also empirically evident in the relative stability range of the Al-oxides and oxyhydroxides. Unlike the Fe-oxides and oxyhydroxides, where the oxide hematite is the stable bulk phase under hydrous conditions, the Al-(oxy)hydroxide phases (*e.g.,* gibbsite, boehmite, diaspore - the main components of bauxite) are significantly more stable than the oxide phases (*e.g.,* corundum) [70].

The favorable energetics of the coupled Al and excess hydroxyl defects might also be explained by observing the opposing volumetric effects of the two defect types. The dilatation of the lattice induced by the excess OH defect is countered by the contraction induced by Al substitution, resulting in reduced lattice strain when the defects are found in close proximity (Figure 4-8). For hematite, goethite, and ferrihydrite, coupled Al-substitution and cation vacancy defects show very low defect formation volume, defined as the difference in supercell volume of the fully-relaxed defected cell and the fully relaxed undefected cell. In all cases except lepidocrocite, the formation volume of the coupled Al-vacancy defect is roughly the sum of the formation volumes of the Al and vacancy defects found in isolation. The nonconforming volumetric behavior of lepidocrocite in this instance is likely attributable to the layered structure of lepidocrocite, in which the layers are joined by relatively compliant hydrogen bonds that more easily accommodate the local expansion induced by the proton compensated cation vacancy defect.

Table 4-5: Calculation details and analysis for combined Al-dopant and excess hydroxyl vacancy ('V') defects. The second to last column gives the defect-defect interaction energies, given as the coupled defect formation energy minus the DFE's of the defects in isolation (see Tables 4-2 and 4-6). The coupled Al-V defects show negative interaction energies, indicating an attractive coupling between two defects that co-stabilize each other. The moderate formation volumes of the combined defects are attributable to the opposite volumetric effects of the two defect types – Al contracts the Fe-oxide/oxyhydroxide lattice, while the excess hydroxyl defects are dilatory (Figure 4-8).

Isostructure	Simulation Stoichiometry	Total Energy (eV)	Supercell Size	kpoint Mesh	Relaxed Cell Parameters (Å)			cell volume (Å^3)	*Vac-Al interaction energy (eV/V)*	*Combined Vac-Al defect formation energy (eV)*
					a	*b*	*c*			
V-Al-hematite	$Fe_{10}Al_1O_{18}H_3$	-216.8749	1×1×1	662G	5.10	5.07	13.91	311.86	-0.06	1.14
V-Al-goethite	$Fe_{30}Al_1O_{64}H_{35}$	-807.8983	1×4×2	323M	10.01	12.18	9.27	1130.26	-0.12	0.86
V-Al-lepidocrocite	$Fe_{22}Al_1O_{48}H_{27}$	-603.9757	3×1×2	324M	9.23	12.45	7.85	902.91	0.01	0.72
V-Al-fhyd, Fe1 site	$Fe_{38}Al_1O_{16}H_5$ (Al1)	-770.6285	2×2×1	334G	11.95	11.90	9.41	1158.73	-0.05	0.32
V-Al-fhyd, Fe1 site	$Fe_{38}Al_1O_{16}H_5$ (Al2)	-770.3397	2×2×1	334G	11.95	11.90	9.39	1156.52	-0.25	0.61
V-Al-fhyd, Fe1 site	$Fe_{38}Al_1O_{16}H_5$ (Al3)	-770.4607	2×2×1	334G	11.94	11.89	9.41	1158.31	-0.19	0.49
V-Al-fhyd, Fe2 site	$Fe_{38}Al_1O_{16}H_5$ (Al1)	-770.1992	2×2×1	334G	11.96	11.96	9.34	1157.54	-0.16	0.75
V-Al-fhyd, Fe3 site	$Fe_{38}Al_1O_{16}H_5$ (Al1)	-770.5843	2×2×1	334G	11.96	11.96	9.34	1156.77	-0.07	0.37

Figure 4-7: The summed formation energies of isolated Al-dopants and isolated proton-compensated cation vacancies in the Fe-oxyhydroxide materials studied (stacked, light blue, leftmost columns) are larger than the formation energy of the defects when placed on neighboring cation sites in the same simulation cell (medium blue center columns). Thus Al-dopants and proton compensated vacancies show weak but attractive interactions between these two defect types (dark blue, rightmost columns). In ferrihydrite, all Al-substitutions were performed on the Fe1 symmetry site, as this site has the lowest energetic cost for Al-substitution (Table 4-6). The left-hand columns are shown as stacked bars – the vacancy defect formation energy is added above the Al-dopant defect formation energy to show the sum of the two defect formation energies. None of the energies represented in this figure include ZPE in the defect formation energy, as vibrational frequencies were not calculated separately for the coupled Al-vacancy defect cells.

Table 4-6: Calculation details for isolated Al dopants on Fe cation sites in the Fe-oxide, hematite, and Fe-(oxyhydr)oxides. The second-to-last column gives the dilute impurity energy, which is effectively the defect formation energy of the isolated Al dopant, and is equivalent to the enthalpy of mixing of Al on the Fe lattice when using isostructural Fe/Al end members as reference states for the thermodynamic calculation (e.g. goethite and diaspore). Refer to Tables 4-2 and 4-4 for the pure-Fe and pure-Al end member energies needed to compute the dilute impurity energy.

Isostructure	Simulation Stoichiometry	Al dopant content (%)	Total Energy (eV)	Supercell Size	kpoint Mesh	Relaxed Cell Parameters (Å)			Cell Volume (Å^3)	*Dilute Impurity Energy (eV/Al)*
						a	*b*	*c*		
Al-hematite	$Fe_{47}Al_1O_{72}$	2.1%	-852.6803	2×2×1	443G	10.16	10.16	13.92	1243.39	0.36
Al-goethite	$Fe_{31}Al_1O_{64}H_{32}$	3.1%	-804.6745	1×4×2	323M	9.24	10.02	12.17	1127.23	0.19
Al-lepidocrocite	$Fe_{23}Al_1O_{48}H_{24}$	4.2%	-600.5537	3×1×2	324M	9.24	12.48	7.84	904.65	0.11
Al-fhyd, Fe1 site	$Fe_{39}Al_1O_{64}H_8$	2.5%	-766.7740	2×2×1	334G	11.92	11.92	9.36	1151.84	0.12
Al-fhyd, Fe2 site	$Fe_{39}Al_1O_{64}H_8$	2.5%	-766.2852	2×2×1	334G	11.93	11.93	9.35	1152.15	0.60
Al-fhyd, Fe3 site	$Fe_{39}Al_1O_{64}H_8$	2.5%	-766.4657	2×2×1	334G	11.92	11.92	9.37	1153.09	0.42

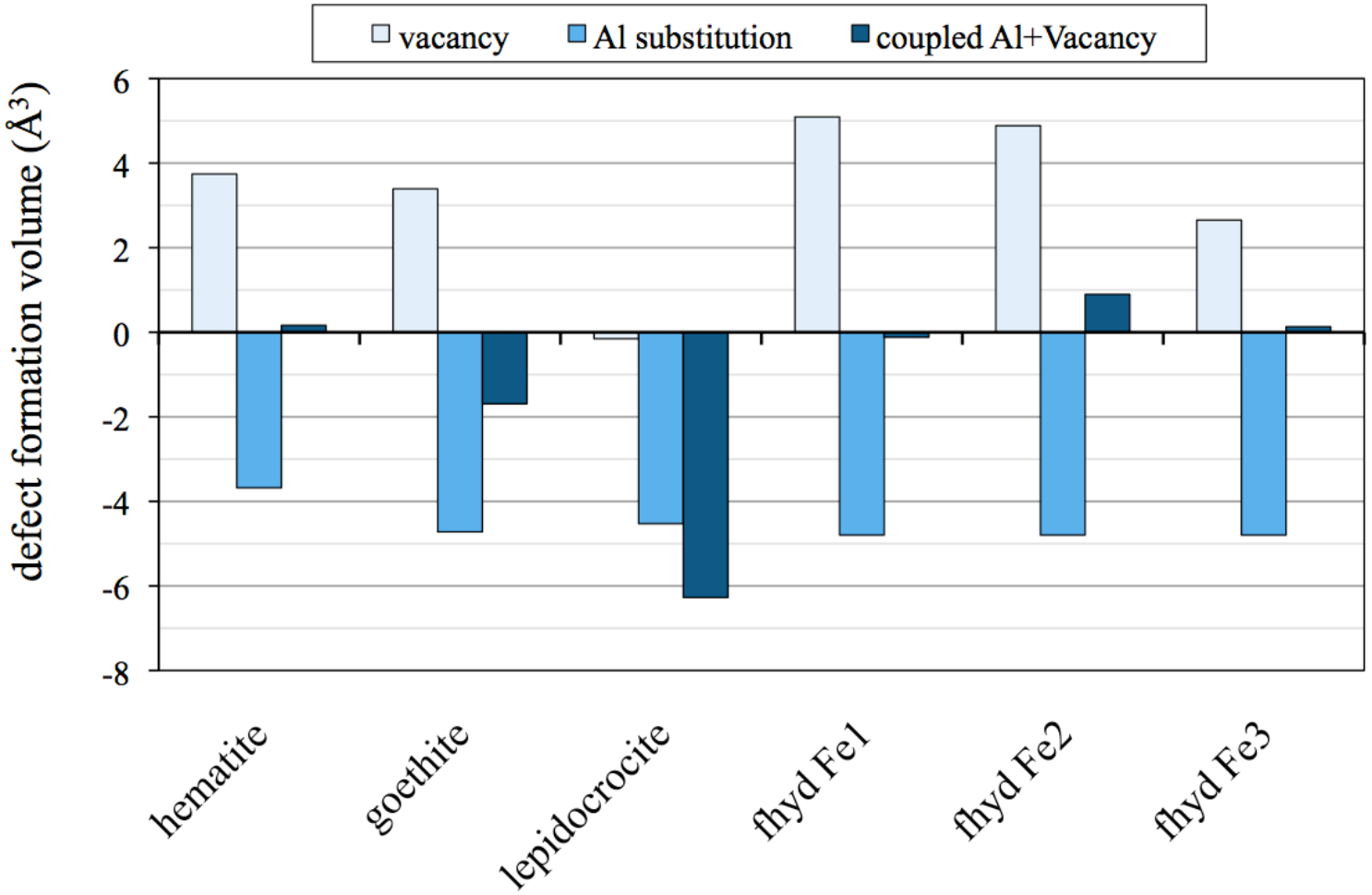

Figure 4-8: Defect formation volumes of proton-compensated cation vacancies (left columns, light blue), isolated Al-substitutions (center columns, medium blue), and coupled Al-vacancy defects in close proximity (right columns, dark blue). The opposing volumetric effects of the Al-substitution (contraction) and cation vacancy defects (dilation) act to minimize the formation volume of the coupled defect. With the exception of lepidocrocite, the formation volumes of the coupled Al-vacancy defects are nearly zero, inducing little lattice strain on the surrounding Fe-oxide or oxyhydroxide structure.

Table 3.7: Calculated OH stretch frequencies of stoichiometric OH units (excluding corundum) and excess hydroxyls found at Al^{3+} cation vacancy sites in corundum, diaspore, boehmite, and akdalaite ('V' notation refers to the host structure in which the vacancy is found). The modes of the 3 hydroxyl units trapped at the defect cation vacancy sites are calculated as coupled modes (see Section 4.3 in the above text).

OH group(s)	ν, OH stretch (cm^{-1})	OH bond (Å)	O---H bond (Å)	ν, OH deform (cm^{-1})		ZPE (eV/H^+)	ZPE (eV/defect)
corundum stoichiometric	*n/a*	*n/a*	*n/a*	*n/a*	*n/a*	*n/a*	*n/a*
V-corundum ($Al_{11}O_{18}H_3$)	3374	1.003	-	1271	1014	0.637	1.912
	2848	1.030	1.700	1233	970		
	2811	1.030	1.719	1136	762		
diaspore stoichiometric ($Al_{16}O_{32}H_{16}$)	*2761*	*1.034*	*1.578*	*1173*	*1099*	0.624	*n/a*
V-diaspore ($Al_{15}O_{32}H_{19}$)	3586	0.993	-	1042	778	0.645	1.934
	3541	0.994	-	1011	745		
	3408	1.002	-	860	629		
boehmite stoichiometric ($Al_{16}O_{32}H_{16}$)	*2818*	*1.029*	*1.580*	*1158*	*1116*	0.631	*n/a*
V-boehmite ($Al_{15}O_{32}H_{19}$)	*3406*	1.002	-	1339	813	0.635	1.904
	3354	1.004	-	1100	727		
	3003	1.022	1.824	996	616		
akdalaite stoichiometric ($Al_{10}O_{16}H_2$)	*3357*	*1.003*	-	*766*	*743*	0.603	*n/a*
V-akdal1, Al1 vacant ($Al_9O_{16}H_5$)	3528	0.997	-	1193	838	0.644	1.933
	3494	0.995	-	1079	725		
	3322	1.006	-	905	508		
V-akdal2, Al2 vacant ($Al_9O_{16}H_5$)	3590	0.992	-	1027	892	0.636	1.909
	3279	1.004	1.842	1005	796		
	3187	1.008	1.779	965	659		
V-akdal2, Al2 vacant ($Al_9O_{16}H_5$)	3662	0.987	-	997	703	0.000	0.000
	3499	0.993	1.865	971	618		
	3370	0.999	1.864	945	567		

4.7 Conclusions

We have presented an *ab initio* study of proton-compensated cation vacancies in the common Fe- and Al-oxide/oxyhydroxides. This defect type can be equivalently referred to as a form of structurally bound water, or excess hydroxyl content, and is alternatively known as a Ruetschi or hydrogarnet defect in other materials. The formation of the proton-compensated cation vacancy defect can be written as a hydration reaction involving only the pure oxide or oxyhydroxide material and water, ostensibly occurring during rapid precipitation where chemisorbed water at the mineral surface is subsumed by the mineral precipitating around it. The structurally bound water found in this specific defect type is dissociated, forming hydroxyl groups around the vacant cation site. It should be noted that other types of structurally bound water may occur as well, including molecular water found in larger voids within the crystal structure, but in this study we have considered only that associated with a single cation vacancy.

Ab initio simulation results show that the proton-compensated cation vacancy defect destabilizes each of the common minerals hematite, goethite, lepidocrocite, and ferrihydrite to varying degrees, with the destabilization effect being largest for hematite and smallest for two of the three Fe symmetry sites within ferrihydrite, assuming the three-site Michel model of the ferrihydrite crystal structure as the undefected bulk structure of ferrihydrite. Formation energies of the proton-compensated cation vacancy in the isostructural Al-oxide/oxyhydroxides parallel those of the Fe-based isostructures. While experimental literature does not commonly discuss excess OH defects in Al-(oxyhydr)oxides, they are found in small concentrations in corundum, and should be expected to form during the precipitation of Al-(oxyhydr)oxides via similar mechanisms to those occurring during the precipitation of Fe-(oxyhydr)oxides. The varying formation energies of the cation vacancy defect across the family of Fe-oxide/oxyhydroxides can have a significant impact on the relative stability among phases. If the trapped hydroxyls at vacancy defects are assumed to be transferred to the product material during a phase transformation, as is suggested by experimental evidence, the presence of even a few percent cation vacancies, for example in ferrihydrite, could shift the relative phase

stabilities of the materials to the extent that phase transformations would occur at higher temperatures than for undefected materials, due to the reduced thermodynamic driving force for transformation. For higher vacancy concentrations (~>10% of Fe sites) the transformations could be impeded altogether (*e.g.,* ferrihydrite-to-hematite transformation). The impact of proton-compensated cation vacancy defects on relative stability parallels that of Al-dopants in the Fe-oxide and oxyhydroxides materials, in that both defect types are more easily formed (lower formation energies) in the phases that are metastable in the bulk. Ferrihydrite, in particular among the Fe-based materials studied, is the most tolerant of both proton-compensated cation vacancies and Al-dopants. This trend can be rationalized from the perspective that defect formation is easier in less stable phases, due to the lower cohesive energies of the bulk phase. Such an argument underlies the Ostwald Step Rule, which states that less stable phases precipitate form solution first due to their lower surface and structural energies. Cation vacancy and Al substitution defects, like surfaces, disrupt the structure, and this disruption is better tolerated in less stable structures.

From the literature, the presence of proton-compensated cation vacancies in the Fe-oxides/oxyhydroxides has been observed to occur in tandem with Al substitution. Calculations show that, as compared with isolated Al-substitutions and isolated cation vacancy defects, coupled Al+ proton-compensated cation vacancy defects in hematite, goethite, lepidocrocite and ferrihydrite show negative (exothermic) interaction energies, and are thus co-stabilizing when placed in close proximity. The two defect types have opposite volumetric effects and thus work to cancel out the lattice strain induced by each defect when found in isolation.

FTIR studies suggest that non-stoichiometric OH groups in defective, nanocrystalline Fe-oxides and oxyhydroxides have higher O-H stretching frequencies due to inadequate bonding environments, specifically the inability to form an opposing hydrogen bond. These elevated O-H stretch frequencies can be attributed to surface OH groups, or to defective OH groups within the bulk of the material, ostensibly at vacant cation sites.

The stretching modes of both the stoichiometric and defective OH groups were calculated for goethite, lepidocrocite, and ferrihydrite, and the defective OH modes calculated for hematite (which, being an oxide, has no stoichiometric OH groups). While calculated O-H stretch frequencies are considerably lower than experimental references for the stoichiometric OH groups in goethite and lepidocrocite, the calculated defective O-H modes in both materials are uniformly higher than the calculated modes of stoichiometric OH, in agreement with the hypothesis that assigns observed elevated O-H modes to defective OH groups that lack proper hydrogen bonding. In ferrihydrite, due to the limited hydrogen bonding possible for the stoichiometric OH group, the O-H stretch frequencies are often quite similar for both stoichiometric and excess OH species in this material. This result has important implications for interpreting FTIR data on ferrihydrite as the stoichiometric and excess OH groups cannot be distinguished as easily as for goethite and lepidocrocite. OH groups are not present in undefected hematite, thus any modes in the typical range for OH stretch/bend modes should be assigned to either OH groups at the surface, water or OH within structural voids, or in cation-vacancy defects as described in this work.

We present these results to aid in the interpretation of phase stability, phase transformation behavior and reactivity observations involving natural and synthetic Fe-oxides and oxyhydroxides. As these materials are typically poorly crystalline, nano-sized, and often contain cation dopants (especially Al^{3+}), it is important to better understand the nature of intrinsic defects and their impact on phase stability, as well as their interaction with extrinsic defects like cation dopants.

5 *Ab initio* study of Li+ adsorption on the goethite (101) Surface

5.1 Chapter Abstract:

Density Functional Theory simulations of Li^+ adsorption on the goethite (101) surface are used to determine low energy surface binding configurations. Simulations are performed with charge states that approximate solution conditions at intermediate pH near the goethite PZC and at high pH. Surface slab simulations of deprotonation reactions of surface hydroxyl groups are used to test and validate a charge correction scheme that allows for the calculation of relative configurational energies of adsorbates and solvation layer(s) at a charged slab surface. Bulk supercell simulations are also used to evaluate the local structure of the Li^+ within goethite tunnels to complement surface structure observations and support interpretation of NMR data. Relative energies and bond arrangements of the calculated Li^+ sorption configurations and bulk substitutions are shown to be consistent site assignments based on NMR observations reported in the literature.

5.2 Introduction

Fe-(oxyhydr)oxide materials are common, naturally occurring minerals in soils and sediments, and are often in direct contact with ground and surface water systems where they play an important role in the transport and geochemical fate of a variety of chemical species of environmental interest. Via aqueous surface sorption processes, Fe-(oxyhydr)oxide materials can regulate and/or remediate aqueous contaminants including metal cations (e.g., Pb^{2+}, Cd^{2+}, Zn^{2+}, U^{6+}, among others) and oxyanions (AsO_4^{3-}, AsO_3^{3-}, PO_4^{3-}, SO_2^{4-},CrO_4^{2-}, among others) from both natural and anthropogenic sources [1]. The high specific surface areas of typical nanoparticulate Fe-oxyhydroxides make them particularly effective sorbents on a per-volume basis [2]. Sorption processes can be reversed by desorption or dissolution as solution conditions change, or can alternatively lead to more-permanent co-precipitation and/or structural incorporation of the contaminant species within the Fe-(oxyhydr)oxide mineral structure. In addition to solution conditions like temperature and pH, these sorption processes are dependent on the molecular structures of the sorbent mineral surfaces, which are in turn closely connected to the bulk crystal structure of the mineral materials.

Characterization of the structure and reactivity of Fe-(oxyhydr)oxide surfaces is an ongoing research challenge, with particular challenges arising in cases where the sorbent materials are nanoparticulate and often highly defected (e.g., ferrihydrite). Better-characterized Fe-(oxyhydr)oxide minerals and mineral surfaces (e.g. those of crystalline goethite or hematite), while still challenging in their own right, can serve as model systems for experimental and theoretical techniques that seek to extend surface characterization capabilities to more-complex mineral materials [107]. Many sorbate species of environmental interest are polyatomic and variably speciated/protonated in solution over typical pH ranges, making their sorption physics very complex, often involving multiple sorption configurations including outer- and inner-sphere bindings and multi-dentate complexes. Monatomic cation sorbates (e.g., Li^+, Na^+, Ag^+) have more consistent aqueous speciation and can be used as model surface probes to aid in surface characterization, especially where these species are well suited for experimental methods

to describe surface and binding structure (e.g., NMR, EXAFS) [132, 133]. Where experimental challenges remain, theoretical methods, including semi-empirical methods [e.g., the CD-MUSIC model [134-136, 106]] and fully *ab initio* methods (e.g., Density Functional Theory study) [137-140], can provide additional insight and aid in the interpretation of experimental data.

As a general description, in solution conditions where pH is less than ~7, Fe-oxyhydroxide mineral surfaces have appreciable positive charge, being occupied by protons forming –OH or $–OH_2$ terminal groups at the mineral surface. In this regime, adsorption of cations is deterred by both electrostatic forces that repel positively charged ions and by crowding effects that limit the number of potential binding sites for sorbates. At intermediate pH levels near the point-of-zero-charge (goethite PZC is approximately 9), hydroxyl groups at the goethite surface begin to deprotonate and cation solutes begin to adsorb, binding to the -O groups newly exposed at the surface. At high pH, further deprotonation of the mineral surface results in a negative surface charge and a broader availability of binding sites for the sorption of cations.

This work performs *ab initio* simulations for comparison with the conclusions of two studies of Li^+ sorption and intercalation in the Fe-oxyhydroxides goethite and lepidocrocite [132, 133]. These studies base their conclusions primarily on solid-state NMR techniques that measure ^6Li Fermi contact shifts for Li^+ sorbed at the goethite and lepidocrocite particle surfaces, as well as intercalated within the bulk of the materials. Li^+ was chosen as a model monatomic sorbate due to its suitability for study with NMR methods and the significant amount of extant literature describing ^6Li and ^7Li NMR measurements in paramagnetic materials associated with battery technology that are similar to goethite.

The Fermi contact (or hyperfine) shift mechanism involves the transfer of unpaired d^5 spin density from the Fe^{3+} cation to the Li^+ sorbate via a Li-O-Fe linkage, thereby inducing a shift in the nuclear magnetic resonance frequency of ^6Li when bonded to Fe-O materials. When multidentate binding configurations involve two or more Li-O-Fe

linkages, each linkage path contributes a resonance shift of approximately equivalent magnitude, and as such the Fermi contact shifts are effectively additive. In principle, Fermi contact shifts associated with linkages having different bond lengths and angles might be expected to have different Fermi contact shift values, due to the different configurations of Fe^{3+} 3*d*-orbital overlap for different bond configurations. In the case of Li-O-Me^{N+} linkages in materials where Fermi contact shifts have been measured, positive/additive shifts of similar magnitude are observed for Li-O-Mn^{4+} linkages with angles around 90° associated with partially-filled t_{2g} orbitals, and for Li-O-Ni^{2+} linkages with angles around 180° associated with partially-filled e_g orbitals [141, 142, 133]. Both of these orbital linkage configurations should be qualitatively replicated by Li-O-Fe^{3+} structures formed in goethite and related Fe-oxyhydroxides (e.g. lepidocrocite), based on the octahedral coordination and high-spin state of the Fe^{3+} cation, which splits the Fe^{3+} *d*-electrons into the $t_{2g}^3e_g^2$ configuration. By examining the Fermi contact shifts for various Li-O-Fe linkage configurations in bulk materials and at surface sites, an approximate ppm-shift value per Li-O-Fe linkage is inferred for linkages of similar bond chemistry and topology.

The work of [132] reports aggregate ^{6}Li resonance shifts of 55 ppm for Li^+ sorbed on the surface of goethite particles at intermediate, and 140 ppm at high pH, reflecting at least two distinct Li-O-Fe binding configurations, with the latter site have significantly larger number of Li-O-Fe linkages than the former. Goethite where bulk H^+ have been exchanged for Li^+ via solution processes, referred to as Li-intercalated goethite [132] or goethite-like $LiFeO_2$ [143], shows an even larger shift value of 289 ppm, this higher value likely reflecting the greater number of Li-O-Fe linkages available in multiple directions within the tunnels of the bulk goethite structure. The precise number of Li-O-Fe linkages per Li^+ within goethite-like $LiFeO_2$ is dependent on the specific position assumed by Li^+ within the goethite tunnels and is discussed further in Section 3.3.

Further NMR study detailed in [133] explores ^{7}Li resonance shifts in lepidocrocite and offers geometrical interpretation of the likely binding sites of Li^+ on the lepidocrocite and goethite surfaces and within Li-intercalated bulk compounds. This interpretation suggests

a bidentate inner-sphere configuration of Li^+ on the predominant (101) surface at intermediate pH, in which the sorbed Li^+ bridges two neighboring singly-coordinated $Fe_1O_{II}H$ or Fe_1O_{II} groups (the protonation state is undetermined). At higher pH levels (pH 11 and above) where significant surface deprotonation can be expected, Kim et al. suggest that Li^+ adopts a multi-dentate binding configuration that preserves the Li-O linkages formed at lower pH while also binding to one or more neighboring Fe_3O_{II} groups [132, 133]. Kim et al. conclude that Li-O-Fe linkages contribute an effective shift between 20-30 ppm. A later NMR study of a similar Li^+ sorption phenomena on akaganeite, a metastable FeOOH polymorph assign a per-linkage shift value of 15 ppm to the Li-O-Fe configurations in that material, suggesting that the range of shift values for Li-O-Fe linkages may be more variable than had been determined from the goethite and lepidocrocite studies alone [144].

In this study we model the sorption of single Li^+ ions on the goethite (101) surface using a periodic slab geometry to represent the mineral surface. The speciation of the (101) surface is adjusted (namely, deprotonated) to simulate the effects of changing pH and surface charge on the geometry and energetics of Li^+ sorption at the mineral surface. We also consider the formation of Li-intercalation defects within the bulk of the goethite matrix, as well as a bulk phase of goethite-like $LiFeO_2$ in which all H^+ have been replaced with Li^+. These bulk-phase and point-defect calculations aid in interpretation of NMR Fermi contact shift data for Li-intercalated goethite and provide additional perspective on the binding habits of Li^+ in and on Fe-oxyhydroxide materials. We also examine the stability of protonation sites in goethite to validate the modeling approaches used to study the Li+ sorption.

Ab initio computations of Fermi contact shifts for Li^+ binding configurations are possible with recently developed techniques [145] but are not pursued here. This study instead focuses on energy criteria for binding and seeks to determine the lowest-energy binding sites and configurations for Li^+ on goethite as a function of pH and surface charge/protonation state.

This work also does not seek to establish absolute adsorption or desorption energies for either Li^+ or H^+ at the mineral surface. Such quantities are quite challenging to obtain using existing computational methods due to the difficulty of establishing suitable thermodynamic reference states for solvated ions away from the mineral surface [although these values can be fit to experiments [146]], in addition to the complications arising from surface charge physics within periodic boundary conditions (Section 5.3.2.3). While computational approaches have been developed to address these challenges [147, 148, 138, 140, 149], such studies are not the focus of this work.

5.3 Materials and Techniques

5.3.1 Surface Chemistry Details

Goethite (α-FeOOH) is chosen as the model Fe-oxyhydroxide sorbent due to the relatively large amount of literature available that characterizes the structure and reactivity of the surfaces of this material. The goethite (101) surface [Pnma space group setting [1]] is selected as the surface of interest, as this surface comprises approximately 90% of the surface area of typical goethite nano- and micro-particles, and also contains a variety of reactive surface OH sites suitable for binding of sorbate species [135]. As most of the surface reactions of environmental interest occur in aqueous or humid environments, the goethite surface will be examined with the inclusion of surface hydration, including both chemisorbed/dissociated water molecules and physisorbed/solvating water molecules.

For Li^+ sorption at the goethite (101) surface, two effective pH regimes are examined: intermediate pH (approx. pH 8-9) and high pH (approx. pH 11-12), corresponding to near-neutral and negatively-charged mineral surfaces. The structure and protonation of surface oxo- and hydroxo- groups in the two pH regimes was guided by the MUSIC model [134, 105] that establishes site-specific acid dissociation constants (pK_a) for the variously-coordinated OH sites that comprise the goethite (101) surface (Figure 1-1, upper surface). The deprotonation reactions that lead to the determination of site pK_a values are also simulated within the *ab initio* periodic slab framework and compared with

experimental and theoretical benchmarks to ensure that the surface protonation conditions chosen for the modeling of Li^+ sorption were reasonable.

The naming conventions for the OH surface groups established in the MUSIC literature were adopted for this study, with minor modifications [150]. In this scheme, surface OH groups are labeled according to the number of Fe-O bonds anchoring the OH group, and the oxygen atoms are labeled according which of the two symmetry sites they would occupy in bulk goethite (O_I and O_{II}) [151]. For example, the site labeled $Fe_{3b}O_IH$ is the triply-coordinated surface OH group which contains an O_I atom. Two of the triply-coordinated sites shown in Figure 1-1, $Fe_{3a}O_IH$ and $Fe_{3b}O_IH$, are labeled as distinct OH sites at the surface despite being symmetrically-equivalent if considered within the bulk. It is not clear whether the latter of these two sites, $Fe_{3b}O_IH$, should be considered a true surface OH site, as this site retains the same hydrogen bond coordination as it would within the bulk. While the $Fe_{3b}O_IH$ site is not usually treated separately in the MUSIC or bond-valence literature [152], it is structurally distinct from the $Fe_{3a}O_IH$ site at the (101) surface and should therefore have distinct electrostatic and binding properties. Additionally the $Fe_{3b}O_IH$ site is proposed as a potential Li^+ binding site at high pH in the aforementioned NMR studies [132, 133], thus it is investigated as a sorption site in this study. In each pH regime, the model Li^+ sorbate ion was modeled in a variety of positions, with a variety of local protonation arrangements, intended to span the range of possible binding configurations on the slab surface.

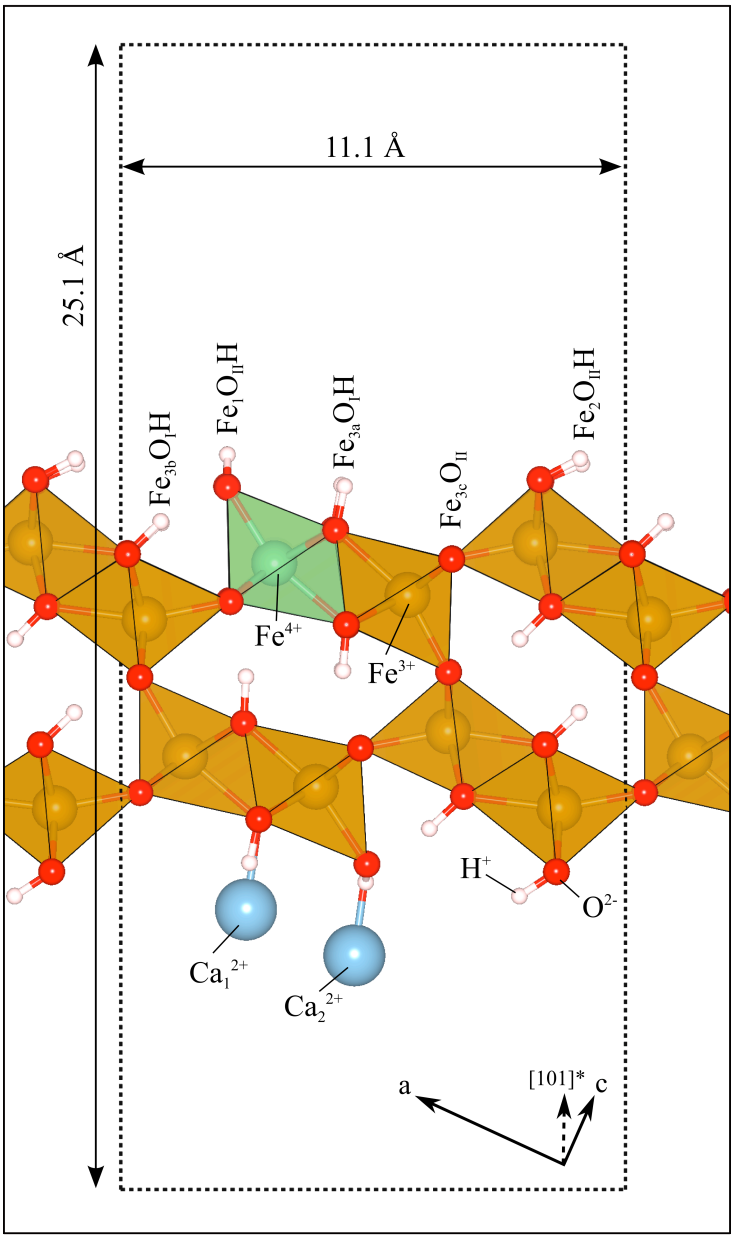

Figure 5-1: The goethite (101) slab surface model consists of two layers of goethite 'double-chains' along the [101] direction. The periodic boundary of the slab supercell is shown as a narrow dashed line. The primitive unit cell of goethite is outlined with a wide dashed line. Hydroxyl groups on the top, active surface of the slab are labeled according to the naming conventions typical in goethite surface literature. Two charge-correction mechanisms employed to simulate the high pH (101) surface are illustrated. In the first scheme, an Fe^{4+} cation is formed near the top surface due to the removal of one electron from the slab system to neutralize the negative charge caused by deprotonation of OH groups at the (101) surface. In the second scheme, a Ca atom is placed on the lower slab surface at positions where H^+ would otherwise bond. Illustrated are the two separate Ca positions chosen (modeled independently, but illustrated together for comparison). During simulation, these Ca ionize to Ca^{2+}, effectively donating an electron to the top slab surface to recreate the desired local negative surface charge induced by deprotonation. Details of the charge-correction schemes are described in Section 5.3.2.3.

5.3.2 *Ab-initio* Simulation Details

5.3.2.1 Computational Methods

The Density Functional Theory (DFT) simulations reported in this study were performed with the periodic, plane-wave based Vienna Ab-initio Simulation Package (VASP) [6, 153, 7, 8] employing the projector-augmented wave (PAW) method [23, 24]. The atomistic simulation geometries constructed to model reactions at the goethite (101) surface were fully periodic slabs, described in Section 5.3.2.2. Electron exchange and correlation were treated using the generalized gradient approximation (GGA) as formulated by Perdew, Burke, and Ernerhof (PBE) [25]. Standard GGA functionals were used to describe all atoms except Fe. As is common for oxide and oxyhydroxide materials containing Fe^{3+} cations, the GGA+U method was applied to Fe *3d* electrons to account for the demonstrated failure of standard GGA to capture coulomb and exchange interactions within these localized orbitals [26]. The GGA+U implementation of Dudarev [30] was chosen, in which a single effective parameter, $U_{effective}$=U-J, is used to perform the correction. In this implementation, U is the rotationally-invariant Hubbard parameter that describes the coulomb interaction between 3d electrons, while J represents the screened exchange energy between these electrons. U and J were set at 4.0 and 1.0 eV, respectively, for Fe *3d* electrons in all simulations, in keeping with previous GGA+U simulation studies that demonstrate optimal agreement with experimental lattice parameters, bond lengths, redox and formation energies, and magnetic properties for $U_{effective}$=U-J values near ~3-4 eV [27, 28, 31, 9]. All other Fe electron orbitals were treated with standard GGA, or equivalently $U_{effective}$=0.0 eV.

VASP-supplied pseudopotentials were employed for all atoms. The *Fe_pv* pseudopotential was chosen for Fe, which explicitly treats *3p* electrons as part of the valence shell with configuration [core]$3p^6 3d^7 4s^1$. Similarly for Ca atoms, which are used in one of the charge correction methods described in Section 5.3.2.3, the *Ca_pv* pseudopotential was chosen which treats Ca *3p* electrons as part of the valence shell with configuration [core]$3p^6 3s^2$. H, O, and Li electron configurations were $1s^1$, [core]$2s^2 2p^4$, and [core]$2s^1 2p^0$, respectively, and these atoms were simulated using default standard

pseudopotentials.

All calculations were performed with spin-polarization. Magnetic moments on Fe atoms were initialized in the antiferromagnetic ordering of low-temperature bulk goethite with spin values of ±5 μ_B. All other atoms were assigned zero magnetic moment, and spins were allowed to relax during energy minimization. In all simulations except for the series in which an electron was removed from the slab supercell for the purposes of charge-neutralization (Section 5.3.2.3), the antiferromagnetic ordering of bulk goethite was preserved throughout the calculations and the net magnetic moment of the supercell remained zero. For those cases where an electron was removed from the supercell, one of the surface Fe atoms was observed to transition to a spin value of ±4 μ_B, resulting in a net magnetic moment of ±1 μ_B for the supercell as a whole.

In order to explore a wide range of surface configurations, including Li^+ and H^+ binding permutations at the (101) surface, as well as water molecule rearrangements within the solvation layer, *ab initio* molecular dynamics (AIMD) simulations were performed on all starting geometries for protonation and Li^+ sorption configurations using 2-layer slabs (see Section 5.3.2.2 for geometry details). In these simulations, the atomic positions of the lower half of the goethite slab were held fixed to bulk-like positions, while the positions of the upper half of the slab, surface OH groups, Li^+ sorbate, and solvation layer water molecules were allowed to rotate and translate to explore the configurational space (see Section 5.3.2.2 for detailed description of atomic geometries). Although 5-layer slabs are used for a subset of the calculations to better represent a bulk-like surface substrate (see Section 5.3.2.2) AIMD simulations were performed on only the two layer slabs due to computational resource limitations. The optimal surface geometries of the 2-layer slabs obtained in the AIMD simulations were then translated onto equivalent positions in 5-layer slab supercells, and relaxations of the 5-layer slab geometries were then performed separately.

For AIMD simulations, a T=10 K thermostat was applied throughout the simulation for 1000 timesteps of 1.0 fs duration each (1.0 ps total simulation duration). This timestep

value is roughly $1/10^{th}$ the duration of period of the fastest atomic vibrations expected in the system, which are the asymmetric stretching modes of the solvating water molecules, with frequencies near 100 THz (period =10 fs). Even at this low temperature, significant re-ordering of the surface water molecules was observed during the AIMD simulations, as well as translation of the Li^+ sorbate from initial binding site placements to other, more stable sites. After the AIMD simulations were complete, the atomic configuration with lowest potential energy from each AIMD simulation run was extracted and re-relaxed at T=0 K. During these static relaxations little significant atomic relaxation was observed. The collection of energies from these static optimizations of various surface configurations form the basis for the conclusions reported in this work.

AIMD simulations at higher temperature (T=100 K, 300 K) were also performed with the same timestep and simulation duration as those performed at T=10 K, but the higher level of thermal energy often caused water molecules in the solvation layer to unpredictably separate from the mineral surface, forming solvation configurations that varied in energy by a much greater degree than those simulations performed at T=10 K, and with energy variance larger than the physical phenomena being targeted (deprotonation, Li^+ sorption configuration). The goal of the AIMD approach was to explore a wide swath of configurational space at the slab surface, not to quantitatively describe solvation physics at room temperature. This goal was essentially accomplished by the T=10 K AIMD simulations, thus the higher-temperature AIMD simulations were not investigated any further.

AIMD simulations were performed using the VASP medium precision level and a plane-wave cut-off energy of 400 eV, which is equivalent to the maximum plane wave energy used to construct the O pseudopotential. Given the large size of the slab supercells employed, AIMD simulations were performed with a single Γ k-point mesh using the gamma-point optimized VASP executable. The lowest energy atomic configurations obtained during the AIMD simulations were recalculated using a higher maximum plane-wave cutoff energy of 500 eV and a 4×2×1 Monkhorst-Pack k-point mesh, corresponding to the supercell real-space dimensions of 6.1×11.1×25.1 Å for 2-layer slabs, and

6.1×11.1×41.0 Å for 5-layer slabs. This kpoint density in reciprocal space is comparable to that shown to be sufficient to achieve well-converged results in bulk Fe-oxyhydroxides [9], which is approximately 25 kpts per $Å^{-1}$ or greater in all dimensions.

5.3.2.2 Simulation geometries

Most *ab initio* studies of sorption and protonation physics on hydrated mineral surfaces choose between either periodic slab or cluster simulation geometries. Periodic slab models [154-159] suitably recreate the periodic nature of the mineral surface, as well as benefitting from the computational efficiency of plane-wave based basis set methods. However, the periodicity of the slab system also imposes limitations on the types of physical phenomena that can be simulated with confidence. In particular for charged surfaces, coulomb interactions between slab surfaces in the direction normal to the slab surface introduce spurious electrostatic contributions to the system total energy, and monopole and dipole interactions between surface species in the plane of the slab may introduce additional energy terms that may obscure the targeted physical phenomena (i.e. sorption energies). Additionally, the geometric configurations of water molecules included in the cell for the purpose of recreating a hydrated or aqueous environment are constrained to the periodicity of the cell, and for small supercells these molecules can be prevented from forming realistic hydration environments. Larger supercells minimize the negative impacts of configuration and symmetry constraints, but impose higher computational resource costs.

Cluster model simulations [137-139, 156, 140, 160], in which a 3-dimensional particle is chosen to represent certain surface features, sidestep many of the the constraints of periodic boundary conditions, but introduce other errors or uncertainties that must be corrected or otherwise accounted for. In particular, computationally tractable cluster models often are comprised of small clusters that do not include all possible surface sites, especially for complex mineral structures, thereby neglecting the possible influence of these sites on the phenomena of interest. The artificial terminations of the boundaries of cluster model geometries typically consist of protons or fractional charges used to terminate dangling O bonds, likely introducing spurious interactions that would not be

present at a real mineral surface. Furthermore, the non-planar nature of a cluster model intended to mimic a flat, continuous mineral surface may also result in unphysical hydration environments around key surface sites when water molecules are added and relaxed to local minima surrounding the convex mineral cluster.

While both simulation geometry approaches offer some benefits and a variety of caveats, we choose to employ periodic slab models for this work. The slab supercells chosen are large enough such that concerns over periodicity constraints should be minimal. Electrostatic interactions across periodic boundary conditions are evaluated and controlled for using several methods, and the results are shown to be consistent independent of correction method.

Slab supercells representing the goethite (101) surface were built using the GDIS utility [103] having surface dimensions of 6.113 × 11.068 Å, corresponding to two primitive (101) surface cells tiled along the goethite [010] dimension. The slab model was constructed using the dimensions and atomic positions from a DFT-calculated fully-relaxed goethite bulk primitive cell (stoichiometry $Fe_4O_8H_4$), as described in [9]. The stoichiometries of each type of slab simulation performed are reported in Table 5-1. Two sets of slab geometries were constructed, the first having a depth of two layers of Fe octahedral double chains (about 8 Å deep, 16 Fe atoms total), and the second having a slab depth of 5 Fe octahedral layers (about 20 Å deep, 40 Fe atoms total).

While deep slabs might better mimic a bulk-like substrate, increasing slab depth incurs significant additional computational costs. Moreover, similar *ab initio* studies employing cluster geometries comprised of as few as 4-6 Fe octahedra to represent the goethite surface proved reasonably accurate for describing protonation and ion sorption phenomena [138, 140]. However, computational studies of deprotonation energies on TiO_2 surfaces suggest that a slab depth of 5 layers is necessary to achieve converged results [158].

Figure 5-2 illustrates sample results for calculations of relative Li^+ binding energies on a

charged goethite surface using both 2 layer and 5 layer slabs, both using the neutral-slab (NS) charge correction method. Please refer to results in Section 5.4.3 for a more detailed discussion of relative energies of Li^+ sorbate configurations, and to Section 5.3.2.3 for explanation of the NS method. The results presented in Figure 5-2 are shown merely to demonstrate the sensitivity of calculated configurational energies to changes in slab depth. The results obtained for the 5-layer deep slabs differ from the 2-layer slabs by energies of 36 meV rms, and the overall qualitative picture of relative binding energetics is commonly shared between the two slab depths, indicating that the interpretations of likely binding phenomena are not significantly affected by the choice to simulate using shallower slab geometries. Ongoing simulation work will establish complete results using the 5-layer deep slabs for the purposes of publication.

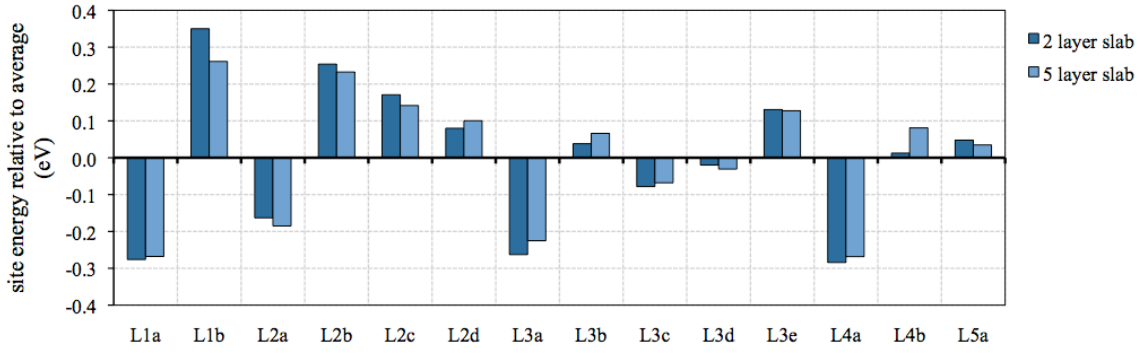

Figure 5-2: Relative Li binding energies on the goethite (101) surface at high pH for 2 layer deep and 5-layer deep slab geometries. The rms relative energy difference between the 2-layer and 5-layer datasets is 36 meV. While the calculated relative energies are not ideally converged with respect to slab depth at 2 layers, the qualitative ordering of site energies is well established for 2 layer slabs. Thus, 2 layer slab depth simulations appear sufficient to establish qualitative description of sorption site stability trends.

For all slab geometries, the upper and lower slab surfaces were terminated with two dissociated water molecules each (divided into H and OH groups), which is necessary to form full octahedral coordination shells around each Fe^{3+} ion. This process creates an initially symmetric slab with surface protonation reflecting a neutrally-charged goethite (101) surface and a neutrally-charged supercell with atomic valence states of Fe^{3+}, O^{2-}, and H^+ (illustrated in Figure 5-1, upper surface). The resulting surface structure is

comprised of singly-protonated $Fe_1O_{II}H$, $Fe_2O_{II}H$, $Fe_{3a}O_IH$ and $Fe_{3b}O_IH$ surface groups, while $Fe_{3c}O_{II}$ groups were fully deprotonated, in keeping with the majority of surface-charge and protonation literature describing the goethite (101) surface speciation as a function of pH [161, 104, 105, 151, 150, 162, 106, 163]. The H^+ at the lower surface were initially relaxed to local low energy positions, then were held fixed for all subsequent slab calculations to eliminate any configurational energy changes associated with these atoms. Surface deprotonation and Li^+ sorption simulations were only performed at the upper slab surface, with the adsorbed Li^+ bonding to one or more of the 10 Fe_xOH sites terminating the (101) surface plane, at Li-O distances less than 2.5 Å. During these production simulations, the atomic coordinates of the lower layers of the slab were fixed to their bulk geometries, while the positions of the upper-layer Fe atoms, surface O and OH groups, sorbate Li^+ and solvating water molecules were allowed to fully relax. The vacuum layer separating the solvated slab surface from its periodic image along the [101] direction was approximately 10Å in thickness after the addition of the adsorbed Li^+ ion and solvation layer (described following), resulting in a total supercell depth of 25 Å in the Z dimension for 2-layer slabs, and 41 Å for 5-layer slabs. The total energies of a subset of neutral slab geometries (Li^+ sorption at intermediate pH, Section 5.4.2) were found to shift by roughly 30 meV with respect to a 5 Å increase of supercell vacuum depth, but the shift was approximately constant across the series of 5 configurations tested. The relative energies between Li^+ configurations, which form the basis for the conclusions in this work, changed by no more than 4 meV when the supercell vacuum dimension was increased by 5 Å. A similar trend was observed for the simulation of deprotonation reactions, in which charge correction methods were applied. In this case, a 5 Å increase in vacuum depth led to insignificant changes in the relative deprotonation energies (7 meV or less).

The layer of 10 additional water molecules added to the top surface creates a minimal local solvation environment for the surface OH groups and Li^+ sorbate. The choice of 10 water molecules was driven by the presence of 10 terminal active O/OH groups at the upper slab supercell surface, thus permitting each surface O/OH group to form a hydrogen bond with the solvation layer, if possible. In practice, steric crowding affects

cause the water molecules in the solvation layer to relax into somewhat staggered positions along the direction normal to the slab, and hydrogen bonds between the relaxed water molecules and surface O/OH groups were not distributed uniformly across the surface. During AIMD simulations, the solvation layer water molecules were observed to rotate and translate significantly, exploring many hydrogen bonding arrangements in the duration of the simulation. After extracting the low-energy arrangements from the AIMD simulations and re-relaxing the coordinates at T=0 K, the resulting 10-molecule solvation layers for all configurations were approximately 6 Å in depth.

Table 5-1: Stoichiometries and molecular composition of the 2-layer slab geometries simulated in this study. All 2-layer slab supercells have cell dimensions of 11.1×6.1×25.1 Å, with the goethite [101] direction oriented pointed along the Z-dimension of the slab. The water molecules added to the bare goethite surface are divided into two groups – those dissociated H_2O required to complete the octahedral coordination environments of surface Fe, marked $H_2O^{dissoc.}$, and the molecular H_2O forming the solvation layer above the slab surface, marked as $H_2O^{solv.}$. The 5-layer slab geometries reported in Figure 5-2 add 24 FeOOH units to the 2-layer slab geometries, with a cell Z-dimension of 41 Å, but are otherwise identical in surface structure and composition.

Simulation Type	Stoichiometry	Composition
Deprotonated Fe_xOH site	$Fe_{16}O_{46}H_{43}$	$16(FeOOH)+4(H_2O^{dissoc.})+10(H_2O^{solv.})-H^+$
Deprotonated Fe_xOH site (EDI method)	$Fe_{16}O_{46}H_{42}Ca$	$16(FeOOH)+4(H_2O)^{dissoc.}+10(H_2O)^{solv.}-2H^++Ca^{2+}$
Li sorption, intermediate pH	$Fe_{16}O_{46}H_{43}Li$	$16(FeOOH)+4(H_2O)^{dissoc.}+10(H_2O)^{solv.}-H^++Li^+$
Li sorption, high pH	$Fe_{16}O_{46}H_{42}Li$	$16(FeOOH)+4(H_2O)^{dissoc.}+10(H_2O)^{solv.}-2H^++Li^+$
Li soption, high pH (EDI method)	$Fe_{16}O_{46}H_{41}LiCa$	$16(FeOOH)+4(H_2O)^{dissoc.}+10(H_2O)^{solv.}-3H^++Li^++Ca^+$

For Li^+ sorption calculations, a single Li^+ ion was added to the upper slab surface, resulting in a sorbate density of 1 Li^+ per 0.68 nm^2, or 1.47 Li^+/nm^2. Li^+ sorption in the intermediate pH regime was simulated as a charge-neutral swap of one surface H^+ for a Li^+ cation. In this regime, the resulting slab supercell remains neutrally charged and no artificial dipoles are introduced, thus no significant electrostatic interactions should be expected across periodic boundary conditions. To model Li^+ sorption at high pH, where

the (101) surface should be negatively charged due to deprotonation of surface OH groups, the energies of a single Li^+ sorbate, accompanied by the removal of *two* H^+, are compared. One H+ can be considered the effect of the high pH, while the second is associated with substitution of H+ by Li+. The overall process of removing two H+ and adding one Li+ leaves a net charge of -1e^- in the slab supercell, at which point a more sophisticated treatment of periodic electrostatics must be undertaken to account for the spurious interactions of the net slab charge with its image charges. This approach is described in detail in Section 5.3.2.3

While we discuss simulations as occurring in one of two pH regimes (intermediate vs. high), the actual proton activity or proton concentration of the solvation layer are not adjusted to account for changing pH due to the impracticality of modeling the many orders of magnitude of change in H^+/OH^- concentrations necessary to realistically represent various pH solution conditions. Instead, the mineral surface is reconfigured to reflect likely O/OH speciations at various pH levels via the removal of surface protons, without adjusting the number of neutral water molecules in the solvation layer, which remains constant across all simulations. This approximate method recreates local electrostatic effects at the mineral surface, as well as providing a realistic local hydration/solvation environment, without the need to explicitly model huge numbers of solvating water molecules.

5.3.2.3 Surface charge and dipole correction methods

At high pH, the goethite (101) surface is negatively charged due to successive deprotonation of surface Fe_xOH groups. This surface condition is simulated by removing multiple H^+ from upper surface OH groups in the slab supercell. To evaluate the deprotonation reactions themselves, individual H^+ were removed from the $Fe_1O_{II}H$, $Fe_2O_{II}H$, $Fe_{3a}O_IH$ and $Fe_{3b}O_IH$ surface groups. The removal of a proton from the system induces a negative surface charge density of -0.237 C/m^2 on the upper slab surface, which corresponds approximately to the observed goethite surface charge above pH 12, although the precise value of surface charge as a function of pH is dependent on solution ionic concentration, the effects of which are not modeled here [150]. For the simulation of Li^+ sorption at high pH, the removal of two H^+ in exchange for one Li^+ results in the

same net charge density. For slab geometries within periodic boundary conditions, absent any correction scheme, this net surface charge leads to large spurious electrostatic interaction energies between the surface charge and its image charge across the slab vacuum layer. We examine three distinct correction schemes that deal with this issue and compare their effectiveness below.

In all simulations, including those without net slab charge, standard dipole correction algorithms were employed to measure and correct for undesired dipole-dipole (and further multipole) interactions across periodic boundary conditions. These corrections, as implemented within VASP, essentially follow the correction schemes described in [164] and [165]. The reliability and accuracy of these dipole corrections should be considered a separate issue from that of the charged slab correction issue, which adds the additional complexity of a monopole interaction term while also exacerbating dipole image interaction issues. All energy quantities reported in this work reflect the addition of the dipole energy correction terms to the cell total energies, unless otherwise noted.

5.3.2.3.1 Uniform compensating background charge (UCBC) method

The most common method for dealing with net charge in a periodic supercell (and the default behavior within VASP when unbalanced charges are initialized) is to introduce a uniform background charge density that neutralizes the net charge within the cell. This method is well established for solid-state bulk materials, particularly for charged point defects in solids, but does not produce well-behaved total energy convergence trends for charged slab geometries. The ineffectiveness of the UCBC method when dealing with charged slabs is at least partially due the large monopole, dipole (and other multipole) interactions induced by the surface charge and background correction charge density and the dependence of these energies on the cell geometry. This correction method should be expected to fail entirely to produce accurate total energies due to the indeterminate and poorly-converged nature of the electrostatic interactions within and between slab images, however it may perform more reliably to extract *relative* configurational energies between slab geometries with tightly controlled geometries where the energies associated with image interactions might be expected to cancel.

In this spirit, we calculated the relative deprotonation energies for four the FeOH groups at the (101) surface, as well as the relative energies of Li^+ adsorbed in a variety of binding configurations using the UCBC approach, all using 2-layer slabs. In each series of simulations, the slab supercell geometries were kept constant in all dimensions, and the atomic composition and surface charge density were identical across each series of calculations, in order to allow for the cancellation of many spurious electrostatic terms when comparing relative energies across similar supercells. While the relative energies describing deprotonation were shown to be in good agreement with experimental references, as well as in qualitative agreement with the results obtained from other correction methods (following sections), the relative Li^+ configurational energies were found to be inconsistent with the results obtained by the other two charge correction schemes. Additionally, AIMD simulation of Li^+ sorption while employing the UCBC scheme resulted in significant structural changes within the solvation layer, in which water molecules were observed to dissociate and re-protonate the charged surface, leaving a mixture of H_2O and OH^- within the solvation layer. This dissociation reaction causes considerable shifts in the cell total energy, and the resultant energies could no longer be interpreted as accurately representative of Li^+ sorption alone, but rather a mixture of coupled reactions for which separate energies that could not be obtained. The results of the UCBC correction scheme are thus not reported among the results shown in this work, although a summary of simulation results using this method are reported in Appendix A.

5.3.2.3.2 Neutral slab (NS) method

The second and perhaps simplest correction scheme is to simply remove the excess electron from the deprotonated slab, equivalent to initially removing an H atom (instead of H^+) from the slab supercell to simulate the deprotonation reaction. This leaves the slab supercell with a net neutral charge, but with one electron less than what is necessary to satisfy the formal valence of each of the remaining atoms (as Fe^{3+}, O^{2-}, H^+, Li^+). When the *ab initio* simulation is performed under these constraints, the outcome in each case is

that one Fe^{3+} cation is oxidized to Fe^{4+}, with all other atoms' valence configurations being unaffected. While this Fe^{4+} cation (illustrated in Figure 5-1) represents an unrealistic and unphysical addition to the simulation system, the presence of the Fe^{4+} cation at the slab surface is commonly shared across all of the charged slab configurations simulated, including both deprotonation and Li^+ sorption simulations. While this artificial defect surely destabilizes the slab as a whole, if the energy of this destabilization effect is approximately constant and independent of the surface configuration, the energy of this fixed defect will not affect the evaluation of relative energies between configurations. However, some unphysical electronic effects might be expected near the defect Fe^{4+} site. This possibility is considered when comparing the results of the NS method with the EDI method, described in Section 5.3.2.3.

Using the NS method, AIMD simulations were numerically well-behaved and produced reasonable surface protonation, Li^+ sorption, and most significantly, solvation layer geometries. No dissociation of solvation layer water molecules was observed during AIMD simulations, and electronic and ionic convergence were easily achieved as compared to the difficulties experienced with the UCBC method.

5.3.2.3.3 Electron donor ion (EDI) method

Another charge-correction procedure for computational study of charged systems is to introduce oppositely-charged counter-ions within the cell to cancel the net charge induced by charged slabs or defects. In the most common manifestation of this method used for charged slabs, charged counter ions (often Na^+, Cl^-) are introduced into the solvation layers above the charged slab, effectively re-creating the electric double layer (EDL) expected for realistic solution conditions [166, 156].

However, the use of solvated counter-ions requires the addition of many additional water molecules necessary to solvate the counter-ions at a suitable distance from the slab surface, which in turn increases the configurational space available to both the counter ions and solvating water molecules. While the explicit simulation of the EDL adds

physical accuracy to the slab/sorbate and sorbate/solvation interactions in terms of local bonding and electrostatics, extracting well-converged and stable energies from this system becomes more difficult due to the large energy uncertainty introduced by the many configurational degrees of freedom available to the extensive solvation layer. Although thermodynamic averaging techniques [149] can reasonably account for this broad configurational space, such techniques would require long calculations times and are impractical to implement within the DFT framework for a large number of surface sorption configurations, as desired within this work.

The variation on this method introduced in this work is to couple the compensating counter-ion to the lower surface of the slab, forming a fixed defect that sidesteps the configurational uncertainty of the solvation-based approach. In this work, a Ca atom is substituted for an H atom on the lower surface of the slab (illustrated in Figure 5-1), forming Ca^{+} at the lower surface. When simulating deprotonation or high pH conditions at the top surface, an additional neutral H *atom* is removed from the top surface, creating a surface configuration like that produced by the ND method in which the formal valence states of one or more surface Fe atoms are not satisfied. At this point the Ca^{+} at the lower surface, being strongly electropositive, readily donates an additional electron to the slab system, becoming Ca^{2+}, thereby satisfying the formal valences of the entire slab as Fe^{3+}, O^{2-}, H^{+} and Ca^{2+}. The bond length of this Ca-O configuration is then optimized in a separate relaxation simulation, forming a Ca-O bond length of approximately 2.1 Å, after which the Ca position is held fixed relative to the slab for all subsequent simulations.

While this compensation mechanism, referred to as the electron donor ion (EDI) method, introduces a spurious Ca-O species to the lower surface of the slab, the geometry of this species is held constant across all upper-surface configurations and the thus energy offset induced by this fixed defect can be expected to cancel when evaluating relative energies of upper-surface configurations with equivalent charge states. The benefits of this method over the NS method are that a net-neutral slab geometry can be constructed that also reproduces the local electrostatics expected at the upper slab surface, namely negative surface charges localized at deprotonated O groups, without causing unrealistic

oxidation of surface Fe atoms.

As a way to reduce computational costs, the relaxed upper-surface solvation and Li^+ sorption geometries obtained from the AIMD+static relaxation simulations using the NS method were then re-tested using the EDI correction method, without repeating the AIMD procedure for the EDI method. Single Ca atoms were substituted independently at two different locations on the lower slab surface, and the energies of the charged-surface configurations were re-evaluated for each Ca position. Two positions were chosen in an effort to demonstrate that the EDI method achieves comparable results independent of the Ca position chosen at the lower slab surface. The series of configurational energy results for the two Ca positions are referred to by the labels Ca1 and Ca2 in subsequent results.

Overall, all 3 charge-correction approaches (NS, EDI Ca1, and EDI Ca2) create a charge distribution that is a primitive substitute for the solvation electric double layer (EDL) that would be present in all real aqueous charged surface systems. The charge correction mechanism in each method is held as fixed as possible, and is assumed to impose an approximately constant shift on system energies. These approaches will therefore, at best, only be accurate to the extent that the actual EDL that forms in real systems does not significantly affect the relative energies of varying surface configurations of equivalent net charge. We therefore must make clear our assumption that the EDL energy in the real system is constant enough between the similar surface structures we are comparing to not significantly impact the order of their relative stabilities.

In practice, the NS and EDI methods produce slightly different relative configurational energies for both deprotonation and Li^+ sorption simulations at high pH (see results in Sections 5.4.1 and 5.4.3). These energy differences are on the order of 100 meV, which we use an approximate estimate of the error bar when using calculated energies to determine stable site configurations. However, the overall range of relative configurational energies is roughly one order of magnitude larger than this error bar, and the qualitative ordering of stable sites is largely consistent between charge correction methods, giving us confidence that *ab initio* results can provide reliable predictions for

stable site configurations.

5.4 Results

5.4.1 Deprotonation of Fe_xOH groups at the (101) surface

Simulations of the deprotonation of $Fe_1O_{II}H$, $Fe_2O_{II}H$, $Fe_{3a}O_IH$ and $Fe_{3b}O_IH$ surface groups were performed using the AIMD approach, then relaxed at T=0 K. Because the deprotonation of the (101) surface leaves behind a negatively charged surface, these calculations employ the charge correction methods described in Section 5.3.2.3. This series of deprotonation energies can be considered a benchmark data set, as experimental and theoretical references for these deprotonation energies exist [105, 151, 140]. We present relative deprotonation energies for the four sites simulated, and compare to similar relative energies derived from the literature references as follows:

Deprotonation energies in the literature are typically reported as acid dissociation constants, or pK_a, which encapsulate the relative energies of the neutral and deprotonated surface sites, as well as the solvated proton. For a generic deprotonation reaction at the surface (Eq. 4.1):

$$Fe_xOH \leftrightarrow Fe_xO^- + H^+_{aq.} \qquad (4.1)$$

where Fe_xOH refers to any of the singly-, doubly-, or triply-coordinated surface OH groups, the acid dissociation constant, pK_a, can be written as a function of the free energy change associated with the deprotonation reaction (Eq. 4.2) [51]:

$$pK_a = \frac{\Delta G_{rxn}}{\ln(10)kT} \qquad (4.2)$$

From the set of reference pK_a values for the deprotonation reactions of interest, we calculate the free energies of reaction using Eq. 4.2. The relative values of these free energies of reaction can be compared to the relative energies calculated for the deprotonation simulations. While the *ab initio* simulations only rigorously model the formation enthalpies of the deprotonated surface sites at T=0 K (assuming PV energy terms are negligible), the main contributors to the entropic and finite-temperature terms

encapsulated in pK_a or ΔG_{rxn} should effectively cancel in the evaluation of relative energies between surface sites. For example, the largest entropy (TS) term in the calculation of ΔG_{rxn} will be the entropy associated with the solvated proton that desorbed from the surface. In the evaluation of relative energies between surface sites, this entropy term, which is a property of the solvated proton and not the specific surface configuration, will completely cancel.

The final three columns of Table 5-2 show in italics the relative deprotonation energies calculated in this work as computed using the NS and EDI methods (Section 5.3.2.3). These energies including simulations results using the NS and EDI methods on 2-layer slabs, including simulation series with two distinct Ca positions (Ca1 and Ca2, respectively) for the EDI method results. The relative deprotonation energies are also plotted in Figure 5-3. The energies for each data series are evaluated relative to the average energy for that series (e.g. the average energy of the four deprotonation simulations performed using the NS method). However, because the experimental reference data only specify deprotonation energies for the $Fe_1O_{II}H$, $Fe_2O_{II}H$, and $Fe_{3a}O_{I}H$ sites, the series averages are calculated using only those sites, even for the three calculated series where a fourth deprotonation site is explicitly modeled. The use of an internal energy reference (the series average energy) allows the experimental data and various calculation types to be compared directly as distributions of relative values. In this sense, a look at the calculated relative deprotonation energies for a series of sites will determine which order the sites are likely to become deprotonated as a function of pH, but will not determine the pH level at which this process begins. Because aggregate surface protonation and charging behavior are well characterized in goethite, there is little motivation to tackle the additional complication of assigning an absolute energy scale to the calculated relative deprotonation trends. If an absolute measure of deprotonation energy were desired, a constant energy shift could be applied to all calculated data within a series and fitted such that the predicted PZC matched the value observed experimentally.

Table 5-2: Experimental and theoretical pK_a and associated ΔG_{rxn} values for the deprotonation of Fe_xOH sites at the goethite (101) surface. Literature values are reported in columns labeled a, b, and c, with references given below. The final set of three italicized columns show results calculated in this work. For this work, ΔG_{rel} is calculated by comparing the total energies of slab supercells simulating the deprotonated sites. Entropy terms are assumed to cancel in the evaluation of relative energies and are thus not calculated explicitly.

site	pKa			ΔGrxn (eV)			ΔGrxn vs. average (eV)					
	a	b	c	a	b	c	a	b	c	*NS*	*EDI Ca1*	*EDI Ca2*
$Fe_1O_{II}H$	19.6	17.6	15.1	1.16	1.04	0.89	0.30	0.26	0.18	*0.13*	*0.33*	*0.22*
$Fe_2O_{II}H$	12.3	11.5	9.5	0.73	0.68	0.56	-0.13	-0.10	-0.15	*-0.02*	*-0.15*	*-0.11*
$Fe_{3a}O_IH$	11.7	10.5	11.7	0.69	0.62	0.69	-0.17	-0.16	-0.02	*-0.12*	*-0.18*	*-0.12*
$Fe_{3b}O_IH$	n/a	n/a	n/a	n/a	n/a	n/a	n/a	n/a	n/a	*0.04*	*-0.04*	*0.06*

(a) [104], (b) [151], (c) [140]

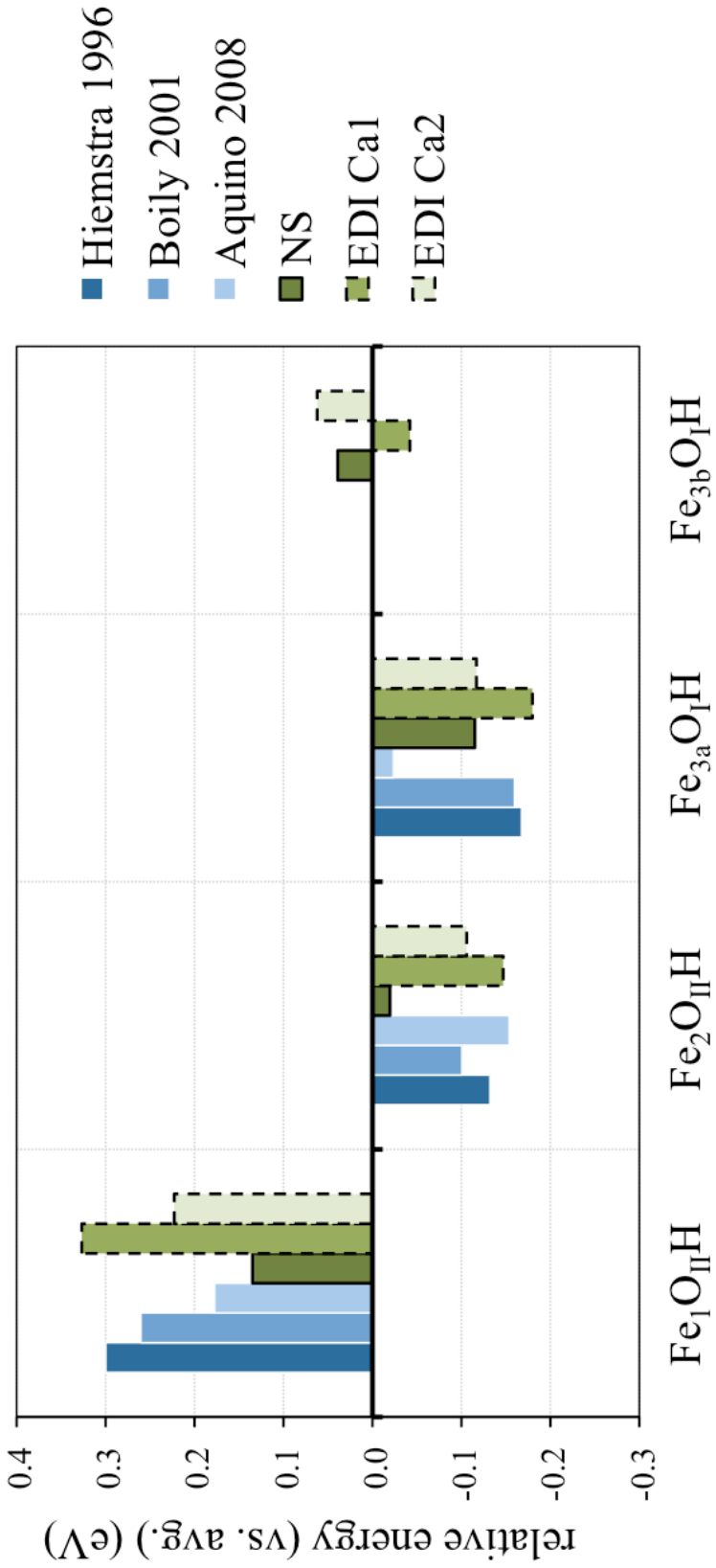

Figure 5-3: Relative deprotonation energies of the four Fe_xOH sites at the goethite (101) surface. Values shown in blue without outlines are taken from literature references that include both experimental (Hiemstra, Boily) and theoretical (Aquino) approaches. Experimental values are not reported for the deprotonation energy of the $Fe_{3b}O_IH$ site, thus no blue columns appear associated with that site. Values shown in green with solid outlines are calculated in this work using the NS charge correction method for 2 layer slabs. Shown in green with dashed outlines are the relative energies computed using the EDI method, with the Ca donor ion placed at two different positions on the lower slab surface (Figure 5-1).

The simulated relative deprotonation energies yield good qualitative agreement with the literature references, especially for those based on titration data and the MUSIC approach [104, 151]. The NS, EDI Ca1, and EDI Ca2 datasets show rms differences of 119, 19 and 55 meV, respectively, when compared to the original MUSIC dataset [104] for the first three deprotonation sites (the deprotonation of the $Fe_{3b}O_IH$ site is not reported separately in the MUSIC reference). In a qualitative sense, the NS and EDI methods perform acceptably well to describe the expected deprotonation trends at the (101) surface as a function of increasing pH, namely that the $Fe_2O_{II}H$ and $Fe_{3a}O_IH$ sites are expected to deprotonate most easily (lowest deprotonation energy), while the $Fe_1O_{II}H$ site is more difficult to fully deprotonate, requiring a lower proton chemical potential (high pH) to drive the deprotonation reaction forward. The fourth site reported, the partially-embedded $Fe_{3b}O_IH$ site, is not typically considered to be a separate surface site in the MUSIC literature (it is assumed to be equivalent to $Fe_{3a}O_IH$) but is calculated here to have a different deprotonation energy using both the NS and EDI methods. For the purposes of simulating further charging and sorption phenomena on the (101) surface, the $Fe_{3b}O_IH$ will be treated as a separate sorption site in this work.

Figure 5-4 illustrates the stable solvation environments around each of the deprotonated sites after AIMD simulation, as calculated using the NS method. In the case of the Fe_1O_{II}, Fe_2O_{II}, and $Fe_{3a}O_I$ sites, one of the solvation layer water molecules donates a hydrogen bond to the bare O atom remaining at the surface. The donating hydrogen bond at the $Fe_{3a}O_I$ site is quite long, however, at a distance of 2.17 Å. When deprotonated, the embedded $Fe_{3b}O_I$ site does not show any hydrogen bonding activity, likely due to the steric crowding of the nearby Fe octahedra that effectively prohibit water molecules from approaching the site closely enough to form a hydrogen bond.

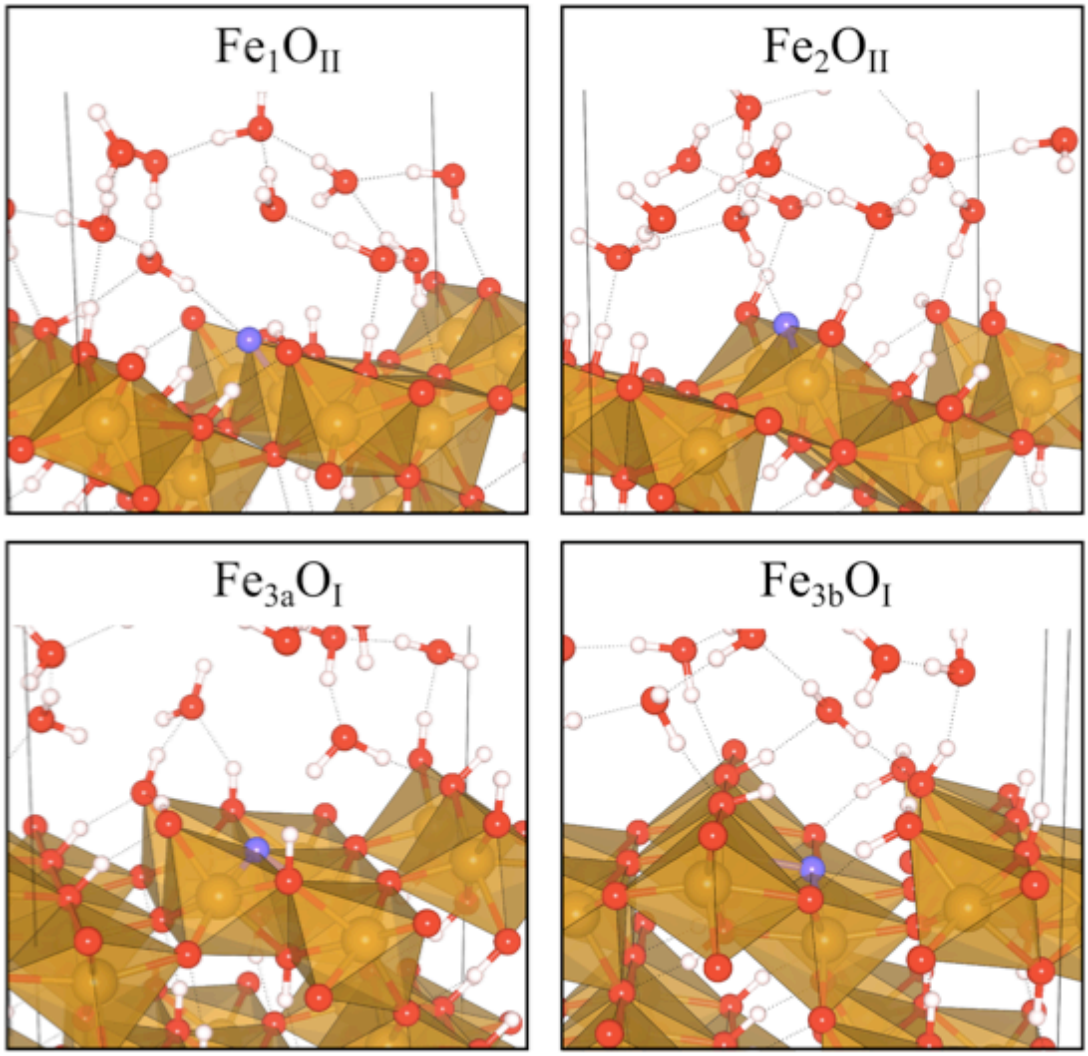

Figure 5-4: Calculated solvation geometries surrounding the four deprotonation sites at the goethite (101) surface. In each image, the deprotonated O group is shown as a purple atom. Other oxygen atoms are shown as red spheres. Fe octahedra are shown in brown. Protons are shown as white spheres. For ease of visualization, the atoms within each slab supercell were uniformly translated to locate the deprotonated site at the center of the slab surface.

5.4.2 Li^+ sorption at intermediate pH

At intermediate pH levels near the PZC, single-, double-, and triple-coordinated Fe_xOH groups on the (101) surface are still largely populated with protons. In this regime, Li^+ sorption is modeled as a charge-neutral swap of a single surface proton (H^+) for the Li^+ sorbate ion. To accomplish this, one proton was removed from a surface Fe_xOH site and replaced with a Li^+ forming an Li-O bond longer than, but similar to the H-O bond that was removed. Starting with this initial Li^+ sorbate position AIMD simulations were performed allowing relaxation of the surface geometry, including reconfiguration of Li-O bonds and the relaxation of the positions of solvating water molecules. During the AIMD simulations, the Li^+ ion typically shifted to positions that bridged two or more $Fe_xO(H)$ groups on the surface, creating bi- and multi-dentate configurations in most cases. The resulting set of (meta)stable configurations are illustrated together in Figure 5-6, and associated bond lengths and energies relative to the series average are reported in Table 5-3.

Ab initio results suggest that the stable sites under these conditions are multi-dentate (sites L2 and L4). Sites L1 and L2 resemble the site proposed by Kim et al. [133] as the likely sorption configuration at intermediate pH, but of these only the L2 site appears to be stable, whereas the L1 site appears to be considerably higher in energy, and therefore metastable.

The intermediate pH sorption site proposed by Kim et al. is described as a bridging position between neighboring $Fe_1O_{II}(H)$ groups, for which specific protonation states were not clearly specified. For the stable L2 site, the Li^+ is closely bound to a still-protonated $Fe_1O_{II}H$ group (1.86 Å), as well as bridging to the next $Fe_1O_{II}H$ at a slightly longer distance (1.89 Å). These Li-O-Fe linkages for angles of 101° and 104°, respectively. That the $Fe_1O_{II}H$ groups remain singly-protonated at intermediate pH is consistent with the deprotonation energies calculated in Section 5.4.1, and with the pK_a values for this site reported in the literature, which suggest that it will be singly-protonated at pH levels above roughly pH 8 and will not be fully deprotonated even at high pH levels (pK_{a2} = 19.6) [104].

Table 5-3: Calculated Li-O bond lengths and site energies of Li^+ sorption configurations on the goethite (101) surface at conditions near the PZC (approximately pH 8-9). In these simulations, Li^+ was used to replace one H^+ at the surface, and allowed to explore configurational space through AIMD simulation. Li-O bonds up to 2.25 Å are reported here, longer Li-O bonds are omitted. Bonds between the Li^+ sorbate and solvation layer water molecules are reported in the column labeled H_2O.

Li^+ site label	deprotonated Fe_xOH site	Li-O bond distances - 2 layer slab (Å)						site relative energy vs. avg. (eV)
		$Fe_1O_{II}(H)$	$Fe_2O_{II}(H)$	$Fe_{3a}O_I(H)$	$Fe_{3b}O_I(H)$	$Fe_{3c}O_I$	H_2O	
L1	$Fe_{3b}O_I$	1.86, 2.03	-	-	2.03	-	-	0.268
L2	Fe_1O_{II}	1.86, 1.89	-	-	-	-	1.94	-0.237
L3	$Fe_{3a}O_I$	1.87	-	1.96	-	-	1.93	0.072
L4	Fe_2O_{II}	-	1.93	-	-	2.11, 2.20	1.98	-0.168
L5	Fe_2O_{II}	-	1.91	-	2.12	-	1.97	0.065

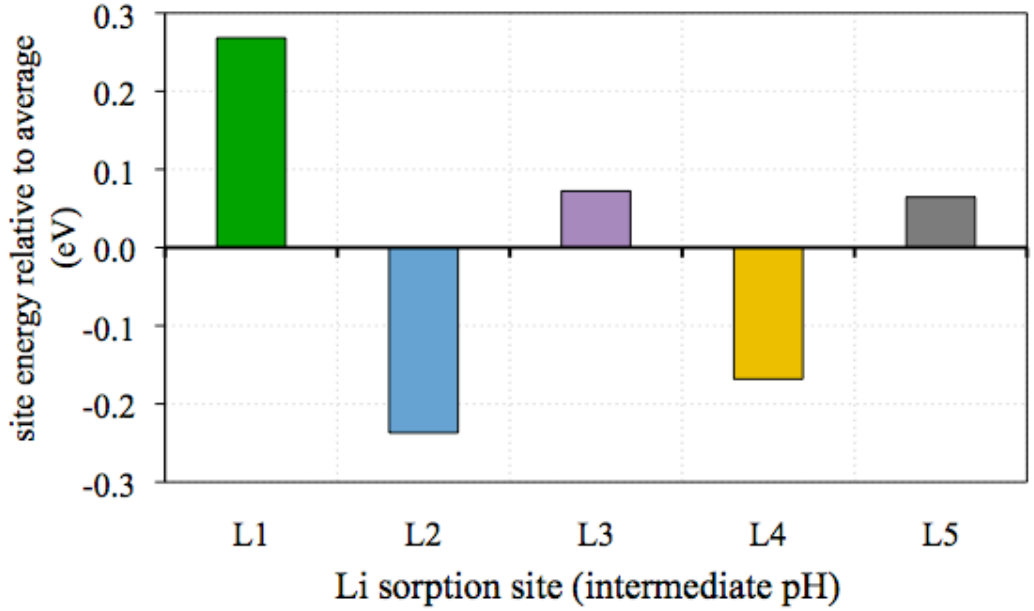

Figure 5-5: Relative energies of the Li^+ sorption configurations on the goethite (101) surface, color coded to correspond to the site geometries illustrated in Figure 5-6. Energies are evaluated relative to the average total energy of all of the site configurations within the data series.

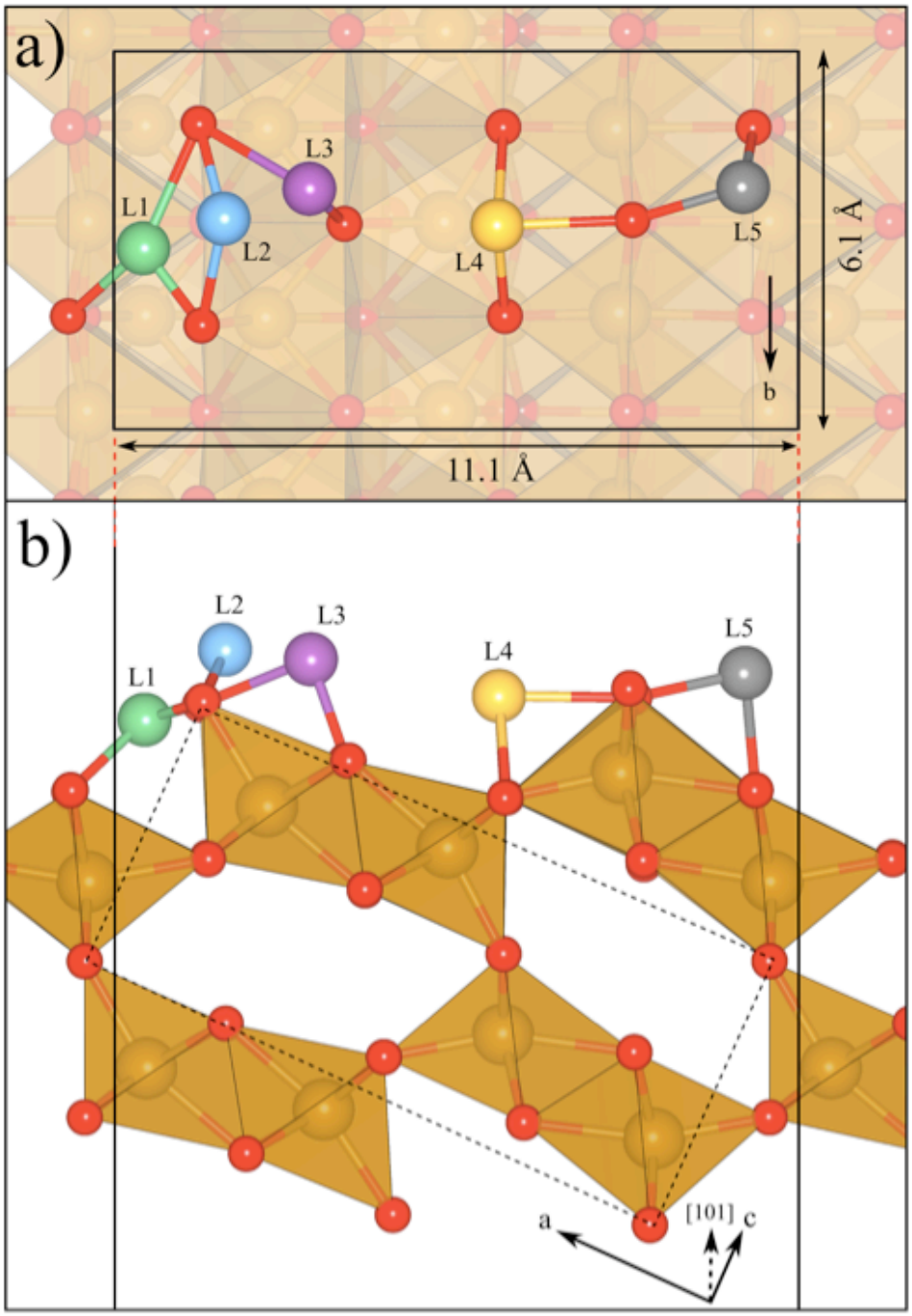

Figure 5-6: The (meta)stable Li^+ configurations at the goethite (101) surface after AIMD simulations. Protons and solvation layer water molecules are not shown to the sake of clarity. The same geometry is shown in two projections – along the [101] direction (a), and along the [010] direction (b). The goethite bulk primitive cell is illustrated with a dashed outline in (b). Relative energies of these configurations are shown in Table 5-3.

Interestingly, the L2 configuration was originally initialized with one deprotonated Fe_1O_{II} group, but during the AIMD simulation the proton at the nearby $Fe_{3b}O_IH$ site moved from that site across the goethite half-tunnel and bonded at the Fe_1O_{II} site, where it remained for the remainder of the AIMD and static simulations (this proton is highlighted in Figure 5-7 with a dashed blue circle). A manual reconfiguration of this proton back to the $Fe_{3b}O_IH$ site was simulated and found to be higher in energy. This observation is in agreement with the results presented in Section 5.4.1, in which the $Fe_{3b}O_IH$ site is shown to have a lower (easier) deprotonation energy than the $Fe_1O_{II}H$ site.

The L4 site, which is equal in energy to the stable L2 site to within the accuracy of the calculations, is distinct from the sites proposed in Kim et al. for both intermediate and high pH. This site is unique in that it forms long bridging Li-O bonds with two $Fe_{3c}O_{II}$ sites (at 2.11 and 2.20 Å), while remaining anchored to the deprotonated Fe_2O_{II} site at a distance of 1.91 Å. Whether these longer Li-O distances should be considered to be chemical bonds is uncertain, although they are drawn as bonds in Figure 5-7 for the purposes of illustration. For comparison, Kim et al. [133] cite a range of 1.7-2.0 Å as typical for Li-O bonds in oxide compounds containing Fe and Li. Li-O-Fe bond angles associated with the 1.91 Å Fe_2O_{II} bond are 92° and 94°, similar to those observed at the L2 site. The angles associated with the longer bonds to $Fe_{3c}O_{II}$ sites are more varied, with angles of 81°, 85°, and 145° for one bond, and 79°, 85°, and 147° for the other.

The implications of these Li-O bond geometries and corresponding Li-O-Fe linkages in the context of comparing with NMR Fermi contact shift data are discussed in Section 5.5.1.

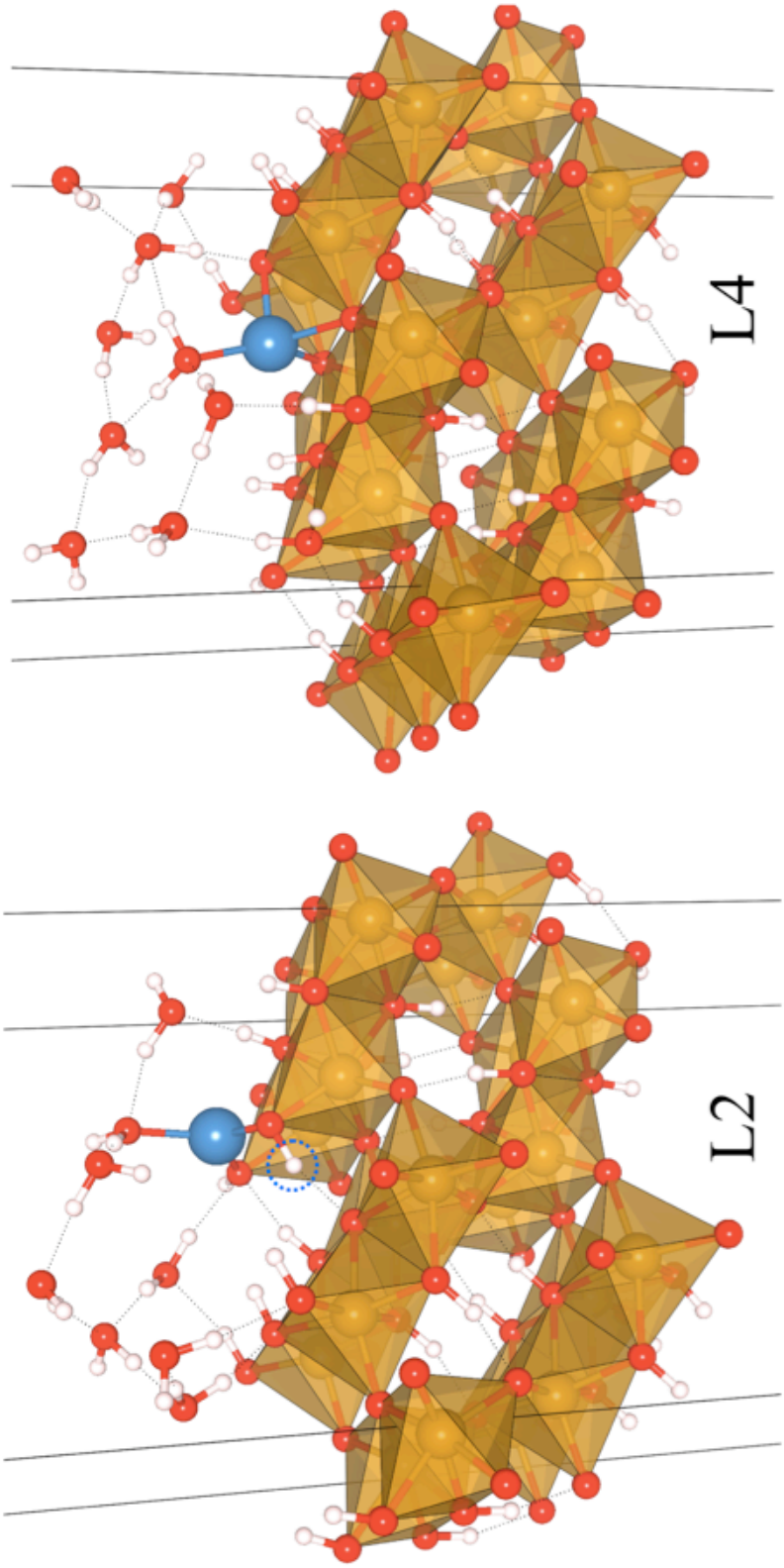

Figure 5-7: The two stable Li^{+} sorption configurations on the goethite (101) surface at intermediate pH. Site L2 closely resembles the site proposed by Kim et al. based on interpretation of NMR Fermi contact shift data. Site L4 is distinct from that described by Kim et al., but could reasonably be interpreted as being in agreement with the NMR measurements based on the Li-O-Fe linkage counting procedure described above.

5.4.3 Li+ sorption at high pH

At pH levels above the PZC, additional Fe_xOH groups at the surface have become deprotonated, leaving a large number of bare O groups suitable for Li^+ coordination. To simulate this phenomenon on the slab supercell, two H^+ were removed from various surface OH groups, and a single Li^+ was added, leaving a net negative surface charge, which is corrected for using the methods described in Section 5.3.2.3. A wide variety of different Li^+ and O^-/H^+ configurations were calculated in this regime, the result of varying configurations of deprotonated sites surrounding the five Li^+ positions found at intermediate pH. While previous studies and the *ab initio* results presented in Section 5.4.1 suggest that the $Fe_2O_{II}H$ and $Fe_{3a}O_IH$ surface OH groups should be easiest to deprotonate, other surface deprotonation configurations (e.g. deprotonation of the $Fe_1O_{II}H$ and $Fe_{3b}O_IH$ sites) were also studied to explore whether Li^+ configurations that bridge neighboring O(H) sites might be energetically favorable enough to overcome the unfavorable energetics of deprotonation of the individual sites. After AIMD simulation of all conceivable initial permutations of Li sites and proton arrangements within our supercell, fourteen surface configurations were found to yield stable geometries and convergent energies. Other configurations either failed to converge or spontaneously reconfigured during the AIMD simulations to one of the fourteen configurations reported. The resulting geometries are sorted into configuration groups that share similar Li-O bonds at the (101) surface, as shown in Figure 5-8 and these groups are color-coded with the same nomenclature introduced for the intermediate pH simulations. In addition to site numbers, letter subscripts for each configuration correspond to differing (de)protonation arrangements neighboring the Li^+ sorbate. These deprotonation arrangements are specified alongside Li-O bond distances for the high pH geometries in Table 5-4. Table 5-5 lists the bond angles formed by the Li-O-Fe connectivities for each configuration.

Figure 5-9 plots the calculated relative energies of the fourteen simulated Li^+ sorption configurations at high pH, expressed relative to the average energy for all simulations in each series. The first set of columns with solid outlines correspond to the simulation series using the NS charge correction method on 2-layer (16 Fe) goethite slabs. Calculations using the EDI method (Figure 5-9, dashed outlines) were performed using

the optimized geometries from the NS-series calculations, with the exception of the Ca atom swap performed at the lower slab surface, replacing a lower-surface proton and forming a Ca-O bond approximately 2.1 Å long. (as described in Section 5.3.2.3). While the Ca atom was held fixed at the lower surface of the slab, full relaxation of the surface atoms was performed for the EDI simulations, allowing any geometrical artifacts due to initialization using the NS geometries to relax to new local minima. However, relatively little surface reconfiguration was observed, indicating that the local electrostatic features of the (101) slab surface were relatively similar for both charge correction methods.

The qualitative agreement between the configurational relative energies calculated with the different charge correction methods suggest that the relative energies largely reflect the Li^+, H^+, and solvation layer configurations at the upper slab surface. However, some dependence on the charge correction method is apparent from the energy results, which for the NS method show the L1a, L3a, and L4a sites as competitively stable, while the EDI method shows the L4a site as distinctly more stable than other sites. However, within the two series of simulations performed using the EDI method, no systematic dependence on the Ca donor ion position is evident.

Comparing the relative energies obtained by the EDI to NS methods, it is evident that the choice of charge correction method will have non-negligible impact on determination of likely stable site configurations. The relative energies obtained by the NS and EDI methods differ by 103 and 73 meV comparing NS results with the EDI Ca1 and EDI Ca2 results, respectively. The rms difference between the Ca1 and Ca2 series using the EDI method is 38 meV, indicating that the choice of position of the Ca^{2+} donor ion within the EDI method has a relatively smaller impact on relative energy results than the choice of an alternate charge correction method. The largest of these rms difference values (103 meV) is approximately 14% of the ~0.75 eV energy scale associated with the different Li binding sites.

With these comparisons in mind, we conclude that different approximations made in the NS and EDI charge correction methods result in an effective error bar for relative site

energies on the order of 100 meV, applicable to any simulations modeling sorption at charged slab surfaces. However, because the general pattern for the ordering of stable and unstable site configurations is qualitatively maintained throughout all simulation methods, and the differences between stable and unstable configurations are considerably larger than 100 meV, we can have confidence that the true stable configuration(s) will be among the sites found to be more stable than average by both charge correction methods.

The L4a site shown to be dominantly stable using the EDI method calculations, and competitively stable using the NS approach, closely resembles the L4 site shown to be stable in the intermediate pH series of calculations. The L4a site shows one short Li-O bond with a deprotonated Fe_2O_{II} group (d=1.96 Å) forming Li-O-Fe dihedral angles at 91° and 92°, and two relatively longer Li-O distances to underlying $Fe_{3c}O_{II}$ groups (d=2.14 and 2.15 Å, respectively). These longer Li-O bonds in turn form Li-O-Fe dihedral angles of two basic types; four relatively acute angles of 81°, 81°, 81° and 84°, and two rather straight Li-O-Fe linkages with angles of 148° and 151°.

The second-most stable site calculated using both the EDI and NS methods, L1a, most closely resembles the high pH sorption configuration proposed by Kim et al. This site bridges between one $Fe_1O_{II}H$ group and one deprotonated $Fe_{3b}O_I$ group with relatively short bond Li-O lengths of 1.88 and 1.90 Å, respectively. The relative stability of this site is in contrast to the high relative energy associated with the geometrically similar L1 site calculated in the intermediate pH case. This site forms Li-O-Fe dihedral angles of 108°, 113°, 118°, and 129° (Table 5-5).

The general trend proposed by Kim et al. that favors the presence of multi-dentate Li^+ adsorption sites at a negatively charged, deprotonated surface at high pH is confirmed in these results, as several bi- or multidentate site configurations initially shown to be unstable at intermediate pH (L1, L3) are found among the several most stable sites when the surface has been further deprotonated (L1a, L3a). However, as an exception to this phenomenon, the relatively favorable stability of the L4 site at intermediate pH is maintained at high pH via the stable L4a configuration. Comparing the intermediate and

high pH geometries, the local bonding structure of the L4/L4a site appears to be essentially unaffected by nearby (de)protonation processes.

The implications of the simulated site energies and bonding geometries in the context of observed NMR Fermi contact shifts for adsorbed Li^+ are discussed in Section 5.5.1.

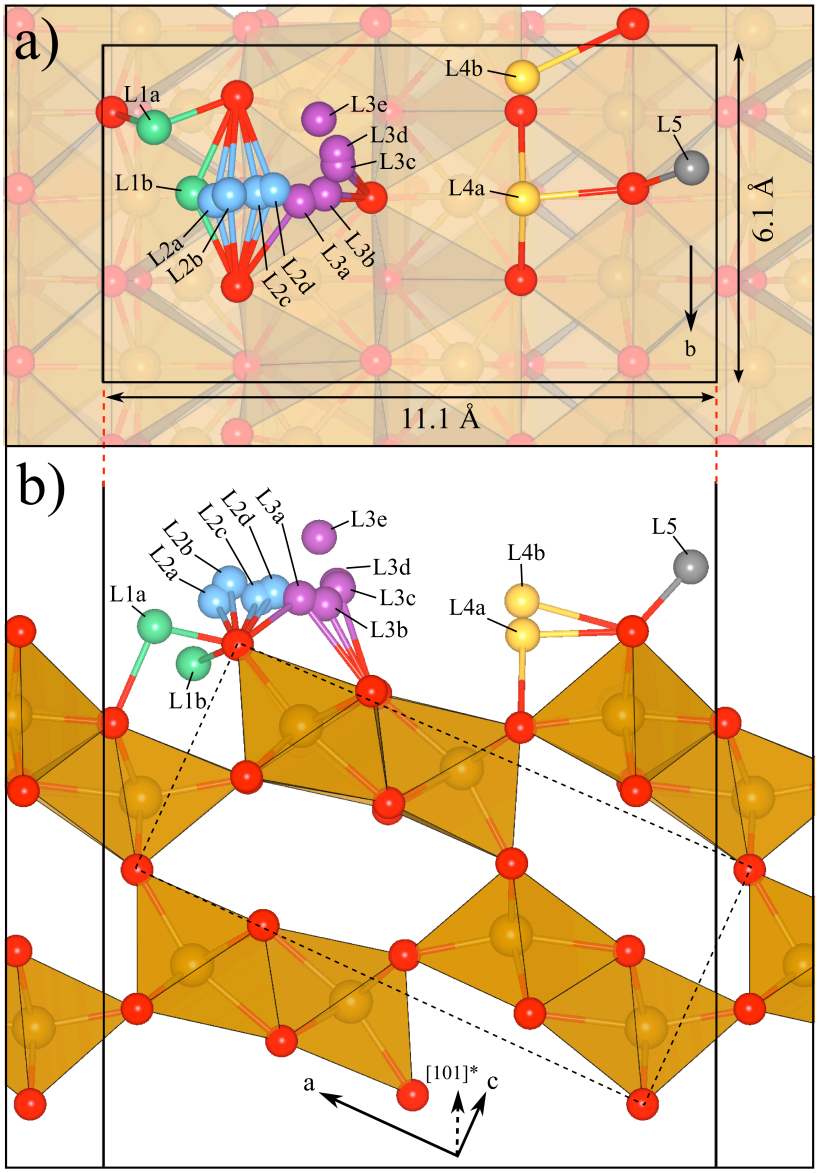

Figure 5-8: Li^+ configurations at the goethite (101) surface at high pH after two surface OH sites have been deprotonated. Fourteen resultant Li^+ sites are illustrated together for comparison. Solvation layer water molecules and protons are not illustrated for clarity. Specific solvation and hydrogen bonding geometries for the most stable sites are illustrated in detail in Figure 5-10. The Li-O bond lengths shown in this illustration are not fully quantitative, as slight relaxations of surface Fe_xOH groups occurred for each configuration, allowing for slightly shorter Li-O bond distances than are possible to represent simultaneously for all configurations. Detailed Li-O bond distances are reported in Table 5-4.

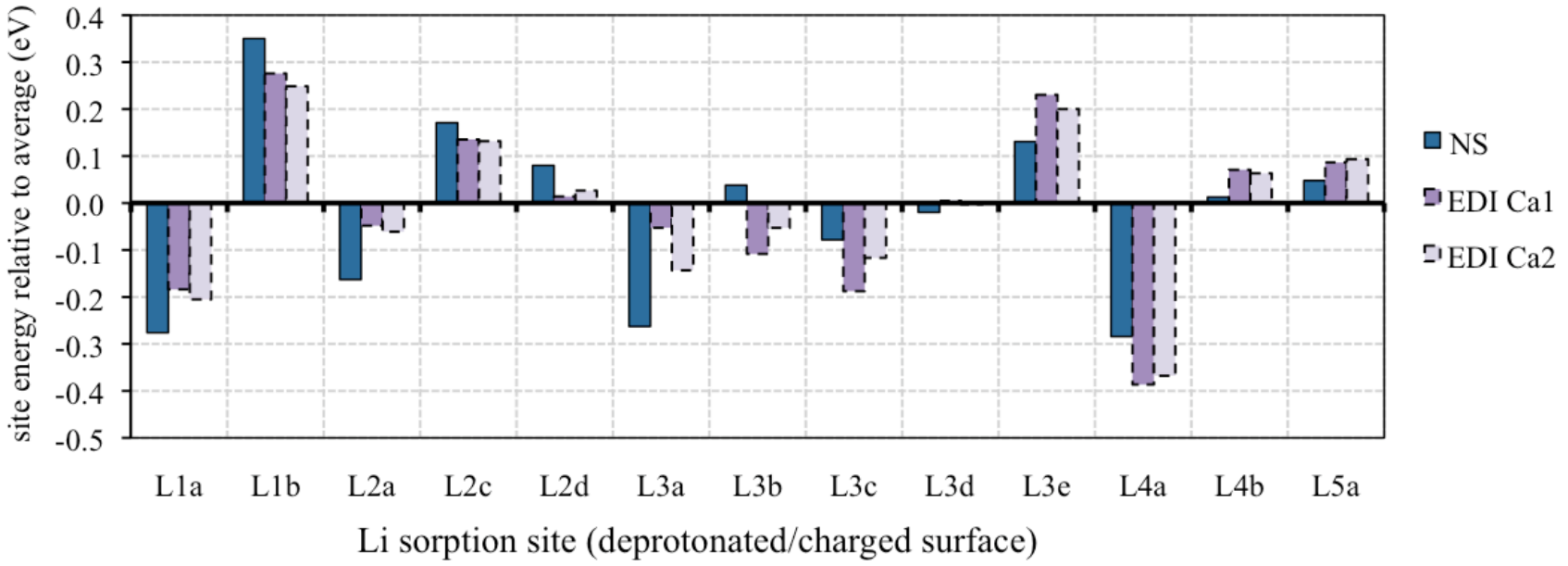

Figure 5-9: Relative Li^+ sorption energies for the Li^+/H^+ configurations at high pH detailed in Table 5-4, and following the site labeling illustrated in Figure 5-8. Two charge correction methods are applied to these simulations, as the goethite (101) surface has a net negative surface charge due to deprotonation at high pH. The results for the NS method (described in Section 5.3.2.3) are shown as blue columns with solid outlines. Results for two independent tests using the EDI method using two different Ca donor ion positions (Ca1, Ca2) are shown in purple with dashed outlines.

Table 5-4: Deprotonation configurations, Li-O bond distances, and calculated relative site energies for Li^+ configurations on the goethite (101) surface at high pH, in which two surface Fe_xOH groups have been deprotonated, leaving a negatively charged surface. The three rightmost columns report calculated relative site energies for three calculation series, one using the NS charge correction method, and two series employing the EDI method using two distinct donor-ion positions (Ca1, Ca2). Charge correction methods are described in Section 5.3.2.3. Bond angles associated with these configurations are reported in Table 5-5.

Li+ site label	deprotonated Fe_xOH sites		Li-O bond distances (Å) – NS 2L geometry						site relative energy vs. avg. (eV)		
			$Fe_1O_{II}(H)$	$Fe_2O_{II}(H)$	$Fe_{3a}O_I(H)$	$Fe_{3b}O_I(H)$	$Fe_{3c}O_I$	H_2O	*NS*	*EDI Ca1*	*EDI Ca2*
L1a	Fe_2O_{II}	$Fe_{3b}O_I$	1.88	-	1.90	-	-	1.99	*-0.28*	*-0.24*	*-0.21*
L1b	$Fe_{3b}O_I$	$Fe_{3b}O_I$	1.94, 1.99	-	-	2.21, 2.27	-	-	*0.35*	*0.22*	*0.25*
L2a	Fe_2O_{II}	$Fe_{3b}O_I$	1.86, 1.88	-	-	-	-	1.94	*-0.16*	*-0.08*	*-0.06*
L2b	Fe_2O_{II}	$Fe_{3a}O_I$	1.84, 1.88	-	-	-	-	1.98	*0.25*	*0.26*	*0.19*
L2c	Fe_1O_{II}	$Fe_{3b}O_I$	1.83, 1.91	-	-	-	-	1.92	*0.17*	*0.11*	*0.13*
L2d	Fe_2O_{II}	$Fe_{3a}O_I$	1.87, 1.97	-	-	-	-	1.97	*0.08*	*0.03*	*0.03*
L3a	Fe_1O_{II}	$Fe_{3a}O_I$	1.98, 2.08	-	2.12	-	-	2.16, 2.22	*-0.26*	*-0.10*	*-0.14*
L3b	Fe_2O_{II}	$Fe_{3a}O_I$	2.06, 2.09	-	1.89	-	-	1.91	*0.04*	*-0.11*	*-0.05*
L3c	Fe_2O_{II}	$Fe_{3a}O_I$	2.01	-	2.03	-	-	2.13, 2.15	*-0.08*	*-0.22*	*-0.12*
L3d	Fe_1O_{II}	$Fe_{3a}O_I$	2.00	-	2.11	-	-	2.04, 2.18	*-0.02*	*-0.05*	*0.00*
L3e	Fe_2O_{II}	$Fe_{3b}O_I$	1.87	-	-	-	-	1.99, 2.00	*0.13*	*0.15*	*0.20*
L4a	Fe_2O_{II}	$Fe_{3a}O_I$	-	1.96	-	-	2.14, 2.15	1.95	*-0.28*	*-0.34*	*-0.37*
L4b	Fe_2O_{II}	$Fe_{3b}O_I$	-	1.90	-	-	1.97, 2.49	1.90	*0.01*	*0.32*	*0.06*
L5a	Fe_2O_{II}	$Fe_{3b}O_I$	-	1.92	-	-	-	1.89, 2.01	*0.05*	*0.06*	*0.09*

Table 5-5: Li-O-Fe dihedral angles associated with the Li-O-Fe linkages detailed in Table 5-4. These angles are computed from the NS method geometries. Bond angles associated with simulations performed using the EDI method, are very similar, differing by no more than 1-2 degrees.

Li+ site label	deprotonated Fe_xOH site		Li-O bond angles (degrees)				
			$Fe_1O_{II}(H)$	$Fe_2O_{II}(H)$	$Fe_{3a}O_I(H)$	$Fe_{3b}O_I(H)$	$Fe_{3c}O_I$
L1a	Fe_2O_{II}	$Fe_{3b}O_I$	118	-	108, 113, 129	-	-
L1b	$Fe_{3b}O_I$	$Fe_{3b}O_I$	90, 91	-	-	78, 135, 121-81, 122, 133	-
L2a	Fe_2O_{II}	$Fe_{3b}O_I$	111, 115	-	-	-	-
L2b	Fe_2O_{II}	$Fe_{3a}O_I$	119, 119	-	-	-	-
L2c	Fe_1O_{II}	$Fe_{3b}O_I$	101, 111	-	-	-	-
L2d	Fe_2O_{II}	$Fe_{3a}O_I$	96 101	-	-	-	-
L3a	Fe_1O_{II}	$Fe_{3a}O_I$	90, 98	-	88, 89, 160	-	-
L3b	Fe_2O_{II}	$Fe_{3a}O_I$	86, 87	-	91, 91, 154	-	-
L3c	Fe_2O_{II}	$Fe_{3a}O_I$	89	-	88, 112, 142	-	-
L3d	Fe_1O_{II}	$Fe_{3a}O_I$	94	-	86, 116, 141	-	-
L3e	Fe_2O_{II}	$Fe_{3b}O_I$	128	-	-	-	-
L4a	Fe_2O_{II}	$Fe_{3b}O_I$	-	91, 92	-	-	81, 81, 148 - 81, 84, 151
L4b	Fe_2O_{II}	$Fe_{3a}O_I$	-	82, 121	-	-	88, 105, 129
L5a	Fe_2O_{II}	$Fe_{3b}O_I$	-	111, 127	-	-	-

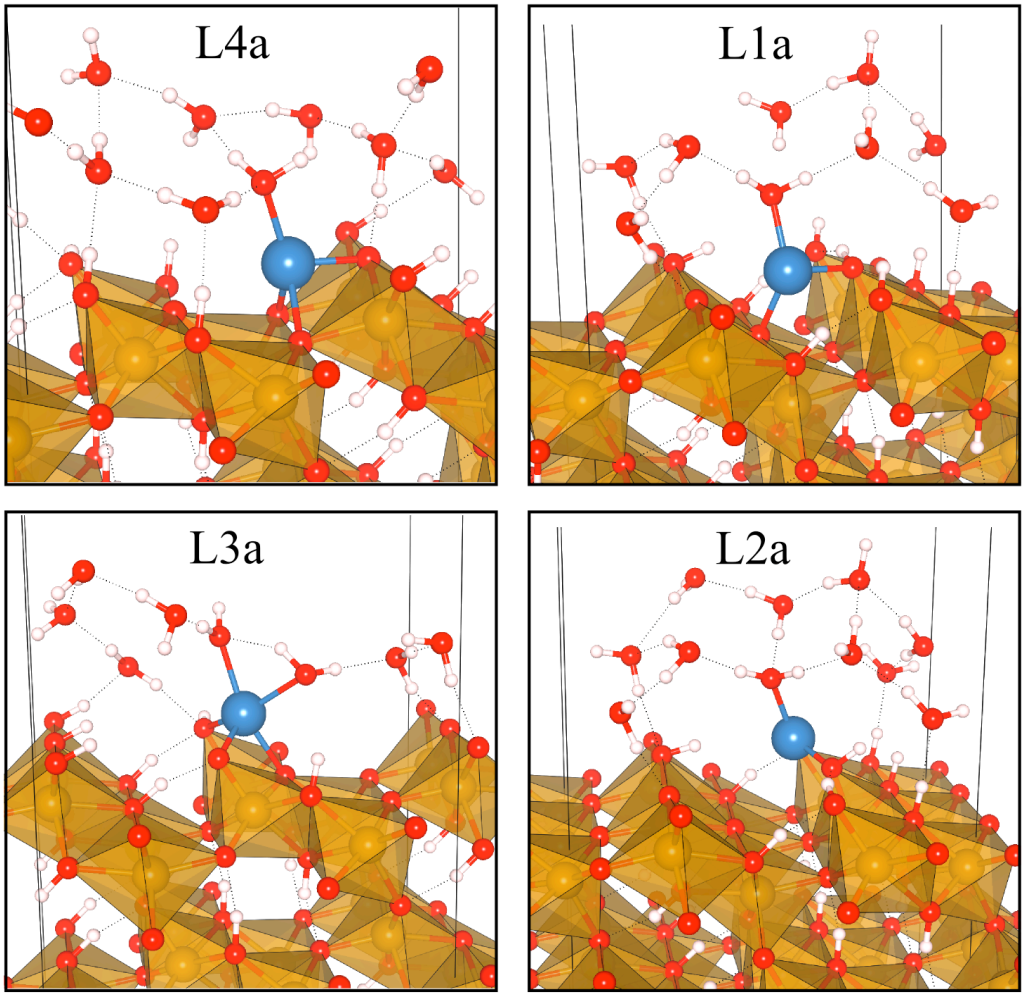

Figure 5-10: The four most stable Li^+ sorption configurations calculated at surface conditions approximating high pH, in which two surface Fe_xOH groups are deprotonated per Li^+ sorbate. Specific bonding details are described in Section 5.4.3 and bond distances are tabulated in Table 5-4. For the purpose of easier visualization, slab supercells are shifted in the XY plane in order to place the Li^+ sorbate near the center of the cell representation. Li-O distances up to d=2.25 Å are illustrated as bicolored bonds.

5.4.4 Li^+ substitution/intercalation in bulk goethite

The simulation of Li^+ in bulk goethite is undertaken to aid in the geometric interpretation of the 289 ppm Fermi contact shift observed by Nielsen et al. [132], assigned to Li^+ intercalated within goethite tunnels forming bonds with neighboring O atoms in a tetrahedral arrangement. The case of Li-substitution or intercalation within goethite arguably provides the best reference case for a Li-O-Fe configuration whose bonding structure can reasonably be inferred from crystallographic insights. Being a fully encapsulated defect with Li-O bonds available in all but two directions (either way along the tunnel direction), it is reasonable to conclude that a maximal aggregate Fermi contact shift should be associated with the intercalated Li^+ configuration, assuming a positive shift contribution from each Li-O-Fe linkage. If the local structure the intercalated Li defect can be more precisely determined, this maximal Fermi contact shift configuration can be used to help set the scale for the shift-per-linkage model used to analyze surface configurations with relatively fewer overall linkages, as discussed further in Section 5.5.1.

To model the case of Li intercalation, simulations were performed on two distinct material models intending to bookend the configurational space available to Li^+ within the goethite tunnel structure. These materials include a fully Li-substituted $LiFeO_2$ goethite analogue (goethite-like $LiFeO_2$), akin to that described in [143] and an isolated Li^+ defect in otherwise undefected goethite bulk supercell, achieved by simply replacing one bulk H^+ with Li^+ and relaxing the supercell in the presence of this point defect.

Due to the small size of the goethite/$LiFeO_2$ primitive unit cell (16 atoms), a conventional Monkhorst-Pack (non-Γ) k-point mesh was chosen for bulk supercell cell simulations (details in Table 5-6), while other calculation parameters, including plane-wave energy cutoff, pseudopotentials, Fe spin states, and GGA+U parameters, were shared with the surface slab simulations. These bulk simulations are not susceptible to many of the methodological obstacles associated with simulation of periodic slabs and related electrostatic challenges, and thus can additionally serve as a cross-check on the bonding geometry trends observed for the more challenging surface simulations.

The calculated lattice parameters and primitive unit cell volume of undefected goethite (α-FeOOH, *Pnma* setting) are reported in Table 5-4. These values closely match those reported in previous DFT study of goethite and related bulk materials [9], although the use of a different O pseudopotential causes the calculated goethite lattice parameters to differ slightly from those reported in previous work (now in better agreement with experiment). Additional calculation data is shown for an undefected goethite bulk supercell (1×4×2 unit cells) for ease of comparison with the isolated Li^+ substitution defect simulated in an equivalent supercell.

To construct the fully-intercalated goethite-like $LiFeO_2$ phase, each of H atoms in the goethite primitive unit cell were swapped with Li, and the cell lattice parameters, angles, and internal coordinates were fully relaxed and optimized using standard DFT methods within VASP. The resulting structure is very similar to that described in [143] and is distinct from more common and stable $LiFeO_2$ polymorphs. The optimized Li-substituted structure retains the double-chain and tunnel configuration of the goethite parent structure, but is compressed in the *a*- and *b*-dimensions, and elongated in the *c*-dimension, as compared to undefected goethite. This structure retains the symmetry of the *Pnma* space group setting of undefected goethite, in agreement with the symmetry group assigned to the structure by [143]. The lattice parameters and unit cell volume of the goethite-like $LiFeO_2$ phase are reported in Table 5-6 along with those of bulk goethite, for comparison. Table 5-7 lists the calculated primitive lattice coordinates of both goethite and the goethite-like $LiFeO_2$ phase.

Table 5-6: Experimental (italics) and calculated (non-italics) structural parameters for fully Li-substituted goethite-like $LiFeO_2$, bulk goethite, and a supercell including a single Li^+ substituted at a proton site within bulk goethite.

Structure (supercell size)	supercell size	kpoint mesh	simulation stoichiometry	a (Å)	b (Å)	c (Å)	cell volume (Å3)
goethite-like LiFeO2, expt. [143]	1×1×1	n/a	-	9.68	2.93	5.01	n/a
goethite-like LiFeO2, calculated	1×1×1	3×8×6	$4(LiFeO_2)$	9.73	2.92	4.98	141.35
goethite, expt. [1]	1×1×1	n/a	-	9.96	3.02	4.61	n/a
bulk goethite, calculated	1×1×1	3×8×6	4(FeOOH)	9.92	3.01	4.58	136.93
bulk goethite, calculated	1×4×2	3×2×3	32(FeOOH)	9.93	12.02	9.13	1089.90
isolated Li+ substitution	1×4×2	3×2×3	$Fe_{32}O_{64}H_{31}Li$	10.93	12.01	9.16	1093.00

Table 5-7: Primitive cell coordinates of goethite and the goethite-like $LiFeO_2$ phase optimized using ab initio methods. Both structures have *Pnma* space group symmetry.

goethite, α-FeOOH, *Pnma*

atom	x	y	z
Fe	0.1443	0.25	0.9479
H	0.9090	0.25	0.5924
O1	0.8028	0.25	0.3064
O2	0.9450	0.25	0.7996

goethite-like $LiFeO_2$, *Pnma*

atom	x	y	z
Fe	0.1346	0.25	0.0800
Li	0.9004	0.25	0.4116
O1	0.7570	0.25	0.1026
O2	0.9892	0.25	0.7660

Table 5-8: Calculated Li-O bond lengths and Li-O-Fe linkages for the bulk supercell calculations of goethite-like $LiFeO_2$ and the isolated Li^+ substitution in goethite. Shown in italics are Li-O distances longer than 2.10 Å, which are not considered to be participating bonds for this study.

goethite-like $LiFeO_2$			isolated Li^+ substitution		
Li-O distance	# Li-O-Fe linkages	Li-O-Fe angles (°)	Li-O distance	# Li-O-Fe linkages	Li-O-Fe angles (°)
1.964	3	94, 94, 164	1.756	3	92, 108, 139
2.016	3	88, 88, 175	1.862	3	81, 103, 118
2.016	3	88, 88, 175	1.962	3	71, 117, 151
2.076	3	79, 89, 89	*2.441*	*3*	*71, 104, 152*
2.319	*3*	*72, 86, 128*	*2.594*	*3*	*64, 100, 136*
2.319	*3*	*72, 86, 128*			

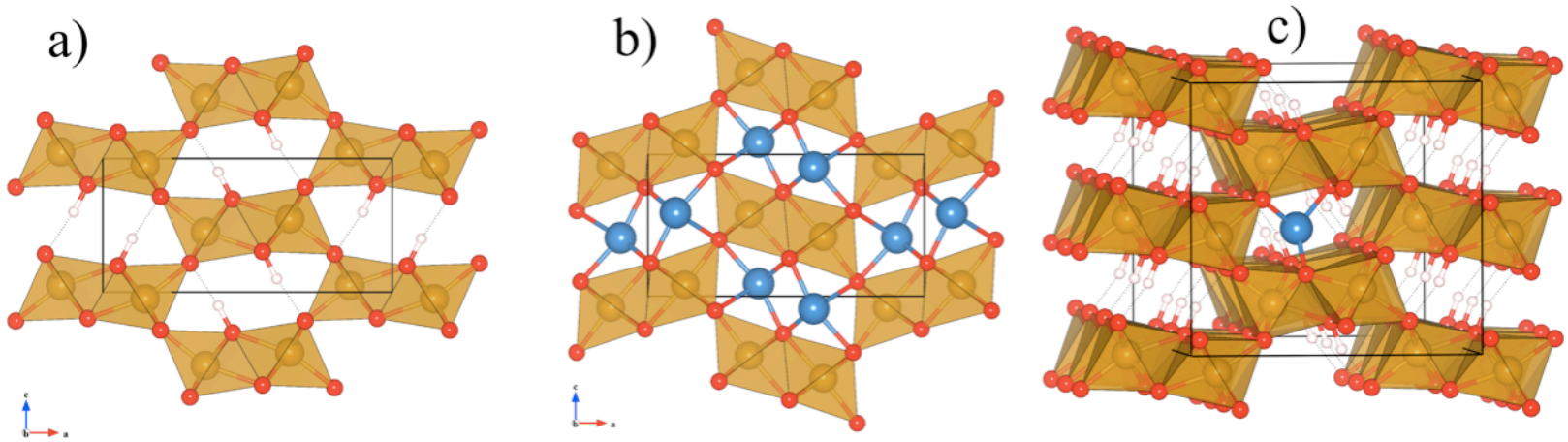

Figure 5-11:

a) Bulk structure of goethite looking down the characteristic tunnels along the b-axis. The primitive unit cell is outlined with a black solid line. Fe atoms shown as brown octahedral. O atoms are shown as red spheres. H atoms are shown as white spheres.

b) The calculated structure of goethite-like $LiFeO_2$, which shares the chain and tunnel structures of goethite while adopting a different primitive cell size and shape. Li ions are shown as blue spheres.

c) The binding of an isolated Li^+ ion substituted on a proton site in bulk goethite.

Referring to Figure 5-11, the Li^+ ions in the goethite-like $LiFeO_2$ structure form distorted octahedral structures with 6 Li-O bonds at distances of 1.96, 2.02, 2.02, 2.08, 2.32 and 2.32 Å, all shared with O atoms having three underlying Fe-O bonds characteristic of the bulk structure. The four shorter Li-O bonds with d ≤2.08 Å are arranged in an asymmetric planar configuration about the central Li^+ ion. Three of these Li-O bonds have Li-O-Fe dihedral angles near 170°, while the remaining nine have angles near 90°. The next set of Li-O bonds are found at d=2.32 Å, with each bond forming Li-O-Fe angles of 72°, 86° and 128°.

As an alternative perspective on the geometry of Li^+ in goethite, a final configuration simulates the local binding environment of Li^+ in bulk goethite as an isolated substitution, without inducing the bulk phase transformation to the goethite-like $LiFeO_2$ end member. This structure more closely represents the case of incomplete Li-exchange in the goethite tunnels, such that the overall structure of goethite is preserved. While complete Li-exchange was reported in one reference [143], the NMR-based literature [132] reports that incomplete Li-exchange was likely the case for their samples, due to the detection of un-reacted Li species (likely LiOH, Li_2CO_3) in solution that would not be present had the reactant goethite microparticles been fully Li-exchanged, based on a mass-balance assessment of reactants and products. The authors hypothesize that most Li-exchange occurs near the surface of the goethite microparticles, while the particles retain the goethite structure more generally.

In this calculation, a single H^+ position was substituted with Li^+ in a 1×4×2 goethite supercell, and the cell lattice parameters and internal coordinates were allowed to fully relax. The larger ionic radius of Li^+ compared to H^+ causes a slight expansion of the surrounding goethite lattice, resulting in a defect formation volume of roughly +3.1 $Å^3$. The isolated Li-substitution defect forms three Li-O bonds with neighboring bulk O atoms at d=1.76, 1.86 and 1.96 Å, with a variety of Li-O-Fe dihedral angles ranging from 71-151° (tabulated in Table 5-8).

To assess the geometrical similarities of the structure of Li^+ within the goethite tunnels

and the structures calculated for adsorbed Li^+ at the goethite surface, the isolated Li^+ substitution defect structure was mapped onto the goethite (101) surface for comparison with the surface configurations already simulated. Figure 5-12 illustrates the isolated Li^+ defect supercell after either side of the (101) plane bisecting the defect site has been removed. This procedure was done only for visualization purposes and no surface relaxation or optimization was performed, nor was a stable surface protonation structure investigated for this purpose. The bisected cells have been rotated such that visual comparison is more straightforward. The first manifestation of the bulk isolated Li^+ defect mapped to the goethite surface (Figure 5-12a) most closely resembles the L5 family of sites described in Sections 5.4.2 and 5.4.3, which were not among the relatively stable sites calculated. The second manifestation (Figure 5-12b) most closely resembles site L1a, the third-most stable site calculated for the high pH surface regime, and the site that most closely matches the configuration proposed by Kim et al. In both manifestations of the bulk defect at the goethite surface, the Li^+ ion is bound more closely to the surface than is observed for the relaxed surface sorption configurations, arguably attributable to the presence of one or more solvating water molecules present in the surface simulations that serve to draw the Li^+ ion somewhat toward the hydrogen-bonded solvation layer.

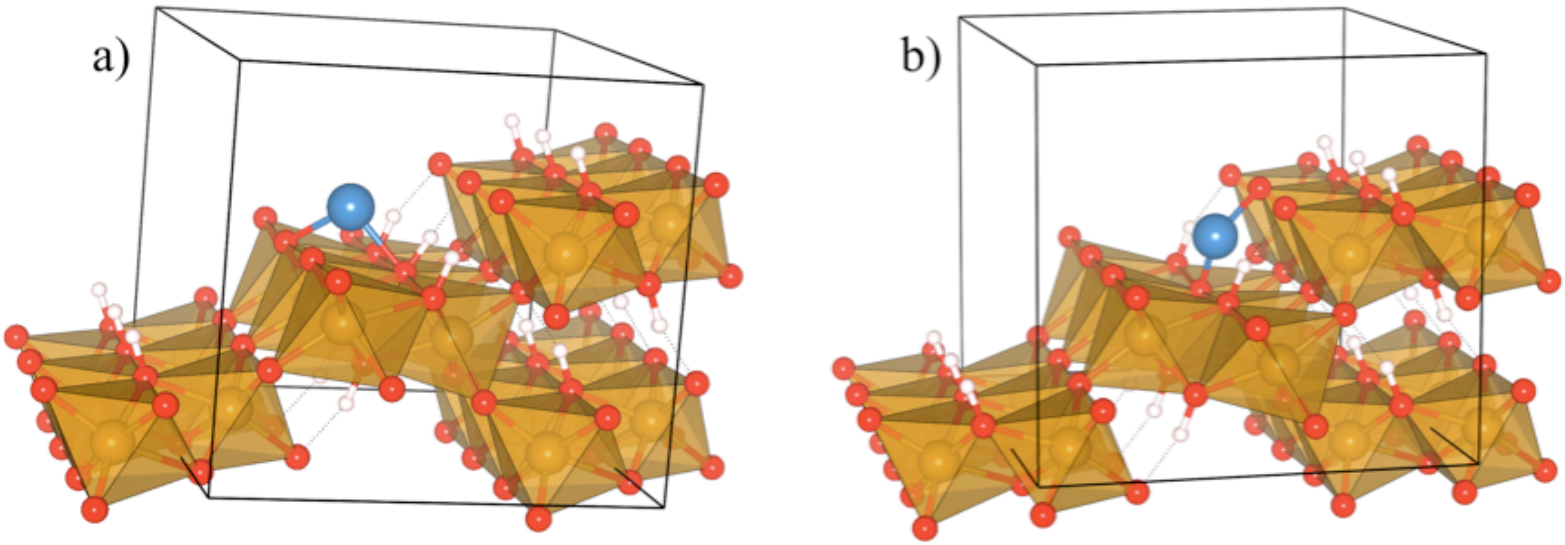

Figure 5-12: The isolated Li^+ substitution mapped onto the goethite (101) surface, which runs diagonally across the defect supercell, outlined in black. No relaxation or optimization of coordinates was performed for this figure, which is presented as a visualization aid only. Depending on which face of the (101) plane is removed (i.e., the upper or lower half of the cell), the Li^+ defect can be interpreted as occupying either of two distinct positions at the goethite (101) surface.

5.5 Discussion

5.5.1 Li^+ linkage counting and projected Fermi contact shifts

The *ab initio* results for Li^+ adsorption at intermediate and high pH are now analyzed using the simple shift-per-linkage model to compare the projected Fermi contact shifts of the simulated geometries with NMR observations. While linkage counts are computed for all simulated configurations, particular attention is paid to the linkage counts those configurations found to be low in energy, and therefore more likely to be present in real systems. The linkage counting procedure assigns one Li-O-Fe linkage for each underlying Fe atom coordinated to the surface O(H) group participating in the Li-O bond. In this manner, the singly-coordinated $Fe_1O_{II}(H)$ site contributes one linkage when bonded to a Li^+ sorbate, the doubly-coordinated $Fe_2O_{II}(H)$ site contributes two linkages, and so forth. For linkages associated with the intercalated Li^+ defect within bulk goethite, all Li-O bonds contribute three linkages, as each O atom within bulk goethite is bound to three Fe atoms.

For the first iteration of the linkage counting procedure, only Li-O bonds with distances less than d=2.05 Å are assumed to contribute to the Fermi contact shift effect, as linkages formed by longer Li-O bonds are not mentioned as contributors to observed NMR signals in related materials [132]. However, because Li-O bonds of slightly longer length are observed in many configurations, bonds with Li-O distances between 2.05-2.25 Å are also analyzed and tabulated separately for the purpose of providing additional structural context. An arbitrary upper limit of d=2.25 Å is chosen for the bond distance search, although this choice does not exclude any additional Li-O distances that might be expected to contribute to bonding behavior as the next Li-O shell is at a distance of at least d=2.32 Å for all simulated configurations.

Figure 5-13 plots the linkage counts associated with the bulk simulations, including the fully Li-substituted goethite like $LiFeO_2$ phase and the isolated Li^+ substitution defect. In this plot, the lower, darker set of columns corresponds to linkage counts with Li-O bond lengths less than 2.05 Å, while the upper columns (lighter in color) add to the lower

columns the additional linkages formed by Li-O distances between 2.05-2.25 Å. The fully substituted $LiFeO_2$ phase has three bonds below the d=2.05 Å length, forming nine Li-O-Fe linkages, and another slightly longer bond at d=2.08 Å, forming another three linkages if this longer bond is counted toward the linkage total. The isolated Li^+ substitution defect has three bonds below d=2.05 Å, forming nine Li-O-Fe linkages. No Li-O bonds within the range of d=2.05-2.25 Å are formed by the isolated Li^+ substitution defect.

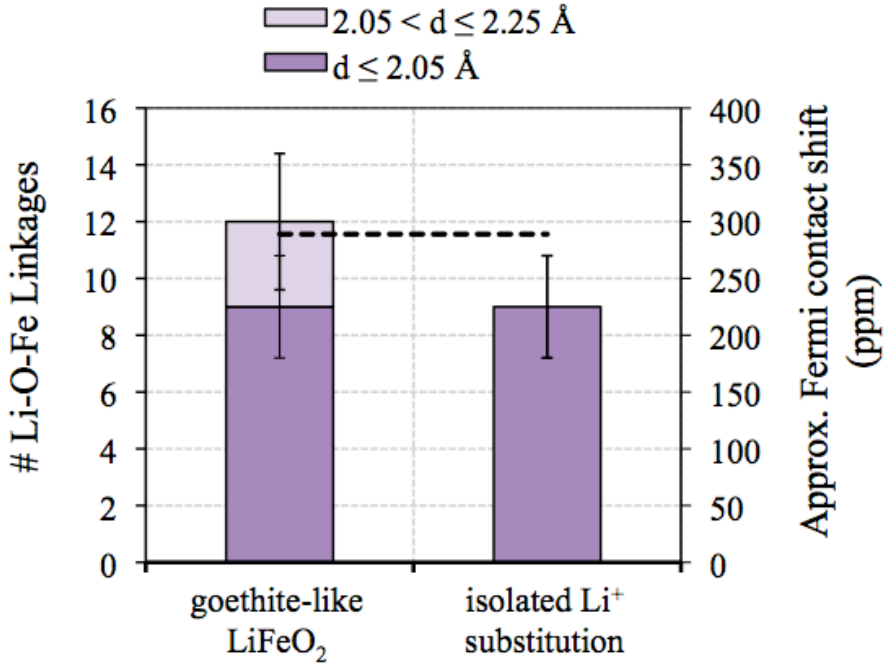

Figure 5-13: Li-O-Fe linkage counts associated with simulated Li^+ coordination environments in two bulk environments. Bond lengths and angles for these structures are reported in Table 5-8. The right ordinate axis reflects the assignment of a uniform Fermi contact shift of 25 ppm per Li-O-Fe linkage. The error bars on the columns reflect uncertainty in this shift assignment, illustrating the aggregate shift range that would result from using a shift-per-linkage value ranging anywhere between 20-30 ppm. The horizontal dashed line marks the 289 ppm aggregate Fermi contact shift measurement reported by Nielsen et al. {Nielsen, 2005 #235} for Li-intercalated goethite.

The 289 ppm Fermi contact shift measured by Nielsen et al. for Li-intercalated goethite can now be divided by the linkage counts formed by the bulk structures to establish an effective shift-per-linkage value. Assuming a uniform, additive Fermi contact shift for each linkage, the two simulated bulk intercalation structures would yield shifts ranging

between of 23.75 and 32.1 ppm per linkage, calculated by dividing the 289 ppm aggregate value by 12 or 9 linkages, respectively. This range is in agreement with the approximate range of 20-30 ppm used by Kim et al. when making site assignments of Li^+ at the goethite surface.

We project an estimation of Fermi contact shift values associated with the Li-O-Fe linkage counts on the right-hand y-axis of Figure 5-13. This measure maps each linkage to a uniform Fermi contact shift value of 25 ppm, the center of the range proposed by Kim et al. Error bars shown on the linkage count columns do not correspond to uncertainties in the number of linkages, but rather to uncertainties in the expected total Fermi contact shift associated with each configuration. The error bars indicate the possible range of Fermi contact shifts for each configuration assuming an average shift-per-linkage value anywhere between 20-30 ppm.

The dashed horizontal line shown in Figure 5-13 marks the 289 ppm Fermi contact shift measurement obtained for goethite intercalated with Li^+. The fully Li-substituted $LiFeO_2$ phase most closely reproduces the aggregate Fermi contact shift observed experimentally based on the shift-per-linkage value estimate range, if the slightly longer Li-O bond (2.08 Å) for this configuration can be assumed to contribute to the aggregate Fermi contact shift. The estimated Fermi contact shift of the isolated Li-substitution defect, with nine linkages, falls short of the 289 ppm aggregate shift value under the 20-30 ppm shift-per-linkage range adopted, although the discrepancy is small. We do not intend for these aggregate Fermi contact shift estimates to be taken as independent evaluations of the accuracy of either of the bulk Li-intercalation simulation geometries, but rather to provide additional structural context for the assignment of Fermi contact shift estimates to the surface Li^+ sorbate configurations.

Figure 5-14 plots the linkage counts associated with the Li adsorption geometries simulated at intermediate pH (energy and geometry details are reported in Section 5.4.2). Figure 5-15 accordingly plots the linkage counts associated with the sorption geometries simulated at high pH (details in Section 5.4.3). Both plots adopt the two-tiered linkage

counting framework described above for Figure 5-13, in which Li-O bonds are divided into two groups, with those bonds with Li-O distances below d=2.05 Å and between d=2.05-2.25 Å being treated separately, and adopt the same Fermi contact shift-per-linkage estimate ranges employed in Figure 5-13.

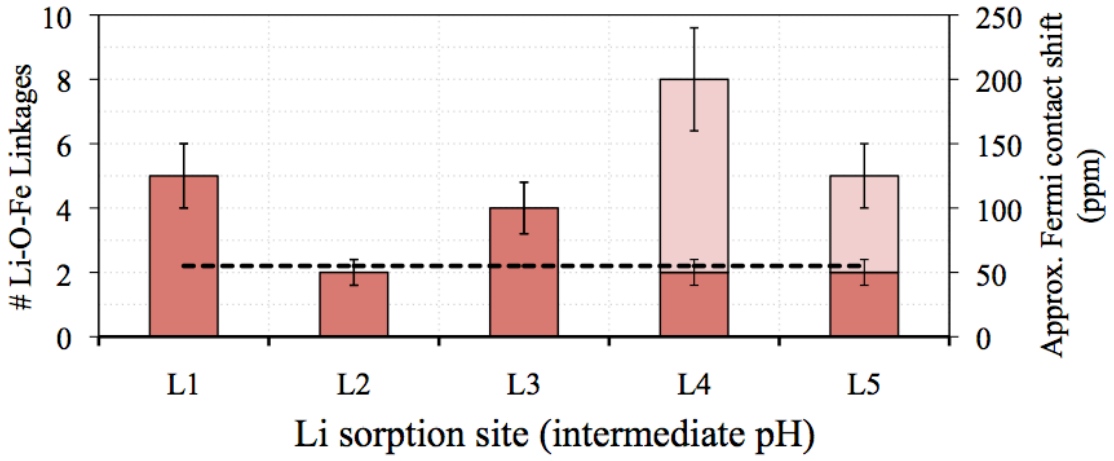

Figure 5-14: Li-O-Fe linkage counts for the simulated Li^+ sorption configurations at intermediate pH. The linkage counts have been divided into two distance regimes. The dark red bars count Li-O-Fe linkages with Li-O distances shorter than d=2.05 Å. The light red bars count linkages with longer Li-O distances, larger than d=2.10 Å (no Li-O bonds are observed in the intermediate range). The right-hand ordinate axis represents the estimated approximate Fermi contact shift associated with each Li configuration, assuming a constant shift of 25 ppm per Li-O-Fe linkage. Because this per-linkage shift value is uncertain, error bars assigned to the linkage counts represent the range of total Fermi contact shift that would be associated with each configuration for shift values between 20-30 ppm per Li-O-Fe linkage. The 55 ppm Fermi contact shift associated with Li sorption at intermediate pH reported by Nielsen et al. is shown as a dashed horizontal line.

The dashed horizontal line in Figure 5-14 marks the 55 ppm Fermi contact shift measured by Nielsen et al. for Li^+ adsorbed on goethite at intermediate pH, setting a target level for estimated Fermi contact shifts of the various simulated configurations in this pH regime. Among these configurations, considering only the tier of shorter Li-O bonded linkages (dark columns), the L2, L4 and L5 configurations are shown to have linkage counts within the acceptable range, while configurations L1 and L3 have too many linkages to be considered in agreement with the experimental observations. If longer Li-O bond configurations participate to any degree in the Fermi contact shift mechanism, only the L2 site will remain in agreement with the shift value observed by NMR measurements.

The L2 site, illustrated on the left side of Figure 5-7 in the previous section is effectively indistinguishable from the site proposed by Kim et al. as the Li^+ binding configuration at intermediate pH, and is also the most energetically stable among the simulated intermediate pH configurations.

The L4 site has only slightly higher energy than the L2 site, but a completely different bonding configuration (right side Figure 5-7). While the L4 site has one clearly-defined bond to the deprotonated Fe_2O_{II} group (contributing two Li-O-Fe linkages), the Li^+ sorbate is arguably also bonded (or perhaps only electrostatically attracted) to two nearby $Fe_{3c}O_{II}$ groups at slightly longer Li-O distances (2.11, 2.20 Å), a binding configuration that was not discussed in the NMR literature. However, if the $Fe_{3c}O_{II}$ groups associated with the L4 site do not contribute to the Fermi contact shift value due to their relatively long Li-O distances, then the L4 site should also be considered as a potential binding configuration at intermediate pH.

In addition to having linkage counts leading to aggregate Fermi contact shift estimates higher than the experimental target value, the L1, L3, and L5 configurations are relatively unstable configurations, at least 200 meV less stable than the L4 site, and are therefore considered unattractive candidates for sorption site assignments at the intermediate pH goethite surface.

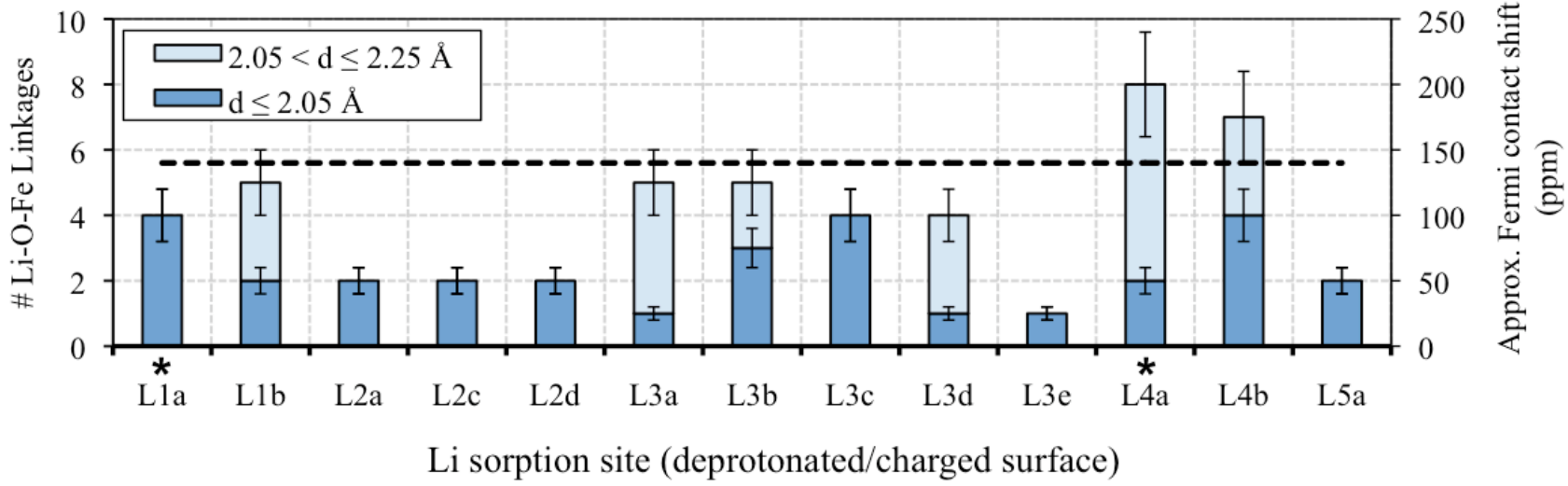

Figure 5-15: Li-O-Fe linkage counts for the Li^+ configurations on the goethite (101) surface at high pH. Dark columns sum the number of Li-O-Fe linkages with Li-O bond distances up to d=2.05 Å. Light columns sum the number of Li-O-Fe linkages with longer Li-O distances, d=2.05 Å and greater, with an upper Li-O distance limit set at d=2.25 Å. The right-hand ordinate axis represents the estimated approximate Fermi contact shift associated with each Li configuration, assuming a constant shift of 25 ppm per Li-O-Fe linkage. Because this per-linkage shift value is uncertain, error bars assigned to the linkage counts represent the range of total Fermi contact shift that would be associated with each configuration for shift values between 20-30 ppm per Li-O-Fe linkage. The dashed horizontal line at 140 ppm marks the experimentally measured Fermi contact shift for Li adsorbed on goethite at high pH [132]. Asterisks mark the L4a and L1a sites, which are the most and second-most energetically stable sites, respectively.

Figure 5-15 shows the Li-O-Fe linkage totals associated with each Li^+ configuration at high pH. As was done for the intermediate pH configurations, the Li-O bonds are separated into two groups – those with Li-O distances up to 2.05 Å, and those with longer bonds, up to d=2.25 Å. Specific Li-O distances to surface Fe_xOH groups and solvation layer water molecules for these configurations are reported in Table 5-4. The dashed horizontal line in Figure 5-15 marks the 140 ppm Fermi contact shift observed by NMR methods [132, 133] associated with adsorbed Li on goethite at high pH. As with the intermediate pH case, this experimental value is used as a target aggregate shift value for the evaluation of calculated sorption configurations.

With the relative energies of the high pH adsorption configurations in mind, we draw particular attention to the linkage counts of the few most stable sites, marked with asterisks in Figure 5-15.

The most stable Li^+ adsorption configuration at high pH, site L4a, closely resembles the L4 site that was shown to be second-most stable in the intermediate pH series of calculations. The L4a site shows two relatively long Li-O distances to underlying $Fe_{3c}O_{II}$ groups (d=2.14 and 2.15 Å, respectively) and one shorter Li-O bond with a deprotonated Fe_2O_{II} group (d=1.96 Å). By summing the linkages of this configuration for bonds shorter than d<2.05 Å, the L4a site is found to possess only two linkages, both due to the 1.96 Å bond with an Fe_2O_{II} group. The projected Fermi contact shift of two linkages is 40-60 ppm, far below the 140 ppm target value obtained by experiment. Alternatively, if the longer Li-O distances found for this site are considered to fully contribute to aggregate Fermi contact shift, the L4a site forms 8 linkages in total, leading to a projected Fermi contact shift between 160-240 ppm; considerably beyond the experimentally measured value of 140 ppm.

Sites L1a and L1b most closely resemble the high pH sorption configuration proposed by Kim et al. However, these sites have rather different relative energies, with the L1a site being the second-most stable site of those tested for both the NS and EDI methods, while

the L1b site is among the least stable. Due to this relative instability, we rule out the L1b configuration as a candidate sorption configuration at high pH. The L1a site, which bridges between one $Fe_1O_{II}H$ group and one deprotonated $Fe_{3b}O_I$ group forms a total of four Li-O-Fe linkages with relatively short bond Li-O lengths of 1.88 and 1.90 Å. Based on the shift-per-linkage model, this site, with four total Li-O-Fe linkages, should produce a Fermi contact shift between 80-120 ppm, significantly smaller that observed by Nielsen et al.

We now discuss the possible implications of the failure of the simple shift-per-linkage model to yield aggregate Fermi contact shift estimates in agreement with experiment for the low-energy Li adsorption configurations at high pH. {Nielsen, 2005 #235}

First, it remains a possibility that *ab initio* simulation results are affected by one or more sources of error that lead to erroneous conclusions about relative site stability. However, results for all simulation methods (NS method, EDI methods Ca1/Ca2, and testing using deeper slabs) suggest similar qualitative site energy orderings, and predict the overall stability of the L4a site at high pH. The rms differences associated with these calculation methods are considerably smaller than the energies that separate the L4a site from the average total energy for each calculation series, indicating that the consistency in predicting the stability of the L4a site is not a coincidental result.

We instead call into question the applicability of an inflexible shift-per-linkage model in the presence of a variety of Li-O-Fe configurations of varying bond distance, angle, and coordination number. In the case of the L4a site, the choice to exclude slightly longer Li-O bonds as potential contributors to the Fermi contact shift mechanism results in an aggregate shift far too low to be in agreement with experiment. Conversely, the choice to include these longer Li-O linkages as fully-participating contributors to the Fermi contact shift mechanism results in an overestimation of the aggregate shift value, as compared to experiment. However, if these long Li-O linkages were to contribute a smaller but nonzero shift to the aggregate value (on the order of 12-15 ppm/linkage), the estimated

aggregate shift of the L4a site would agree quite well with the experimentally measured value of 140 ppm.

The reduced shift value implied for the two longer linkages found in the L4a configuration might be attributable to either or both of two factors. The first is that the longer Li-O distances associated with these linkages (2.14, 2.15 Å) simply result in a reduced amount of spin density transfer/overlap from Fe atoms to the Li^+ orbitals. A similar explanation is offered by Kim et al. when considering possible Li binding sites on/in akaganeite {Kim, 2010 #379}, in which an asymmetric bidentate binding arrangement is proposed to account for an observed shift value that falls between integral multiples of the assumed shift-per-linkage value. Another potential mitigating factor for the estimated shift of the L4a site is the distribution of Li-O-Fe dihedral angles in this configuration, which includes six angles near or below 90°, and two relatively broader angles of 148° and 151°. The linkages with relatively acute Li-O-Fe angles might be expected to better contribute to the Fermi contact spin density transfer mechanism due to the relatively close arrangement of Li and Fe atoms. But the larger-angle linkage configurations, coupled with the relatively long length of the Li-O bonds forming the linkages, might be expected to contribute a smaller shift component, or none at all, depending on the degree of spin density transfer between Li and Fe atoms spaced at remote ends of the Li-O-Fe linkage.

A full assessment the sensitivity of the Fermi contact shift mechanism to changes in bond length, angle, and other structural and electronic factors is an open task for future research on these materials, but is beyond the scope of this work.

5.5.2 Simulating ion sorption at charged surfaces

The relative configurational energies of Li^+ sorbates at a charged, deprotonated surface were shown to be largely independent of the choice between two distinct methods used to correct for spurious electrostatic interactions that are inescapable in a simulation regime employing periodic boundary conditions. Both methods (NS and EDI) depend upon the

formation of a positively charged point defect (Fe^{4+}, Ca^{2+}) to compensate for the negative charge density associated with the deprotonated surface. The two correction methods operate by different charge-transfer mechanisms and locate the counter-charge at different locations within the slab. When the two correction methods are applied uniformly to the same series of surface sorbate geometries, the relative energies among the sorbate geometries are found to be qualitatively similar. This effect was demonstrated for simulations of both deprotonation and Li+ sorption for the goethite surface. The similarity of relative energies for the NS and EDI methods suggests that the relative energies among the series of surface configurations are governed principally by the local surface geometries rather than the method of treating the charged surface. Additional benefits of the NS and EDI methods for modeling charged surfaces are that large numbers of solvation layer water molecules are not necessary to form hydration shells around aqueous counter-ions, and because the imposed defects are fixed within/below the slab, there is effectively no configurational energy uncertainty associated with explicitly modeling the solvation structure of counter ions in the active region of interest (the upper slab surface). We propose the combined NS and EDI methods as a computationally-inexpensive means of evaluating the relative energies of charged-surface sorbates, defects and reconstructions within the periodic slab modeling framework, with some limitations as follows.

We stress that the NS and EDI methods are provide an unphysical and presumably inocorrect, but approximately constant, energy associated with the compensating charges in the system. For a real charged surface this energy would be that associated with solvated counterions in solution near the surface (the electric double layer energy). If the real system has an approximately constant electric double layer energy for a series of local adsorbate structures then the NS and EDI methods can be expected to yield accurate relative energies. However, if electric double layer energies in real systems have significant variations in response to changing local adsorbate configurations, these are unlikely to be captured by the NS and EDI approximations and significant inaccuracies in relative energies may result. We believe the assumption of an approximately constant

electric double layer energy is reasonable for our study, where the structures we compare have identical surface charge and closely related surface structural environments. It is not clear under what circumstances in general different structures can be assumed to have negligible differences between their electric double layer energies, but structures with large changes in surface charge or surface adsorption topology (e.g. inner vs. outer sphere binding) will almost certainly not fit this assumption.

5.6 Conclusions

We have conducted an *ab initio* study of Li^+ sorption at the goethite (101) surface under two simulated pH regimes. Bidentate and multi-dentate Li^+ surface configurations are shown to be the stable arrangements in both pH regimes, intended to simulate intermediate and high pH conditions, although limitations on the accuracy of the *ab initio* methods employed make it difficult to determine the uniquely most stable sites. Estimation of the aggregate Fermi contact shifts of stable Li^+ sorption configurations is attempted based on a bond counting model that attributes a uniform additive shift to each Li-O-Fe linkage formed by the sorbate Li^+, but the results of this strategy do not yield consistent agreement with observed ^6Li Fermi contact shifts measured by NMR experiments reported in the literature. However, the failure of this strategy is arguably due to non-uniform actual Fermi contact shift contributions from Li-O-Fe arrangements of varying bond lengths, angles, and other local configurational variations, all of which serve to complicate the interpretation of both NMR and *ab initio* results. While the uniform shift-per-linkage model may aid in establishing qualitative predictions for adsorption site configurations and sorption trends, it may fail to adequately describe situations where the Fermi contact shift contributions of local atomic configurations vary significantly from the uniform shift value chosen.

A goethite-like $LiFeO_2$ phase and an isolated Li-substitution within otherwise undefected bulk goethite provide additional examples of Li-O-Fe structures that can aid in the interpretation of surface sorption data. The simulated goethite-like $LiFeO_2$ structure shares many structural characteristics with goethite, including the characteristic double-tunnels, but should be considered a distinct phase. The *ab initio* optimized structure of goethite-like $LiFeO_2$ shows excellent agreement with reported experimental lattice parameters and symmetry operations for this structure. This study presents the first known detailed description of the atomic coordinates of the goethite-like $LiFeO_2$ material.

While simulation results do not elicit a simple story describing the sorption behavior of Li^+ at the goethite (101) surface, the simulation methods developed for evaluating charged, deprotonated surfaces (and the surface deprotonation reaction itself) are shown to be effective in overcoming some of the challenges associated with modeling charged surfaces within a periodic slab framework. This is most clearly supported by the results for the relative deprotonation energies of four Fe_xOH groups at the (101) surface agreeing well with equivalent values derived from experiment. The methods described and implemented here offer a computationally inexpensive means of evaluating configurational energies on charged slabs.

Acknowledgments: The authors sincerely appreciate funding support for this project by the National Science Foundation (NSF) Collaborative Research in Chemistry (CRC) Program, Award CHE-0714121. Calculations in this work were performed in part on the supercomputing resources of the Extreme Science and Engineering Discovery Environment (XSEDE), which is supported by National Science Foundation grant number OCI-1053575. We gratefully acknowledge helpful conversations with I. Szlufarska and J.D. Kubicki concerning the research strategy for this work.

5.7 Appendix 5A – the uniform compensating background charge (UCBC) method

This section details results obtained using a third charged-slab correction method that performed more inconsistently than the neutral slab (NS) and electron donor-ion (EDI) methods described in the main manuscript. Because this method is familiar to researchers who perform charged defect calculations in bulk solids, it is a seemingly attractive option to employ for charged slabs. However, key differences in the electrostatic properties of charged slabs versus bulk defects make this method generally inapplicable to periodic slab simulations.

The UCBC method is implemented in VASP by setting the charge state of the simulated atomic configuration by adding or removing electrons from the system. For modeling deprotonation, the user sets up a surface slab geometry with an H atom removed from the supercell (at the target surface group). An additional electron is then added to the system, bringing the system charge state back to where it would have been had the user removed an H^+. The unbalanced net charge in the initial system is countered by the automatic addition of a uniform background charge density that, when summed over the volume of the supercell, exactly cancels the excess electron added by the user. In practice, for slab geometries, this artificial background charge density creates large and unpredictable dipole (and multipole…) moments between the slab surface where negative charge is localized and the positively-charged vacuum layer separating the slab from its periodic image(s). The large electrostatic interaction energies associated with these charge distributions induce unpredictable changes in cell total energy, to a degree that VASP software authors admonish users to avoid performing such calculations [167].

We test whether these uncertain dipole energies can be cancelled when evaluating *relative* energies (*not* total energies) among slabs that vary only in the configuration of surface atoms. The series of slabs constructed have identical atomic and electronic composition, and differ only in the geometric arrangement of atoms on one side of the slab surface (the proton and Li^+ configurations detailed in the main manuscript).

When this procedure is performed using the AIMD approach, in which many atomic arrangements are explored due to thermal displacements, the UCBC method often resulted in the unwanted dissociation of solvation layer water molecules, which tended to separate into H^+ that re-adsorbed on the goethite surface, and OH^- that remained in solution. For these cases, even relative energies between identical slab atomic compositions should not be trusted, as the resulting series of geometries had differing number of neutral water, OH, and H in addition to the variations in surface configurations that were being investigated.

A second test of the UCBC method is performed by adopting the reasonable geometries obtained by AIMD simulation using the neutral slab (NS) method, and recalculating the configuration relative energies with an additional electron added to the system. In this procedure, only a single-point electronic optimization is performed, no geometry re-optimization is performed using the UCBC method. This approach yielded acceptable results for relative energies of deprotonation at the goethite (101) surface (Figure 5-16), but the results for relative configurational energies of Li^+ at the deprotonated surface (Figure 5-17) were inconsistent for geometries where the NS and EDI methods showed better agreement.

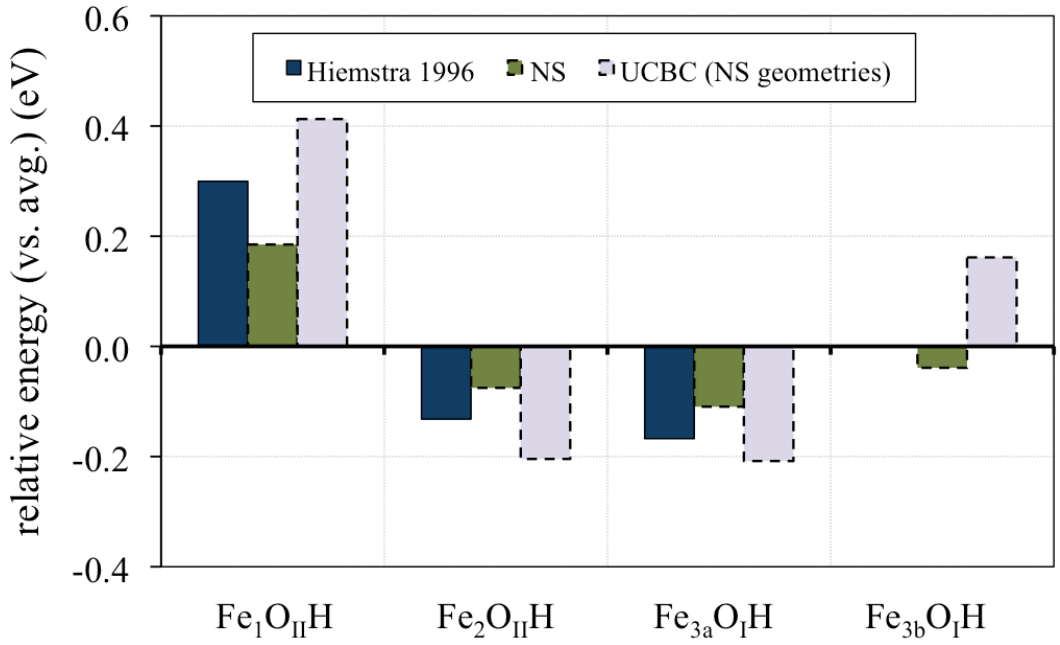

Figure 5-16: Relative deprotonation energies calculated with the NS and UCBC methods, as compared with relative deprotonation energies derived from pK_a of each surface Fe_xOH site. Calculated values are shown with dashed outlines. Results for the NS and UCBC series have rms errors of 81.1 and 80.8 meV, respectively, as compared to the experimental values. Averages within each series are computed using only the first three sites, as the $Fe_{3b}O_IH$ site is not reported separately in the experimental literature. These results are obtained using only gamma-point precision calculations for both the NS and UCBC methods, due to the difficulty in obtaining timely electronic convergence for high precisions calculations when employing the UCBC method.

Figure 5-16illustrates the relative Li^+ binding energies calculated using the NS and UCBC methods. While some sites have similar relative energies across both series, relative energies unpredictably and significantly vary for some configurations (e.g. L3b, L3c). Whereas the NS and EDI methods compared more favorably, with rms differences of 70-100 meV when comparing between series, the UCBC method performs more poorly, with rms of 145 meV when compared with the NS results.

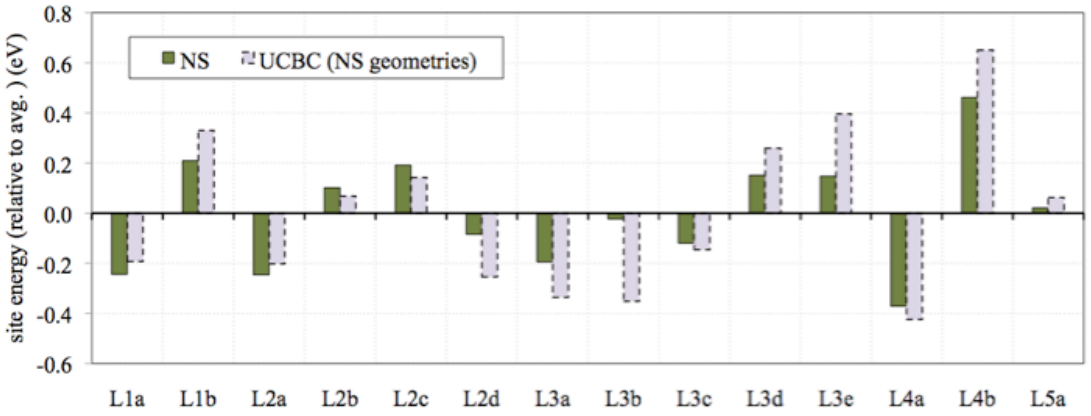

Figure 5-17: Calculated relative energies for Li^+ configurations using the NS (dark columns with solid outline) and UCBC (light columns with dashed outline) charge correction methods for slabs. The rms difference between the matching data points in the two series is 145 meV.

Given the relative consistency of the NS and EDI methods for calculating both deprotonation reactions and Li sorbate configurational energies on the goethite (101) slab, along with the relative inconsistency of the UCBC method, we chose not to include the results of the UCBC method in the main manuscript results. The results presented in this Appendix may serve as a guide for future research involving charged slab systems where the relative merits and inadequacies of different surface charge correction methods should be considered.

6 Open Issues and Future Directions

The work presented in this thesis represents a small sample of the types of materials phenomena suitable for study with *ab initio* and other computational materials methods. The methods and results presented here may serve as a starting point or guide for future research on Fe-oxyhydroxides or similar materials. Within the Fe-oxyhydroxide family there are many additional areas where application of computational methods may provide valuable insight into the structure, composition, and mechanical, thermodynamic and (electro)chemical properties of these materials.

6.1 Resolving bulk structures

While much recent work has been focused on resolving the crystal structure of ferrihydrite, there is still an active and ongoing debate over this fundamental material property. The *ab initio* methods detailed in this work demonstrate a rapid and resource-efficient means of evaluating proposed crystal structures using the single-phase Michel-model ferrihdyrite structure as a case study of the potential outcomes of this approach. However, few of the proposed structural models for ferrihydrite can so easily be incorporated into a computational model. Phases optimal for study using standard *ab initio* methods must meet certain criteria, namely that the structures should be single-phase and without random atomic site occupation. Multi-phase structures (e.g., the three-phase Drits model for ferrihydrite)[19, 15] could be examined as a combination of structures each evaluated independently, provided each sub-structure meets the single-phase requirements and interfacial energies between substructures can be shown to be minimal or estimable. Similarly, random site occuptation can be treated, e.g., using large unit cell so-called Special Quasirandom Structures [ref S. H. Wei, L. G. Ferreira, J. E. Bernard, and A. Zunger, Electronic properties of random alloys: special quasirandom structures, Phys. Rev. B 42, p. 9622-9649 (1990).] but add significant complexity to analysis. Where uncertainties in proposed structures exist (e.g., unknown position or occupation of ions for which experimental diffraction sensitivity is low), standard *ab initio* methods can be used to explore the space of possible configurations and evaluate

their stability and geometric/bonding properties. Insights from these results can help guide additional experimental efforts in an iterative process until the structure is understood.

More sophisticated computational approaches can begin to address uncertainties about more-complicated structural models, including those characterized by the presence of structural waters, cation vacancies or partial occupancies with short-range order, and other point-like defect types [19, 15, 119] . In these cases, the first steps of a computational approach would seek to evaluate these defects in isolation, while controlling as many other structural parameters as possible. For instance, one might study the relative energies of varying cation configurations on a partially-occupied lattice, with the goal of building a site-based interaction model for cation occupation/vacancy. After assembling *ab initio* results that describe site-based interactions, a Monte Carlo-based simulation approach could use these interaction energies to build out a model of the material structure over spatial domains larger than those possible to simulate using density functional theory methods alone.

6.2 Surface properties and applications

While the bulk properties of Fe-oxides and oxyhydroxides are employed in some applications of these materials (e.g. magnetic data storage media), the surface properties of micro- or nanoparticulate Fe-oxides and oxyhydroxides have primary functional importance in many industrial and environmental applications of these materials. Continuing study of these surface phenomena using both experimental and complementary computational techniques may uncover new applications or improve existing processes.

Fe-oxyhydroxides, in particular, are readily synthesized from solution as nanoparticles with high specific surface area and high observed reactivity toward a variety of waterborne ions. While these materials are already used at industrial scale as water filtration media for the removal of heavy metals, continuing studies on their surface

properties have demonstrated their potential for a number of other advanced applications. For instance, the photoinduced oxidation of toxic As^{3+} to relatively-benign As^{5+} at the ferrihydrite surface has been observed [168], potentially offering a pathway for the remediation of As contaminated groundwater that impacts millions of people worldwide. Additionally, due to the strong adsorption of carbonate ions on the surfaces of most Fe-oxyhydroxides, these materials have been proposed as sorption media to be used in carbon capture and storage (CCS) systems [139, 3, 5]. On the surfaces of these materials, when multiple ionic species are present in solution, ion binding is often either competitive or cooperative, depending on the preferred binding mechanisms of the different ions and the atomic structure of the mineral interface [4, 169]. By allowing study of specific targeted binding arrangements, computational techniques can offer insight into these complicated surface binding phenomena, which often involving multiple binding sites and cooperative binding arrangements that cannot be isolated in experimental samples.

Fe-oxide materials have been employed for decades as catalysts for the industrial production of ammonia. In recent years, hematite has also been studied as a catalyst for photo-induced water oxidation, or inorganic photosynthesis [170, 171]. While the efficiency of this catalytic process is low compared to more expensive and rare catalysts, the effectiveness of the cheap and abundant Fe-oxide catalyst is improved by the presence of metal dopants or point defects at the material surface [172-174]. Ongoing study of these surface defect properties using both experimental and computational techniques may enable the synthesis of competitive water-splitting catalysts based on common and stable Fe-oxides.

6.3 Computational challenges

The study of mineral surfaces, especially in the presence of liquid water, is a challenging task for modern computational methods. Purely *ab initio* methods are subject to size-scaling limitations that make them unable to directly simulate physically realistic sorption phenonema on the size scales present in nature. Even if realistic size scales were readily

achievable, the dynamic nature of the hydrogen bonded network of water molecules that comprises the solvation environment of real systems is difficult to replicate or measure using *ab initio* techniques, which are better suited to measure static phenomena involving fixed bonds. Classical potential models can reasonably accomplish the size and time scales requisite to simulate realistic aqueous surface environments at room temperature, but the complex chemistries of ion solvation, sorption, and surface hydration make it difficult to build robust potentials for this purpose. Continued development of advanced potential models that accommodate the dynamic chemistries of surface sorbates (e.g. ReaxFF-based models) may result in breakthroughs for the accuracy and applicability of this approach, but much work remains [175]. Within the *ab initio* modeling framework, development of methods to more accurately treat dispersion forces have recently been implemented and may aid in the simulation of solvation-mediated phenomena [125].

Many present approaches to surface modeling rely on approximate methods that simulate surface phenomena by the use of simplified or abbreviated atomic configurations, such as those described in the last chapter of this work. These methods, which include slab and cluster geometries with varying amounts of explicit solvation, can be used as a proxy for more realistic systems provided that the uncertainties or negative consequences of these configurational approximations can be controlled and accounted for. Implicit solvation methods, which add a continuum of virtual dielectric media to the simulated solvated surface, can offer another way around the obstacle of explicit representation of many layers of solvating water molecules, but are not widely implemented at present for slab geometry simulations, and are challenging to implement on charged species even for simple cluster geometries.

Accurate treatment of surface charge and the description of the electric double layer (EDL) remains an obstacle for both *ab initio* and classical simulation methods. The polarization of the solvation layers within the EDL, and the distribution of compensating counter ions that form the outer boundary of the EDL, while readily described from a statistical or analytical standpoint, are not practically replicable with present *ab initio* techniques due to size and computational speed limitations. These limitations make it

challenging to explicitly model any aqueous surface phenomena that are governed by surface charge, which include most of the geochemical and environmental phenomena of interest in the Fe-oxyhydroxides. Continued efforts to understand and model surface charge and solvation layer polarization in the context of explicit simulation of surface, solvent and sorbate atoms are necessary for the advance of computational study of mineral surface phenomena.

7 REFERENCES

[1] Cornell, R. M. and Schwertmann, U., 2003. *The Iron Oxides: Structure, Properties, Reactions, Occurrences and Uses*. Wiley-VCH.

[2] Navrotsky, A., Mazeina, L., and Majzlan, J., 2008. Size-driven structural and thermodynamic complexity in iron oxides. *Science* **319**, 1635-1638.

[3] Hausner, D. B., Bhandari, N., Pierre-Louis, A. M., Kubicki, J. D., and Strongin, D. R., 2009. Ferrihydrite reactivity toward carbon dioxide. *Journal of Colloid and Interface Science* **337**, 492-500.

[4] Strongin, D. R., Grey, C. P., Parise, J. B., and Kubicki, J. D., 2010. Surface science studies of environmentally relevant iron (oxy)hydroxides ranging from the nano to the macro-regime. *Surface Science* **604**, 1065-1069.

[5] Lammers, K., Murphy, R., Riendeau, A., Smirnov, A., Schoonen, M. A. A., and Strongin, D. R., 2011. CO2 Sequestration through Mineral Carbonation of Iron Oxyhydroxides. *Environmental Science & Technology* **45**, 10422-10428.

[6] Kresse, G. and Hafner, J., 1993. Ab Initio molecular-dynamics for open-shell transition-metals. *Physical Review B* **48**, 13115-13118.

[7] Kresse, G. and Furthmuller, J., 1996. Efficiency of ab-initio total energy calculations for metals and semiconductors using a plane-wave basis set. *Computational Materials Science* **6**, 15-50.

[8] Kresse, G. and Furthmuller, J., 1996. Efficient iterative schemes for ab initio total-energy calculations using a plane-wave basis set. *Physical Review B* **54**, 11169-11186.

[9] Pinney, N., Kubicki, J. D., Middlemiss, D. S., Grey, C. P., and Morgan, D., 2009. Density Functional Theory Study of Ferrihydrite and Related Fe-Oxyhydroxides. *Chemistry of Materials* **21**, 5727-5742.

[10] Michel, F. M., Ehm, L., Antao, S. M., Lee, P. L., Chupas, P. J., Liu, G., Strongin, D. R., Schoonen, M. A. A., Phillips, B. L., and Parise, J. B., 2007. The structure of ferrihydrite, a nanocrystalline material. *Science* **316**, 1726-1729.

[11] Majzlan, J., Grevel, K. D., and Navrotsky, A., 2003. Thermodynamics of Fe

oxides: Part II. Enthalpies of formation and relative stability of goethite (alpha-FeOOH), lepidocrocite (gamma-FeOOH), and maghemite (gamma-Fe2O3). *American Mineralogist* **88**, 855-859.

[12] Majzlan, J., Lang, B. E., Stevens, R., Navrotsky, A., Woodfield, B. F., and Boerio-Goates, J., 2003. Thermodynamics of Fe oxides: Part I. Entropy at standard temperature and pressure and heat capacity of goethite (alpha-FeOOH), lepidocrocite (gamma-FeOOH), and maghemite (gamma-Fe2O3). *American Mineralogist* **88**, 846-854.

[13] Majzlan, J., Navrotsky, A., and Schwertmann, U., 2004. Thermodynamics of iron oxides: Part III. Enthalpies of formation and stability of ferrihydrite (similar to Fe(OH)(3)), schwertmannite (similar to FeO(OH)(3/4)(SO4)(1/8)), and epsilon-Fe2O3. *Geochimica Et Cosmochimica Acta* **68**, 1049-1059.

[14] Janney, D. E., Cowley, J. M., and Buseck, P. R., 2000. Structure of synthetic 2-line ferrihydrite by electron nanodiffraction. *American Mineralogist* **85**, 1180-1187.

[15] Janney, D. E., Cowley, J. M., and Buseck, P. R., 2001. Structure of synthetic 6-line ferrihydrite by electron nanodiffraction. *American Mineralogist* **86**, 327-335.

[16] Jansen, E., Kyek, A., Schafer, W., and Schwertmann, U., 2002. The structure of six-line ferrihydrite. *Applied Physics a-Materials Science & Processing* **74**, S1004-S1006.

[17] Rancourt, D. G. and Meunier, J. F., 2008. Constraints on structural models of ferrihydrite as a nanocrystalline material. *American Mineralogist* **93**, 1412-1417.

[18] Manceau, A., 2009. Evaluation of the structural model for ferrihydrite derived from real-space modelling of high-energy X-ray diffraction data. *Clay Minerals* **44**, 19-34.

[19] Drits, V. A., Sakharov, B. A., Salyn, A. L., and Manceau, A., 1993. Structural model for ferrihydrite. *Clay Minerals* **28**, 185-207.

[20] Janney, D. E., Cowley, J. M., and Buseck, P. R., 2000. Transmission electron microscopy of synthetic 2-and 6-line ferrihydrite. *Clays and Clay Minerals* **48**, 111-119.

[21] McHale, J. M., Navrotsky, A., and Perrotta, A. J., 1997. Effects of increased

surface area and chemisorbed H2O on the relative stability of nanocrystalline gamma-Al2O3 and alpha-Al2O3. *Journal of Physical Chemistry B* **101**, 603-613.

[22] Yamaguchi, G. and Okumiya, M., 1969. Refinement of structure of tohdite 5Al2O3.H2O

REFINEMENT OF STRUCTURE OF TOHDITE 5AL203.H20. *Bulletin of the Chemical Society of Japan* **42**, 2247-&.

[23] Blochl, P. E., 1994. Projector Augmented-Wave Method. *Physical Review B* **50**, 17953-17979.

[24] Kresse, G. and Joubert, D., 1999. From ultrasoft pseudopotentials to the projector augmented-wave method. *Physical Review B* **59**, 1758-1775.

[25] Perdew, J. P., Burke, K., and Ernzerhof, M., 1996. Generalized gradient approximation made simple. *Physical Review Letters* **77**, 3865-3868.

[26] Anisimov, V. I., Aryasetiawan, F., and Lichtenstein, A. I., 1997. First-principles calculations of the electronic structure and spectra of strongly correlated systems: The LDA+U method. *Journal of Physics-Condensed Matter* **9**, 767-808.

[27] Rollmann, G., Rohrbach, A., Entel, P., and Hafner, J., 2004. First-principles calculation of the structure and magnetic phases of hematite. *Physical Review B* **69**.

[28] Zhou, F., Cococcioni, M., Marianetti, C. A., Morgan, D., and Ceder, G., 2004. First-principles prediction of redox potentials in transition-metal compounds with LDA + U. *Physical Review B* **70**.

[29] Wang, L., Maxisch, T., and Ceder, G., 2006. Oxidation energies of transition metal oxides within the GGA+U framework. *Physical Review B* **73**.

[30] Dudarev, S. L., Botton, G. A., Savrasov, S. Y., Szotek, Z., Temmerman, W. M., and Sutton, A. P., 1998. Electronic structure and elastic properties of strongly correlated metal oxides from first principles: LSDA+U, SIC-LSDA and EELS study of UO2 and NiO. *Physica Status Solidi a-Applied Research* **166**, 429-443.

[31] Rollmann, G., Entel, P., Rohrbach, A., and Hafner, J., 2005. High-pressure characteristics of alpha-Fe2O3 using DFT plus U. *Phase Transitions* **78**, 251-258.

[32] Monkhorst, H. J. and Pack, J. D., 1976. Special points for Brillouin-zone integrations. *Physical Review B* **13**, 5188-5192.

[33] Saalfeld, H. and Wedde, M., 1974. Refinement of crystal-structure of gibbsite, Al(OH)3. *Zeitschrift Fur Kristallographie* **139**, 129-135.

[34] Hill, R. J., 1979. Crystal-structure refinement and electron-density distribution in diaspore. *Physics and Chemistry of Minerals* **5**, 179-200.

[35] Corbato, C. E., Tettenhorst, R. T., and Christoph, G. G., 1985. Structure refinement of deuterated boehmite. *Clays and Clay Minerals* **33**, 71-75.

[36] Demichelis, R., Noel, Y., Zicovich-Wilson, C. M., Roetti, C., Valenzano, L., and Dovesi, R., 2008. Ab-initio quantum mechanical study of akdalaite (5Al 2O 3ldrH 2O): structure and vibrational spectrum. *Journal of Physics: Conference Series* **117**, 012013 (8 pp.)-012013 (8 pp.).

[37] Gronvold, F. and Westrum, E. F., 1959. Alpha-ferric oxide: Low temperature heat capacity and thermodynamic functions. *Journal of the American Chemical Society* **81**, 1780-1781.

[38] Ditmars, D. A., Ishihara, S., Chang, S. S., Bernstein, G., and West, E. D., 1982. Enthalpy and heat-capacity standard reference material - synthetic sapphire (alpha-Al2O3) from 10 to 2250 K. *Journal of Research of the National Bureau of Standards* **87**, 159-163.

[39] Perkins, D., Essene, E. J., Westrum, E. F., and Wall, V. J., 1979. New thermodynamic data for diaspore and their application to the system Al2O3-SiO2-H2O1. *American Mineralogist* **64**, 1080-1090.

[40] Hemingway, B. S., Robie, R. A., and Apps, J. A., 1991. Revised values for the thermodynamic properties of boehmite, AlO(OH), and related species and phases in the system AL-H-O. *American Mineralogist* **76**, 445-457.

[41] Hemingway, B. S., Robie, R. A., Fisher, J. R., and Wilson, W. H., 1977. Heat-capacities of gibbsite, Al(OH)3, between 13 and 480 K and magnesite, MgCO3, between 13 and 380 K and their standard entropies at 289.15 K, and heat-capacities of calorimetry conference benzoic-acid between 12 and 316 K. *Journal of Research of the Us Geological Survey* **5**, 797-806.

[42] Jiang, D. E. and Carter, E. A., 2003. Adsorption and diffusion energetics of hydrogen atoms on Fe(110) from first principles. *Surface Science* **547**, 85-98.

[43] Jiang, D. E. and Carter, E. A., 2004. Diffusion of interstitial hydrogen into and

through bcc Fe from first principles. *Physical Review B* **70**.

[44] Born, M. and Huang, K., 1954. Dynamical theory of crystal lattices. *Dynamical theory of crystal lattices*, xii+420 pp-xii+420 pp.

[45] Rosso, K. M. and Rustad, J. R., 2001. Structures and energies of AlOOH and FeOOH polymorphs from plane wave pseudopotential calculations. *American Mineralogist* **86**, 312-317.

[46] Demichelis, R., Noel, Y., Civalleri, B., Roetti, C., Ferrero, M., and Dovesi, R., 2007. The vibrational spectrum of alpha-AlOOH diaspore: An ab initio study with the CRYSTAL code. *Journal of Physical Chemistry B* **111**, 9337-9346.

[47] Kubicki, J. D., Paul, K. W., and Sparks, D. L., 2008. Periodic density functional theory calculations of bulk and the (010) surface of goethite. *Geochemical Transactions* **9**.

[48] Cambier, P., 1986. Infrared study of goethites of carying crystallinity and particle size. 1. Interpretation of OH and lattice vibration frequencies. *Clay Minerals* **21**, 191-200.

[49] Wolverton, C. and Ozolins, V., 2006. First-principles aluminum database: Energetics of binary Al alloys and compounds. *Physical Review B* **73**, 14.

[50] McQuarrie, D. A. and Simon, J. D., 1999. *Molecular Thermodynamics*. University Science Books.

[51] Atkins, P., 1997. *Physical Chemistry*. W.H. Freeman and Co, New York.

[52] Michel, F. M., Cismasu, A. C., Strongin, D. R., Parise, J. B., and Brown Jr., G. E., 2009. Real-space structural analysis of ferrihydrite nanoparticles*The 237th ACS National Meeting*, Salt Lake City, UT.

[53] Michel, F. M., Barron, V., and Brown, G. E., 2010. Cation vacancies and lattice strain in nano-sized ferrihydrite reveal clues to surface structure. *Geochimica Et Cosmochimica Acta* **74**, A706-A706.

[54] Michel, F. M., Barron, V., Torrent, J., Morales, M. P., Serna, C. J., Boily, J. F., Liu, Q. S., Ambrosini, A., Cismasu, A. C., and Brown, G. E., 2010. Ordered ferrimagnetic form of ferrihydrite reveals links among structure, composition, and magnetism. *Proceedings of the National Academy of Sciences of the United States of America* **107**, 2787-2792.

[55] Manceau, A., 2011. Critical evaluation of the revised akdalaite model for ferrihydrite. *American Mineralogist* **96**, 521-533.

[56] Zergenyi, R. S., Hirt, A. M., Zimmermann, S., Dobson, J. P., and Lowrie, W., 2000. Low-temperature magnetic behavior of ferrihydrite. *J. Geophys. Res.-Solid Earth* **105**, 8297-8303.

[57] Berquo, T. S., Banerjee, S. K., Ford, R. G., Penn, R. L., and Pichler, T., 2007. High crystallinity Si-ferrihydrite: An insight into its Neel temperature and size dependence of magnetic properties. *J. Geophys. Res.-Solid Earth* **112**, 12.

[58] Berquo, T. S., Erbs, J. J., Lindquist, A., Penn, R. L., and Banerjee, S. K., 2009. Effects of magnetic interactions in antiferromagnetic ferrihydrite particles. *Journal of Physics-Condensed Matter* **21**.

[59] Pankhurst, Q. A. and Pollard, R. J., 1992. Structural and magnetic-properties of ferrihydrite. *Clays and Clay Minerals* **40**, 268-272.

[60] Seehra, M. S., Babu, V. S., Manivannan, A., and Lynn, J. W., 2000. Neutron scattering and magnetic studies of ferrihydrite nanoparticles. *Physical Review B* **61**, 3513-3518.

[61] Punnoose, A., Phanthavady, T., Seehra, M. S., Shah, N., and Huffman, G. P., 2004. Magnetic properties of ferrihydrite nanoparticles doped with Ni, Mo, and Ir. *Physical Review B* **69**.

[62] Guyodo, Y., Banerjee, S. K., Penn, R. L., Burleson, D., Berauo, T. S., Seda, T., and Solheid, P., 2006. Magnetic properties of synthetic six-line ferrihydrite nanoparticles. *Physics of the Earth and Planetary Interiors* **154**, 222-233.

[63] Silva, N. J. O., Amaral, V. S., Carlos, L. D., Rodriguez-Gonzalez, B., Liz-Marzan, L. M., Berquo, T. S., Banerjee, S. K., Bermudez, V. d. Z., Millan, A., and Palacio, F., 2008. Evidence of random magnetic anisotropy in ferrihydrite nanoparticles based on analysis of statistical distributions. *Physical Review B* **77**.

[64] Morgan, D., Wang, B., Ceder, G., and van de Walle, A., 2003. First-principles study of magnetism in spinel MnO2. *Physical Review B* **67**.

[65] van de Walle, A., Asta, M., and Ceder, G., 2002. The Alloy Theoretic Automated Toolkit: A user guide. *Calphad-Computer Coupling of Phase Diagrams and Thermochemistry* **26**, 539-553.

[66] Berquo, T. S., Imbernon, R. A. L., Blot, A., Franco, D. R., Toledo, M. C. M., and Partiti, C. S. M., 2007. Low temperature magnetism and Mossbauer spectroscopy study from natural goethite. *Physics and Chemistry of Minerals* **34**, 287-294.

[67] Bengtson, A., Persson, K., and Morgan, D., 2008. Ab initio study of the composition dependence of the pressure-induced spin crossover in perovskite (Mg1-xFex)SiO3. *Earth and Planetary Science Letters* **265**, 535-545.

[68] Tsuchiya, T., Wentzcovitch, R. M., da Silva, C. R. S., and de Gironcoli, S., 2006. Spin transition in magnesiowustite in earth's lower mantle. *Phys Rev Lett* **96**, 198501.

[69] Lee, Y. L., Kleis, J., Rossmeisl, J., and Morgan, D., 2009. Ab initio energetics of LaBO3(001) (B=Mn, Fe, Co, and Ni) for solid oxide fuel cell cathodes. *Physical Review B* **80**.

[70] Robie, R. A. and Hemingway, B. S., 1995. Thermodynamic properties of minerals and related substances at 298.15 K and 1 bar (105 Pascals) pressure and at higher temperatures. *U.S. Geological Survey Bulletin* **2131**.

[71] Campbell, C. T., Parker, S. C., and Starr, D. E., 2002. The effect of size-dependent nanoparticle energetics on catalyst sintering. *Science* **298**, 811-814.

[72] Hummer, D. R., Kubicki, J. D., Kent, P. R. C., Post, J. E., and Heaney, P. J., 2009. Origin of Nanoscale Phase Stability Reversals in Titanium Oxide Polymorphs. *Journal of Physical Chemistry C* **113**, 4240-4245.

[73] Waychunas, G. A., Kim, C. S., and Banfield, J. F., 2005. Nanoparticulate iron oxide minerals in soils and sediments: unique properties and contaminant scavenging mechanisms. *Journal of Nanoparticle Research* **7**, 409-433.

[74] Pinney, N. and Morgan, D., 2013. Thermodynamics of Al-substitution in Fe-Oxyhydroxides *Geochimica et Cosmochimica Acta*.

[75] Pinney, N. and Morgan, D., 2013. Ab initio study of structurally bound water at cation vacancy sites in Fe- and Al-oxyhydroxide materials. *Geochimica Et Cosmochimica Acta* **114**, 94-111.

[76] Jambor, J. L. and Dutrizac, J. E., 1998. Occurrence and constitution of natural and synthetic ferrihydrite, a widespread iron oxyhydroxide. *Chemical Reviews* **98**, 2549-2585.

[77] Scheinost, A. C., Schulze, D. G., and Schwertmann, U., 1999. Diffuse reflectance spectra of Al substituted goethite: A ligand field approach. *Clays and Clay Minerals* **47**.

[78] Scheinost, A. C., Stanjek, H., Schulze, D. G., Gasser, U., and Sparks, D. L., 2001. Structural environment and oxidation state of Mn in goethite-groutite solid-solutions. *American Mineralogist* **86**.

[79] Kaur, N., Singh, B., and Kennedy, B. J., 2010. Dissolution of Cr, Zn, Cd, AND Pb single- and multi-metal-substituted goethite: relationship to structural, morphological, and dehydroxylation properties. *Clays and Clay Minerals* **58**.

[80] Tang, Y. Z., Michel, F. M., Zhang, L. H., Harrington, R., Parise, J. B., and Reeder, R. J., 2010. Structural Properties of the Cr(III)-Fe(III) (Oxy)hydroxide Compositional Series: Insights for a Nanomaterial "Solid Solution". *Chemistry of Materials* **22**, 3589-3598.

[81] Lewis, D. G. and Schwertmann, U., 1979. INFLUENCE OF A1 ON IRON-OXIDES .3. PREPARATION OF A1 GOETHITES IN M-KOH. *Clay Minerals* **14**, 115-126.

[82] Schwertmann, U., Fitzpatrick, R. W., Taylor, R. M., and Lewis, D. G., 1979. Influence of aluminum on iron-oxides. 2. Preparation and properties of Al-substituted hematites. *Clays and Clay Minerals* **27**, 105-112.

[83] Schulze, D. G. and Schwertmann, U., 1984. The influence of aluminum on iron-oxides. 10. Properties of Al-substituted goethites. *Clay Minerals* **19**, 521-539.

[84] Murad, E. and Schwertmann, U., 1983. THE INFLUENCE OF ALUMINUM SUBSTITUTION AND CRYSTALLINITY ON THE MOSSBAUER-SPECTRA OF GOETHITE. *Clay Minerals* **18**, 301-312.

[85] Wolska, E. and Szajda, W., 1987. TEMPERATURE EFFECTS ON COPRECIPITATED AL, FE-HYDROXIDES DURING HYDROTHERMAL TRANSFORMATIONS. *Journal of Thermal Analysis* **32**, 797-805.

[86] Liu, Q. S., Torrent, J., Yu, Y. J., and Deng, C. L., 2004. Mechanism of the parasitic remanence of aluminous goethite alpha-(Fe, Al)OOH. *J. Geophys. Res.-Solid Earth* **109**.

[87] Jentzsch, T. L. and Penn, R. L., 2006. Influence of aluminum doping on

ferrihydrite nanoparticle reactivity. *Journal of Physical Chemistry B* **110**, 11746-11750.

[88] Liu, H., Ma, M. R., Qin, M., Yang, L. J., and Wei, Y., 2010. Studies on the controllable transformation of ferrihydrite. *Journal of Solid State Chemistry* **183**, 2045-2050.

[89] Cismasu, A. C., Michel, F. M., Stebbins, J. F., Levard, C., and Brown, G. E., Jr., 2012. Properties of impurity-bearing ferrihydrite I. Effects of Al content and precipitation rate on the structure of 2-line ferrihydrite. *Geochimica Et Cosmochimica Acta* **92**.

[90] Liu, H., Chen, T., Frost, R. L., Chang, D., Qing, C., and Xie, Q., 2012. Effect of aging time and Al substitution on the morphology of aluminous goethite. *Journal of Colloid and Interface Science* **385**.

[91] Wolska, E., 1984. THE EFFECT OF SMALL DEVIATIONS IN AL0.5FE0.5(OH)3 STOICHIOMETRY ON THE DIRECTION OF AGING OF COPRECIPITATED AMORPHOUS ALFE-HYDROXIDES. *Journal of Materials Science Letters* **3**, 817-820.

[92] Wolska, E., 1988. Relations between the existence of hydroxyl ions in the anionic sublattice of hematite and its infrared and x-ray characteristics. *Solid State Ionics* **28**, 1349-1351.

[93] Ruan, H. D. and Gilkes, R. J., 1995. Dehydroxylation of aluminous goethite - unit-cell dimensions, crystal size and surface-area. *Clays and Clay Minerals* **43**, 196-211.

[94] Ruan, H. D., Frost, R. L., Kloprogge, J. T., and Duong, L., 2002. Infrared spectroscopy of goethite dehydroxylation. II. Effect of aluminium substitution on the behaviour of hydroxyl units. *Spectrochimica Acta Part a-Molecular and Biomolecular Spectroscopy* **58**, 479-491.

[95] Blanchard, M., Morin, G., Lazzeri, M., and Balan, E., 2010. First-principles study of the structural and isotopic properties of Al- and OH-bearing hematite. *Geochimica Et Cosmochimica Acta* **74**, 3948-3962.

[96] Wolska, E., 1988. RELATIONS BETWEEN THE EXISTENCE OF HYDROXYL IONS IN THE ANIONIC SUBLATTICE OF HEMATITE AND

ITS INFRARED AND X-RAY-CHARACTERISTICS. *Solid State Ionics* **28**, 1349-1351.

[97] Schwertmann, U. and Murad, E., 1983. Effect of pH on the formation of goethite and hematite from ferrihydrite. *Clays and Clay Minerals* **31**, 277-284.

[98] Schwertmann, U. and Cornell, R. M., 2000. Iron oxides in the laboratory: preparation and characterization. *Iron oxides in the laboratory: preparation and characterization*, xviii + 188 pp.

[99] Schwertmann, U., Friedl, J., Stanjek, H., and Schulze, D. G., 2000. The effect of Al on Fe oxides. XIX. Formation of Al-substituted hematite from ferrihydrite at 25 degrees C and pH 4 to 7. *Clays and Clay Minerals* **48**, 159-172.

[100] Ruan, H. D., Frost, R. L., and Kloprogge, J. T., 2001. The behavior of hydroxyl units of synthetic goethite and its dehydroxylated product hematite. *Spectrochimica Acta Part a-Molecular and Biomolecular Spectroscopy* **57**, 2575-2586.

[101] Bazilevskaya, E., Archibald, D. D., Aryanpour, M., Kubicki, J. D., and Martinez, C. E., 2011. Aluminum coprecipitates with Fe (hydr)oxides: Does isomorphous substitution of Al(3+) for Fe(3+) in goethite occur? *Geochimica Et Cosmochimica Acta* **75**, 4667-4683.

[102] Kubicki, J. D., Aryanpour, M., Kabalan, L., and Zhu, Q., 2012. Quantum mechanical calculations on Fe-O-H nanoparticles. *Geoderma* **189/190**.

[103] Fleming, S. and Rohl, A., 2005. GDIS: a visualization program for molecular and periodic systems. *Zeitschrift Fur Kristallographie* **220**, 580-584.

[104] Hiemstra, T., Venema, P., and VanRiemsdijk, W. H., 1996. Intrinsic proton affinity of reactive surface groups of metal (hydr)oxides: The bond valence principle. *Journal of Colloid and Interface Science* **184**, 680-692.

[105] Venema, P., Hiemstra, T., Weidler, P. G., and van Riemsdijk, W. H., 1998. Intrinsic proton affinity of reactive surface groups of metal (hydr)oxides: Application to iron (hydr)oxides. *Journal of Colloid and Interface Science* **198**, 282-295.

[106] Ponthieu, M., Juillot, F., Hiemstra, T., van Riemsdijk, W. H., and Benedetti, M. F., 2006. Metal ion binding to iron oxides. *Geochimica Et Cosmochimica Acta* **70**,

2679-2698.

[107] Hiemstra, T. and Van Riemsdijk, W. H., 2009. A surface structural model for ferrihydrite I: Sites related to primary charge, molar mass, and mass density. *Geochimica Et Cosmochimica Acta* **73**, 4423-4436.

[108] de Fontaine, D., 1994. Cluster Approach to Order-Disorder Transformations in Alloys, in Solid State Physics. *Solid State Physics* **47**, 33-176.

[109] Liu, H., Cao, F. L., Li, P., Wei, Y., and Hou, D. L., 2010. The formation of discoid hematite particles from Al-doped ferrihydrite: The effect of trace Fe(II) and the introduction procedures of Al(III). *Chemical Engineering Journal* **157**, 254-262.

[110] Lewis, D. G. and Schwertmann, U., 1979. Influence of aluminum on the formation of iron-oxides. 4. Influence of [Al], [OH], and temperature. *Clays and Clay Minerals* **27**, 195-200.

[111] Burleson, D. J. and Penn, R. L., 2006. Two-step growth of goethite from ferrihydrite. *Langmuir* **22**, 402-409.

[112] Ruetschi, P., 1984. Cation vacancy model for MnO2. *Journal of the Electrochemical Society* **131**, 2737-2744.

[113] Morgan, D., Balachandran, D., and Ceder, G., 2003. A drastic influence of point defects on phase stability in MnO2. *Solid-State Chemistry of Inorganic Materials Iv* **755**, 43-48.

[114] Wolska, E. and Szajda, W., 1985. STRUCTURAL AND SPECTROSCOPIC CHARACTERISTICS OF SYNTHETIC HYDROHEMATITE. *Journal of Materials Science* **20**, 4407-4412.

[115] Wolska, E. and Szajda, W., 1988. THE EFFECT OF CATIONIC AND ANIONIC SUBSTITUTION ON THE ALPHA-(AL, FE)2O3 LATTICE-PARAMETERS. *Solid State Ionics* **28**, 1320-1323.

[116] Wolska, E., Szajda, W., and Piszora, P., 1994. EFFECT OF THE ANIONIC SUBLATTICE HYDROXYLATION ON THE GOETHITE- MAGHEMITE TRANSFORMATION IN THE ALXFE1-XOOH SYSTEM. *Materials Letters* **21**, 191-195.

[117] Wolska, E., 1981. THE STRUCTURE OF HYDROHEMATITE. *Zeitschrift Fur*

Kristallographie **154**, 69-75.

[118] Pomies, M. P., Morin, G., and Vignaud, C., 1998. XRD study of the goethite-hematite transformation: application to the identification of heated prehistoric pigments. *European Journal of Solid State and Inorganic Chemistry* **35**, 9-25.

[119] Xu, W. Q., Hausner, D. B., Harrington, R., Lee, P. L., Strongin, D. R., and Parise, J. B., 2011. Structural water in ferrihydrite and constraints this provides on possible structure models. *American Mineralogist* **96**, 513-520.

[120] Hiemstra, T., 2012. Surface and Mineral Structure of Ferrihydrite. *Geochimica et Cosmochimica Acta*

[121] Ruan, H. D., Frost, R. L., Kloprogge, J. T., and Duong, L., 2002. Infrared spectroscopy of goethite dehydroxylation: III. FT-IR microscopy of in situ study of the thermal transformation of goethite to hematite. *Spectrochimica Acta Part a-Molecular and Biomolecular Spectroscopy* **58**, 967-981.

[122] Schwertmann, U., 1984. The double dehydroxylation peak of goethite. *Thermochimica Acta* **78**, 39-46.

[123] Beran, A. and Rossman, G. R., 2006. OH in naturally occurring corundum. *European Journal of Mineralogy* **18**, 441-447.

[124] Dion, M., Rydberg, H., Schroder, E., Langreth, D. C., and Lundqvist, B. I., 2004. Van der Waals density functional for general geometries. *Physical Review Letters* **92**.

[125] Grimme, S., 2006. Semiempirical GGA-type density functional constructed with a long-range dispersion correction. *Journal of Computational Chemistry* **27**, 1787-1799.

[126] Tkatchenko, A., Romaner, L., Hofmann, O. T., Zojer, E., Ambrosch-Draxl, C., and Scheffler, M., 2010. Van der Waals Interactions Between Organic Adsorbates and at Organic/Inorganic Interfaces. *Mrs Bulletin* **35**, 435-442.

[127] Reckien, W., Janetzko, F., Peintinger, M. F., and Bredow, T., 2012. Implementation of empirical dispersion corrections to density functional theory for periodic systems. *Journal of Computational Chemistry* **33**, 2023-2031.

[128] Cambier, P., 1986. Infrared study of goethite of varying crystallinity and particle-size. 1. Interpretation of OH and lattice vibration frequencies. *Clay Minerals* **21**,

191-200.

[129] Prasad, P. S. R., Prasad, K. S., Chaitanya, V. K., Babu, E. V. S. S. K., Sreedhar, B., and Murthy, S. R., 2006. In situ FTIR study on the dehydration of natural goethite. *Journal of Asian Earth Sciences* **27**, 503-511.

[130] Ohno, K., Okimura, M., Akai, N., and Katsumoto, Y., 2005. The effect of cooperative hydrogen bonding on the OH stretching-band shift for water clusters studied by matrix-isolation infrared spectroscopy and density functional theory. *Physical Chemistry Chemical Physics* **7**, 3005-3014.

[131] Rustad, J. R. and Boily, J.-F., 2010. Density functional calculation of the infrared spectrum of surface hydroxyl groups on goethite (alpha-FeOOH). *American Mineralogist* **95**, 414-417.

[132] Nielsen, U. G., Paik, Y., Julmis, K., Schoonen, M. A. A., Reeder, R. J., and Grey, C. P., 2005. Investigating sorption on iron-oxyhydroxide soil minerals by solid-state NMR spectroscopy: A Li-6 MAS NMR study of adsorption and absorption on goethite. *Journal of Physical Chemistry B* **109**, 18310-18315.

[133] Kim, J., Nielsen, U. G., and Grey, C. P., 2008. Local environments and lithium adsorption on the iron oxyhydroxides lepidocrocite (gamma-FeOOH) and goethite (alpha-FeOOH): A H-2 and Li-7 solid-state MAS NMR study. *Journal of the American Chemical Society* **130**, 1285-1295.

[134] Hiemstra, T. and VanRiemsdijk, W. H., 1996. A surface structural approach to ion adsorption: The charge distribution (CD) model. *Journal of Colloid and Interface Science* **179**, 488-508.

[135] Venema, P., Hiemstra, T., and vanRiemsdijk, W. H., 1996. Multisite adsorption of cadmium on goethite. *Journal of Colloid and Interface Science* **183**, 515-527.

[136] Ponthieu, M., Benedetti, M. F., Hiemstra, T., and van Riemsdijk, W. H., 2002. Generic CD MUSIC description of metal ions sorption to various oxyhydroxides. *Abstracts of Papers of the American Chemical Society* **223**, 096-GEOC.

[137] Paul, K. W., Kubicki, J. D., and Sparks, D. L., 2006. Quantum chemical calculations of sulfate adsorption at the Al- and Fe-(Hydr)oxide-H2O interface-estimation of Gibbs free energies. *Environmental Science & Technology* **40**, 7717-7724.

[138] Aquino, A. J. A., Tunega, D., Haberhauer, G., Gerzabek, M. H., and Lischka, H., 2007. Quantum chemical adsorption studies on the (110) surface of the mineral goethite. *Journal of Physical Chemistry C* **111**, 877-885.

[139] Kubicki, J. D., Kwon, K. D., Paul, K. W., and Sparks, D. L., 2007. Surface complex structures modelled with quantum chemical calculations: carbonate, phosphate, sulphate, arsenate and arsenite. *European Journal of Soil Science* **58**, 932-944.

[140] Aquino, A. J. A., Tunega, D., Haberhauer, G., Gerzabek, M. H., and Lischka, H., 2008. Acid-base properties of a goethite surface model: A theoretical view. *Geochimica Et Cosmochimica Acta* **72**, 3587-3602.

[141] Carlier, D., Menetrier, M., Grey, C. P., Delmas, C., and Ceder, G., 2003. Understanding the NMR shifts in paramagnetic transition metal oxides using density functional theory calculations. *Physical Review B* **67**, 14.

[142] Grey, C. P. and Dupre, N., 2004. NMR studies of cathode materials for lithium-ion rechargeable batteries. *Chemical Reviews* **104**, 4493-4512.

[143] Sakurai, Y., Arai, H., Okada, S., and Yamaki, J., 1997. Low temperature synthesis and electrochemical characteristics of LiFeO2 cathodes. *Journal of Power Sources* **68**, 711-715.

[144] Kim, J. and Grey, C. P., 2010. H-2 and Li-7 Solid-State MAS NMR Study of Local Environments and Lithium Adsorption on the Iron(III) Oxyhydroxide, Akaganeite (beta-FeOOH). *Chemistry of Materials* **22**, 5453-5462.

[145] Middlemiss, D. S., Ilott, A. J., Clement, R. J., Strobridge, F. C., and Grey, C. P., 2013. Density Functional Theory-Based Bond Pathway Decompositions of Hyperfine Shifts: Equipping Solid-State NMR to Characterize Atomic Environments in Paramagnetic Materials. *Chemistry of Materials* **25**, 1723-1734.

[146] Persson, K. A., Waldwick, B., Lazic, P., and Ceder, G., 2012. Prediction of solid-aqueous equilibria: Scheme to combine first-principles calculations of solids with experimental aqueous states. *Physical Review B* **85**.

[147] Liptak, M. D., Gross, K. C., Seybold, P. G., Feldgus, S., and Shields, G. C., 2002. Absolute pK(a) determinations for substituted phenols. *Journal of the American Chemical Society* **124**, 6421-6427.

[148] Kelly, C. P., Cramer, C. J., and Truhlar, D. G., 2006. Aqueous solvation free energies of ions and ion-water clusters based on an accurate value for the absolute aqueous solvation free energy of the proton. *Journal of Physical Chemistry B* **110**, 16066-16081.

[149] Leung, K. and Criscenti, L. J., 2012. Predicting the acidity constant of a goethite hydroxyl group from first principles. *Journal of Physics-Condensed Matter* **24**.

[150] Gaboriaud, F. and Ehrhardt, J., 2003. Effects of different crystal faces on the surface charge of colloidal goethite (alpha-FeOOH) particles: An experimental and modeling study. *Geochimica Et Cosmochimica Acta* **67**, 967-983.

[151] Boily, J. F., Lutzenkirchen, J., Balmes, O., Beattie, J., and Sjoberg, S., 2001. Modeling proton binding at the goethite (alpha-FeOOH)-water interface. *Colloids and Surfaces a-Physicochemical and Engineering Aspects* **179**, 11-27.

[152] Hiemstra, T., Dewit, J. C. M., and Vanriemsdijk, W. H., 1989. MULTISITE PROTON ADSORPTION MODELING AT THE SOLID-SOLUTION INTERFACE OF (HYDR)OXIDES - A NEW APPROACH .2. APPLICATION TO VARIOUS IMPORTANT (HYDR)OXIDES. *Journal of Colloid and Interface Science* **133**, 105-117.

[153] Kresse, G. and Hafner, J., 1993. Ab initio molecular-dynamics for liquid-metals. *Physical Review B* **47**, 558-561.

[154] Filhol, J. S. and Neurock, M., 2006. Elucidation of the electrochemical activation of water over Pd by first principles. *Angewandte Chemie-International Edition* **45**, 402-406.

[155] Taylor, C. D., Wasileski, S. A., Filhol, J. S., and Neurock, M., 2006. First principles reaction modeling of the electrochemical interface: Consideration and calculation of a tunable surface potential from atomic and electronic structure. *Physical Review B* **73**.

[156] Paul, K. W., Kubicki, J. D., and Sparks, D. L., 2007. Sulphate adsorption at the Fe(hydr)oxide-H2O interface: comparison of cluster and periodic slab DFT predictions. *European Journal of Soil Science* **58**, 978-988.

[157] Skulason, E., Karlberg, G. S., Rossmeisl, J., Bligaard, T., Greeley, J., Jonsson, H., and Norskov, J. K., 2007. Density functional theory calculations for the hydrogen

evolution reaction in an electrochemical double layer on the Pt(111) electrode. *Physical Chemistry Chemical Physics* **9**, 3241-3250.

[158] Machesky, M. L., Predota, M., Wesolowski, D. J., Vlcek, L., Cummings, P. T., Rosenqvist, J., Ridley, M. K., Kubicki, J. D., Bandura, A. V., Kumar, N., and Sofo, J. O., 2008. Surface Protonation at the Rutile (110) Interface: Explicit Incorporation of Solvation Structure within the Refined MUSIC Model Framework. *Langmuir* **24**, 12331-12339.

[159] Rossmeisl, J., Skulason, E., Bjorketun, M. E., Tripkovic, V., and Norskov, J. K., 2008. Modeling the electrified solid-liquid interface. *Chemical Physics Letters* **466**, 68-71.

[160] Rustad, J. R. and Boily, J. F., 2010. Density functional calculation of the infrared spectrum of surface hydroxyl groups on goethite (alpha-FeOOH). *American Mineralogist* **95**, 414-417.

[161] Hiemstra, T., Vanriemsdijk, W. H., and Bolt, G. H., 1989. MULTISITE PROTON ADSORPTION MODELING AT THE SOLID-SOLUTION INTERFACE OF (HYDR)OXIDES - A NEW APPROACH .1. MODEL DESCRIPTION AND EVALUATION OF INTRINSIC REACTION CONSTANTS. *Journal of Colloid and Interface Science* **133**, 91-104.

[162] Villalobos, M., Trotz, M. A., and Leckie, J. O., 2003. Variability in goethite surface site density: evidence from proton and carbonate sorption. *Journal of Colloid and Interface Science* **268**, 273-287.

[163] Villalobos, M. and Perez-Gallegos, A., 2008. Goethite surface reactivity: A macroscopic investigation unifying proton, chromate, carbonate, and lead(II) adsorption. *Journal of Colloid and Interface Science* **326**, 307-323.

[164] Makov, G. and Payne, M. C., 1995. Periodic boundary conditions in ab-initio calculations. *Physical Review B* **51**, 4014-4022.

[165] Neugebauer, J. and Scheffler, M., 1992. Adsorbate-substrate and adsorbate-adsorbate interactions of Na and K adlayers on Al(111). *Physical Review B* **46**, 16067-16080.

[166] Predota, M., Bandura, A. V., Cummings, P. T., Kubicki, J. D., Wesolowski, D. J., Chialvo, A. A., and Machesky, M. L., 2004. Electric double layer at the rutile

(110) surface. 1. Structure of surfaces and interfacial water from molecular dynamics by use of ab initio potentials. *Journal of Physical Chemistry B* **108**, 12049-12060.

[167] Kresse, G., Marsman, M., and Furthmuller, J., 2013, *VASP the GUIDE*, http://cms.mpi.univie.ac.at/VASP/

[168] Bhandari, N., Reeder, R. J., and Strongin, D. R., 2012. Photoinduced Oxidation of Arsenite to Arsenate in the Presence of Goethite. *Environmental Science & Technology* **46**, 8044-8051.

[169] Kubicki, J. D., Paul, K. W., Kabalan, L., Zhu, Q., Mrozik, M. K., Aryanpour, M., Pierre-Louis, A. M., and Strongin, D. R., 2012. ATR-FTIR and Density Functional Theory Study of the Structures, Energetics, and Vibrational Spectra of Phosphate Adsorbed onto Goethite. *Langmuir* **28**, 14573-14587.

[170] Katz, M. J., Riha, S. C., Jeong, N. C., Martinson, A. B. F., Farha, O. K., and Hupp, J. T., 2012. Toward solar fuels: Water splitting with sunlight and "rust"? *Coordination Chemistry Reviews* **256**, 2521-2529.

[171] Bora, D. K., Braun, A., and Constable, E. C., 2013. "In rust we trust". Hematite - the prospective inorganic backbone for artificial photosynthesis. *Energy & Environmental Science* **6**, 407-425.

[172] Deng, J. J., Zhong, J., Pu, A. W., Zhang, D., Li, M., Sun, X. H., and Lee, S. T., 2012. Ti-doped hematite nanostructures for solar water splitting with high efficiency. *Journal of Applied Physics* **112**, 6.

[173] Zhang, M., Lin, Y. J., Mullen, T. J., Lin, W. F., Sun, L. D., Yan, C. H., Patten, T. E., Wang, D. W., and Liu, G. Y., 2012. Improving Hematite's Solar Water Splitting Efficiency by Incorporating Rare-Earth Upconversion Nanomaterials. *Journal of Physical Chemistry Letters* **3**, 3188-3192.

[174] Yang, T. Y., Kang, H. Y., Sim, U., Lee, Y. J., Lee, J. H., Koo, B., Nam, K. T., and Joo, Y. C., 2013. A new hematite photoanode doping strategy for solar water splitting: oxygen vacancy generation. *Physical Chemistry Chemical Physics* **15**, 2117-2124.

[175] Aryanpour, M., van Duin, A. C. T., and Kubicki, J. D., 2010. Development of a Reactive Force Field for Iron-Oxyhydroxide Systems. *Journal of Physical*

Chemistry A **114**, 6298-6307.